CRISTINA LOIS GÓMEZ

# Study of Silicon Microstrip Detector Properties for the LHCb Silicon Tracker

---

MEMORIA PRESENTADA
NO DEPARTAMENTO DE FÍSICA DE PARTÍCULAS
DA UNIVERSIDADE DE SANTIAGO DE COMPOSTELA
PARA OPTAR Ó GRAO DE DOUTORA EN FÍSICA.
DIRECTORES: **D. Bernardo Adeva Andany**
E **D. Pablo Vázquez Regueiro**

XANEIRO DE 2006

email: `lois@physik.unizh.ch`
web: `http://www.usc.es/gaes/personal/cristina`

D. **BERNARDO ADEVA ANDANY**, catedrático do Departamento de Física de Partículas, e D. **PABLO VÁZQUEZ REGUEIRO**, investigador posdoutoral do Departamento de Física de Partículas, Área de Física Atómica, Molecular e Nuclear da Universidade de Santiago de Compostela.

**INFORMAN:**

Que o traballo titulado **Study of Silicon Microstrip Detector Properties for the LHCb Silicon Tracker** foi realizado baixo a súa dirección por

**Cristina Lois Gómez**

no Departamento de Física de Partículas, Área de Física Atómica, Molecular e Nuclear, da Universidade de Santiago de Compostela, e constitúe a memoria que se presenta para optar ó grao de Doutora en Física.

E para que así conste, asínano en Santiago de Compostela, a 16 de Xaneiro de 2006.

Bernardo Adeva Andany

Pablo Vázquez Regueiro

# Acknowledgments

I wish to express my gratitude to my supervisors B. Adeva and P. Vázquez. Also to the rest of the group and department, and to those who have shared the office with me, especially to Leticia, Oton and Toño for creating a nice atmosphere.

This thesis has been performed inside the context of the LHCb experiment, which involves efforts from hundreds of people. Particularly, I would like to thank the Silicon Tracker group in Zürich. In the end I spent so much time there! I must acknowledge Prof. U. Straumann for allowing me to be a part of his research group. Thanks also to Olaf for correcting all my notes, and to my lab- and officemates Ralf, Matt, Andreas, Markus, Dima, Achim, Johannes, for always treating me in a friendly and respectful manner. Special thanks to Frank Lehner, for all his kind help and support. Thanks so much for helping me! Not only for proposing and supervising my work, but also for encouraging and motivating me to finish this thesis. My gratitude to all the members of the group for their help and kind hospitality during the time I spent there.

Most of the measurements presented in Chapter 10 have been performed by a group of undergraduate students from the University of Zürich. Thanks to Gisela, Dominic, Lukas, Angela, Nicola, Eveline, Ananda, Thomas, Samuel, Tiziano and Patrick for all the work they have done.

I would also like to thank my friends for helping me through the difficult times, and who made my frequent change of residence much easier. Thanks to Alberto, Belén, Thorsten, Ralf, Javi, Lara, and many others for their unconditional friendship.

My gratitude to my parents, Elena and Ramón, and my sister, Gema, who have supported me always, and who have suffered my absence, my stress and the little time I have had for them during these past years.

Thanks over all to Iván. Thanks for being there, for your continuous help and support. Thanks for reading and correcting every single line I wrote, but

especially for believing in me and for convincing me that this would come to a successful end. You know that without you this would not have been possible. This thesis is dedicated to you with all my love.

# Contents

# Chapter 1

# Introduction

## 1.1 Motivation of this work

One of the main goals of particle physics is the determination of the fundamental structure of the matter. The currently accepted model for elementary particle physics, the Standard Model (SM), requires 12 matter elementary particles and four force carrier particles to summarize all what we know about the most fundamental constituents of matter and their interactions. The SM explains and predicts a vast variety of phenomena, and subtle effects predicted by the model have been repeatedly verified in high-precision experiments. Nevertheless, there are important aspects that remain unexplained, like the origin of the mass of particles or the values of some fundamental parameters.

A requirement of any particle physics theory is that every particle (for example a proton) has its antiparticle (in this case called antiproton), as was first pointed out by Dirac [1, 2]. An antiparticle has the same mass as the corresponding particle, but with some quantum numbers, like the electric charge, reversed. When a particle meets its antiparticle both annihilate and their masses are transformed into radiation. Existence of antimatter was extensively proved in last century, and nowadays has found applications in everyday life, as for example the use of low-energy antielectrons (called positrons) in medical imaging tools like PET [1] devices.

---

[1] PET (Positron Emission Tomography) is a medical tool which produces images for disease detection. Radioactive nuclei are injected to the patient, and they accumulate in the area or tissue to image. Positrons coming from the decay of these radioactive nuclei annihilate with electrons in nearby atoms, producing energy that emerges as photons. These photons are collected allowing the reconstruction the targeted area.

The cosmological theories currently accepted require that equal quantities of matter and antimatter should have been created after the Big Bang. However, an asymmetry in the quantities of matter and antimatter is at present observed in Nature, which is a key property of our world.[2] The observed imbalance might come from CP violation [3], an effect that occurs only with certain kind of elementary particles.

The CPT Theorem is one of the most basic precepts of particle physics. It considers the three independent transformations C (charge conjugation), P (space reversal or parity), and T (time reversal), and states that the combined operation of time reversal, charge conjugation, and space reversal in any order is an exact symmetry of any interaction, meaning that under the three transformations all physical laws must be invariant.[3] To elaborate, if each particle is replaced with its corresponding antiparticle, and the space coordinates and time are reversed, the dynamics of both particle and antiparticle is the same [4]. In the macroscopic world these three symmetries hold separately. For example, an object going from A to B will follow the same trajectory but backwards, if time is reversed, returning from B to A.

However, CPT theorem does not state anything about the separate operation of one or two of these transformations in the elementary particle world. For example, it was proved [5], after the suggestion by Lee and Yang [6], that when one applies the transformation P to a particle called neutrino, the reversed particle does not exist. One finds in Nature left-handed neutrinos and right-handed antineutrinos, but not right-handed neutrinos and left-handed antineutrinos. This is called P violation in weak interaction, which is the interaction governing the dynamics of these particles. The symmetry of this interaction is restored when one applies the combined CP transformation, that is, left-handed neutrinos follow the same laws as right-handed antineutrinos.

In 1964 it was observed that CP symmetry is violated in systems of neutral K-mesons [7]. Contrary to neutrinos, which are leptons, K-mesons [8] are hadrons, which means that as protons or neutrons, are made up of quarks. CP violation may explain why our world has much more matter than antimatter, due to the slight differences in the way that quarks and antiquarks interact through electroweak interactions. In fact, CP violation was proposed long time ago by Sakharov [9] as one of the three conditions that should be satisfied to have an Universe with different quantities of matter and antimat-

---

[2] If equal quantities of matter and antimatter would exist, they would end up annihilating between them, leaving the Universe made up only of light.

[3] More precisely, what are invariant are the Hamiltonians governing the dynamics of the given particles.

ter.

In the SM, CP violation is inextricably tied up with the existence of at least six quark flavours, and is completely described by a single parameter. This is a complex phase in the Cabibbo-Kobayashi-Maskawa (CKM) matrix [10, 11], which parameterizes transitions between different generations of quarks by a set of four independent parameters.

In any case, CP violation in neutral K-mesons is small, at the level of 0.2%, making difficult to trace back these differences to the theories for elementary particles, as for example this complex phase in the CKM matrix. It is expected that CP violation is stronger in another system of neutral mesons, called B-mesons [8]. The study of CP violation in B-meson systems is the main purpose of the LHCb experiment. Its ability to measure precisely some fundamental parameters in several complementing ways will test the SM picture of CP violation and will provide the exciting possibility of seeing evidence for physics beyond the SM.

To investigate and measure the parameters that describe the matter, physicists made use of accelerators to break up particles into their fundamental constituents. The basics of this procedure is the following. A bunch of well-known particles as electrons or protons are accelerated to huge energies using electric fields. Particles are accelerated very close to the speed of light, acquiring huge kinetic energies. Using a sophisticated system of magnets, the bunch is curved and focused. At a certain time, the bunch is directed against a target (fixed target experiments) or a second bunch of particles traveling in opposite direction (collider experiments). Usually, this second bunch of particles has the same but opposite velocity as the first one, and this kind of collision is called a center-of-mass collision.

When the collision happens, and due to the high kinetic energy of the colliding particles, we can not only investigate their internal structure but also create new exotic particles that do not occur normally in our macroscopic world. In these high-energetic collisions, what interacts are not the colliding particles themselves but their fundamental constituents. This is because the well-known de Broglie formula [12] that, according to the wave-particle duality principle, relates the energy of a particle to its associated wave-length as $\lambda \propto 1/E$. As one should use waves with wave-length of the same size as the details one wants to observe, collisions of particles with high kinetic energies allow to study their internal structure.

In the collision between the highly accelerated particles, their huge kinetic energy is available not only as kinetic energy for the resulting particles, but also as mass to create new particles. This is expressed through the equivalence between energy and mass formulated by Einstein in his famous paper in 1905 [13] as $E = mc^2$. Energy ($E$) can be converted into mass ($m$) and vice versa, with the square of the speed of light ($c$) as conversion factor. If the initial particles have enough energy, they can create new particles heavier than the particles themselves. The set of produced particles depends essentially on various conservation laws and on the amount of center-of-mass energy available in the collision. Therefore high-energy experiments, through energetic collisions of other particles, allow to observe more massive and more exotic particles than the initial ones, which do not occur under normal circumstances in nature.

Many of the particles created in the collision are highly unstable, and decay fast into more stable states, giving rise to more particles. Essentially, the lifetime of the particle before decaying is given by the strength of the interaction involved, and varies between about $10^{-23}$ s for strong interaction and about $10^{-10}$ s for weak interaction. Ultimately, one ends again with a set of "stable" and known particles, as protons, neutrons, electrons, neutrinos and muons. Usually a huge number of them is produced: in a collision between two protons at very high energies, one typically ends up with hundreds of particles.

The production or decay of a given particle depends on the forces governing the behaviour of its constituents, and therefore contains information about the way the basic constituents of the matter interact. This information can be extracted studying the characteristics of new particles, like masses and lifetimes, and through the study of the decay ratios of unstable particles into different states. However, in order to understand the underlaying dynamics, we have to analyze the kinematics. This means that after the collision, we need to count, trace and identify all the different particles that were produced to fully reconstruct the process. A particle can be fully identified when we know its charge and its mass. This is done with a set of very sensitive and specialized particle detectors that are able to measure a specific set of particle properties, such as charge, mass or energy.

The aim of this thesis is to describe the performance and characteristics of the silicon microstrip detectors that will be used in the Silicon Tracker of LHCb experiment. LHCb will be installed at the Large Hadron Collider (LHC) [14], a particle accelerator that is being built at CERN [15], in a subterranean ring of 27 km circumference at the border between France and Switzerland. In LHC, two beams of protons at a center-of-mass energy of 14 TeV will collide at four different points along the ring. Around one of these collision points it will be installed the LHCb spectrometer. As well as having the highest energy of any accelerator in the world, the LHC will also have the most intense beams.

Due to the huge LHC energy, new particles never observed yet may appear after the collision. They will decay very fast, offering the possibility to study the rates of the different decays, never observed before or observed with low statistics, and other rare phenomena. Particle physicists expect to extract through them parameters describing interactions between the fundamental constituents of the matter, in particular, they expect to check whether the SM is an adequate model for describing fundamental forces and particles.

The LHCb experiment [16, 17] has been designed to perform high-precision measurements of CP violating phenomena and rare decays in the B meson systems. B-mesons are bound states of one $b$-antiquark and a lighter quark. The study of B-meson decays is a key process for the precise determination of CP violating parameters since, according to the SM, large CP violation effects are predicted in them. Furthermore, high statistics will be achieved since, in proton-proton collisions at LHC energies, a production of about $10^{12}$ $b\bar{b}$ pairs per year is estimated.[4] CP violation is expected to manifest in time dependent decay rate asymmetries of B and $\overline{\mathrm{B}}$ into the same final state, and in asymmetries in the decay rates of B and $\overline{\mathrm{B}}$ into CP conjugated specific final states. In addition, measurements will be possible in many different decay channels, allowing to over-constrain the parameters and, possibly, to find inconsistencies suggesting the existence of physics beyond the SM.

As it was pointed out above, to measure the rate of the different decays, all decay products have to be identified. To do this, specialized particle detectors measure a specific set of particle properties, such as momentum, charge, mass or energy. A central element of any high energy physics experiment is the tracking system, which records the traces of charged particles created in the collision. Together with a magnetic field, it allows in addition the determination of the momentum of those particles.

In LHCb, excellent momentum resolution is required in order to measure precisely the invariant mass of B decay candidates and separate the B meson signal from the background. To that purpose, precise track determination is necessary. It was decided to construct the tracking system combining two detector technologies: the outer region, away from the beam-pipe, is covered by the straw-tube drift chambers, and it is called Outer Tracker [18]. The inner region, around the beam-pipe, where particle densities are higher, is covered by silicon microstrip detectors, and it is called Silicon Tracker (ST) [19, 20].

---

[4] At LHC energies, the B production cross-section is estimated to be around 0.5 mb, yielding about $10^{12}$ $b\bar{b}$ pairs per year at the nominal luminosity of $\mathcal{L}= 2 \times 10^{32}$ cm$^{-2}$ s$^{-1}$.

Simulation studies have shown that a spatial resolution of around 60 $\mu$m is adequate for the ST. These silicon microstrip detectors are very thin $n$-doped silicon wafers, with thicknesses between 320 and 500 $\mu$m, where fine strips of $p^+$-doped silicon are implanted using photolitographic and etching techniques. Typical sizes are about $10 \times 10$ cm$^2$ sensors with around 500 parallel 50 $\mu$m wide strips, with centers separated approximately 200 $\mu$m. Each microstrip forms with the silicon bulk a $pn$-junction. When a charged particle crosses the microstrip detector generates electron-hole pairs. By applying a reverse polarization to the $pn$-junctions, this charge is collected in the $p^+$-strips. An individual readout of the $p^+$-strips allows the determination of the position of the traversing particle through the analysis of the charge collected in each strip. A throughout understanding of the silicon microstrip detector properties and the optimization of some design parameters, such as thickness or strip geometry, to achieve the desired performance are the main points at issue in this thesis.

## 1.2 Sketch of contents

This thesis describes the different tests carried out on silicon microstrip detectors to be installed in the Silicon Tracker (ST) of the LHCb experiment, starting from the characterization of different prototypes up to the final tests on the detectors that are being installed at CERN.

The results of the work summarized along this thesis can be divided in three main blocks. The first one comprises an exhaustive characterization of the several prototype sensors that were selected as suitable candidates for the experiment. The goal of this part of the work has been to contribute to the decision upon the design parameters of the sensors, such as thickness or strip geometry, fitting best with the experiment requirements. This has been achieved through a complete set of measurements, including electrical characterizations, mechanical and thermal measurements, laboratory tests of the performance of modules (sensors connected to the readout electronics) and, finally, test-beam measurements at CERN. The results of this first part are presented in Chapters 6 to 9.

The second part consists of the study of irradiated prototype sensors and modules. Once a final design for the sensors is decided, it is necessary to check that their performance will not be dramatically affected by the hard irradiation that they will suffer during the 10 years of expected operation of the LHCb experiment. The results of this second part are presented in Chapter 10.

The third part is related to the development and implementation of the sensor quality assurance procedures followed by the ST group, to verify the characteristics of the sensors delivered by the manufacturer prior to their final installation in the detector. The results of this third part are presented in Chapter 11.

The organization of the thesis follows the chronological order in which each set of measurements presented here were done. The numbers, dimensions, and design parameters given throughout the chapters correspond to the ones at the time when the measurements were performed. This order is altered in the introductory chapters, were the final design of the experiment is presented. The thesis is intended to a separate reading of each chapter, and this implies certain degree of repetition in definitions. The contents of the next chapters are outlined below.

In Chapter 2, we introduce CP violation and analyze the physics objectives of the LHCb experiment. In Chapters 3 and 4, we briefly describe the LHC accelerator and the LHCb detector, mainly focusing in the ST. In Chapter 5, we review the physics of silicon microstrip detectors discussing the main concepts that will be used in the rest of the work.

In Chapter 6, we present the results of the electrical characterization of different prototype sensors with strip geometry parameters similar to those foreseen for the ST, and with three different thicknesses. We performed measurements of leakage currents, depletion voltages, total strip capacitances, inter-strip capacitances, coupling capacitances, and polysilicon resistors. The best sensors were selected to build modules that were later tested in a laser test-stand and in a test-beam.

In Chapter 7, we present results of thermal and thermo-mechanical measurements on a test module. Modules will be built at room temperature, but will be operated below 5°C. Different thermal expansion coefficients of the materials used in the construction of the modules will give rise to mechanical stress. The aim of these measurements is to investigate how the structure formed by the silicon sensors, their mechanical support and the hybrids react to temperature variations, and to demonstrate that the detectors can withstand the expected thermal gradients without damage.

In Chapter 8, we investigate the performance of different prototype modules within a laser test-stand as part of studies carried out to determine the optimal wafer thickness for the ST sensors. Measurements were performed to study the response of the silicon microstrip detectors together with the readout chips. The performance of the modules, like signal shape characteristics, charge sharing between strips, or charge-loss between strips, were studied and determined for different settings of bias voltage, shaping time of the readout chips and position of the laser with respect to the strip.

In Chapter 9, we present the results of a dedicated test-beam on the prototype modules that complements and confirms the results of the previous chapter. Signal shapes were studied, and the parameters meeting the specifications for the ST were determined. Signal-to-noise ratios were obtained and the minimum sensor thicknesses to provide full detection efficiencies for each module length were determined.

In Chapter 10, we present the results of radiation studies on prototype sensors that were irradiated up to fluences equivalent to and larger than the expected particle fluence in the innermost region of the IT detector after 7 years of operation at nominal luminosity. The measurements include an electrical characterization of the irradiated sensors and a study of the performance of the irradiated modules using the same laser test-stand as in Chapter 9. A comparison to unirradiated sensors and modules is carried out.

In Chapter 11, we give a description of the three types of sensors that will be finally used in the ST, and present the sensor quality assurance program followed by the ST group. A total of 1400 sensors will be installed, and have to be tested to ensure their functionality and check that they pass the specified acceptance criteria. We summarize the results for the first batches of sensors, which involve about 10% of the total production, including sensors of all three types.

# Chapter 2

# CP violation and physics objectives of the LHCb experiment

In this chapter, we briefly describe the physics goals of the LHCb experiment, which constitute the real scientific motivation of the work presented in this thesis. The experimental search of new physics beyond the Standard Model is outlined, including the role of the accelerator and the constraints imposed on the spectrometer.

## 2.1 Introduction

The theory currently used to describe particle interactions, the Standard Model (SM), has been tested and verified with a high number of experiments and to a high level of precision, but it is known to be still incomplete. Important aspects remain unexplained, like the origin of fermion masses and mixing or the structure of heavy particle spectrum. In order to probe the limits of the SM, the exploration of physics with $b$ flavoured hadrons appears to be very promising. This is because the large $b$-quark mass allows a clean determination of its couplings to other quarks, due to the asymptotic freedom property of QCD, necessary to relate hadronic amplitudes to observable decays. If, in addition, the experiment can provide good quark flavour identification in these decays, not only $b \to c$ and $b \to u$ transitions can be studied, but also $b \to s$ (and $b \to d$) which are forbidden at lowest order in the SM. As an example, the latter transitions only receive contributions from electroweak loops, and these are extremely sensitive to the spectrum of new heavy particles.

CP is the combined transformation of charge conjugation C and parity transformation P. Non-conservation of the CP symmetry (CP violation) was first discovered in 1964 [7] in neutral-kaon systems as a small effect (0.2%). More recently, it has been also observed in B-meson systems [8] with much larger values ($\sim 30\%$). It implies that matter and antimatter can be distinguished in an absolute, convention-independent way. The existence of CP violation is a necessary condition to generate the matter-antimatter asymmetry observed in the Universe [9]. The SM can accommodate CP violation through quark-mixing with three quark generations [11], but it does not explain it. Conversely, measurements of CP violating asymmetries can be interpreted as measurements of quark mixing phases. It is worth to note in this respect, that quark phases can only arise from the fermion mass generation mechanisms, whether or not in compliance with the SM.

As a matter of fact, the level of CP violation that is required to explain the observed cosmological matter-antimatter imbalance is several orders of magnitude larger than that predicted within the SM, which hints for new potential sources of CP violation beyond the current electroweak theory. Therefore, CP violation has developed into one of the most important and actively pursued fields of research in particle physics.

The outline of this chapter is the following. In Section 2.2, we briefly explain how CP violation is accommodated within the SM. In Section 2.3, we introduce the B-meson systems and explain their importance for the determination of precise CP violating parameters. In addition, recent results of some of these parameters, obtained at B-factories, are reported. In Section 2.4, the physics objectives of the LHCb experiment are presented, and the processes where CP violation will be studied are summarized.

## 2.2 Quark mixing and CP violation within the Standard Model

The $3 \times 3$ quark-mixing matrix that relates mass to electroweak eigenstates has exactly four measurable phases, once the non-physical ones, associated to individual quarks, are discounted. They are usually called in the literature [20] $\beta$, $\gamma$, $\chi$ and $\chi'$ . The last two allow for CP-violation in $\mathrm{B_s^0}$–$\overline{\mathrm{B}}{}_\mathrm{s}^0$ and $\mathrm{B^0}$–$\overline{\mathrm{B}}{}^0$ mixing, respectively. The LHCb experiment will measure all of them in a model-independent approach, given the fact that the SM predicts explicitly relationships among them, which can be derived from the matrix unitarity.

In the SM, flavour-changing processes between quarks occur solely through charged-current interactions, with couplings described by a 3 × 3 quark-mixing unitary matrix, which is usually referred to as the Cabibbo-Kobayashi-Maskawa (CKM) matrix [10, 11]. As mentioned above, this matrix connects the electroweak eigenstates $(d', s', b')$ of the down, strange and bottom quarks with the corresponding mass eigenstates $(d, s, b)$:

$$\begin{pmatrix} d' \\ s' \\ b' \end{pmatrix} = \begin{pmatrix} V_{ud} & V_{us} & V_{ub} \\ V_{cd} & V_{cs} & V_{cb} \\ V_{td} & V_{ts} & V_{tb} \end{pmatrix} \begin{pmatrix} d \\ s \\ b \end{pmatrix} = V_{CKM} \begin{pmatrix} d \\ s \\ b \end{pmatrix}$$

A commonly used parametrization, introduced by Wolfstein [24], uses the parameters $A, \lambda, \rho, \eta$. In this parametrization, the matrix unitarity can be maintained to the desired order of precision. To order $\lambda^3$, $V_{CKM}$ is written as:

$$V_{CKM} = \begin{pmatrix} 1-\lambda^2/2 & \lambda & A\lambda^3(\rho - i\eta) \\ -\lambda & 1-\lambda^2/2 & A\lambda^2 \\ A\lambda^3(1-\rho-i\eta) & -A\lambda^2 & 1 \end{pmatrix} + O(\lambda^4)$$

CP violation occurs if $\eta \neq 0$. The parameter $\lambda$ is identical to the Cabbibo angle [11] and has been measured to be $\approx 0.22$, which implies that the diagonal elements of the matrix are close to 1 while the off-diagonal elements are small. One of the advantages of Wolfstein´s parametrization is that it reproduces well the experimental pattern of $V_{CKM}$ moduli, unexplained by the SM, for which $A, \lambda, \rho, \eta$ are arbitrary parameters derived from quark couplings to Higgs fields.

Of the nine unitary relations of the CKM matrix, six have a result of zero and can be drawn as triangles in the complex complex plane as illustrated in Figure 2.1. If there is no CP violation, all triangles degenerate to lines. Only two of the triangles have all three sides of comparable magnitude, namely $O(\lambda^3)$. The corresponding equations, which are the most relevant for B physics, are:

$$V_{ud}V_{ub}^* + V_{cd}V_{cb}^* + V_{td}V_{tb}^* = 0$$

$$V_{tb}V_{ub}^* + V_{ts}V_{us}^* + V_{td}V_{ud}^* = 0$$

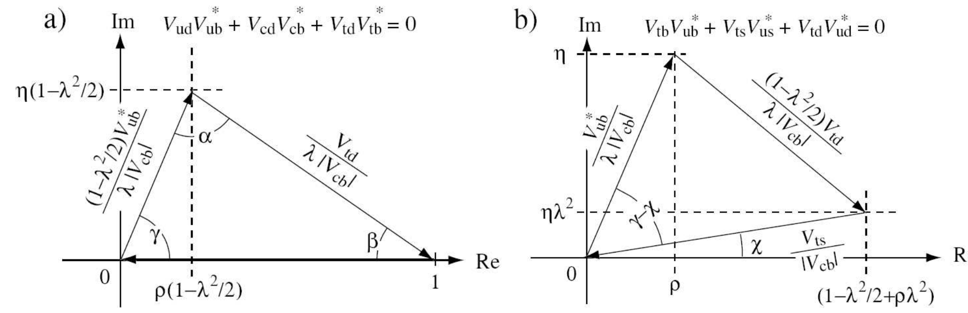

Figure 2.1: Two unitary relations drawn in the complex plane.

The second triangle has a particular relevance to the $B_s^0$ meson system. In the Wolfstein parametrization,

$$\arg V_{td} = -\beta, \qquad \arg V_{ub} = -\gamma, \qquad \arg V_{ts} = -\chi + \pi,$$

and all other elements of the CKM matrix are real. The $\chi'$ phase only arises at order $\lambda^4$, and therefore it is strongly suppressed by the SM.

## 2.3 Brief experimental status of CP violation in B mesons

B-mesons are bound states of one $b$-antiquark and one lighter quark [8]. Their antiparticles, called the $\overline{\mathrm{B}}$-mesons, contain one $b$-quark and one lighter antiquark. Usually B and $\overline{\mathrm{B}}$ mesons together are generically called "B-mesons", unless the discussion requires them to be distinguished from each other. The study of B-meson decays is a key process for the precise determination of CP violating parameters, since large CP violation effects are predicted in them. Furthermore, measurements are possible in many different decay channels, allowing to over-constrain the parameters and, possibly, to find inconsistencies suggesting the existence of physics beyond the SM.

The quantities $|V_{cb}|$ and $|V_{ub}|$ can be determined from various B meson decays generated by tree diagrams [20]. Furthermore, $|V_{td}|$ and $|V_{ts}|$ can be calculated from $B_d^0$–$\overline{B}_d^0$ and $B_s^0$–$\overline{B}_s^0$ oscillation frequency, assuming that the oscillations proceed only via the SM box diagrams shown in Fig. 2.2. Currently, the $B_d^0$–$\overline{B}_d^0$ oscillation frequency is very well measured, $\Delta m_d = 0.502 \pm 0.007$ ps$^{-1}$ [8], but only a lower limit has been set on the $B_s^0$–$\overline{B}_s^0$ oscillation frequency, $\Delta m_s > 14.4$ ps$^{-1}$ (CL> 95%) [8]. Combined, these

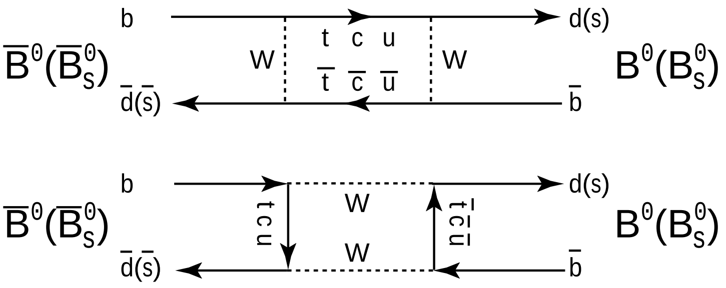

Figure 2.2: The SM box diagrams that generate $B_d^0$–$\overline{B}_d^0$ and $B_s^0$–$\overline{B}_s^0$ oscillations.

measurements determine two sides of the triangle shown in Fig. 2.1 and thus permit to construct the triangle and extract $A, \rho$ and $\eta$.

The so-called B-factories at SLAC (BaBar experiment) and KEK (BELLE experiment) have provided us with a wealth of interesting data on $B_d^0$ and $B^\pm$ meson decays originated from the decay of the $\Upsilon$(4S)-resonance using $e^+e^-$ beams. The most important result is the measurement of a time-dependent CP asymmetry in the decay $B_d^0 \to J/\psi K_S^0$ . Both $B_d^0$ and $\overline{B}_d^0$ can decay to the same CP final state, and a small difference in the decay times between the B and the $\overline{B}$ meson to these states is expected. The asymmetry is proportional to $sin2\beta$ and therefore gives a direct measurement of this angle. The latest result of this asymmetry from Belle [25] gives a value $sin2\beta = 0.652 \pm 0.039 \pm 0.020$. This measurement has provided the first observation of CP violation outside the kaon system.

On a more open and recent research level, both BaBar and Belle collaborations have presented first results on the observation of decays $b \to s\bar{s}s$ and $b \to s\bar{d}d$. In the SM, these decays proceed through penguin diagrams, and their CP asymmetry measure the same $sin2\beta$ as it is measured in $b \to c\bar{c}s$. Discrepancies between the two $sin2\beta$ have been reported. BELLE has reported a 2.4 standard deviation discrepancy with respect to the SM expectation [26], in the combined result for $B^0 \to \phi K_S^0$, $K^+K^-K_S^0$, $f_0(980)K_S^0$, $\eta' K_S^0$, $\omega K_S^0$, $K_S^0\pi^0$, and $K_S^0K_S^0K_S^0$ decays. The BaBar Collaboration has also published recent results that indicate a deviation (2.8 $\sigma$) from the SM in channels affected by the same penguin diagrams [27–31]. Since box and penguin diagrams are specially sensitive to new physics effects, it is of utmost importance that these observations are invesigated by a high statistics experiment like LHCb.

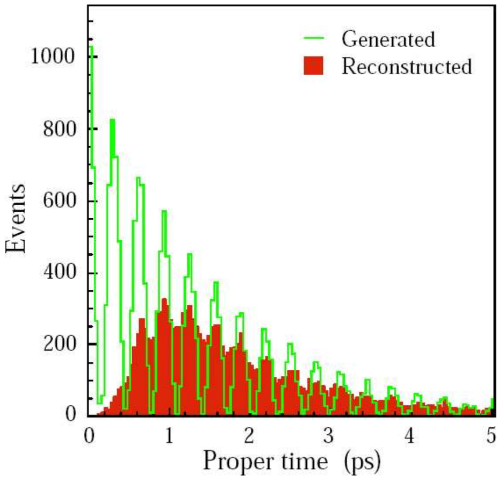

Figure 2.3: Annual yield of $\mathrm{B_s^0} \rightarrow \mathrm{D_s^-}\pi^+$ decays tagged as not mixed, as a function of proper-time, generated (line) and reconstructed (histogram), for $\Delta m_s = 20\ \mathrm{ps}^{-1}$ (SM preferred). Reproduced from [33].

## 2.4 Physics program of the LHCb experiment

The LHCb experiment has been proposed [20] to carry out a complete study of all quark mixing phases, and the main ingredient to achieve that goal is the use of an extremely high energy proton collider, the LHC. The LHCb spectrometer has been designed to exploit the large and strongly forward peaked $\mathrm{b\overline{b}}$ production cross section at 14 TeV pp center of mass energy. With it, correlated b and $\overline{\mathrm{b}}$ quarks can be tagged and CP-violation asymmetries can be accurately measured, as well as neutral $\mathrm{B^0}$–$\mathrm{\overline{B}^0}$ oscillation frequencies. At the nominal luminosity of $\mathcal{L}= 2 \times 10^{32}\ \mathrm{cm}^{-2}\ \mathrm{s}^{-1}$, $10^{12}$ $b\bar{b}$ pairs per year will be produced at LHCb.[1] The experiment will collect approximately the same number of reconstructed $\mathrm{B_d^0}$ events in one year that the B factories in total will have accumulated by the time when LHC will start producing data. But more importantly, LHCb will for first time collect statistically significant samples of $\mathrm{B_s}$, which will allow precise and independent measurements of the $\gamma$ phase. Further details about the spectrometer are given in Section 3.2.

For a comprehensive study of CP violation including possible contributions from new physics, the $\mathrm{B_s^0}$ meson plays an essential role [34]. If indeed new physics such as SUSY is just around the corner, it must contribute to $\mathrm{B^0}$–$\mathrm{\overline{B}^0}$ oscillations and various decay modes which are generated by the loop diagrams, e.g. penguins and boxes. Since CP violation is sensitive to the phases of couplings, it gives a unique opportunity to probe not only the strengths but also the phases of the new couplings.

---

[1] The experiment is currently setting up for a luminosity increase up to $\mathcal{L}= 2.5 \times 10^{32}\ \mathrm{cm}^{-2}\ \mathrm{s}^{-1}$, which is expected to be viable after recent developments of the High Level Trigger [32].

$\mathrm{B_s^0}$ mesons cannot be produced with very high intensity at current $\mathrm{e^+e^-}$ colliders. This is because the B-factories collide electrons and positrons at a combined energy close to 11 GeV, optimum to produce a $\Upsilon$(4S)-resonance. Due to the mass of this state, only $\mathrm{B^\pm}$ and $\mathrm{B_d^0/\overline{B}_d^0}$ are accessible to these experiments. At LHC, due to the much higher center-of-mass energy available, $\mathrm{B_s^0}$ and $\mathrm{B_c^0}$ become also available, allowing a much wider range of measurements that will permit to over-constrain the unitary triangles. Selected LHCb baseline physics measurements are described below.

The B physics sensitivity can be illustrated with the analysis of $\mathrm{B_s^0}$–$\mathrm{\overline{B}_s^0}$ oscillation. This observation is one of the first physics goals of the experiment. To measure this, LHCb will reconstruct the decay $\mathrm{B_s^0} \to \mathrm{D_s^-}\pi^+$, for which 80000 fully-reconstructed events per year of data-taking are expected. The signature of the oscillation is shown in Figure 2.3 before and after reconstruction. The proper-time resolution is about 40 fs for this mode. After including the effect of the acceptance, which removes events at short proper-time, the oscillation signal is still clearly visible [33, 35]. A $5\sigma$ observation of mixing is possible up to $\Delta m_s = 68$ ps$^{-1}$, which is well beyond the SM expectation. Once the effect is seen, the oscillation frequency is expected to be precisely determined with $\sigma(\Delta m_s) \sim 0.01$ ps$^{-1}$.

The angle $\chi$ is feasible at LHCb in two different approaches:

I. A state initially produced as a $\mathrm{B_s^0}(\mathrm{\overline{B}_s^0})$ can either directly decay to J/$\psi\phi$, or can oscillate into a $\mathrm{\overline{B}_s^0}(\mathrm{B_s^0})$ and then decay into J/$\psi\phi$. The interference between these amplitudes results in a time-dependent CP-asymmetry which measures the phase difference between the decay amplitude and the $\mathrm{B_s^0}$–$\mathrm{\overline{B}_s^0}$ oscillation amplitude. In the SM, this phase difference is given [36] by twice the angle $\chi$. As a result, the amplitude of the resulting time-dependent CP-asymmetry is expected to be $sin(-2\chi)$. In the SM, the $\mathrm{B_s^0}$ mixing phase is expected to be small, $\phi_s = 2\chi = 2\eta\lambda^2$, of the order of $-0.04$. The observation of a large CP asymmetry in this channel would therefore be a striking signal for physics beyond the SM. This can be also applied to $\mathrm{B_s^0}(\mathrm{\overline{B}_s^0})$ decays into J/$\psi\eta$ and into $\eta_c\phi$.

II. In the decay $\mathrm{B_s^0} \to \mathrm{D_s^\mp K^\pm}$ the final state is a non-CP eigenstate to which both $\mathrm{B_s^0}$ and $\mathrm{\overline{B}_s^0}$ can decay. The decay $\mathrm{B_s^0} \to \mathrm{D_s^\mp K^\pm}$ can proceed through two tree decay diagrams, shown in Figure 2.4. The interference these tree diagrams gives access to the phase $\gamma - 2\chi$.

The phase of $V_{\mathrm{ub}}$, $\gamma$, will be measured at LHCb in three different ways:

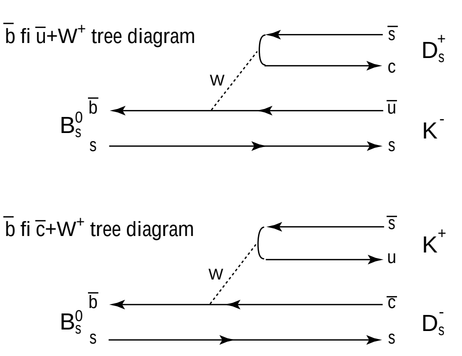

Figure 2.4: The two tree diagrams which generate $B_s^0 \to D_s^+K^-$ and $B_s^0 \to D_s^-K^+$ decays.

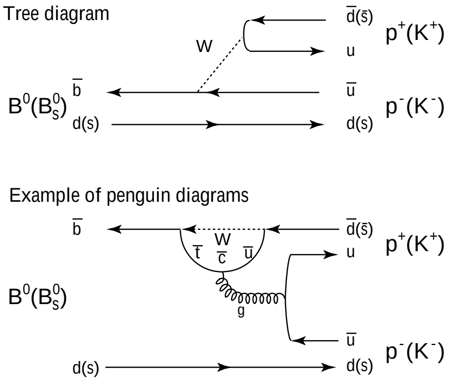

Figure 2.5: The tree diagram and an example of the penguin diagrams which generate $B^0 \to \pi^+\pi^-$ and $B_s^0 \to K^+K^-$ decays.

I. One way to extract $\gamma$, which is essentially independent from new physics contributions, is to incorporate into the experimental analysis the two tree diagrams, $\bar{b} \to \bar{u} + W^+$ and $\bar{b} \to \bar{c} + W^+$. This can be done by studying the time-dependent rates of $B_s^0$ decaying into $D_s^+K^-$ and $D_s^-K^+$ and their CP-conjugated processes [37], as explained above. Figure 2.4 illustrates the corresponding diagrams. From them, one can extract $\phi_s + \gamma$ without any theoretical ambiguity. Here, $\phi_s$ is the phase of $B_s^0$–$\overline{B}_s^0$ oscillations, which can be obtained from the time-dependent CP asymmetry of $B_s^0$ and $\overline{B}_s^0$ decaying into $J/\psi\phi$ (or other CP eigenstates produced by the $b \to c + W^-$ and $\bar{b} \to \bar{c} + W^+$ tree processes). Combining the two results, $\gamma$ can be determined.

II. Another way of measuring $\gamma$ comes from time-dependent asymmetries for $B^0 \to \pi^+\pi^-$ and $B_s^0 \to K^+K^-$, $\mathcal{A}^{CP}(t) = \mathcal{A}^{dir}\cos(\Delta m_d t) + \mathcal{A}^{mix}\sin(\Delta m_d t)$. Both tree and penguin processes contribute to these decays. The diagrams for these processes are shown in Figure 2.5. Four observables are parameterized with seven parameters, $\gamma$, $\phi_d$ and $\phi_s$ and the ratios of penguin over tree contributions. If we assume that the strong interaction dynamics remains invariant under this interchange (U-spin symmetry) [38], the relative contributions of the penguin process with respect to the tree process are identical for the $B^0 \to \pi^+\pi^-$ and $B_s^0 \to K^+K^-$ decays. Under this assumption, $\gamma$ can be determined from the time-dependent CP asymmetry for $B^0$ and $\overline{B}^0$ decaying into $\pi^+\pi^-$ and that for $B_s^0$ and $\overline{B}_s^0$ decaying into $K^+K^-$. Using the $\phi_d$ and $\phi_s$ values obtained from the CP asymmetries measured with $B^0, \overline{B}^0 \to J/\psi K_S^0$

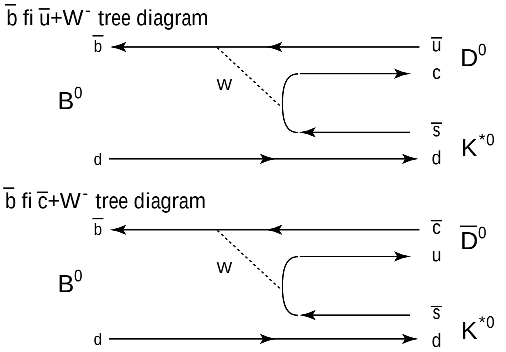

Figure 2.6: The two tree diagrams which generate $B^0 \to D^0K^{*0}$ and $B^0 \to \overline{D}^0K^{*0}$ decays.

and $B_s^0, \overline{B}_s^0 \to J/\psi\phi$ respectively, the assumed U-spin symmetry can be tested as well.

III. Another opportunity for observing the interference between the two tree processes, $\overline{b} \to \overline{u} + W^+$ and $\overline{b} \to \overline{c} + W^-$, and thus extracting $\gamma$, is given by $D^0$–$\overline{D}^0$ mixing [39]. This can be done by measuring the time-integrated decay rates for $B^0 \to D^0K^{*0}$, $B^0 \to \overline{D}^0K^{*0}$, $B^0 \to D^0_{CP}K^{*0}$ and for their CP-conjugated processes, where $D^0_{CP} = (D^0 + \overline{D}^0)/\sqrt{2}$ denotes the CP-even eigenstate of the $D^0$–$\overline{D}^0$ system. Figure 2.6 shows relevant diagrams.

It is important to note that the phase $\gamma$ measured in the first method will not be affected by the possible existence of new particles. The second method makes an explicit use of the penguin processes where new particles can contribute in loop exchanges. Therefore, the extracted value of $\gamma$ could be affected by new physics. Equally for the third method, new physics in $D^0$–$\overline{D}^0$ mixing could affect the extracted value of $\gamma$. From these three measurements, we can determine the angle $\gamma$ and, together with the $|V_{ub}|$ measurements, extract the CKM parameters, $A$, $\rho$ and $\eta$ even in the presence of new physics, and pin down the contribution of new physics to the oscillations and penguin diagrams like those shown in Figure 2.5.

In the SM analysis, using the present knowledge of CKM elements $|V_{ub}|$, $|V_{cb}|$, $|V_{td}|$ and $\sin 2\beta$, $\gamma$ is predicted to be $\sim 65°$ [40].

There are many other CP-violating decay modes where the extracted phases of $V_{td}$, $V_{ub}$ and $V_{ts}$ are affected differently by new physics. Rare-loop induced decays are sensitive to new physics in many extensions of the SM. At LHCb, studies of radiative penguin decays $B^0 \to K^{*0}\gamma$, $B_s^0 \to \phi\gamma$, $B^0 \to \omega\gamma$, electroweak penguin decay $B^0 \to \mu^+\mu^-K^{*0}$, gluonic penguin decays $B^0 \to \phi K_S^0$, $B_s^0 \to \phi\phi$ and the rare decay $B_s^0 \to \mu^+\mu^-$ will be performed. Studies of those decay modes with high accuracy will probably enable to

| Parameter | Channel | Yield | Precision |
|---|---|---|---|
| $\gamma$ | $\mathrm{B_s^0} \to \mathrm{D_s^\mp K^\pm}$ | 5400 | $\sigma(\gamma) \approx 14°$ |
| | $\mathrm{B^0} \to \pi^+\pi^-$ | 26000 | $\sigma(\gamma) \approx 6°$ |
| | $\mathrm{B_s^0} \to \mathrm{K^+K^-}$ | 37000 | |
| | $\mathrm{B^0} \to \mathrm{D^0K^{*0}}$ | 500 | $\sigma(\gamma) \approx 8°$ |
| | $\mathrm{B^0} \to \mathrm{\overline{D}^0K^{*0}}$ | 3400 | |
| | $\mathrm{B^0} \to \mathrm{D^0_{CP}K^{*0}}$ | 600 | |
| $\chi$ | $\mathrm{B_s^0} \to \mathrm{J}/\psi\phi$ | 120000 | $\sigma(\chi) \approx 2°$ |
| $\lvert V_{\mathrm{td}}/V_{\mathrm{ts}}\rvert$ | $\mathrm{B_s^0} \to \mathrm{D_s^-}\pi^+$ | 80000 | $\Delta m_s$ up to 68 $\mathrm{ps^{-1}}$ |
| $\mathcal{A}_{\mathrm{CP}}^{\mathrm{dir}}$ | $\mathrm{B^0} \to \mathrm{K^{*0}}\gamma$ | 35000 | $\sigma(\mathcal{A}_{\mathrm{CP}}^{\mathrm{dir}}) \approx 0.01$ |

Table 2.1: Selected performance after 1 LHCb year. Only statistical errors are taken into account. Reproduced from [35].

determine the structure of the operators governing the new physics, in a complementary way to the direct searches of the Higgs boson that will be performed at ATLAS and CMS. As explained, $\mathrm{B_s^0}$ mesons play a crucial role here. This gives a distinct advantage to hadron machines over $\mathrm{e^+e^-}$ B factories operating at the $\Upsilon(4\mathrm{S})$. Similarly, $\mathrm{B_c^+}$ mesons and b baryons are also an exclusive domain of hadron machines. In addition, for interesting CP-violating $\mathrm{B^0}$ decay modes such as $\pi^+\pi^-$, $\mathrm{K}^\pm\pi^\mp$ and $\mathrm{K}^{*0}\ell^+\ell^-$, the LHCb experiment will be able to collect huge statistics compared to the currently operational experiments.

It is clear from the previous discussion that, in order to perform its function, the LHCb spectrometer must attain the following technical aspects:

- Cope with a very high particle occupancy, specially in the low angle region, close to the accelerator beam pipe. Despite the relatively low luminosity as compared to ATLAS and CMS, particle fluences will reach $5 \times 10^5$ $\mathrm{cm^2s^{-1}}$ in the innermost regions of the detector. This poses a constraint on detector granularity and special care on detector ageing, due to the high irradiation, as we will see in the following chapters.

- Provide single-hit tracking efficiencies larger than 98% and uniformly distributed, in order to collect the required statistics of fully reconstructed $b$-hadron decays, within one year of data-taking time. Since, as we have seen, many of the decay modes of interest involve at least four final state charged particles, it is clear that B-meson reconstruction efficiencies will scale as high powers of single-particle efficiency.

> Therefore, detector efficiencies are indeed critical, which imposes lower limits on charged particle signal-to-noise ratios, as we shall see. Material budgets on the construction of the trackers are also important in this respect, specially concerning hadron interactions of low energy $\pi^{\pm}$ and $K^{\pm}$.

We have mentioned here two key aspects of the LHCb experiment, which are of direct concern to the Silicon Tracker work developed in this thesis. Certainly, other technical challenges of the spectrometer, such as particle identification by the RICH detectors, precision vertexing capability, or electron and muon tagging, are equally important.

In Chapter 4 we will provide a rather detailed description of the Silicon Tracker, before we concentrate on the studies and measurements done on detector properties, which will show that the aspects mentioned above will indeed be met by the spectrometer.

# Chapter 3

# The LHCb spectrometer

In this chapter we give an introduction to the LHC accelerator and the LHCb experiment. We describe the different sub-detectors that compose LHCb, presenting their main purposes and characteristics.

## 3.1 The LHC

The Large Hadron Collider (LHC), at present under construction at CERN, is a proton-proton collider with a center-of-mass energy of $\sqrt{s} = 14$ TeV. The LHC has two low luminosity experiments: ALICE, a dedicated heavy-ion collision experiment, and LHCb, a dedicated B-physics experiment; and two high luminosity experiments, ATLAS and CMS, two general-purpose detectors that aim for a peak luminosity of $10^{34}$ cm$^{-2}$s$^{-1}$. When the LHC is commissioned in 2007, it will be the largest energy collider ever built. Bunch crossing at the LHC will occur every 25 ns, which requires the use of fast pipe-lined electronics in all detectors.

## 3.2 The LHCb spectrometer

The LHCb experiment [16, 17, 20] has been designed to perform high-precision measurements of CP violating phenomena and rare decays in the B meson systems. The luminosity at the LHCb interaction point of $\mathcal{L}= 2 \times 10^{32}$ cm$^{-2}$ s$^{-1}$ yields about $10^{12}$ $b\bar{b}$ pairs per year.[1] The copious pro-

---

[1] LHCb luminosity is reduced by a factor of 50 with respect to ATLAS and CMS experiments in order to maximize the number of single interactions per bunch-crossing.

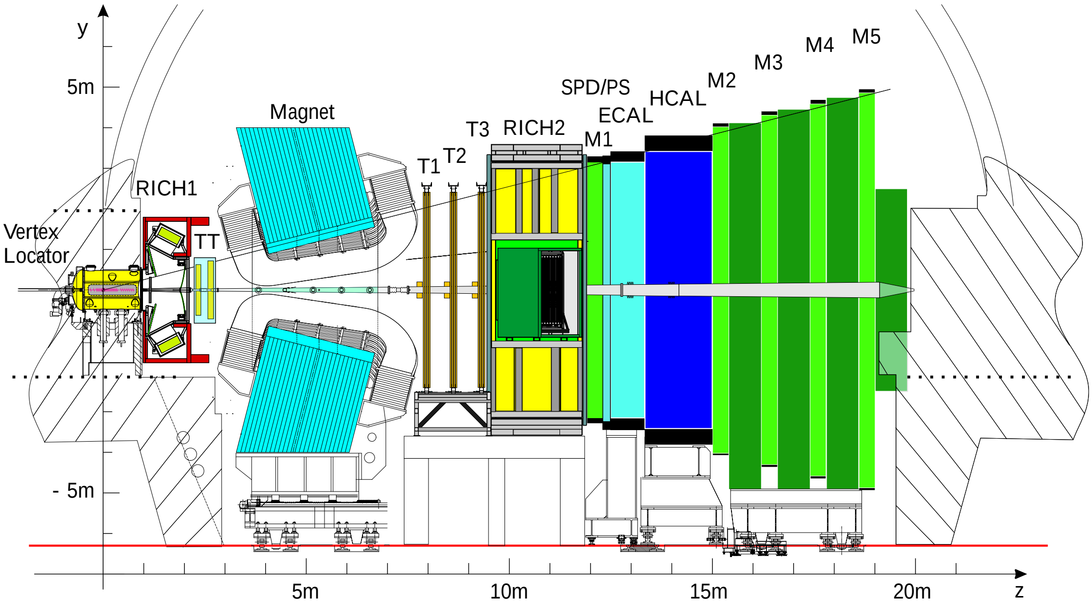

Figure 3.1: Vertical cross section of the LHCb detector.

duction of $B_d$, $B_s$ and $B_c$ mesons and $b$-baryons, together with the unique particle-identification capabilities of the LHCb spectrometer, will allow the experiment to study the physics of hadrons containing $b$-quarks more accurately and in greater detail than any other experiment.

A vertical cross section of the LHCb detector is shown in Figure 3.1. It has been designed as a single-arm magnetic spectrometer, exploiting the large and strongly forward $b\bar{b}$ production cross section at the LHC [16]. The detector acceptance extends out to 300 mrad in the horizontal bending plane of the 4 Tm dipole magnet and to 250 mrad in the vertical plane.

Immediately surrounding the p-p interaction point there is the silicon Vertex Locator (VELO) [41]. It is built in two halves, placed on both sides of the beam, that can be moved close to it during data taking, or retracted during machine injection. Both halves accommodate 21 measuring stations, each made of two half-disks of 300 $\mu$m single-sided silicon microstrip detectors, that allow the measurement of $r$ and $\phi$ coordinates, with stereo angle, for excellent vertex resolution and precise decay lengths measurement.

The main tracking system consists of four planar tracking stations: the Trigger Tracker (TT) station located upstream of the spectrometer magnet, and three stations (T1-T3) located downstream of the magnet. TT station is entirely covered by silicon microstrip detectors, whilst in stations T1-T3 two detector technologies are employed: the outer region, away from the beam-pipe, is covered by the straw-tube drift chambers of the Outer Tracker [18]; the innermost region around the beam-pipe, the Inner Tracker (IT), where particle densities are highest, is covered by silicon microstrip detectors. The IT and TT station form the Silicon Tracker (ST) project. It will be described in detail in Chapter 4.

Particle identification is provided by two Ring-Imaging Cherenkov detectors that are located one upstream (RICH1) and one downstream (RICH2) of the tracking system. The calorimeter system, consisting of a scintillator, a pre-shower detector, an electromagnetic and a hadronic calorimeter (SPD, PS, ECAL, HCAL), provides identification capability for electrons, photons and hadrons. The muon detector (M1-M5) provides muon identification for trigger purposes.

In order to fully exploit its physics potential, the LHCb apparatus must ensure high trigger and event reconstruction efficiencies for all interesting decay channels. At LHCb, the cross section of $b\bar{b}$ production amounts to less than 1% of the total cross-section. The goal is to exclusively reconstruct the B meson decays of interest, measure the proper-time even for the fast oscillating $\mathrm{B_s}$ mesons and provide reliable tagging of the $b$ flavour. Thus, the crucial features of the experiment are robust and efficient trigger, particle identification and decay time resolution. In the high-rate environment of the LHC, efficient and precise reconstruction of the trajectories of charged particles is a key ingredient for providing the required momentum resolution for proper lifetime measurement of B-meson decays.

The reconstruction of the trajectories of charged particles in this harsh environment is challenging. In each p-p crossing producing a $b\bar{b}$ pair, within the LHCb acceptance there are about 50 charged particles. In addition, the amount of material seen by a particle up to the end of the spectrometer amounts to $30 - 40\%$ of a radiation lenght. This leads both to multiple scattering and the generation of secondary particles in hadronic and electromagnetic interactions.

## 3.3 Track reconstruction

LHCb has developed a multiple-pass tracking finding strategy [20, 42]. In a first pass, tracks that traverse the entire spectrometer from the Vertex Locator to the last of the IT stations are searched for. These so called "long-tracks" have the highest precision and are the most important for physics

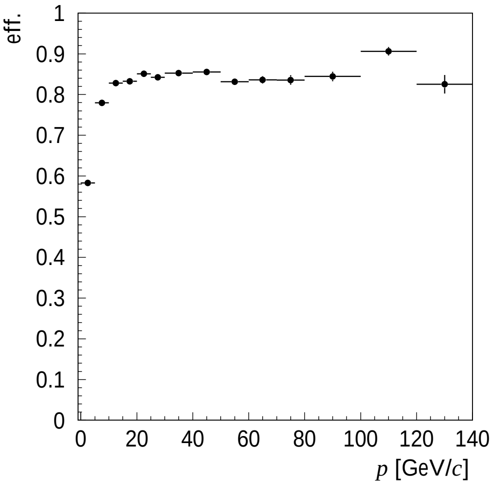

Figure 3.2: Long track reconstruction efficiency as a function of momentum. Reproduced from [20].

analyses. The hits used on these tracks are then flagged as used and a search made for tracks with hits only in the IT stations and the TT station. Typically, these tracks are the decay products of $K_s$ and hyperon decays occurring outside the acceptance of the VELO. Finally, with the remaining unused hits a search is made for low momentum particles which are bent out of the acceptance by the magnet but have hits in the VELO and TT station.

Figure 3.2 shows the efficiency to reconstruct long tracks calculated by Monte Carlo simulations as presented after LHCb reoptimized design [20]. For tracks with momentum higher than 10 GeV, an average efficiency of $\sim$ 95% is found. The corresponding ghost rate depends on the transverse momentum of the particle: if it is required that the $p_{\mathrm{T}}$ of the reconstructed track is larger than 0.5 GeV, as is done in many physics analyses, a ghost rate of 4% is achieved. The plot shows that the search for low momentum particles is more difficult than that for high momentum particles.

All reconstructed tracks are fitted to obtain optimal estimates of the track parameters and the associated covariance matrix. In Figure 3.3, the momentum and impact parameter resolution obtained are shown. The momentum resolution is plotted as a function of the track momentum and is seen to be increasing from $\delta p/p = 0.35\%$ for low momentum tracks to $\delta p/p = 0.55\%$ for tracks at the high end of the energy spectrum. In the same figure, the momentum spectrum for B-decay tracks is also illustrated. The impact parameter resolution is plotted as a function of $1/p_{\mathrm{T}}$ of the track. For comparison, the momentum and $1/p_{\mathrm{T}}$ spectra of B-decay particles in the detector acceptance are plotted in the same figure.

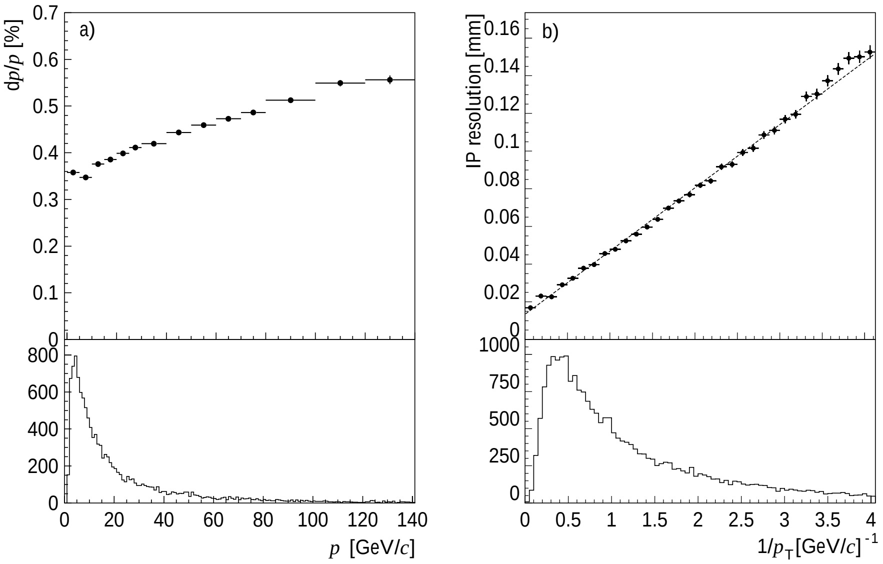

Figure 3.3: (a) Momentum resolution, $\delta p/p$, for long tracks as a function of momentum, $p$. (b) Impact parameter resolution as a function of $1/p_T$. The momentum and transverse momentum spectra of B-decay particles are shown in the lower part of the plots. Reproduced from [20].

# Chapter 4

# The LHCb Silicon Tracker

In this chapter we describe the Silicon Tracker, subdetector for which the sensors studied in the present work were investigated. We focus our attention on the points relevant for our work with silicon sensors. Further details can be found in the references given throughout.

## 4.1 Silicon Tracker

In LHCb, excellent momentum resolution is required in order to measure precisely the invariant mass of $b$ decay candidates and separate the B meson signal from the background. In addition, it is essential for determination of of the neutral meson proper lifetimes, where flavour oscillations will be observed. The main purpose of the tracking system is therefore to recognize the charged particle tracks and determine their momentum and sign of charge.

The Silicon Tracker (ST) is part of the tracking system of LHCb and consists of two sub-detectors that will be built using silicon microstrip technology: the Trigger Tracker (TT) station, and the Inner Tracker (IT). The design of the IT and the TT station is described below. Further information can be found in [19, 20, 43, 44]. Both detectors will be used by the High-Level Trigger (HLT) and offline analysis to determine charged particle momenta (and $\mathrm{p_T}$) of individual tracks, and to fully reconstruct the trajectories of all charged particles. Furthermore, data from the TT station will be employed by the Level-1 trigger [1] to assign transverse momentum information to high impact parameter tracks reconstructed in the VELO.

---

[1] Level-1 trigger will run at the main CPU farm at 1 MHz.

Simulation studies have shown that the momentum resolution in LHCb is dominated by multiple scattering over a wide range of momenta and therefore the material budget has to be minimized. For the ST, this poses a special challenge since parts of the front-end electronics that have to be close to the detector are located inside the acceptance of the experiment. On the other hand, these studies have shown that a moderate spatial resolution of around 60 $\mu$m is adequate for the ST, which naturally leads to a choice of strip pitches of approximately 200 $\mu$m.

At the LHC, bunch crossing occurs every 25 ns. This calls for front-end electronics with fast shaping time in order to avoid the need to reconstruct overlapping events from consecutive bunch crossings. Fast front-end electronics are, however, susceptible to significant Johnson noise if connected to large load capacitances as given by the long readout strips employed in the ST. Silicon sensors and front-end electronics have to be carefully designed and matched to each other in order to optimize the signal-to-noise performance and guarantee high single-hit efficiencies.

### 4.1.1 Inner Tracker

Tracking stations T1-T3 are located downstream of the spectrometer magnet, and are placed at equidistant positions along the beam line (see Figure 3.1). In each of them, the Inner Tracker (IT) covers a cross-shaped area around the beam pipe, where particle densities are highest (see Figure 4.1), and has dimensions of approximately 120 cm wide and 40 cm high. Though it covers only 1.5% of the surface area, 20% of the tracks pass through it.

An isometric view of a IT station is shown in Figure 4.2. Each IT station consists of four detection layers. The first and the fourth layer have vertical readout strips, whereas the second and the third layer have readout strips rotated by a stereo angle of $\pm 5^\circ$. This provides a precise measurement of track coordinates for momentum determination in the bending plane of the magnet and sufficient resolution for pattern recognition in the vertical coordinate. The layout of a detection layer in the IT is shown in Figure 4.3. The shape and dimensions of the IT active area have been optimized to ensure sufficiently low occupancies in the surrounding detector [19]. The dimensions differ slightly for the three tracking stations, due to the conical shape of the beam pipe and the use of standard silicon sensors for all stations.

Each station consists of four independent detector boxes, above, below and to both sides of the beam pipe. The boxes are light-tight and ther-

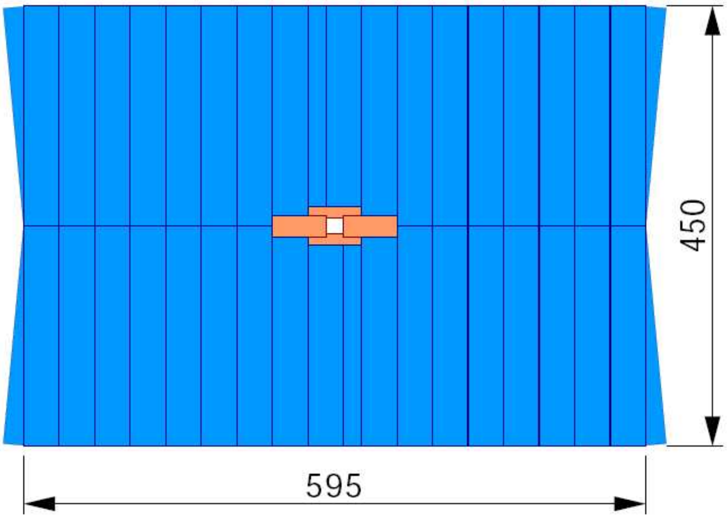

Figure 4.1: Front view of one of the tracking stations T1-T3. The IT covers a cross-shaped area around the beam pipe. The remainder of the acceptance is covered by the long Outer Tracker straw drift-tube modules. The shape and dimensions of the IT are optimized to ensure sufficiently low occupancies in the surrounding detector.

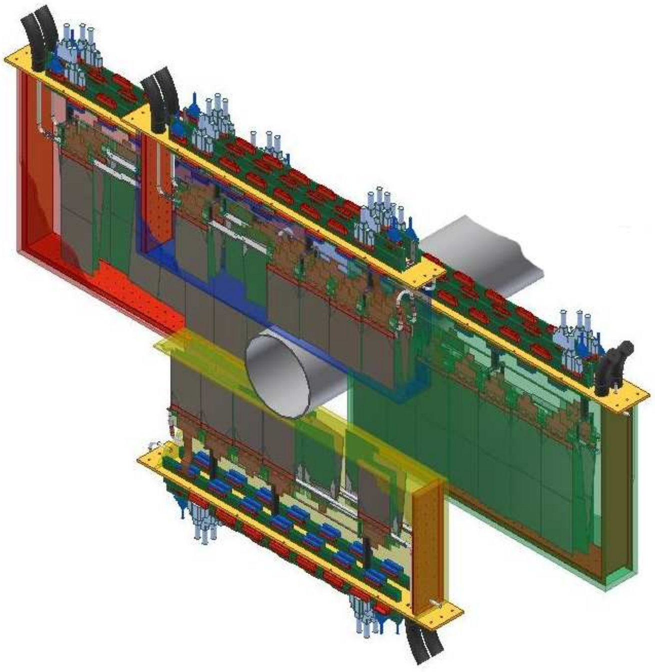

Figure 4.2: Isometric view of a IT station. The downstream walls and some modules are not shown in order to display the interior of the detector boxes.

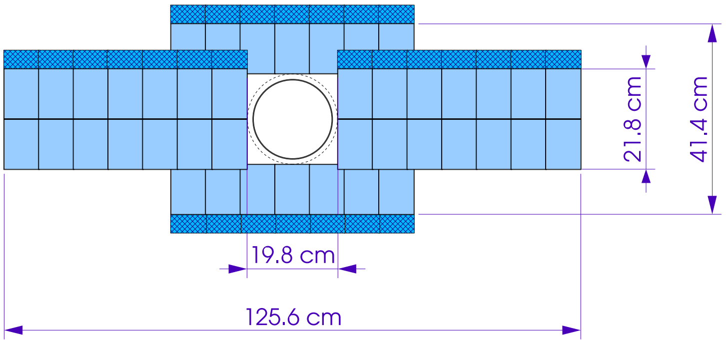

Figure 4.3: Layout of a IT station. Two-sensor long modules use 410 $\mu$m thick sensors, whilst one-sensor long modules use 320 $\mu$m thick sensors.

mally insulating. Liquid cooling provides an operation temperature of 5°C in the IT boxes. A detector box contains 28 silicon modules arranged in four detection layers. One-sensor modules are used in the top/bottom boxes and two-sensor modules in the left/right boxes. Adjacent modules overlap a few millimeters in order to ensure full acceptance coverage and facilitate the relative alignment of the modules using hits from shared tracks.

In the IT, the silicon sensors bonded to the front-end readout electronics are mounted onto a sandwich structure support plate, which consists of an isolating polyimide layer and two carbon fiber sheets, separated by 1 mm of Airex foam. Figure 4.4 shows an expanded view of a two-sensor module.

Each module is read out by integrated circuits, the Beetle chips [45], that are located at the front-end hybrids at the end of the detector modules [46]. The Beetle chip is a 128-channel ASIC device for 40 MHz sampling and multiplexed dead-timeless readout that is manufactured in a 0.25 $\mu$m CMOS process and was irradiation tested up to 40 MRad. The chip features for each channel are a low-noise charge-sensitive preamplifier, an active CR-RC pulse shaper with a minimum rise time ($\sim$ 13 ns) well below the LHCb requirements, and an analogue pipeline with a programmable latency. IT modules carry three Beetle chips each, that are mounted on a printed circuit board. Ceramic pitch adapters are necessary to match the silicon sensor pitch to that of the Beetle input pads.

All modules are mounted in a common cooling plate, which will be kept at low temperature in order to remove the heat generated by the front-end chips and provide cooling for the silicon sensors.

Two types of rectangular silicon sensors of different thickness but otherwise identical design are employed in the IT. All sensors are single-sided $p$-on-$n$ type, measure 11 cm in height and 7.8 cm in width, and have a strip pitch of 198 $\mu$m. The dimensions of the sensors were optimized to fit the acceptance requirements of the IT. The number of 384 readout strips per sensor was chosen to match the granularity of the 128-channel front-end readout chips. In order to minimize material budget, 320 $\mu$m thick sensors are used for the single-sensor modules above and below the beam pipe, whilst 410 $\mu$m thick sensors are required to ensure good enough signal-to-noise performance for the two-sensor long modules to the left and to the right of the beam pipe. Further details about sensor design characteristics are given in Chapter 11.

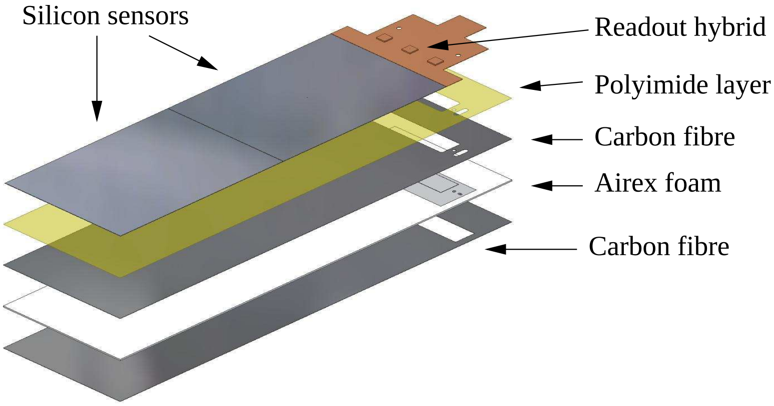

Figure 4.4: Expanded view of a two-sensor module for the IT station.

### 4.1.2 Trigger Tracker Station

The TT station, located upstream of the spectrometer magnet, is entirely built using silicon microstrip technology, and covers the full LHCb acceptance.

An isometric drawing of the TT station is shown in Figure 4.5. The TT station consists of four detection layers that have dimensions of approximately 160 cm width and 130 cm height. The first and fourth layers have vertical readout strips, whereas the second and the third layers have readout strips rotated by a stereo angle of $\pm 5^\circ$. The four layers are arranged in two half stations, TTa and TTb, separated approximately 30 cm along the beam axis. All silicon sensors are kept in a common light-tight, dry and thermally insulating detector housing with an ambient temperature of about 5℃ provided by liquid cooling. The TT detector box is horizontally split in two half stations allowing a retraction from the beam pipe.

The layout of a detection layer in the TT station is illustrated in Figure 4.6. The basic detector unit is a seven-sensor long module that is electronically split into several readout sectors, as indicated by the different shadings in the figure. An isometric view of such an unit is shown in Figure 4.7. Long readout strips covering the full height of the station would lead to unacceptable large strip capacitances and noise performance of the front-end readout amplifier. Front-end hybrids carrying four Beetle [45] chips and associated mechanics for all readout sectors are located above and below the sensitive region, outside the acceptance of the experiment. The outermost readout

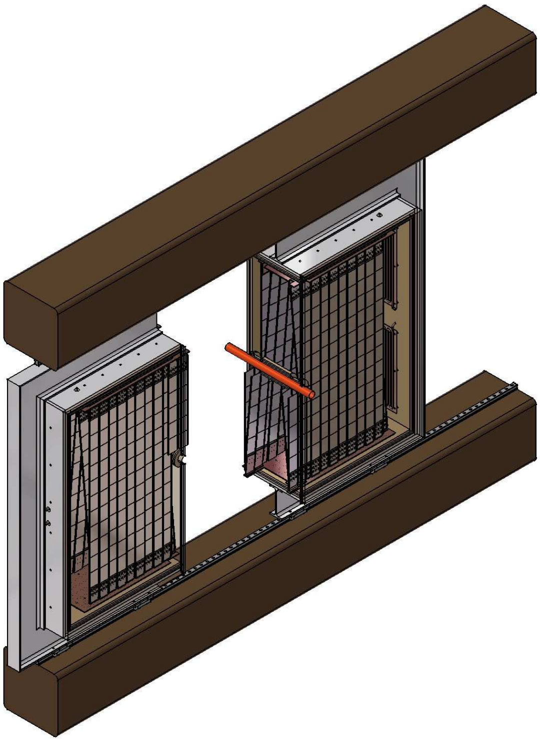

Figure 4.5: Isometric view of the TT station. One detector half is shown retracted from the beam pipe and the downstream wall of the enclosure is not shown in order to display the interior of the detector box.

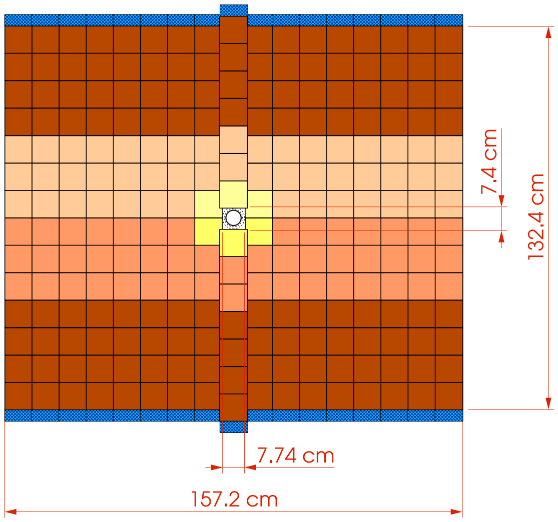

Figure 4.6: Layout of a detection layer in the TT station. Readout sectors are indicated by different shadings. All silicon sensors are 500 $\mu$m thick. Dimensions are in cm and refer to the sensitive area covered by the silicon sensors.

sectors on each module consist of four sensors that are directly bonded to their respective front-end hybrids. The next sectors consist of three sensors, that are connected to the front-end hybrids via 40 cm long kapton interconnect cables. In the modules directly surrounding the beam-pipe, the innermost sector is additionally divided into a two-sensor and a one-sensor readout sectors, the innermost one connected to its front-end hybrid via an approximately 60 cm long interconnect cable.

The TT station will contain longer readout sectors than the IT, resulting in higher strip capacitances and a worse noise performance of the front-end readout amplifier. This requires the use of thicker sensors to obtain larger signals and ensure good enough signal-to-noise performance. TT station makes use of the silicon sensors that were developed for the outer barrel of the CMS silicon tracker [47]. Sensors have a thickness of 500 $\mu$m and measure 9.4 cm in length and 9.6 cm in width, and have a strip pitch of 183 $\mu$m. Further details about the sensor design characteristics are given in Chapter 11.

The performance of these long silicon ladders had to be studied to demonstrate that a good signal-to-noise ratio could be achieved, at the same time as the “spill-over” (the fall-time of the preamplifier signals) of signals to the

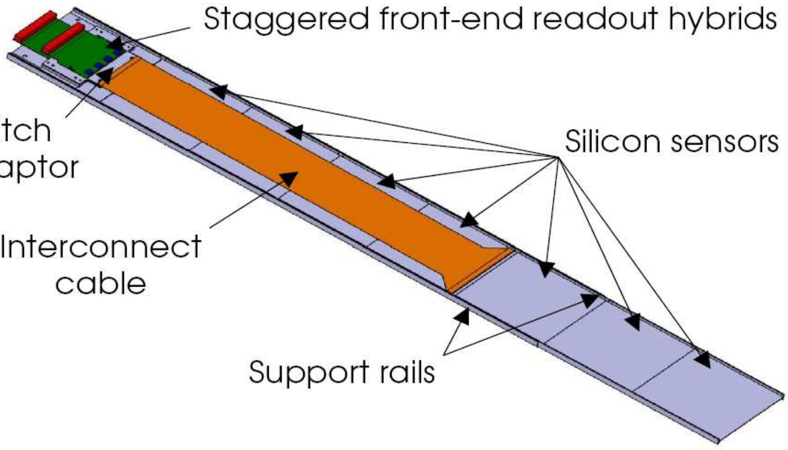

Figure 4.7: Isometric view of a TT half module, showing the readout hybrids and the kapton interconnect cable employed to read out the inner readout sector.

following bunch crossings could be kept sufficiently small in order not to compromise physics performance. This R&D conforms an important part of the work presented in the following chapters.

# Chapter 5

# Silicon microstrip detectors

In this chapter we give an introduction to the physics and technology of silicon microstrip particles detectors, focusing our attention on the operating principles of these detectors and the aspects relevant for the work presented in the following chapters.

## 5.1 Introduction

Semiconductor detectors, and in particular silicon detectors, play an increasingly important role in high-energy physics experiments. For charged particle detection, silicon strip and pixel detectors are presently the most precise tracking devices. In addition, these detectors are radiation hard and fast-responding, which allows for applications in high-rate environments. Excellent treatments of the the basics and developments on silicon detectors have been documented in several publications [48–52].

The outline of this chapter is the following. In Section 5.2, the basic properties of silicon and of a $p-n$ junction are described, and the principles of operation of these detectors are presented. In addition, the planar processing technology is briefly described. In Section 5.3, the radiation induced damage of silicon detectors is discussed.

## 5.2 Physics and properties of silicon detectors

### 5.2.1 Silicon properties

Silicon sensors are attractive because of their very good intrinsic energy resolution (an electron-hole pair is obtained for every 3.6 eV released by a particle traversing the medium). Furthermore, the high density of the medium reduces the range of secondary electrons, allowing very good spatial resolution. Because of these characteristics, they are used as tracking systems.

For applications as particle detectors, silicon is mainly used in a single crystal formation. The silicon atoms are arranged in a diamond-like face-centered cubic lattice where each atom is surrounded by four nearest neighbours in a tetrahedral configuration. Each atom shares its four outer (valence) electrons with the neighbouring atoms, thus forming covalent bonds.

At 0 K, all valence electrons participate in the covalent bondings, and no free electrons are available for electrical conduction. However, at higher temperatures, the electrons can be thermally excited out of a covalent bond and become free to participate in electrical conduction. At the same time, electron vacancies (holes) in the covalent bond can be refilled by other electrons, giving rise to a movement of holes which also contributes to the electrical conductivity.

In addition to thermal excitation, externally triggered processes such as ionizing radiation or exposure to electromagnetic waves in the visible or UV range, alter temporary the conductivity by creating free electron-hole pairs. The capability of silicon to collect this created charge allows its use as a particle detector. To do this, almost all free intrinsically generated charge carriers have to be removed from the silicon bulk to avoid that the signal generated by a particle crossing the detector would be covered by the fluctuations of the detector current. One way to increase the signal-to-noise ratio is to cool the crystal, which is not very practical. The method commonly used in modern particle detectors to remove free carriers from the silicon bulk is the formation of a $p-n$ diode structure.

### 5.2.2 The $p-n$ junction

The $p$- and $n$-type materials are obtained by replacing some of the silicon atoms by atoms from the groups III and V, respectively, which is referred

| | |
|---|---|
| Atomic number | 14 |
| Average atomic mass | 28.09 |
| Density (g/cm$^3$) | 2.329 |
| Dielectric constant ($\epsilon_0$) | 11.9 |
| Radiation length (cm)<br>(g/cm$^2$) | 9.36<br>21.82 |
| Band gap (eV) | 1.12<br>indirect |
| Intrinsic carrier concentration (cm$^{-3}$) | $1.4 \times 10^{10}$ |
| Mean energy to create e-h pair (eV) | 3.62 |
| Drift mobility $\mu$ (cm$^2$/V$s$) | |
| Electrons $\mu_n$ | 1450 |
| Holes $\mu_p$ | 450 |
| Saturation field (V/cm) | $2 \times 10^4$ |

Table 5.1: Selected properties of silicon.

to as doping. Elements from the group III have three valence electrons, and easily attach an electron from silicon atoms. They are called acceptors. Attachment of electrons creates holes, which are the majority carriers in $p$-type semiconductors. The elements from the group V, the donors, have five electrons in the valence shell and very low energy is required to bring one of them to the conduction band. The majority carriers in $n$-type materials are electrons. In both $p$- and $n$-types materials there are carriers of the other type, coming from thermal excitation of silicon atoms, that are called minority carriers.

If $p$- and $n$-type semiconductor materials are brought together to form a $pn$-junction, diffusion of majority carriers into the other type semiconductor region occurs as a result of the gradient of densities: holes from the $p$ side diffuse into the $n$ side, and electrons from the $n$ side diffuse into the $p$ side. Around the junction, this migration leaves in the $p$ side a negative net charge and a positive one in the $n$ side, in the so called depletion region. This space charge is due to unneutralized, immobile acceptor and donor ions in regions $n$ and $p$, respectively, and generates an electric field. This creates a drift component of current opposing the diffusion, and the initial migration of carriers across the junction sets up a barrier to further migration, and equilibrium is reached.

The width of the region with no free charges, the depletion region, is given by the sum of the depletion depths into the $n$-side, $W_n$, and into the $p$-side,

$W_p$:

$$W_n = \sqrt{\frac{2\epsilon V_0}{q}\frac{N_a}{N_d(N_a+N_d)}} \tag{5.1}$$

$$W_p = \sqrt{\frac{2\epsilon V_0}{q}\frac{N_d}{N_a(N_a+N_d)}} \tag{5.2}$$

where $\epsilon$ is the dielectric constant, q is the absolute value of the electron charge, and $N_a$, $N_d$ represent the concentration of acceptors and donors, respectively. $V_0$ stands for the potential between both sides.

The depletion zone extends into the $p$ and $n$ sides in inverse proportion to the concentrations of impurities. Detectors typically use an asymmetric structure, e.g. a highly doped $p$ electrode and a lightly doped $n$ region, so that the depletion region extends predominantly into the light doped volume.

The charge created in the depletion region by a traversing particle could be collected at the junction and read out, whilst the charge created in the neutral, non-depleted zone, mainly recombines and is lost. It means that increasing the width of the depletion region increases the collected signal. Ideally one would like to have the whole thickness of the sensor depleted of free carriers.

The width of the depletion region can be altered by applying an external voltage across the junction. A positive voltage applied to the $p$-side and a negative one to the $n$-side (forward biasing) would oppose the built up internal voltage. As a result, the depletion region is reduced and the current between the terminals grows exponentially with the voltage. On the contrary, when a negative voltage is applied on the $p$-side and a positive one on the $n$-side (reverse biasing), the depletion region grows and only a constant and small current is expected (up to high applied voltages, when breakdown may be reached). The application of silicon as particle detectors is only possible if the presence of free charge carriers is minimized, which is achieved with a maximum depletion region. Hence, this can be done by applying the necessary voltage to fully deplete a reverse biased $pn$-junction. In fact, in order to avoid looses in charge collection and reduce the time invested in it, silicon sensors are operated with a bias voltage higher than the required for full depletion of the junction, i.e. "overbiased".

Since there is a voltage dependent charge associated with the depletion zone, one may speak of a junction capacitance. This decreases with increasing the bias voltage as $C \propto V^{1/2}$, arriving at a constant value when the depletion

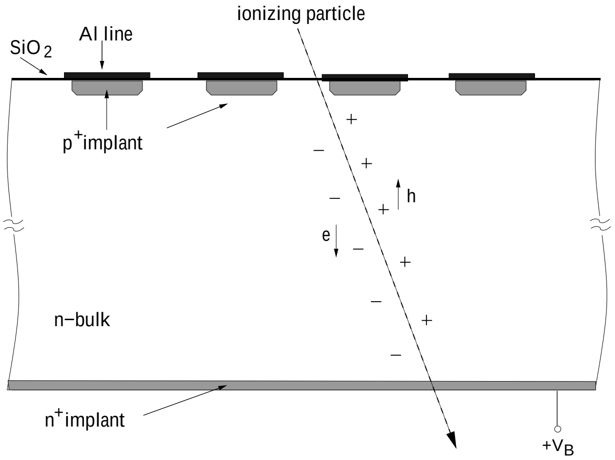

Figure 5.1: Scheme of the basic operation of a single-sided $p^+n$ Si-detector, showing the $p^+$ implants insulated from the AC-coupled Al electrodes by a layer of SiO$_2$. It consists essentially of a reverse biased diode, operated at a voltage sufficient to fully deplete the thick $n$ layer.

layer reaches the back of the crystal because a further increase of the biasing voltage would not increase the charge.

### 5.2.3 Silicon microstrip detectors

The position localization accuracy of silicon detectors is achieved by dividing the large-area $pn$-diode into many small regions, pixel-like or fine parallel strips, that act as individual independent electrodes. This section restricts to the description of silicon microstrip detectors, in particular single-sided $p^+n$ detectors ($p^+$ strips on $n$-type substrate), as the ones used in the Silicon Tracker of LHCb. A schematic cross-section of this type of microstrip detectors is shown in Figure 5.1.

When an incident particle ionizes the $n$-bulk, the resulting holes and electrons drift towards the $p^+$ (cathode) and $n^+$ (anode) sides due to the electric field caused by the depletion voltage. The collected charge produces a current pulse on the electrodes, which are individually read out by amplifiers. Thereby, the position of the strip at which the signal was generated yields the position of the traversing particle.

Most detectors are fabricated using high-resistivity $n^+$-type silicon wafers as the bulk material, which serves as the detection volume. The $p^+$ implants

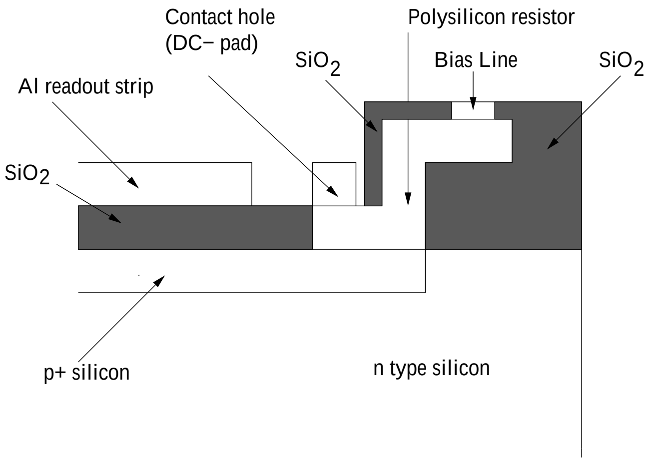

Figure 5.2: Cross section along a strip of a detector with integrated coupling capacitance and polysilicon biasing resistors.

are used to deplete the $n$-bulk and act as measuring electrodes. The aluminium readout lines serve as a contact to the input of the amplifier of the readout electronics. It can be in direct ohmic contact with the strip implant, but then the constant detector leakage current would flow into the amplifier. This might result in a serious operation problem by saturating the charge amplifier. Thus, an insulating layer is usually placed between the aluminium metal layer and the $p^+$ implants. The capacitance formed by the strip implant, the insulator (typically a multilayer structure of $SiO_2$ and $Si_3N_4$, and the readout line, known as the coupling capacitance, enables the signal current to be induced in the readout line at the time as avoids the leakage current to achieve it (this is called AC-coupling). The $n^+$ backplane connection is used as an ohmic contact to the $n$-type material.

The individual strip implants are connected to a “bias line” which provides a fixed potential to all strips, through resistors integrated in the detector. The resistance for these bias resistors has to be high enough to separate the strip from the others. The resistor values also have to be constant since large variations in them can lead to variations in the applied bias voltage to each strip. Figure 5.2 shows a cross section along a strip of such a structure. The resistors are made of implanted polycrystalline silicon (called from now on polysilicon), and its resistance depends on the doping level, their length and width.

Furthermore, the sensor is enclosed by one or several “guard rings” that define the active depletion volume of the detector, prevent the sensor from

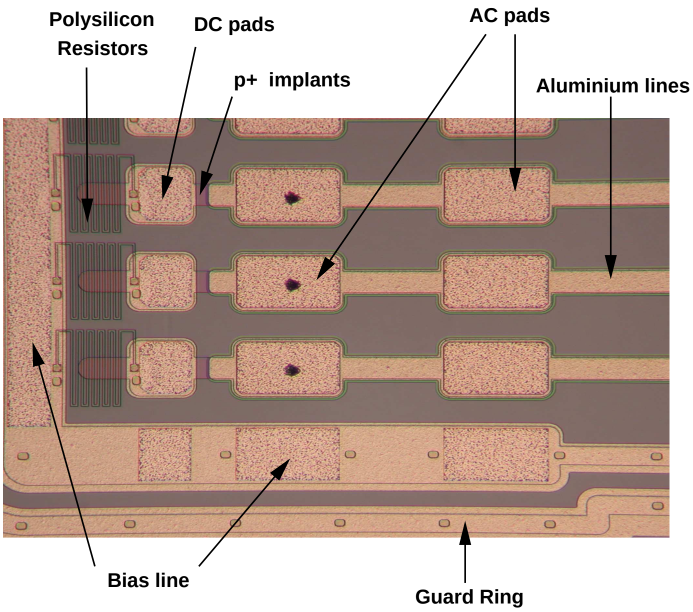

Figure 5.3: Photograph of a corner of a prototype sensor. The different elements are labeled.

field border effects (charge accumulations in the silicon edges), and prevent the leakage current from being absorbed by the edge strips, which would spoil their performance. The guard rings also degrade the potential towards the cut edge of the silicon, where otherwise large currents could flow.

Typical dimensions for silicon microstrip detectors are strip pitches (distance between strip centers) from 20 $\mu$m to 250 $\mu$m, and a thickness between 250 and 500 $\mu$m. These parameters depend on the application, and have to be optimized considering the readout electronics. As an example [53], the spatial resolution depends on the readout pitch but also on the readout method. For a digital readout it can be shown that the measurements precision, defined here as the root-mean-square distance of the measured coordinate to the true hit position, cannot be less than $p/\sqrt{12}$, where $p$ is the readout pitch. For analogue readout the precision can be improved by calculating the center of gravity of the signal or other interpolation techniques if the charge is spread over several strips.

Another crucial specification of the detector is the signal-to-noise ratio which directly translates into a hit finding efficiency. In silicon, higher signal is obtained with thicker sensors. On the other hand, for tracking detectors, radiation length is an important issue and therefore sensors should be as thin as possible. In addition, the noise critically depends on the detector capacitive load, which is a function of the sensor geometry, as well as on other requirements such as fast readout and radiation hardness. The sensor geometry has thus to be carefully chosen in order to optimize the detector performance.

### 5.2.4 Processing of microstrip detectors

Planar technology allows to make a very thin layer of $p$-type silicon on a $n$-type wafer. Thanks to this method it is also possible to make narrow strips with very good precision.

For detectors, high-resistivity $n$-type silicon is mainly used as substrate. The chosen lattice orientation is typically $\langle 111 \rangle$, because it gives the highest energy loss, or $\langle 100 \rangle$ material, due to its lower density of dangling bonds at the silicon/silicon dioxide surface, and hence lower trapped charge at the interface. In the present technology of silicon production, ingots of a diameter up to 6 inches can be grown. Those ingots are sliced to wafers about 500 $\mu$m thick and then polished to obtain a very smooth and clean surface with the desired thickness.

In Figure 5.4, a simplified production sequence is illustrated. First the $n$-type silicon wafer is chemically cleaned and oxidized by heating it in an oxygen atmosphere at around 1000℃ to have the whole surface passivated. Using photolithographic and etching techniques, windows are opened in the oxide to enable doping of silicon in the desired areas. Using appropriate masks, any geometry of pads or strips is feasible. Doping of silicon can be performed by either ion implantation or diffusion. Figure 5.4 shows schematically ion implantation and typical values of ions energies and densities. The $p^+$ strips are implanted with boron, and the back contact is made with phosphorus or arsenic ions. The next step after ion implantation is annealing (heating at $600 - 800$℃) to reduce the damage to the crystal caused by the irradiation with the heavy ions and to get the implanted atoms properly built into the lattice.

Implanted strips must be metalized because ultrasonic bonding is possible only on metals. The surface of the wafer is covered with aluminium and using appropriate masks, the desired pattern is generated. The back of the wafer is usually aluminized too. The wafer is then ready for cutting.

An alternative method of doping silicon to obtain the $p^+$ layer is by diffusion of impurities atoms. Gaseous boron is deposited on the surface of the

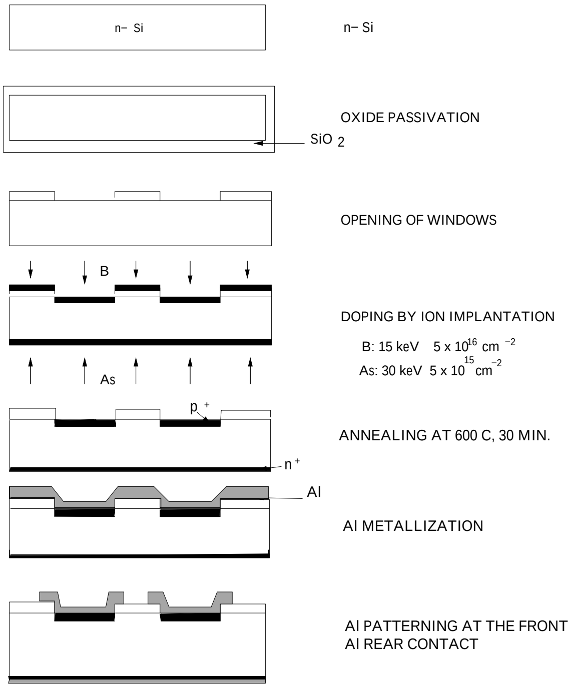

Figure 5.4: The planar process for detector fabrication.

wafer forming boron glass, which is then stripped away. During the deposition, ions diffuse into silicon. The diffusion is performed at 930℃ and a layer of oxide is grown on the $p^+$ strips. This oxide can be etched away to apply metal directly on the strips or leave it to make a capacitor to decouple the leakage current from the input of the amplifier (integrated coupling capacitors).

## 5.3 Radiation induced damage of silicon detectors

Radiation damage in silicon can be divided into surface and bulk damage that have relative importance depending on the kind of radiation and structure of the detector. A brief overview of these effects is given below. Further information can be found in [48, 56].

Electron-hole pairs created by Ionizing Energy Loss (IEL) —photons or charged particles— do not cause permanent damage in crystalline silicon. On the contrary, the amorphous oxide insulator is very sensitive to the ionizing radiation. Because of the large band gap of insulators (8.8 eV for $SiO_2$ compared to the 1.12 eV for Si), free electrons and holes can be trapped by deep levels associated with defects in the oxide. From these levels, the emission of captured carriers into the conduction and valence bands is very unlikely at room temperature. In addition, electron mobility is several orders of magnitude higher than that of holes, so the capture of holes is the dominant process that changes the material's properties. Therefore, the radiation damage of the oxide manifests as an accumulation of positive charges in the oxide and the silicon-oxide interface. Macroscopic effects are changes in the inter-strip capacitance (noise factor), breakdown behaviour, or an increase of surface generation current.

Bulk damage is due to Non Ionizing Energy Loss (NIEL). The bulk is mainly damaged by displacement of the lattice atoms producing damage of the crystal structure, and is generated by massive particles such as hadrons and heavy ions. The essential radiation induced changes in macroscopic detector properties due to bulk damage are an increase in leakage current, a change in the effective doping concentration, and a degradation in charge collection efficiency.

The bulk damage leads to an increase of the leakage current. The leakage current increase due to radiation scales linearly with the received fluence $\phi$ and is proportional to the depleted volume $V$ of the detector:

$$\Delta I = \alpha V \phi. \tag{5.3}$$

The proportionality factor $\alpha$ is the current related damage constant, which depends on the particle type and energy and is independent of the specific material. The increase in leakage current gives rise to an increase of shot noise, and might derivate in thermal runaway of the detectors.

Radiation damage in the silicon bulk produces a change in the effective doping concentration. The original dopants such as phosphorus or boron may be captured into new defects induced by the radiation, thereby losing their original function as donors or acceptors (called donor- /acceptor-removal) [48]. In addition to complexes involving the original dopants, complexes with other impurities, as well as other radiation-generated primary defects such as divacancies, can be formed giving rise to the formation of new dopants.

The effective doping concentration of an initially $n$-type silicon wafer is shown as a function of the irradiation fluence in Figure 5.5. It can be seen that the effective doping decreases with the irradiation fluence and that the silicon becomes intrinsic at an irradiation fluence of approximately

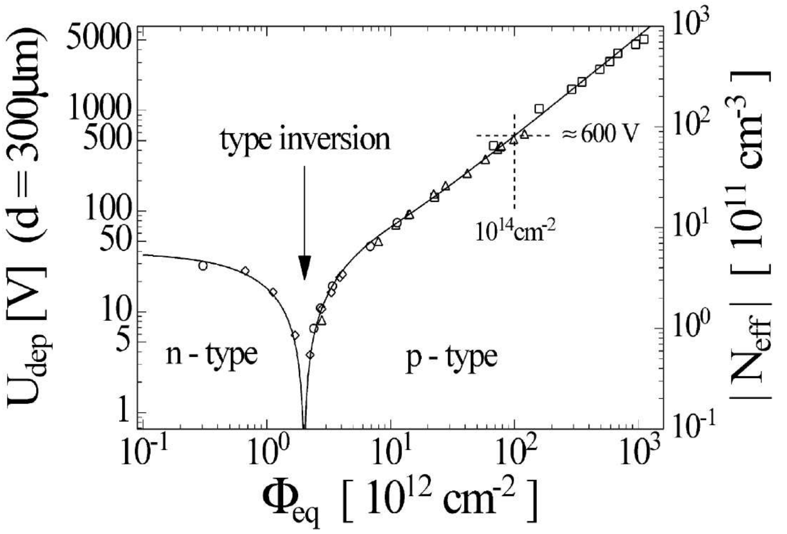

Figure 5.5: Effective doping concentration and full depletion voltage for an initially $n$-type silicon sensor as a function of the equivalent 1 MeV neutrons, as measured directly after irradiation. Reproduced from [57].

$2\times10^{12}$ 1MeV n/cm$^2$. Above this value the silicon becomes effectively $p$-type. This behaviour is referred to as type inversion [48].

The change in the effective doping concentration produces a change in the full depletion voltage, as

$$V_{depl} = ed^2\frac{N_{eff}}{2\epsilon\epsilon_0}. \tag{5.4}$$

The full depletion voltage after irradiation depends on the initial doping concentration, the received fluence and the temperature.

The interaction of the radiation with the silicon lattice leads to permanent material changes such as trapping centers. This gives rise to an increase of charge carrier trapping, which may be released too late for detection, causing a degradation of the charge collection efficiency and the signal.

After the end of the irradiation process, the radiation induced damage in the detector (which manifests itself in an increase of leakage current, effective doping change, and trapping probability) diminishes with time. The rate of damage decrease is strongly dependent on the temperature at which the detector is kept during the waiting period.

# Chapter 6

# Electrical characterization of different prototype sensors

In this chapter we present the electrical characterization of three groups of prototype sensors with strip geometry parameters very similar to those foreseen for the Silicon Tracker, but with three different thicknesses, being thus well suited for initial measurements. These tests were the first step for the determination of the optimal wafer thickness for silicon sensors that will be used in the detector.

## 6.1 Introduction

The silicon sensor geometry for the TT station differs from the one used in the Inner Tracker (IT) mainly on the thickness (see Chapter 4). The TT station will consist of longer silicon modules than the IT, resulting in a higher noise due to the higher load capacitance connected to the readout electronics. Therefore, thicker sensors have to be employed in order to obtain larger signals and a sufficiently high signal-to-noise ratio.

The design of the TT station is driven to minimize the mass in the active area. Therefore we consider long analog cables which connect the silicon sensors to the readout electronics outside the active area. The characteristics of these interconnects also influence the noise performance and had to be studied in great detail.

This chapter describes the electrical characteristics of three groups of wide pitch silicon sensors that were studied for the Silicon Tracker (ST), and presents the results of leakage currents, depletion voltages, total strip capacitances, inter-strip capacitances, coupling capacitances, and polysilicon resistor values. These measurements were performed on 320 $\mu$m thick Hamamatsu LHCb Multi-Geometry sensors, 410 $\mu$m thick GLAST2000 sensors, and 500 $\mu$m thick OB2-type CMS silicon sensors (purchased from the CMS silicon tracker group). The aim of these measurements was to achieve a thorough understanding of the electrical properties of these sensors, and to select the best sensors of each group according to the electrical characteristics. These sensors were later assembled to three sensor long modules, and were tested in a laser test-stand and in a test beam in May 2003. Details of this tests are given in Chapters 8 and 9, and in [58, 59]. In addition, capacitance measurements of long flex kapton interconnect prototype cables are presented.

The tests were carried out in the Physik-Institut der Universität Zürich using a manual probe station (PM 5 Karl Suss), a Keithley 487 unit (picoammeter + voltage source) and an HP 4192A LF LCR-meter.

The outline of this chapter is the following: the three groups of studied prototype sensors are described in Section 6.2. Results of the electrical characterization, including leakage currents, depletion voltages, total strip capacitances, inter-strip capacitances, coupling capacitances, and bias resistor measurements are presented in Section 6.3. The kapton interconnect prototype cables are described, and results of capacitance measurements are given in Section 6.4.

## 6.2 Prototype silicon sensors

Three groups of silicon microstrip sensors were electrically characterized, each group consisting of five sensors. All these prototype detectors are p-on-n type single-sided AC-coupled sensors, produced from 6" wafers. Tables 6.1 and 6.2 summarize the sensor details. Their main characteristics are explained below:

- Hamamatsu LHCb Multi-Geometry sensors

  The multi-geometry Hamamatsu sensors (from now on called LHCb) were manufactured by Hamamatsu Photonics, Japan, according to the specifications of the ST group. The five sensors were coming from an overrun and were delivered to us in addition to the 15 officially ordered. The 15 officially shipped sensors are characterized in [60].

  The sensors have physical dimensions of 110 × 78 $\text{mm}^2$ and a nominal thickness of 320 $\mu$m of the $n$-type substrate. The actual thickness of the

| | Hamamatsu LHCb | GLAST2000 | OB2 CMS |
|---|---|---|---|
| Wafer size | 6” | 6” | 6” |
| Sensor size | $110 \times 78$ mm$^2$ | $89.5 \times 89.5$ mm$^2$ | $96 \times 94$ mm$^2$ |
| Crystal orientation | $\langle 100 \rangle$ | $\langle 100 \rangle$ | $\langle 100 \rangle$ |
| Active area | $108 \times 75.6$ mm$^2$ | $87.5 \times 87.5$ mm$^2$ | $94 \times 92$ mm$^2$ |
| Nominal thickness | $(320 \pm 20)$ $\mu$m | $(410 \pm 15)$ $\mu$m | $(500 \pm 20)$ $\mu$m |
| Bulk material | $n$ type | $n$ type | $n$ type |
| Implant | $p^+$ type | $p^+$ type | $p^+$ type |
| Pitch | see table 6.2 | 228 $\mu$m | 183 $\mu$m |
| Implant width | see table 6.2 | 56 $\mu$m | 46 $\mu$m |
| # of strips | 352 | 384 | 512 |
| Biasing | polysilicon | polysilicon | polysilicon |
| readout coupling | AC | AC | AC |

Table 6.1: Geometry parameters and characteristics of Hamamatsu LHCb Multi-Geometry, GLAST2000, and OB2 CMS sensors.

| Region | Pitch | # of strips | Implant width | $w/p$ |
|---|---|---|---|---|
| A | 198 $\mu$m | 64 | 50 $\mu$m | 0.252 |
| B | 198 $\mu$m | 64 | 60 $\mu$m | 0.303 |
| C | 198 $\mu$m | 64 | 70 $\mu$m | 0.354 |
| D | 237.5 $\mu$m | 80 | 70 $\mu$m | 0.295 |
| E | 237.5 $\mu$m | 80 | 85 $\mu$m | 0.358 |

Table 6.2: Geometry parameters of the Hamamatsu LHCb Multi-Geometry sensors.

sensors were measured over the whole surface on the optical metrology machine [1] at the Physik Institut in Zürich which resulted in a thickness average of 316$\pm$8 $\mu$m. The sensors consist of five different regions. Two different pitches of $p^+$ strips, 198 $\mu$m and 237.5 $\mu$m, are implemented on the sensor. Additionally, the width of the $p^+$ strips is varied. The 198 $\mu$m region has implant widths of 50 $\mu$m, 60 $\mu$m and 70 $\mu$m, whereas the width of the strips in the 237.5 $\mu$m region is 70 $\mu$m and 85 $\mu$m, respectively. This design results in five different values of the ratio strip width to strip pitch, $w/p$, although two are almost the same. The width of the aluminium electrodes is specified to be 8 $\mu$m wider than the implant width, which gives rise to a more stable operation with respect to high bias voltages.

The five sensors that we studied have serial numbers from 0001 to 0005, and are here called LHCb 1 to LHCb 5, respectively.

- GLAST2000 sensors

  The SSD S8743 GLAST2000 sensors (from now on called GLAST) were fabricated by Hamamatsu Photonics, Japan.

  The physical dimensions of these sensors are 89.5 × 89.5 mm$^2$. The nominal thickness of the $n$-type substrate is given as 410 $\mu$m. Our measurements however, yielded an average thickness of 418 $\pm$ 5 $\mu$m. The $p^+$ strip pitch is 228 $\mu$m and the width is 56 $\mu$m, resulting in a $w/p$ ratio of 0.246. The width of the aluminium electrodes is specified to be 8 $\mu$m wider than the implant width.

  The sensors we studied have serial numbers from 04096 to 04100, and are here called GLAST 1 to GLAST 5, respectively.

- OB2 CMS sensors

  The OB2-type CMS sensors (from now on called CMS) were manufactured by ST Microelectronics, Italy, and were purchased from the CMS Silicon Tracker group.

  The physical dimensions of these sensors are 94.4 $mm \times$ 94.6 mm$^2$. The nominal thickness of the $n$-type substrate is given as 500 $\mu$m. Our measurements however, yielded an average thickness of 515 $\pm$ 5 $\mu$m. The $p^+$ strip pitch is 183 $\mu$m and the width is 46 $\mu$m, which results in a $w/p$ ratio of 0.251. The width of the metal strips is 58 $\mu$m (12 $\mu$m wider than the implant strips).

---

[1] Mahr OMS 600 Multisensor Metrology Machine.

| | Hamamatsu LHCb | GLAST2000 | OB2 CMS |
|---|---|---|---|
| Leakage current | $< 1$ μA<br>at 80 V | $< 500$ nA<br>at 150 V | $< 10$ μA<br>at 450 V |
| Breakdown voltage | $> 300$ V | $> 175$ V | $> 550$ V |
| Depletion voltage | 40-100 V | $< 120$ V | 100-300 V |
| Inter-strip capacitance | not specified | $< 1.5$ pF/cm | $< 1.3$ pF/cm |
| Coupling capacitance | $> 125$ pF/mm$^2$ | $> 500$ pF | $> 520$ pF |
| Bias resistors | $(1.5 \pm 0.5)$ MΩ | 20 - 80 MΩ | $(1.5 \pm 0.5)$ MΩ |

Table 6.3: Specifications of Hamamatsu LHCb Multi-Geometry [60], GLAST2000 [61], and OB2 CMS sensors [62–64].

The sensors have serial numbers 30210414735xxx. The three last numbers (xxx) are related with the name given to the sensor as follows: 814 is called CMS 1, 804 is CMS 2, 813 is CMS 3, 710 is CMS 4 and 821 is CMS 5.

## 6.3 Results

### 6.3.1 Leakage current

The leakage current is the reverse current of the *pn*-junctions. It gives rise to a background noise and is caused by thermally excited minority carriers that are generated in the depleted region and, due to the electric field, drift to the electrodes. For a given bias voltage, the size of the leakage current depends to a certain extent on environmental factors, like temperature, humidity and time of operation of the sensor, but its variation will in general be small (of the order of a few hundreds nA at the full depletion voltage for a good sensor).

The current between the backplane and the bias ring was measured for all 15 sensors as a function of the reverse bias voltage, using a Keithley 487 unit (picoamperemeter + voltage source). The bias voltage was increased in steps of 5 V up to 500 V (or up to breakdown if observed before) over a period of 5 minutes. We define the breakdown voltage as the reverse bias voltage at which a sharp increase in the current occurs. The measurements were performed at room temperature, typically about 20°C, and at a relative humidity below 30%.

The measured leakage currents and breakdown voltages are compared to the specifications of each type of sensor in Table 6.4.

The *I*-*V* curves measured for all 15 sensors are shown in Figure 6.1. Currents are divided by the sensor volume in order to facilitate the comparison among the different prototypes.

At the top, the currents measured for the LHCb sensors are shown. Two of the five sensors evidence breakdown before 500 V: LHCb 1 at 80 V, and LHCb 5 at 420 V. LHCb 3 shows a steady increase in leakage currents and a clear breakdown voltage limit can therefore not be derived. The curves have very different shapes, which shows that these sensors are not uniform with respect to leakage currents. It can be seen that the currents of two of the sensors (LHCb 1 and LHCb 3) are higher than the specifications, and therefore they must be rejected if they would have come from a normal production run. In addition, breakdown occurs before 300 V for sensor LHCb 1.

The middle plot shows the currents measured for the GLAST sensors. The bias voltage was increased up to 500 V without evidence of breakdown in any of the 5 sensors.These sensors agree with both specifications, showing very low currents (about 120 nA at 500 V) and no breakdown in all the voltage range provided by the source. This group of sensors have a great uniformity with respect to the currents. We compared our measurements with the ones provided by the manufacturer, and we found ours to be about 30% lower. This difference can mainly be attributed to the differences on the setup or ambient conditions, like temperature [2] or humidity.

The measured currents for the CMS sensors are shown at the bottom. A large increase in current after 250 or 300 V is observed. According to our breakdown definition, all these sensors evidence breakdown before 500 V. In the CMS specifications the sensors shall satisfy the condition $\Delta I_{leak}/\Delta \mathrm{V} <$ 10 nA/V in the range 450-550 V. Although the total magnitude of currents is within specifications, the sensors fail in the breakdown voltage specification completely.

Currents were divided by the sensor volume in order to facilitate the comparison between different prototypes. As shown in Figure 6.1, GLAST sensors have the lowest leakage currents, being one and even two orders of magnitude lower than CMS and LHCb sensors, respectively.

---

[2] Hamamatsu measures the leakage current at 25 ± 2°C whilst we measure at room temperature, typically about 20°C.

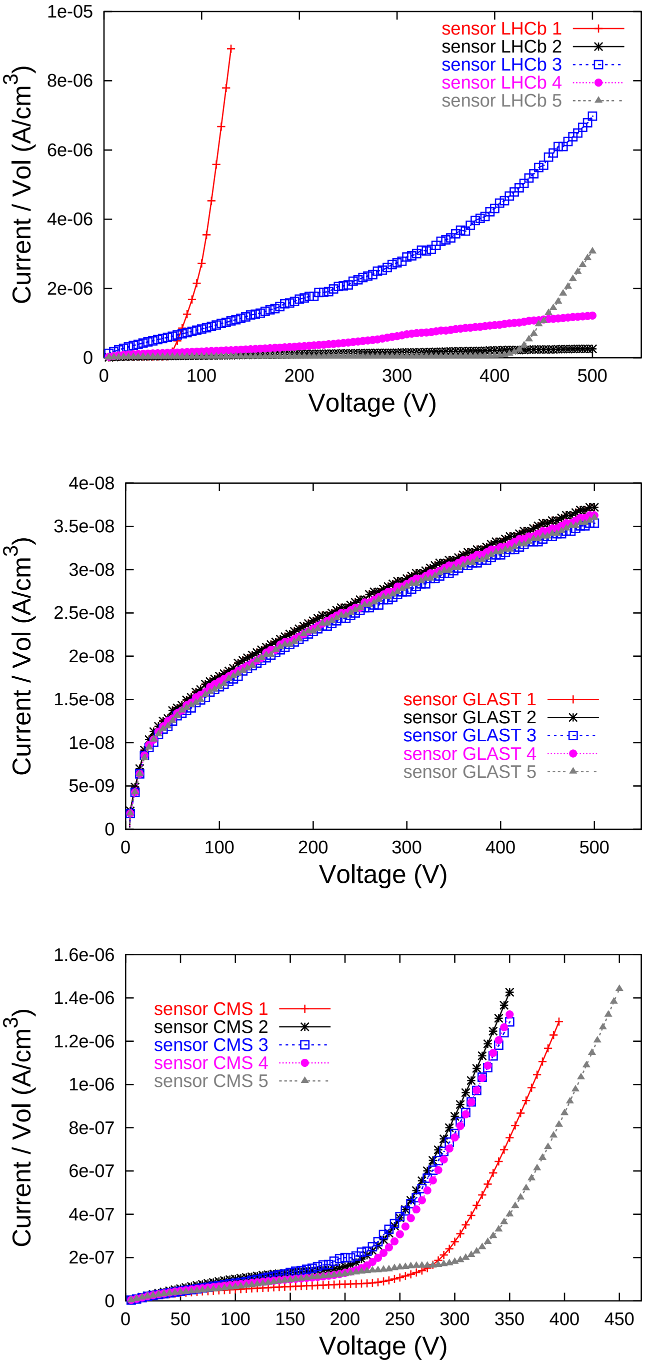

Figure 6.1: Leakage currents as a function of the bias voltage for the different sensors. The currents are normalized by the sensor volume in order to facilitate the comparison among the prototypes. Note the difference in the vertical scale for each plot.

| Sensor | Leakage current | | Breakdown voltage | |
|---|---|---|---|---|
| | Measured | Specifications | Measured | Specifications |
| LHCb 1 | 2.4 $\mu$A | $I_{leak} < 1\mu$A at 80 V | $V_b = 80$ V | $V_b > 300$ V |
| LHCb 2 | 0.2 $\mu$A | | $V_b > 500$ V | |
| LHCb 3 | 1.9 $\mu$A | | not defined | |
| LHCb 4 | 0.4 $\mu$A | | $V_b > 500$ V | |
| LHCb 5 | 0.1 $\mu$A | | $V_b = 420$ V | |
| GLAST 1 | 69 nA | $I_{leak} < 500$ nA at 150 V | $V_b > 500$ V | $V_b > 175$ V |
| GLAST 2 | 65 nA | | $V_b > 500$ V | |
| GLAST 3 | 67 nA | | $V_b > 500$ V | |
| GLAST 4 | 66 nA | | $V_b > 500$ V | |
| GLAST 5 | 67 nA | | $V_b > 500$ V | |
| CMS 1 | 1.2 $\mu$A | $I_{leak} < 5\mu$A at 300 V | $V_b = 275$ V | $V_b > 500$ V |
| CMS 2 | 3.9 $\mu$A | | $V_b = 200$ V | |
| CMS 3 | 3.5 $\mu$A | | $V_b = 200$ V | |
| CMS 4 | 3.4 $\mu$A | | $V_b = 200$ V | |
| CMS 5 | 0.8 $\mu$A | | $V_b = 300$ V | |

Table 6.4: Comparison between measured values and the specifications for leakage currents and breakdown voltages. The leakage currents of two sensors, LHCb 1 and LHCb 3, are higher than the specifications. CMS sensors fail the breakdown voltage specifications, as well as sensor LHCb 1.

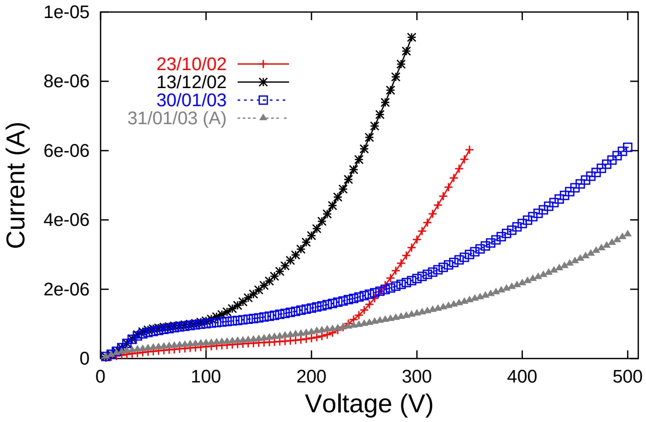

Figure 6.2: Leakage current of CMS 4 measured on different days. Huge variations were observed without any apparent reason. The curve labeled with “A” was made immediately after annealing, and has the lowest currents.

### 6.3.2 Stability of $I$-$V$ curves

The $I$-$V$ curves were repeated for one sensor in each group after some days as a check of the stability. For the GLAST and LHCb sensors, the curves were consistent and stable. The currents for the CMS sensors were, however, not reproducible. Figure 6.2 shows different $I$-$V$ curves obtained for sensor CMS 4 (this behaviour is representative for the others). Large current variations were observed without any apparent reason. After a visual inspection under microscope, we found chipping edges, which could be the underlying problem of these variations. A possible explanation is that the sensors could attract some moisture at the edges, which may affect the currents. As a test, an annealing of CMS 4 was made (it was kept in an oven flashed with argon at 85 ° C for 2.5 hours), and afterwards the current was immediately re-measured. It was found to be lower than in preceding measurements (see Figure 6.2, curve labeled with “A”), which somehow confirm our explanation. Later it was observed [66], that the leakage currents for sensors of the same type, manufactured by the same company, depended critically on the application of vacuum to the chuck of the probe station. Although this dependence was not investigated on these five sensors, it is likely that the mechanical stress is affecting the currents.

Moreover, the current stability of two sensors of each group was investigated and verified in a $\sim$ 40 h long biasing test, while temperature and

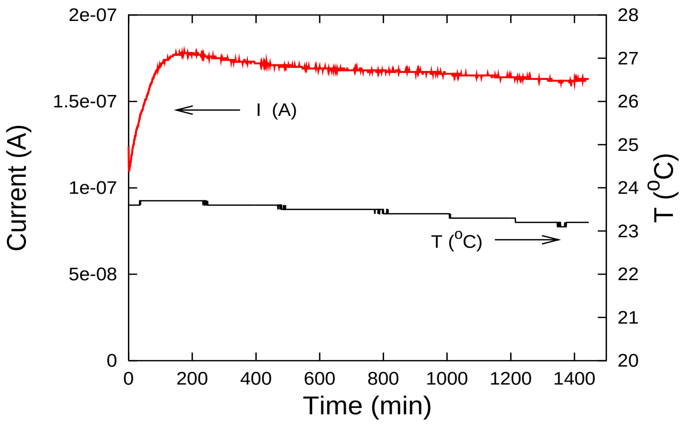

Figure 6.3: Current stability test for the GLAST 5 sensor. The sensor was biased at 200 V during 25 hours. No significant variations of the leakage current were observed after stabilization in the first hours.

relative humidity were monitored. No significant variations of the leakage currents were observed over the duration of this test.

### 6.3.3 Depletion voltage

The full depletion voltage determines the operation voltage of the sensors. We estimated the full depletion voltage from the measurement of the bulk capacitance as a function of the applied bias voltage. The bulk capacitance of the sensor is the capacitance of all readout strips to the backplane. It is proportional to the inverse of the square root of the bias voltage applied to the sensor until full depletion is reached, and then assumes a constant value. We plot $1/C^2$ as a function of the bias voltage and estimate the depletion voltage as the intersection of two straight lines fitted to the rising part and the flat part of the curve.

The capacitance measurements were performed using a Keithley 487 unit as a voltage source and an HP 4192 LCR-meter to measure the capacitance between the bias line and the backplane. Figure 6.4 shows the measured curves of $1/C^2$ as a function of the bias voltage for all 15 sensors.

The upper plot in the figure shows the measurements for all five LHCb sensors. The $C$-$V$ curves were made using a signal frequency of 1 kHz and a signal amplitude of 0.1 V. The obtained full depletion voltages are between

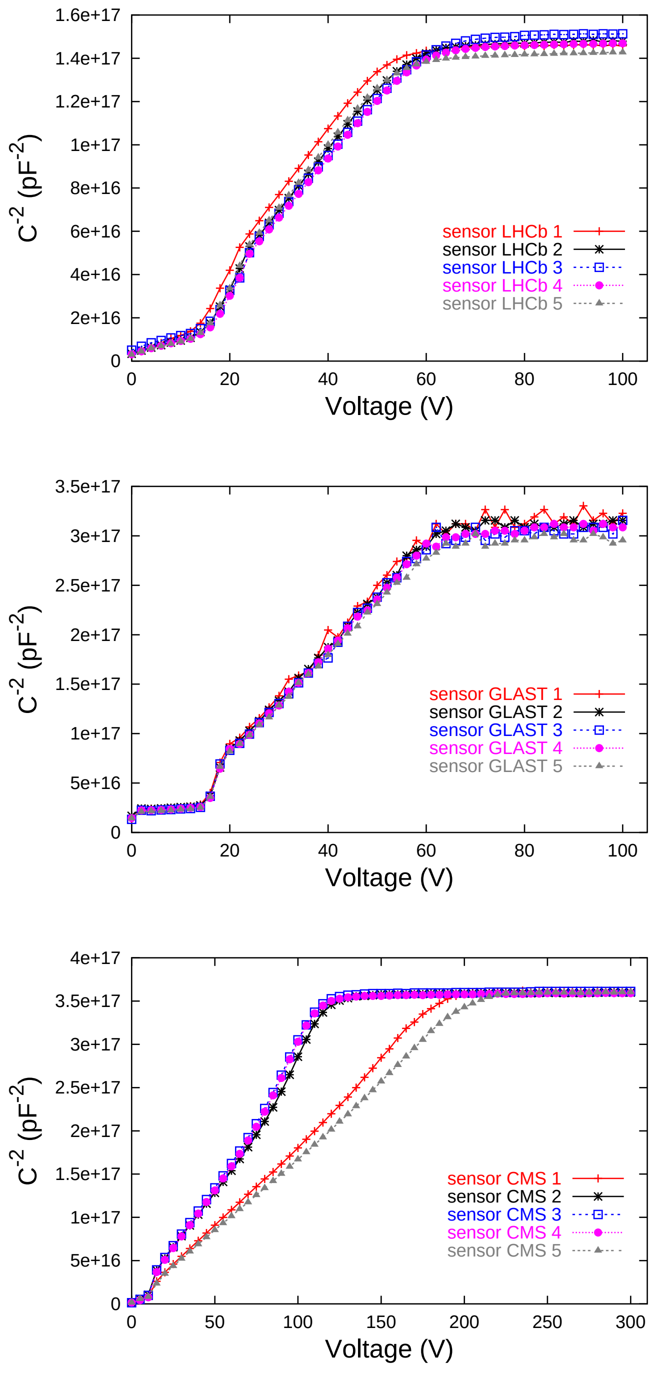

Figure 6.4: $1/C^2$ versus bias voltage for the different sensors. The full depletion voltage is extracted from each curve as the intersection of two straight lines.

| Sensor | Depletion Voltage | |
|---|---|---|
| | Measured | Specifications |
| LHCb 1 | 60 V | $V_d : 40 - 100$ V |
| LHCb 2 | 64 V | |
| LHCb 3 | 64 V | |
| LHCb 4 | 64 V | |
| LHCb 5 | 62 V | |
| GLAST 1 | 70 V | $V_d < 120$ V |
| GLAST 2 | 70 V | |
| GLAST 3 | 70 V | |
| GLAST 4 | 70 V | |
| GLAST 5 | 70 V | |
| CMS 1 | 190 V | $V_d < 300$ V |
| CMS 2 | 130 V | |
| CMS 3 | 130 V | |
| CMS 4 | 130 V | |
| CMS 5 | 220 V | |

Table 6.5: Comparison between specifications and measured full depletion voltages for all 15 sensors. All of them are within specifications.

60 and 64 V (detailed values can be found in Table 6.5).

The middle plot shows $1/C^2$ vs bias voltage for all five GLAST sensors. These sensors have high-value bias resistors (of about 50 M$\Omega$) which, together with the bulk capacitance that we want to measure, act as low-pass filters. Therefore, a lower measuring frequency was used with these prototypes. The signal frequency was 100 Hz and the signal amplitude 0.1 V. Some scattering in the measurements, due to this low frequency, can be observed. Nevertheless, a good estimation of the full depletion voltage is still possible. It was found to be of the order of 70 V for all these sensors.

The lower plot shows $1/C^2$ vs bias voltage for all five CMS sensors. A signal frequency of 1 kHz and a signal amplitude of 0.1 V were used for these measurements. The full depletion voltage of three of the sensors is 130 V, while the remaining deplete at higher voltages (about 200 V). This can be explained as the sensors have different bulk resistivities, as they come from different batches. Detailed values are summarized in Table 6.5.

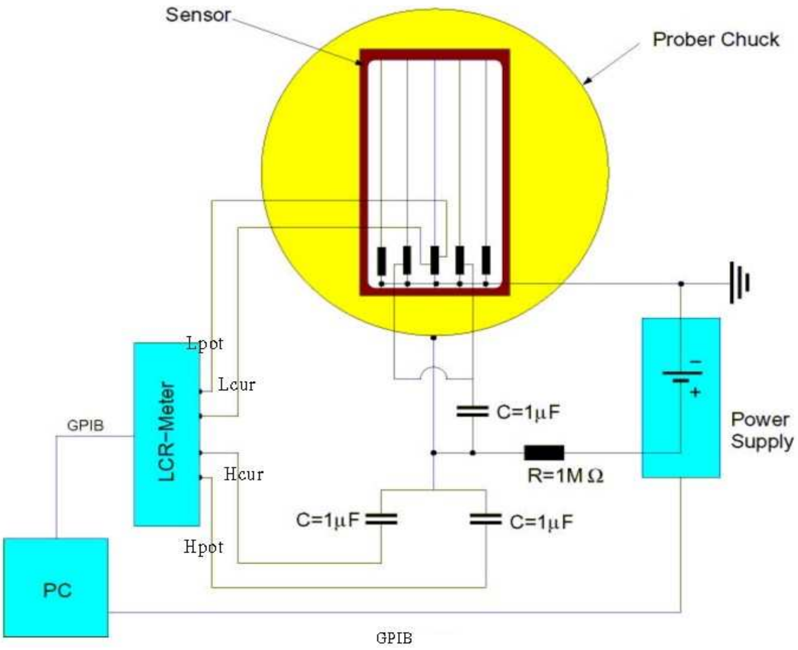

Figure 6.5: Setup for the total strip capacitance measurements.

### 6.3.4 Total strip capacitance

The total strip capacitance is here defined as the sum of the capacitance to the backplane and the capacitance to adjacent strips, measured at a signal frequency of 1 MHz [67]. The effect of the remaining strips was neglected in view of the large pitch of the sensors. The two closest neighbours were AC-coupled to the backplane. A sketch of the measurement setup can be seen in Figure 6.5.

The interest in these measurements lays in the fact that the total strip capacitance limits the achievable signal-to-noise ratio of a sensor connected to fast readout electronics, since the Johnson noise from the load capacitance at the input of the pre-amplifier is the main contribution to the noise of the front-end amplifier.

In addition, the full depletion voltage could also be estimated from these measurements. As mentioned before, the capacitance to the backplane is proportional to the inverse of the square root of the bias voltage until full depletion is reached, and then assumes a constant value. Since the inter-strip capacitance is almost independent of the bias voltage, this argument holds also for the total strip capacitance. Nevertheless, the method based in bulk

| Sensor | $w/p$ | $\overline{C}$(pF) | $\overline{C}/L$ (pF/cm) |
|---|---|---|---|
| GLAST 1 | 0.246 | 14.7 ± 0.7 | 1.7 ± 0.1 |
| GLAST 2 | | 14.0 ± 0.5 | 1.6 ± 0.1 |
| GLAST 3 | | 14.0 ± 0.4 | 1.6 ± 0.1 |
| GLAST 4 | | 13.5 ± 0.5 | 1.5 ± 0.1 |
| GLAST 5 | | 11.3 ± 0.1 | 1.30 ± 0.01 |
| CMS 1 | 0.251 | 12.6 ± 0.6 | 1.4 ± 0.1 |
| CMS 2 | | 13.0 ± 0.8 | 1.4 ± 0.1 |
| CMS 3 | | 12.5 ± 0.6 | 1.4 ± 0.1 |
| CMS 4 | | 13.5 ± 0.3 | 1.48 ± 0.03 |
| CMS 5 | | 12.4 ± 0.6 | 1.3 ± 0.1 |

| Sensor | Reg. | $w/p$ | $\overline{C}$(pF) | $\overline{C}/L$ (pF/cm) |
|---|---|---|---|---|
| LHCb 1 | A | 0.252 | 15.1 ± 0.3 | 1.37 ± 0.03 |
| | B | 0.303 | 16.1 ± 0.3 | 1.46 ± 0.03 |
| | C | 0.354 | 17.2 ± 0.1 | 1.56 ± 0.01 |
| | D | 0.295 | 16.0 ± 0.2 | 1.45 ± 0.02 |
| | E | 0.358 | 17.4 ± 0.3 | 1.58 ± 0.03 |
| LHCb 2 | A | 0.252 | 15.4 ± 0.4 | 1.40 ± 0.04 |
| | B | 0.303 | 16.2 ± 0.4 | 1.47 ± 0.04 |
| | C | 0.354 | 17.3 ± 0.1 | 1.58 ± 0.01 |
| | D | 0.295 | 16.7 ± 0.3 | 1.55 ± 0.03 |
| | E | 0.358 | 17.4 ± 0.6 | 1.61 ± 0.05 |
| LHCb 3 | A | 0.252 | 15.6 ± 0.1 | 1.44 ± 0.01 |
| | B | 0.303 | 16.7 ± 0.0 | 1.55 ± 0.00 |
| | C | 0.354 | 18.4 ± 0.2 | 1.70 ± 0.02 |
| | D | 0.295 | 16.5 ± 0.5 | 1.53 ± 0.05 |
| | E | 0.358 | 18.1 ± 0.1 | 1.68 ± 0.01 |
| LHCb 4 | A | 0.252 | 15.6 ± 0.1 | 1.44 ± 0.01 |
| | B | 0.303 | 16.7 ± 0.1 | 1.55 ± 0.01 |
| | C | 0.354 | 17.6 ± 0.1 | 1.63 ± 0.01 |
| | D | 0.295 | 16.5 ± 0.1 | 1.53 ± 0.01 |
| | E | 0.358 | 17.9 ± 0.0 | 1.66 ± 0.00 |
| LHCb 5 | A | 0.252 | 15.5 ± 0.1 | 1.44 ± 0.01 |
| | B | 0.303 | 16.5 ± 0.1 | 1.53 ± 0.01 |
| | C | 0.354 | 17.9 ± 0.1 | 1.66 ± 0.01 |
| | D | 0.295 | 17.0 ± 0.0 | 1.57 ± 0.00 |
| | E | 0.358 | 18.0 ± 0.0 | 1.67 ± 0.00 |

Table 6.6: Total strip capacitance and capacitance normalized by the strip length for the different sensors. The numbers given here are the mean value of the measured capacitances for five strips on each GLAST and CMS sensors, and for two strips on each region of the LHCb ones. The errors correspond to the RMS of the data.

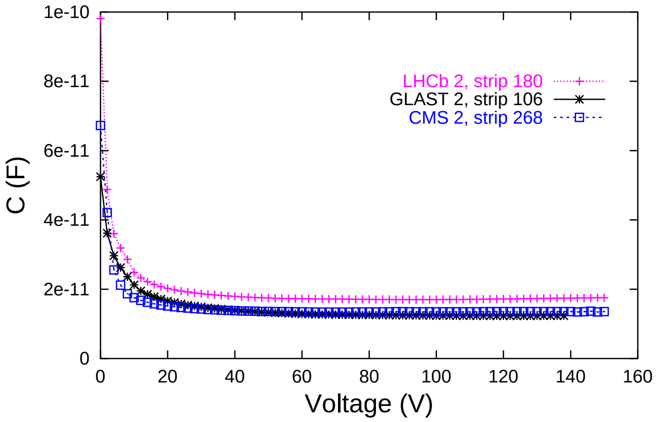

Figure 6.6: Total strip capacitance as a function of the bias voltage for one strip of each type of sensor.

capacitance measurements is more precise, since it takes into account the whole sensor, and not only one particular strip.

Measurements of the total strip capacitance as a function of the bias voltage were carried out for five strips in each of the GLAST and CMS sensors, and for two strips in each region for the LHCb ones. Figure 6.6 shows an example of this dependence for one strip in one sensor of each type. The obtained capacitance values, at bias voltages above the full depletion voltage, are summarized in Table 6.6. The mean value was calculated for each sensor and the error assigned to it corresponds to the RMS of the individual measurements for this sensor. For the LHCb sensors, this was done separately for each region. Since LHCb sensors have in three regions different $w/p$, the total strip capacitance is not uniform. As expected, the capacitance increases roughly linear towards higher $w/p$ ratio.

### 6.3.5 Inter-strip capacitance

The inter-strip capacitance as a function of the bias voltage was measured for one sensor of each type to make an estimation of the relative contributions of the inter-strip capacitance and the capacitance to the backplane to the total strip capacitance.

The capacitance was measured between five pairs of strips for the GLAST and CMS sensor, and for two pairs in each region of the LHCb one. The

| Sensor | Reg. | $w/p$ | $\overline{C}$(pF) |
|---|---|---|---|
| LHCb 5 | A | 0.252 | 3.62 ± 0.06 |
| | B | 0.303 | 4.1 ± 0.1 |
| | C | 0.354 | 4.42 ± 0.01 |
| | D | 0.295 | 3.75 ± 0.03 |
| | E | 0.358 | 4.4 ± 0.2 |
| GLAST 1 | | 0.246 | 3.6 ± 0.2 |
| CMS 4 | | 0.251 | 3.9 ± 0.1 |

Table 6.7: Inter-strip capacitances to one neighbouring strip, measured at 1 MHz.

signal frequency of the LCR-meter was 1 MHz, and the signal amplitude 0.1 V. The bias voltage was varied between 0 and 200 V. As expected, the inter-strip capacitance decreases with the applied voltage up to this reaches a few volts and the region in the proximity of the two strips is depleted. Towards higher bias voltages the value of inter-strip capacitance is constant. The mean values of the inter-strip capacitances for the three sensors are shown in Table 6.7.

Inter-strip and backplane capacitance measurements were compared to a numerical calculation carried out using the Finite-Elements-Analysis-Software ANSYS. Capacitances were calculated for seven different sensor geometries: the five different regions of the LHCb sensors, the GLAST sensors and the CMS sensors. Details of the simulation are given in [68, 69].

There is an increase of the contribution of the inter-strip capacitance compared to the backplane capacitance to the total strip capacitance for thicker sensors. The total capacitance of the 500 $\mu$m thick CMS sensors is roughly in the same range as the ones of the 400 $\mu$m thick GLAST sensor and region A of the LHCb sensor, with 320 $\mu$m thickness.

Figure 6.7 compares the calculated and measured values, showing good agreement between them. The total capacitance varies with the $w/p$ ratio at constant sensor thickness. Therefore the regions B and D, as well as C and E, of the LHCb sensors show a comparable total capacitance, although they have different strip pitches. This fact is caused by the increase of the contribution of the inter-strip capacitance to the total strip capacitance for smaller pitches.

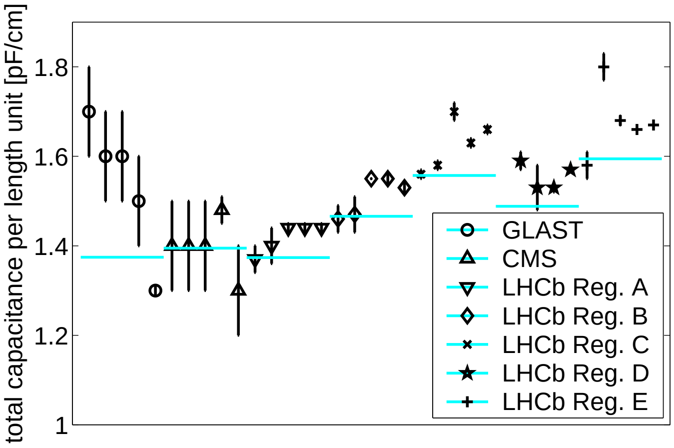

Figure 6.7: Comparison between measured (symbols) and calculated (horizontal lines) values of the total strip capacitance per length unit for seven different sensor geometries. Reproduced from [68].

### 6.3.6 Coupling capacitance

The coupling capacitance is the capacitance between the strip implant and the aluminium readout line. The aluminium readout line serves as a contact to the input of the amplifier but, if it would be in direct ohmic contact with the strip implant, the leakage current would flow into the amplifier. This might result in a serious operation problem by saturating the charge amplifier. When an insulating layer is placed between the aluminium line and the $p^+$ implant, the resulting capacitance enables the signal current to be induced in the readout line at the time as avoids the leakage current to achieve it. The coupling capacitances have to be significantly larger than the inter-strip capacitance in order to ensure a good charge collection.

The coupling capacitance was measured as a function of the excitation frequency by connecting the LCR-meter between the AC- and DC- pads on the sensor. In principle, this capacitance should not depend on the applied bias voltage. However, a small variation of the measured capacitance with the first biasing volts was observed. All measurements were performed with the sensors biased at 50 V.

The coupling capacitance was measured for five strips in one GLAST and one CMS sensor, and for two strips in each region of one LHCb sensor. Due to the finite resistance of the implant and the metal, the circuit behaves as a low-pass filter and the effective capacitance drops off at high frequencies, as shown in Figure 6.8. The true capacitor values were extracted from the

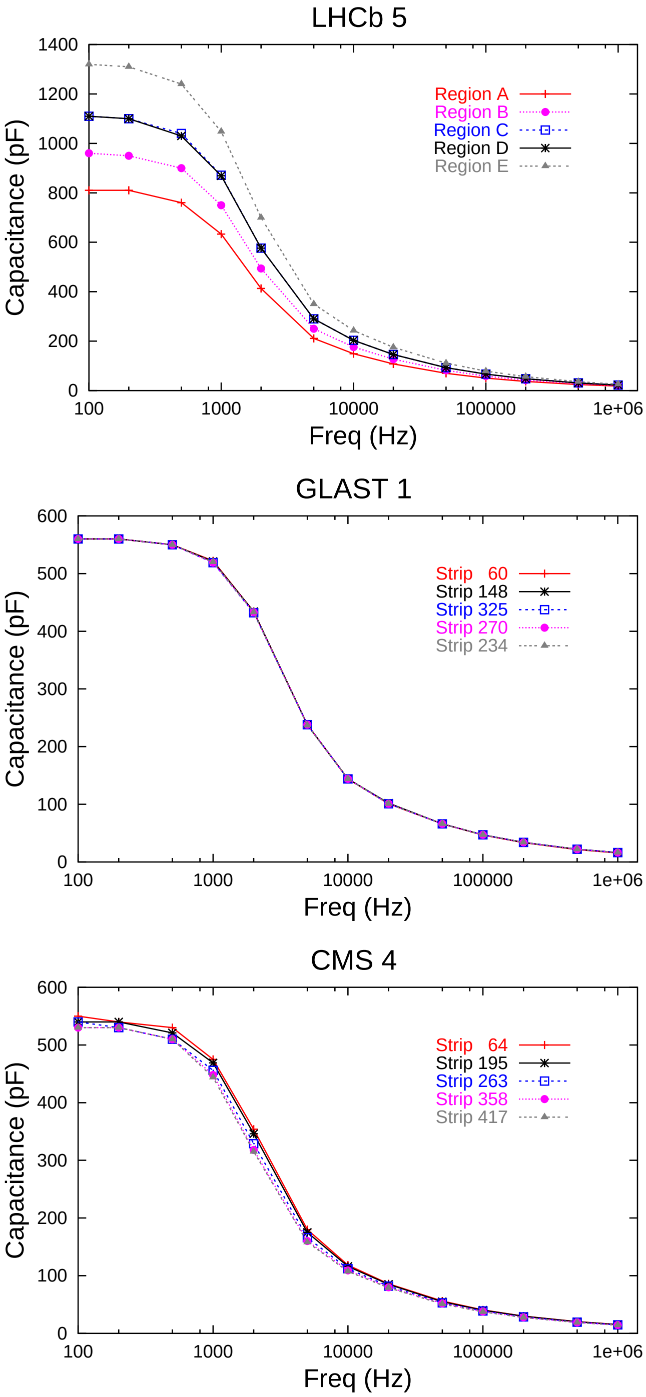

Figure 6.8: Coupling capacitance for one LHCb, one GLAST, and one CMS sensor. The values differ from region to region in the LHCb sensor due to the different implant widths.

| Sensor | Reg. | Width ($\mu$m) | Coupling Capacitance (pF) | |
|---|---|---|---|---|
| | | | Specifications | Measured |
| LHCb 5 | A | 50 | $> 675$ | 807 |
| | B | 60 | $> 810$ | 955 |
| | C | 70 | $> 945$ | 1105 |
| | D | 70 | $> 945$ | 1105 |
| | E | 80 | $> 1080$ | 1315 |
| GLAST 1 | | 56 | $> 500$ | 560 |
| CMS 4 | | 46 | $> 520$ | 540 |

Table 6.8: Measured coupling capacitances for the different sensor geometries. The capacitance values differ from region to region in the LHCb sensor, increasing with the implant width.

measurements at low frequencies and the mean values are shown in Table 6.8. They differ from region to region, due to the different implant widths. All measured coupling capacitances are within specifications.

The frequency dependence of the coupling capacitances measured for the LHCb sensor were compared to calculations obtained with a SPICE model of a lumped RC circuit [68] in Figure 6.9. In the model, the calculated resistance of the aluminium strip and the mean of the measured coupling capacitances are used, leaving the resistance of the $p^+$ implant as the only free parameter. For the comparison the measured and calculated capacitance and resistance values are normalized to a implant width of 1 $\mu$m. For the central curve ($f = 1.0$), a $p^+$ implant resistance of 3.6 M$\Omega$/cm is used. This value is scaled with factors $f = 0.6$ and $f = 1.4$ for the enveloping curves. The agreement between measurements and calculations seen is fairly good.

### 6.3.7 Bias resistors

The bias voltage is provided to the individual strips through polysilicon resistors in all these prototypes. The resistance of these bias resistors has to be high enough to separate the strips from the others. The resistor values have also to be constant, since large variations could lead to variations in the bias voltage applied to the strips and hence to a punch-through or breakdown of strip isolation.

We measured the resistance of polysilicon resistors by applying a voltage across them and measuring the current, with the detector biased above full

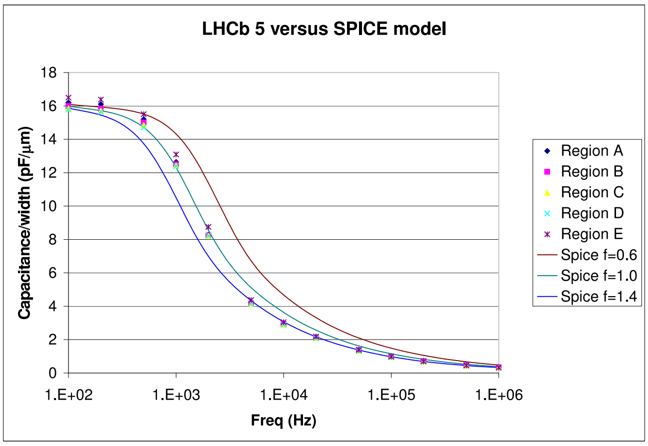

Figure 6.9: The frequency dependences of the coupling capacitances measured on the LHCb sensor and normalized to an implant width of 1 $\mu$m are compared to calculations with a SPICE model of a lumped RC circuit. The $p^+$ implant resistance of 3.6 M$\Omega$/cm ($f = 1.0$) is scaled with factors $f = 0.6$ and $f = 1.4$ for the enveloping curves. Reproduced from [68].

depletion. This test was made for five strips on one sensor of each type. Figure 6.10 shows the measured $I$-$V$ curve for a resistor on each sensor. The curves are fitted to straight lines and the resistance is extracted from the slope. Results are summarized in Table 6.9. The mean value was calculated for each sensor and the error assigned to it corresponds to the RMS of the individual measurements for this sensor. All obtained polysilicon resistor values are within specifications.

| Sensor | Polysilicon Resistors (M$\Omega$) | |
|---|---|---|
| | Specifications | Measured |
| LHCb 3 | 1.5 ± 0.5 | 1.7 ± 0.2 |
| GLAST 1 | 20 - 80 | 47.0 ± 0.9 |
| CMS 4 | 1.5 ± 0.5 | 1.34 ± 0.04 |

Table 6.9: Measured polysilicon resistors. The value given here corresponds to the mean value of five resistors on each sensor, and the error to the RMS of the individual measurements for this sensor.

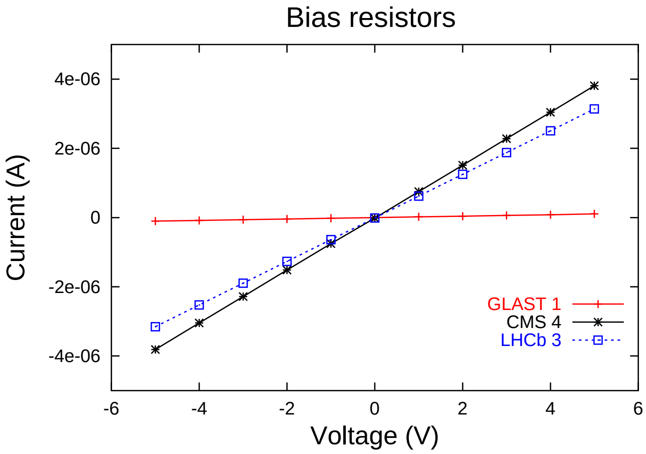

Figure 6.10: Bias resistor measurements, showing $I$-$V$ curves for one resistor on one sensor of each type. Each curve is fit to a straight line and the resistance is extracted from the slope.

## 6.4 Kapton cables

The TT station (see Chapter 4, or [43, 70]) will be covered by long modules that are electronically split into several readout sectors. Front-end hybrids, the associated mechanics, and service lines for all readout sectors are located above and below the sensitive region, outside the acceptance of the experiment. The outermost readout sectors on each module consist of four sensors that will be directly bonded to the their respective front-end hybrids. The next sector consists of three sensors that will be connected to the front-end hybrids via approximately 40 cm long interconnect cables. The innermost sector on the modules directly surrounding the beam pipe are additionally divided into two- and one-sensor readout sectors, the innermost being connected to its front-end hybrid via approximately 60 cm long interconnect cables.

The capacitance of these long cables is added in parallel to the capacitance of the sensors. Therefore, the load capacitance connected to the readout electronics is increased, and correspondingly the noise. The capacitance of the kapton interconnects is significantly lower than the sensors, due to the smaller dielectric constant of kapton compared to silicon and the greater freedom to optimize the strip geometry for low capacitance.

We received prototype cables from the Swiss company Dyconex, which

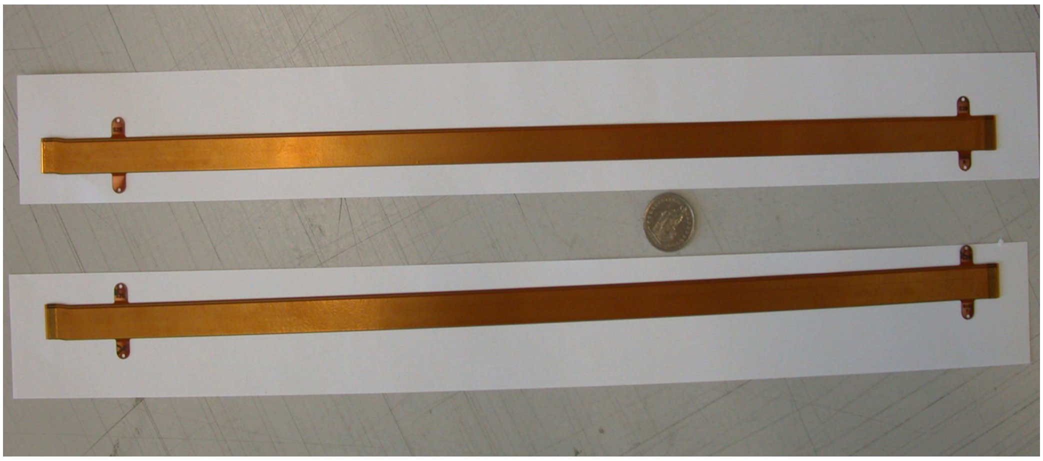

Figure 6.11: Long low-mass kapton interconnects.

were originally designed and produced for the D0 experiment at Tevatron. These cables were well suited for initial measurements as they are similar to those foreseen for the TT station. Several types of cables have been investigated: a cable with a covering solder resist mask on top of the traces, 42 cm long, called here "short with cover"; and two cables without solder resist, 42 and 54.5 cm long, called here "short without cover" and "long without cover", respectively. A photograph of these prototype cables is shown in Figure 6.11.

The cable substrate is kapton, with a thickness of 50 $\mu$m. The roughly 20 $\mu$m thick solder resist is an organic polymer which protects the traces and increases the strength of the cable, but it also enlarges the capacitance. The cables consist of 129 signal traces with a fine pitch of 91 $\mu$m. The width of these traces is 15 $\mu$m, and they are made of 7 $\mu$m thick copper which is gold-plated over the full length. In addition, the cables have one HV bias trace and one ground bias trace. Further details of the cables can be found in [71].

### 6.4.1 Capacitance

The capacitance of the different prototype cables was studied. Its dependence on the type of cable, its length, and the influence of next-to-next neighbouring traces were investigated. The capacitance was measured by connecting the LCR-meter directly between the cable traces and using a signal frequency of 100 kHz (the measured capacitance of these cables does not depend on the

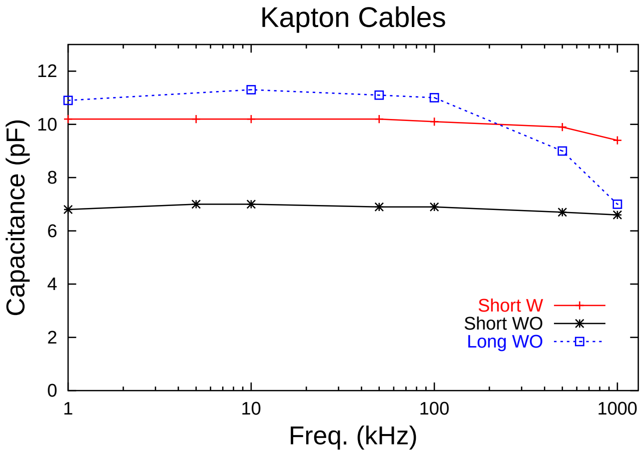

Figure 6.12: Capacitance for the different types of cables: short with cover (W), and short and long without cover (WO). The cable lengths are 42 cm (short) and 54,5 cm (long). For the same length, the capacitance of the cable with cover is significantly larger than the corresponding without cover.

frequency up to several MHz).

### Capacitance dependence on the type of cable

For this test the LCR-meter was placed between pairs of consecutive traces in each type of cable, and the signal frequency was varied between 1 and $10^3$ kHz. In Figure 6.12 the obtained values for the cable with cover (short) and for the long and short without cover are shown. It can be seen that, for the same length, the capacitance of the cable with cover is, as expected, significantly larger than for the cable without cover. This is due to the space above the traces, which is now filled with a dielectric material.

The capacitance was measured for three pairs of traces in each cable, therefore this measurement corresponds to the capacitance just to one neighbour. The mean value of the measured capacitances per unit of length are shown in Table 6.10.

The capacitance to one neighbour trace on the cable was compared to a model done using the Maxwell field simulator (details about the simulation can be found in [68]). The capacitance calculated from the electrostatic fields showed a good agreement to the measurements, for the cables with and without solder resist. The calculations resulted in 10-15% smaller values, which can either be attributed to remaining stray capacitance in the measurements

| Type of cable | Capacitance per unit length |
|---|---|
| Without cover | 0.17 pF/cm |
| With cover | 0.26 pF/cm |

Table 6.10: Capacitance per unit of length for the cables with and without cover. The actual contribution to the capacitance is two times the number given above. The capacitance is significantly higher for the cable with cover.

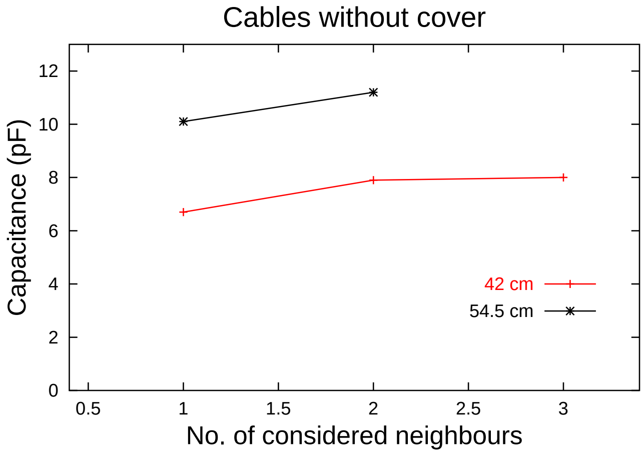

Figure 6.13: Capacitance at 100 kHz as a function of number of considered next-to-next neighbours. The contribution of the second neighbour is significant, while the contribution of the third one is negligible.

or to slightly different geometries.

### Estimation of the next-to-next neighbour contribution

This test was made for the cables without cover, for both the long and short ones since, according to the capacitance measurements presented above, they seem to be more suitable for the TT station. The contribution of the next-to-next neighbour was estimated by shorting together two or three traces in one side of a test trace, and placing the LCR-meter between the test one and the group. The result was compared with the values obtained in the previous section (only between two traces). Data are shown in Figure 6.13. A clear contribution from the second neighbour of $\sim$ 10% can be observed, whilst the contribution from the third one is negligible.

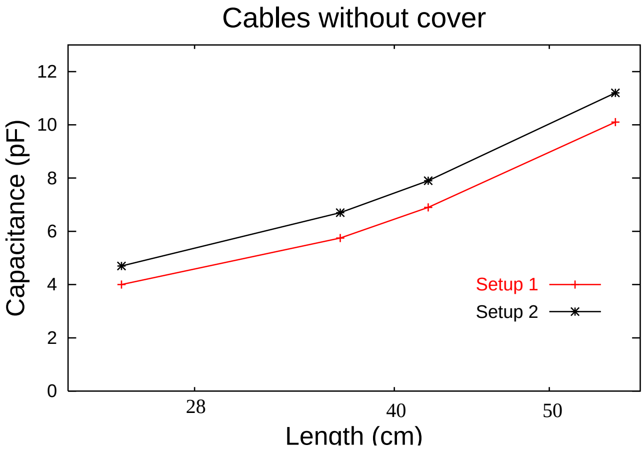

Figure 6.14: Capacitance as a function of the cable length, measured using a signal frequency of 100 kHz. Measurements were made between two traces (setup 1) and also taking into account a second neighbour (setup 2).

### Dependence on the cable length

The capacitance was measured for different lengths of the cable without cover. Results are shown in Figure 6.14 for the capacitance directly measured between two strips (setup 1), and taking into account the contribution of the next-to-next neighbour (setup 2). Initially, the measurements were made for the long and short cables, and afterwards the capacitance was re-measured after cutting to the last one 5 cm and 10 cm, respectively. A linear increase of the capacitance with the length is observed in the tested range of lengths.

## 6.4.2 Peeling tests

To check the mechanical resistance of the cables to eventual mechanical damages such as scratches, the adhesion strength of the copper traces on the cable without cover was tested with a peeling test. This test consisted in the application of an adhesive tape (3M Scotch) over the bonding pad area of the cable and, after setting a weight during some minutes for convenient glueing, the tape was removed. The cable was then inspected under a microscope to see if copper traces would peel off. The cable resulted to be quite resistant. Several peeling tests with different types of adhesive tapes were needed until finally one part of the traces could be peeled off. The state of the cable before and after the last test is shown in Figure 6.15. In the last picture, two open traces can be observed.

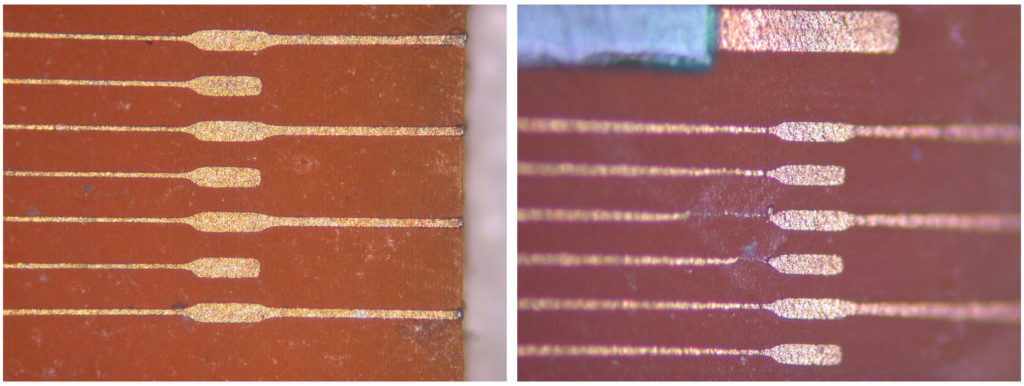

Figure 6.15: State of the kapton cable before the last peeling test (left) and after it (right). Two open traces can be seen in the last picture.

### 6.4.3 Short HV-test

In order to estimate a voltage rating for the cable, a current of a few mA was driven through its bias trace, by applying a high voltage of 500 V. We did not observe any breakdown or sparking effect in the kapton.

## 6.5 Conclusions

An exhaustive electrical characterization of three groups of prototype sensors, with thicknesses 320, 410, and 500 $\mu$m, respectively, and with strip pitches of approximately 200 $\mu$m has been performed. The best sensors from each group, mainly according to the results on leakage currents and breakdown voltages, were selected to build modules with strips up to 33 cm in length.

Capacitance measurements of long flex kapton interconnect prototype cables have been presented. These results were used as starting point to optimize the kapton cable strip geometry and characteristics for low capacitance and resistance requirements.

# Chapter 7

# Mechanical and thermal characterization of a TT half-module prototype

This chapter describes the mechanical effects of thermal cycles on a Trigger Tracker half-module to demonstrate that the detectors can withstand the expected thermal gradients without damage. The stress transferred by the carbon fiber rails and the ceramic to the silicon sensors was investigated, and the deformation that occurred during these tests was measured by strain gauges that were attached to sensors on a test half-module. In addition, heat transfer through the carbon fiber rails was studied.

## 7.1 Introduction

The Trigger Tracker (TT) station [20, 43] will use about 70 cm long half-modules that consist of seven silicon sensors divided electronically into several readout sectors (for further details, see Chapter 4). In order to minimize the dead material in the acceptance of the experiment, the front-end hybrids for all readout sectors are located at the external end of the half-module. All these elements share a common mechanical support. Thus, from a mechanical point of view, half-modules are the basic constituents of the station.

The half-modules will be built at room temperature, but will be operated below 5°C in order to keep radiation-damage induced leakage current at an acceptable level over several years of operation. Different thermal expansion coefficients of the materials used in the construction of the module will give rise to mechanical stress. In this chapter, we present measurements of the stress on the half-modules arising from thermal causes. In addition, heat transfer through the carbon fiber rails that hold the silicon sensors was studied.

The structure of this chapter is the following. In Section 7.2, we describe the experimental setup and briefly introduce the technique used to measure mechanical stress with strain gauges. In Section 7.3, we present results for thermal measurements in a half-module under conditions similar to those expected in the experiment. In Section 7.4, we present results for thermo-mechanical measurements.

## 7.2 Experimental setup

In this section we review the experimental setup, describing the half-modules used in the tests and the measurement equipment.

The TT station will be entirely covered by silicon microstrip detectors identical to CMS OB2 [47, 68]. The detector will be assembled from half-modules, each of which consists of seven silicon sensors with a ceramic substrate carrying the front-end readout hybrids attached to one of its ends. The sensors have lateral dimensions of 9.64 cm in width and 9.44 cm in height, and the half-modules are 66.2 cm long. The ceramic substrates will be mounted onto a cooling block to remove the heat produced by the readout chips. The temperature of the cooling block will be $-20$℃, and the ambient temperature in the box will be $\sim$ 5℃. Mechanical stability of the half-modules will be provided by carbon fiber rails that run along the side edges of the sensors and the ceramic substrates. Further details can be found in Chapter 4 and [43].

To investigate the strain produced by thermal effects in the half-modules, a test module was built using the same materials that will be used for the final modules: silicon plates to simulate the sensors and a piece of ceramic in place of the hybrid, all supported by carbon fiber rails. The ceramic was mounted onto a water-cooled copper block. A heater was attached to the ceramic in the position foreseen for the readout chips. This half-module was, however, built according to an earlier module design [20]. The main differences with respect to the current design are the dimensions and the number of sensors. In this test module, the silicon and the ceramic plates are each 110 mm long, 78 mm wide, and 500 $\mu$m thick. In each half-module, 6 silicon pieces are glued in a column, resulting in a 77 cm long module. The carbon fiber rails are 2 mm thick and 6.5 mm high, with a length of 77 cm. Furthermore, bare

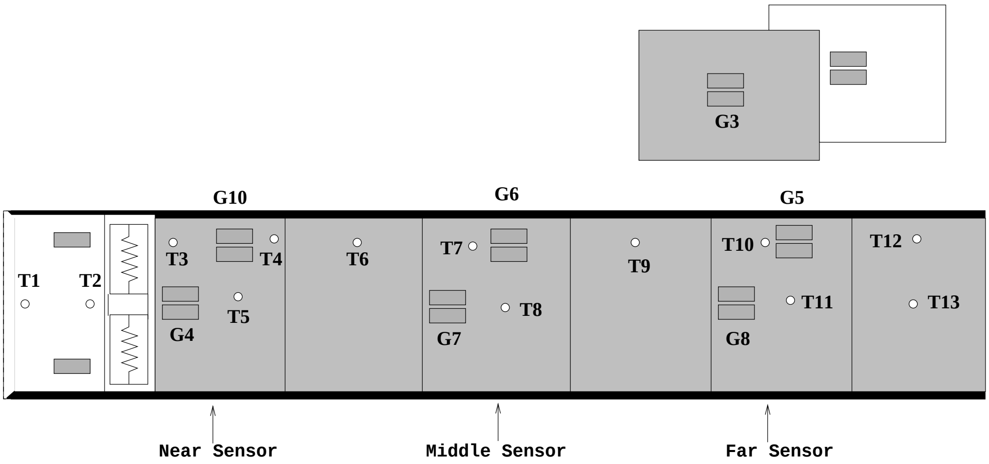

Figure 7.1: Location of the strain gauges (rectangles) and temperature probes (circles) on the surface of the prototype half-module. The same number of strain gauges are placed on the opposite side of the module, directly underneath the ones shown. The letter G refers to a group of four strain gauges (two on each side) arranged in a Wheatstone bridge. The bare silicon and ceramic plates are placed separately. The silicon pieces are represented in grey, whilst the ceramic is in white. The heater resistors are glued to the ceramic. The sketch is not to scale.

silicon and ceramic plates were used as a reference.

The test module and bare pieces were mounted inside a freezer. Temperature and humidity sensors were placed inside the freezer to monitor the ambient conditions.

To measure the strain caused by thermal effects and investigate the thermal flow, unidirectional strain gauges TML type FLA-3-11-1L [72] and temperature probes DS18S20 [73] were attached to the surface of the module. Figure 7.1 shows the location of these elements. The strain gauges are connected in groups of four, arranged in Wheatstone bridges. In each group, two gauges are glued to the top and two directly underneath to the bottom of the silicon sensors (only the ones on the top are shown in the sketch). When a bending of the module occurs, the top and bottom pairs are subject to equal and opposite strains (one pair will measure a positive tensile strain whilst the other will measure negative compressive strain). This strain results in a change in the resistance of the strain gauges that is converted into a voltage output by the Wheatstone bridge circuit.

The strain gauges are connected through lead wires to an amplifier module and a Keithley 7001 unit with a Keithley 7056 multipurpose scanner card. Voltage sources are needed to provide power to the heater, the amplifiers, and the temperature and humidity sensor. These devices were controlled via GPIB bus by Labview programs running on a PC.

## 7.3 Thermal measurements

The main objective of the measurements presented in this section is the determination of the heat profile produced by the readout chips along the half-module, to predict any associated effect on the leakage current of the silicon sensors.

The thermal flow through the carbon fiber rails was investigated by subjecting the module to different thermal conditions. Various temperature settings were applied using the cooling system, the heater, or both together. The temperature along the module was measured using the temperature sensors described in Section 7.2. As shown in Figure 7.1, some sensors are placed close to the rails while the others are placed in the central part of the silicon plates.

Three series of measurements were made, all of them starting at room temperature. In the first series, the heater power dissipation was varied between 5 and 15 W while the chiller was kept off. In the second series, only the chiller was switched on and the coolant was set to temperatures between 20℃ and 10℃. In the third series, both the heater and the cooling system were switched on. Figure 7.2 shows the temperature profile along the module surface for the different settings of the first series of measurements, and Figure 7.3 shows the same for the second series. The ambient temperature was subtracted from each point to avoid effects related to ambient conditions. In the plots, the distances are given with respect to the nearest edge of the heater, which is itself 3 cm wide. The positions of the temperature sensors on the ceramic are considered as negative and the ones on the silicon as positive. The temperature given for each point corresponds to the mean value of the readings taken during approximately 30 min, after about 1.5 hours for stabilization.

As it can be expected, the temperature on the ceramic is higher than on the sensors when only the heater is on, and lower in the case that only the chiller is on. Only the first two silicon sensors (each sensor is 11 cm long) in the module see any temperature effect.

In the third series of runs, both the heater and the cooling system were

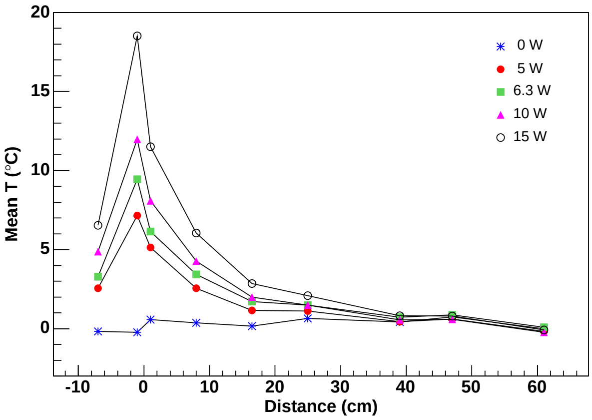

Figure 7.2: Temperature profile along the half-module for different settings of the heater. Negative distances refer to the temperature sensors on the ceramic, whilst positive to the ones on the silicon. Each sensor is 11 cm long.

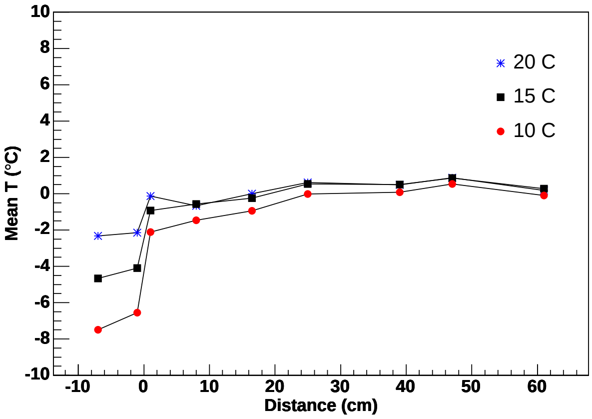

Figure 7.3: Temperature profile along the half-module for different settings of the chiller.

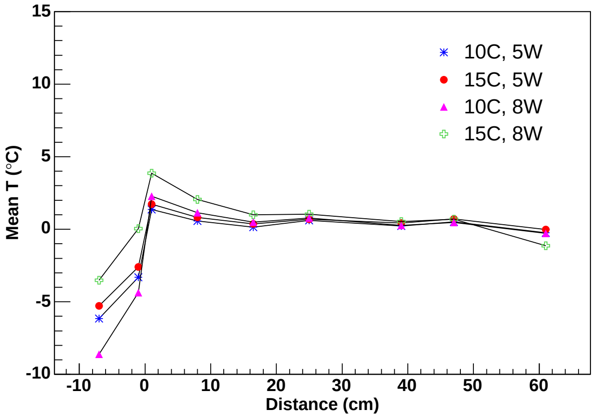

Figure 7.4: Temperature profile along the half-module for different settings of the heater and the chiller.

switched on. Four different settings were applied: heater powers of 5 and 8 W while the chiller was working at 10°C or 15°C. Figure 7.4 shows that the heat produced by the heater (readout chips) is efficiently removed by the liquid cooling under the ceramic. Only the sensor immediately close to it increases its temperature by less than 5°C, which has no dramatic effects on the detector performance.[1]

To study in more detail the efficiency of the liquid cooling to remove the heat, an additional series of measurements was made. The chiller temperature was set to 10°C and the heater power was varied between 0 and 20 W. Figure 7.5 shows the hybrid temperature as a function of the heater power. Again, the ambient temperature was subtracted from each point to avoid effects related to ambient conditions. The results demonstrate once more that the cooling system removes the heat efficiently. For example, at the expected dissipated power per half-module (around 9 W), the hybrid temperature exceeds the temperature measured with the heater off by less than 5°C.

In addition, the temperature in the side of the module (near the carbon

---

[1] This might be relevant for the performance of very irradiated sensors. As an example, according to Figure 10.14, for a sensor irradiated with a fluence equivalent to 7 years of operation in the innermost part of the IT, a temperature variation from 278 to 283 K gives rise to a current variation from 0.3 to 0.5 mA, which implies an increase of $\sim 30\%$ in the thermal noise. Nevertheless, in the final detector boxes the volume of air to be cooled will be significantly lower than in the present setup, and therefore it is expected that the actual temperature variation will be less than the numbers quoted here.

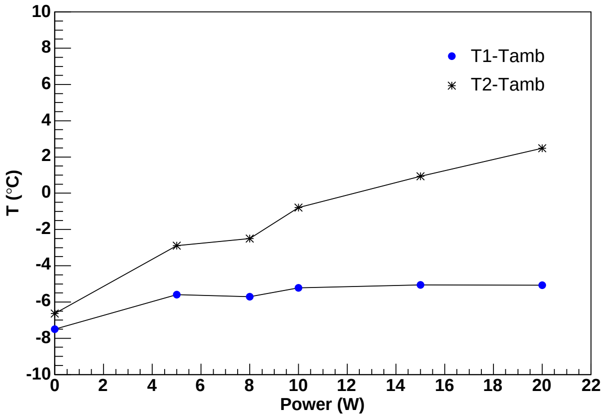

Figure 7.5: Hybrid temperature as a function of the heater power. At the expected dissipated power per half-module (around 9 Watts), the hybrid temperature exceeds the temperature with the heater off by less than 5℃. The chiller temperature was set to 10℃.

fiber rails) was compared to the temperature in the center and, as shown in Figure 7.6, no significant differences were found. This means that the carbon fiber rails act also as thermal insulators, not allowing the heat generated by the chips reach the sensors. Therefore the heat is transported by the surrounding air.

## 7.4 Thermo-mechanical measurements

The mismatch among the coefficient of thermal expansion (CTE) of the materials from which the module is constructed may give rise to stress and local bending when the temperature changes, although the symmetric design of the rails was chosen to minimize the stress and the material. The coefficients of thermal expansion of these materials are given in Table 7.1.

The strain was measured as a function of the temperature during the series of runs explained in Section 7.3 and using the strain gauges described in Section 7.2. An example of these tests is shown in Figure 7.7, where the voltage output of the strain gauge G4 and the readings of the closest temperature sensors are plotted as a function of time. A clear correlation between the two observables can be seen.

---

[2] We do not use the ceramic $Al_2O_3$ as it has a higher CTE ($CTE_{Al_2O_3} = 6.7 \times 10^{-6} K^{-1}$).

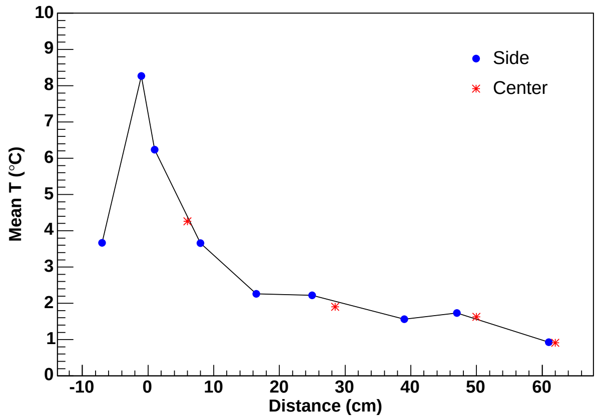

Figure 7.6: Comparison among the temperature readings near the carbon fiber rails (side) and in the center of the module. The ambient temperature was subtracted from each point. The heater was on, dissipating 15 W.

| Material | CTE [K$^{-1}$] |
|---|---|
| Silicon | $2.6\times10^{-6}$ |
| Ceramic (AlN) [2] | $4.5\times10^{-6}$ |
| Carbon Fiber | $1\times10^{-6}$ |

Table 7.1: Coefficients of thermal expansion of the materials that the module consist of.

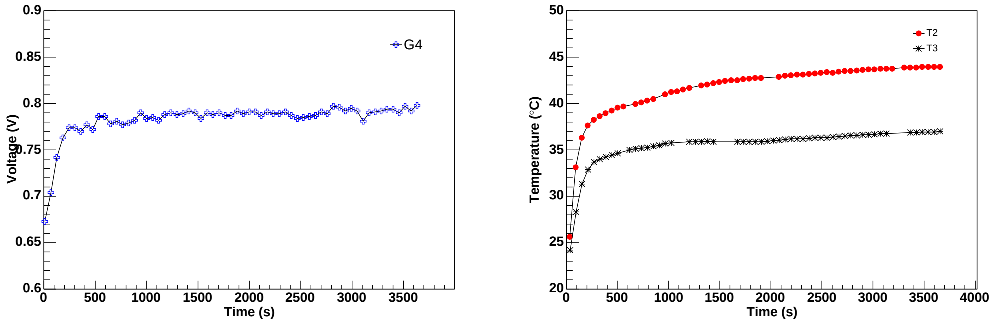

Figure 7.7: Voltage output of the strain gauge G4 (left) and closest temperature sensors readings (right) versus time. A clear correlation between the two data sets can be observed.

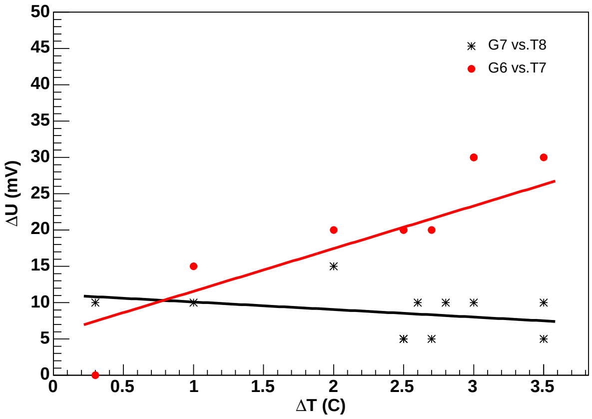

Figure 7.8: Variation of the strain gauges voltage output as a function of the variation of the temperature, for the two gauges located in the middle sensor. It can be seen that the strain near the rails (G6) is higher than in the center (G7), due to the mismatch of the materials CTE.

For these series of runs, we measured the voltage output of the strain gauges as a function of the temperature. Figure 7.8 shows the results for the gauges located on the middle sensor. Results for the far sensor are similar. In the figure, the strain near the rails is compared to the one in the center of the silicon sensor. As can be clearly seen, the strain near the rails (G6) is higher than in the center (G7), due to the mentioned CTE mismatch between carbon fiber and silicon. Extrapolating from the results obtained for G6, we expect an output voltage of $\Delta U \sim 120$ mV at $\Delta T = 20$°C. According to [74]:

$$\Delta U = U_{ex} K G \frac{\Delta l}{l} \tag{7.1}$$

where $U$ is the voltage output, $U_{ex}$ is the excitation voltage (3.3 V), $K$ is the "gauge factor" of the strain gauges (given by the manufacturer as 2.14±1%), and $\frac{\Delta l}{l}$ is the strain, an output voltage of $\Delta U = 100$ mV corresponds to a deflection in the direction perpendicular to the module surface of $\sim$ 0.2 $\mu$m over the length of the strain gauge (8.8 mm), which corresponds to a deflection of $\sim$ 3 $\mu$m over the length of the silicon sensor.

Figure 7.9 shows the same plot for the gauges placed in the sensor near the hybrid, where the temperatures achieve the largest variations. The readings for G4, the strain gauge next to the hybrid and in the center of the silicon, were plotted versus the closest temperature (T3), and were compared to the ones for G10 (strain gauge close to the hybrid and to the rails). It can be

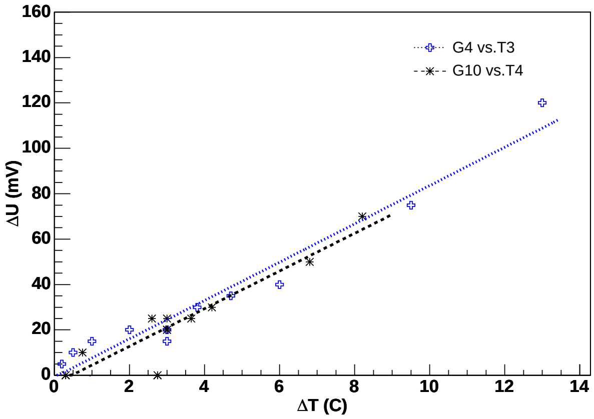

Figure 7.9: Variation of the strain gauges voltage output as a function of the variation of the temperature, for the two gauges located in the sensor near the ceramic, where the temperatures achieve the largest variations.

seen that the output voltage varies linearly with temperature. In this case, the strain observed in both gauges is nearly the same. Note that we are sensitive to local bending effects only.

## 7.5 Conclusions

Different thermal expansion coefficients of the materials used in the construction of the modules will give rise to mechanical stress, since modules will be built at room temperature but will be operated below 5°C. We have presented results of thermal and thermo-mechanical measurements on a test module. It was seen how the structure formed by the silicon sensors, their mechanical support and the hybrids react to temperature variations, demonstrating that no significant deformations are expected. In addition, the heat profile produced by the readout chips along the half-module was determined. It was shown that the cooling system removes the heat efficiently, and therefore no dramatic effects on the detector performance are expected. It was also shown that the heat is transported by the surrounding air and not by the carbon fiber rails.

# Chapter 8

# Laboratory measurements on prototype modules using an infrared laser system

In this chapter we discuss in detail results of measurements made with in a laser test-stand on prototype modules for the Silicon Tracker. Measurements were performed to characterize the silicon microstrip detectors and to study their performance with the Beetle 1.2, as part of studies carried out to determine the optimal wafer thickness for the Silicon Tracker sensors.

## 8.1 Introduction

The decision to construct the Trigger Tracker (TT) station entirely from silicon microstrip technology was taken in May 2002. In the station design, the TT station uses modules of 33 cm in length,[1] and it was necessary to verify the signal-to-noise ($S/N$) performance of such long modules. The longest module tested before for the Inner Tracker (IT) was 22 cm long and 320 $\mu$m thick. It was found to give a $S/N$ performance that was just acceptable. On the other hand, a new generation of the front-end chip – the Beetle 1.2 – is expected to give better $S/N$ performance compared to the Beetle 1.1 that was used in the previous studies [77]. Five prototype modules were constructed, with sensors of 320 $\mu$m, 410 $\mu$m and 500 $\mu$m nominal thickness, in order to study the performance with the Beetle 1.2 and to determine the optimal

---

[1] This corresponds to the design at the time when the tests were performed, and differs slightly from the final one (see Chapter 4 or [70]).

wafer thickness for the TT sensors.

First tests on these modules were made in a laser test-stand at the University of Zürich. Such setups have been widely used in the design and construction of silicon detectors [78–80] and have several advantages. They are relatively easy to construct and allow fast characterization of the performance of both the silicon sensor and the front-end electronics. In addition, the laser spot can be positioned on very specific regions of the sensor allowing studies to be made of the strip-to-strip uniformity, charge sharing and capacitive coupling between adjacent readout strips. On the other hand, the laser setup has some drawbacks. First, the stability of the laser diode with time and temperature must be monitored. Second, care must be taken to avoid internal reflection of the laser signal from the aluminium backplane. In addition, the laser pulse cannot penetrate the metalization of the readout strip. This means it is not possible to make measurements in this region of the detector. Finally, no measurement of cluster finding efficiency is possible in the laser setup since the absolute charge scale is uncertain.

The performance of the modules, essentially though pulse-shape related parameters like remainder or rise-time), was studies as a function of the module capacitance for different chip settings and bias voltages. In addition, the optimal working bias voltage was determined and compared to the full depletion voltage extracted from $C$-$V$ measurements. We investigated the charge loss between strips, an important issue due to the large $w/p$ of these sensors.

It should also be noted that the charge distribution created by the laser pulse is not the same as that created by a charged particle. Ignoring $\delta$-rays the charge distribution due to a charged particle is uniform. The laser produces an exponentially decreasing charge density. The wavelength of the laser used is 1064 nm which corresponds to a penetration depth of 400 $\mu$m [79]. This penetration depth should be compared to the sensor thickness, that are 320 $\mu$m, 410 $\mu$m and 500 $\mu$m for the LHCb, GLAST, and CMS sensors, respectively. The expected charge distributions produced by the laser, assuming that there is no reflection from the backplane, were calculated and compared to those due to a charged particle [58]. It was seen that for the LHCb modules the laser is a reasonable approximation to a charged particle. This statement is less true for the thicker GLAST and CMS modules.

The outline of this chapter is the following: the properties of the prototype modules are presented in Section 8.2. The laser setup is described in Section 8.3. Results of the studies made with the laser, consisting in functionality tests, bias voltage scans, pulse-shape studies, and position scans are presented in Section 8.4.

## 8.2 Prototype module properties

Three types of sensor were available for module construction: the LHCb multi-geometry prototype sensors used in earlier tests for the Inner Tracker [19], GLAST2000 sensors [81], and CMS-OB2 sensors [47]. All the sensors used have a pitch of around 200 $\mu$m and were characterized in Chapter 6. From these sensor types the following modules were built: one module with one sensor of LHCb type (called from now on LHCb1), one module with two sensors of LHCb type (LHCb2), one with three sensors of LHCb type (LHCb3), one module with three sensors of GLAST type (GLAST), and one with three sensors of CMS type (CMS). Each module was equipped with three Beetle 1.2 chips [82].

The relevant properties of the modules are summarized in Table 8.1. The total strip capacitances, $C_{Strip}$, have been calculated using the numbers in [68].

| Module | Strip length (cm) | Nominal thickness ($\mu$m) | Pitch ($\mu$m) | Strip width ($\mu$m) | $C_{Strip}$ (pF) |
|---|---|---|---|---|---|
| LHCb1 | 10.8 | 320 | 198 | 78 | 16.8 |
| LHCb2 | 21.6 | 320 | 198 | 78 | 33.6 |
| LHCb3 | 32.4 | 320 | 198 | 78 | 50.6 |
| GLAST | 26.3 | 410 | 228 | 62 | 41.3 |
| CMS | 28.9 | 500 | 183 | 58 | 37.6 |

Table 8.1: Prototype module properties. The numbers quoted for the LHCb multi-geometry sensors are for Region C.

## 8.3 Laser test-stand setup

An overview over the laser setup is shown in Figure 8.1. To avoid daylight on the photosensitive silicon sensors, the test-modules are mounted in a freezer, which also houses the stepper motor and the laser focusing optics which are described in Section 8.3.1. This also has the advantage of providing good thermal insulation for the detectors and gives a stable temperature inside the box. The readout hybrid of the test module was mounted on a water

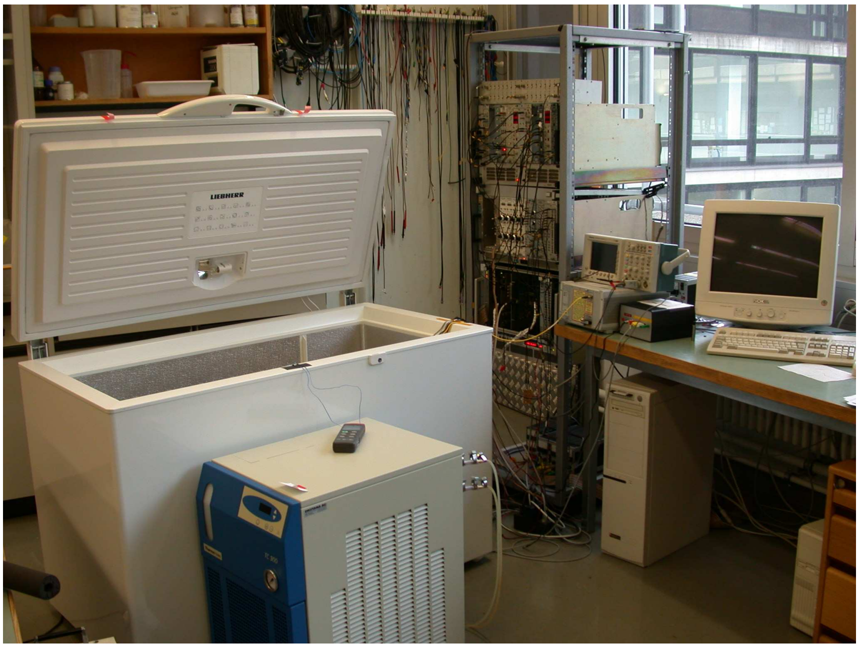

Figure 8.1: Overview of the laser test-stand setup.

cooled copper block. The temperature of the coolant was kept at 12°C during the measurement program. Two PT100 temperature sensors were used to monitor the ambient temperature inside the box and the temperature of the cooling block, that was $(20.9 \pm 0.2)$°C and $(13.3 \pm 0.1)$°C, respectively. A 40 MHz oscillator was used as system clock. The trigger rate was around 20 Hz.

### 8.3.1 Laser and stepper motor

A 1064 nm Nd:YAG laser diode [2] was used to produce a signal in the silicon. This wavelength gives a photon energy of 1.165 eV which is large enough to reach the band gap of silicon ($E_G = 1.1$ eV at T = 300 K). These photons then create electron hole pairs which drift to backplane respectively readout strips and generate the sensor current. The laser is pulsed with a pulse generator with a rise time of $\sim$ 2 ns, which is triggered by the readout trigger. An adjustable delay time between laser pulser and sampling time of the readout chip allows to perform delay scans. The height of the laser signal is determined by the amplitude of the pulse, but is not linear with the

---

[2] The laser system was produced by M. Glaser from the CERN EP-Division.

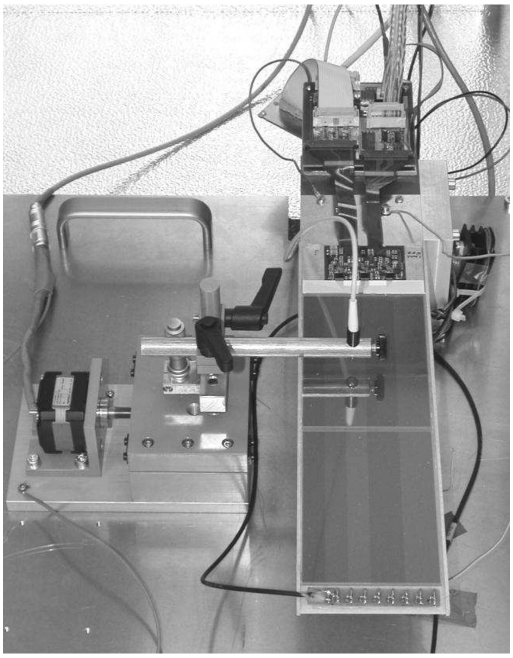

Figure 8.2: Inside view of the freezer. On the left side the stepper motor with the optical unit, in the top part the read-out electronics and under the stepper motor arm a test module is visible.

input voltage. In fact there is a lower edge, below which no signal can be seen. Operating the laser close to this edge results in large instabilities.

Therefore, a high value for the input voltage was chosen and a passive beam splitter was used to attenuate the laser signal. The signal height was adjusted to deliver an ADC signal corresponding to approximately one MIP.[3] The height of the laser signal was found to drift with time. After a measuring period of $\sim 2$ hours fluctuations of the signal height of order $\sim 5\%$ were observed. To reduce this problem the laser was turned off periodically and allowed to cool.

The laser beam is guided via optical fibres from the beam splitter to the optical focusing unit. The shell of the optical unit is fixed in a height adjustable arm of the sledge (see Figure 8.2). According to the laser optics specifications the focal point is 12 mm in front of the lensing system. This height of the arm above the silicon sensor can be adjusted with a micrometer screw in order to focus the laser beam.

The stepper motor is controlled through a LabVIEW program. The axis of the motor is connected via a thread rod with the sledge on which the optical unit of the laser is mounted (see Figure 8.2). The stepper motor is mounted into the test system in a way that the optical unit can be moved

---

[3] As a reference the height of a one MIP signal for each module from the charge calibration, as explained in [58], was used.

perpendicular to the strips of the test sensors. The step size of the stepper motor is 5 $\mu$m.

### 8.3.2 Readout Chain

The sensors are wire bonded to a readout hybrid which holds the three Beetle 1.2 chips [82]. The readout mode of the chips used was 128 analogue channels multiplexed onto one port at 40 MHz. The output signals from the Beetle chips are connected via a 9 cm long Kapton flex cable to a PCB board. On this board the signals are multiplexed and transfered via a 5 m long twisted pair CAT6-cable out of the box. In the other direction the differential control signals (clock, trigger, reset) are transmitted to the Beetle hybrid. The PCB also contains connectors for the high and low voltage, supplied from power supplies outside the freezer, and needed for operation of the Beetle chips and to bias the sensors, respectively. Outside the box the CAT6 cable is connected to an interface which de-multiplexes and amplifies the signals of the three Beetle chips for the following digitization stage. This is carried out by 8-bit FADCs that are located on an ODE prototype board [83]. The ODE board is read out via the VME bus to a PC running a LabVIEW program.

The programming of the Beetle readout chips was performed using with a standard $I^2C$ interface that was controlled via a LabVIEW program provided by the ASIC Lab in Heidelberg. In particular, it is possible to change the shaping time of the Beetle chip within a certain range by setting different values of the parameter $V_{fs}$. Tests were performed using values of $V_{fs}$ set to 0 mV, 400 mV and 1000 mV where a value of 0 mV corresponds to the fastest shaping.

To process and analyze the data a modified version of the software developed for the ST test-beam was used. Details on the procedure used for determining pedestals and common mode noise can be found in [84]. Around two million triggers were recorded in a period of four weeks.

## 8.4 Results

In the following sections the main results of the measurement program carried out with in the laser test-stand are presented.

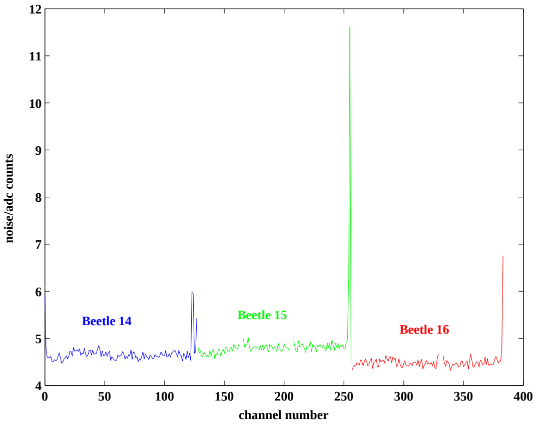

Figure 8.3: Channel noise for the CMS module, $V_{fs} = 400$ mV.

### 8.4.1 Functionality tests

Each module was checked for broken Beetle chips and disconnected channels. One Beetle chip on the LHCb1 module and one chip on the LHCb2 module did not work. The first failure was due to an accident during the installation of this module and was not repairable, the second was due to a disconnected power bond and was later fixed. Two bad bonds were found and repaired on the LHCb1 module.

A search was performed for noisy channels. As an example Figure 8.3 shows the noise, i.e. the RMS of the ADC counts recorded in absence of laser signal versus channel number for the 384 channels on the CMS module. The channels bonded for calibration [58] were found to be more noisy and are masked off in this plot. It can be seen that channels 123 and 124 are noisy, and that there is a tendency for either the first or the last channel on a Beetle chip to be noisy. The second point was also found to be true for the other modules tested. The results of the functionality tests are summarized in Table 8.2.

IV curves were measured for each module. Currents were below 3 $\mu$A at the highest voltage tested (300 V for LHCb and GLAST modules, and 450 V for the CMS module). No breakdown was observed.

| Module | Beetle ID | Working | First channel | Last channel | Other noisy channels |
|---|---|---|---|---|---|
| LHCb1 | B | OK | Noisy | Noisy | — |
| LHCb1 | C | OK | Noisy | Noisy | — |
| LHCb1 | D | Destroyed | — | — | — |
| LHCb2 | E | OK | Noisy | Noisy | — |
| LHCb2 | F | OK | Noisy | OK | — |
| LHCb2 | 10 | Disconnected power bond | — | — | — |
| CMS | 14 | OK | Noisy | Noisy | 123,124 |
| CMS | 15 | OK | OK | Noisy | — |
| CMS | 16 | OK | OK | Noisy | — |
| GLAST | 17 | OK | Noisy | OK | — |
| GLAST | 18 | OK | Noisy | OK | — |
| GLAST | 19 | OK | Noisy | Noisy | — |
| LHCb3 | 1A | OK | Noisy | Noisy | — |
| LHCb3 | 1B | OK | OK | OK | — |
| LHCb3 | 1C | OK | OK | Noisy | — |

Table 8.2: Summary of functionality tests.

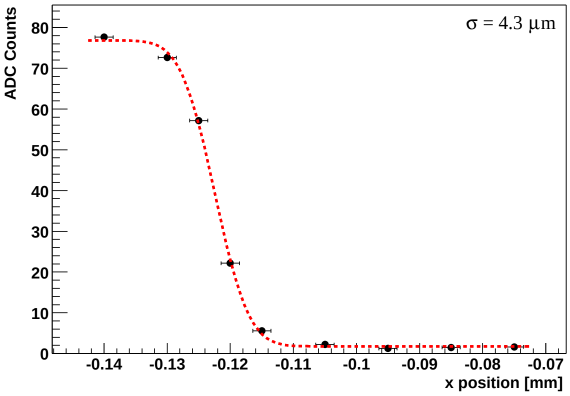

Figure 8.4: Example of a laser focussing run. A $\sigma$ of 4.3 $\mu$m was achieved in this case.

### 8.4.2 Laser Focusing

The first step in the measurement program for each module was to adjust the micrometer screw setting such that the focal point of the laser coincided with the centre of the sensor. The fact that the laser light does not penetrate the metalization of the readout strip can be used to achieve this as follows. First, the rough region of focus is defined by “eye”. A scan is then made moving the laser spot across the sensor. An example of such a scan is shown in Figure 8.4. It can be seen that as the position of the laser spot is moved, there is an edge where the observed signal decreases rapidly to zero. This is the start of the metalization of the readout strip. A fit of an error function is made to this edge. This procedure is then repeated for several micrometer screw settings, and the one with the minimum width, $\sigma$, of the error function is taken as the optimal focus point. Typically, a $\sigma$ of 4 $\mu$m was achieved. This corresponds to a FWHM spot-size of 11 $\mu$m.

### 8.4.3 Bias voltage scans

The charge collected on the readout strips depends on the applied bias voltage. If the detector is not fully depleted, the bulk material is divided into two zones, the depleted zone reaching from the $p-$side into the bulk and the non-depleted zone extending towards the $n-$side. Electron-hole pairs generated in the depletion zone are separated by the electric field. The holes drift to the $p-$side and are collected in the readout strips, and the electrons drift towards the $n-$side. However, the charges generated in the non-depleted zone are not well separated, since there is not electrical field present, and recombine before arriving to the electrodes. Even when full depletion is reached, the collected charge increases with the applied bias voltage until a *plateau* is reached (i.e. all the charge is collected), due to the dependence of the drift velocity on the electric field and the limited integration time of the preamplifier.

A bias voltage scan was performed for each of the five modules in order to obtain their working points. It was seen that the time of the signal maximum depends on the applied bias voltage. Therefore for each bias voltage it was first necessary to determine the optimal sampling time. This was done by taking 4-5 runs with different delay times chosen around the rough position of the signal maximum and fitting a parabola to the measured signal as function of delay time. Once the corrected timing for each voltage was found, the scan was performed. Figure 8.5 shows the maximum signal amplitude versus the applied bias voltage for each module. All the measurements were performed with the Beetle shaping $V_{fs}$ set to 400 mV and with the laser spot positioned close to the metalization of the readout strip.

The measurement showed that the LHCb modules reach the *plateau* at around $100 - 110$ V. For the GLAST module full charge collection starts at 150 V whereas for the CMS module this is the case at 440 V. For the CMS module the time of the maximum does not change up to 260 V.

The *plateau* voltages can be compared with the depletion voltages obtained from $C$-$V$ measurements quoted in Table 8.3. In absolute values, larger over-depletion is needed as the thickness of the sensors increases. For the CMS module, the difference between the measured depletion voltage and the bias voltage for full charge collection is 250 V. This huge difference and the dependence of the time of the signal maximum might be due to the fact, that the depletion voltages for two out of three sensors used for the test module differ by 90 V.

### 8.4.4 Pulse-shape studies

A series of scans were performed in order to investigate the dependence of the pulse shape on the bias voltage, the shaping time of the Beetle chips ($V_{fs}$), and the position of the laser spot with respect to the readout strips. In these scans the delay between the trigger signal and the Beetle sampling time was varied over a range of $\sim 150$ ns in order to observe the full pulse shape. Two different groups of voltages, $V1$ and $V2$ (see Table 8.3), and three different settings of $V_{fs}$ (0, 400 and 1000 mV) were used.

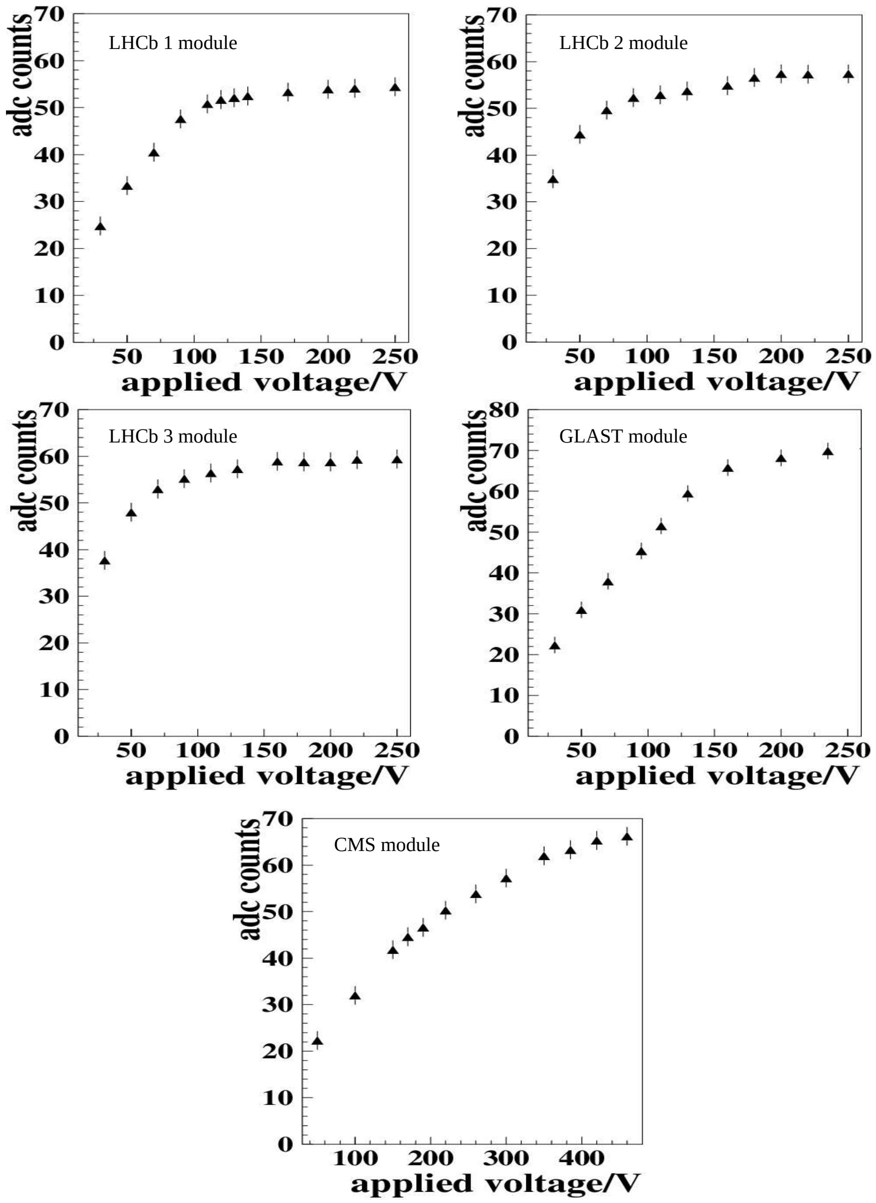

Figure 8.5: Amplitude of the signal as a function of the bias voltage for the five modules.

| Module | Depletion voltage (V) | $V1$ (V) | $V2$ (V) |
|---|---|---|---|
| LHCb1 | 65 | 90 | 200 |
| LHCb2 | 65 | 90 | 200 |
| LHCb3 | 65 | 90 | 200 |
| GLAST | 70 | 95 | 235 |
| CMS | 130-220 | 220 | 385 |

Table 8.3: Chosen values of $V1$ and $V2$ for the delay scans.

The value of $V1$ for each module was chosen to be $20 - 30$ V above the full depletion voltage using the numbers given in Chapter 6. The value of $V2$ was chosen to be well above the full depletion voltage so as to guarantee full charge collection. It should be noted that the three sensors on the CMS modules have quite different full depletion voltages. The corresponding with the illuminated sensor was 190 V. The near strip data was taken at the edge of the metalization and the mid-strip equidistant between the centre of two readout strips.

Two examples from the 45 delay scans taken are shown in Figure 8.6. The upper plot shows the results of a pulse shape scan with the fastest shaping, $V_{fs} = 0$ mV, for the LHCb1 module. The lower plot shows a delay scan with the slowest shaping, $V_{fs} = 1000$ mV, for the LHCb3 module. In these plots, the signals on the neighbouring strips are shown in addition to the signal on the strip illuminated by the laser. The signal on the neighbouring strips, or cross-talk, can be reproduced in a simulation due to capacitive coupling between the readout strips [69]. The signal on the right neighbour is larger than on the left one because the laser is positioned on the right strip of the illuminated strip, allowing some charge sharing in addition to the capacitive coupling.

It can be seen that the signals on the neighbouring strips reach the signal maximum earlier in time than the signal on the illuminated strip. This time difference was found not to depend neither on the bias voltage nor the capacitance of the module, but to increase with increasing $V_{fs}$.

The level of signal cross-talk in the final experiment is determined by the charge on the neighbouring strips at the time of the signal maximum on the illuminated strip. Table 8.4 shows the relative signal amplitudes for the five modules for the near strip data with $V_{fs} = 400$ mV and bias voltage $V2$.

A small but significant signal on the second neighbours of the illuminated strip, with relative maximum height of 0.03, was observed. No signal was

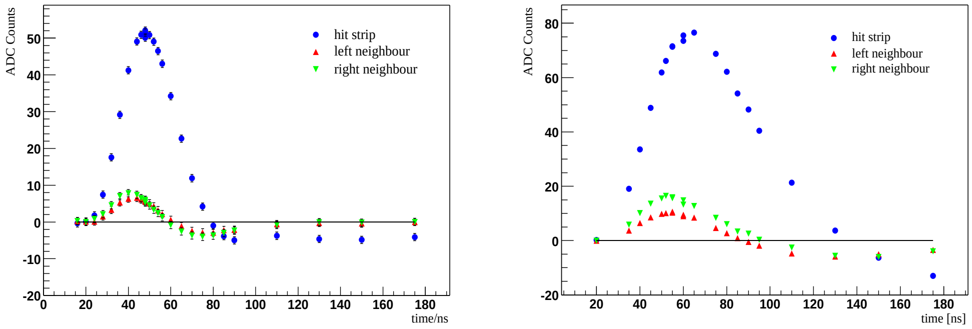

Figure 8.6: On the top, delay scan for the LHCb1 module biased at 200 V, with $V_{fs} = 0$ mV, and the laser near strip. At the bottom, delay scan for the LHCb3 module, biased at 200 V, with $V_{fs} = 1000$ mV, and the laser near strip.

| Module | Relative signal amplitude on neighbour strips |
|---|---|
| LHCb1 | $0.11 \pm 0.03$ |
| LHCb2 | $0.11 \pm 0.03$ |
| LHCb3 | $0.14 \pm 0.03$ |
| GLAST | $0.13 \pm 0.03$ |
| CMS | $0.14 \pm 0.03$ |

Table 8.4: Relative amplitude on neighbouring strips for the five modules, $V2$, $V_{fs} = 400$ mV, near strip data.

observed on the next-to-next neighbours.

An alternative way to visualize this effect is to plot for a fixed trigger delay the average charge seen on the strips around the one illuminated by the laser. This has been done setting the trigger delay such that the signal on the strip closest to the laser spot is at its maximum value. Figure 8.7 shows the obtained shapes for the near strip data, and Figure 8.8 for the mid-strip data.

An important quantity for the operation of the detector in the LHC environment is the fraction of the signal left in the following bunch crossing, i.e. 25 ns after the signal maximum – the signal remainder. Monte Carlo studies of the LHCb detector performance assume a signal remainder of 0.3 for IT and 0.5 for TT [85]. The dependence of the remainder on $V_{fs}$ and

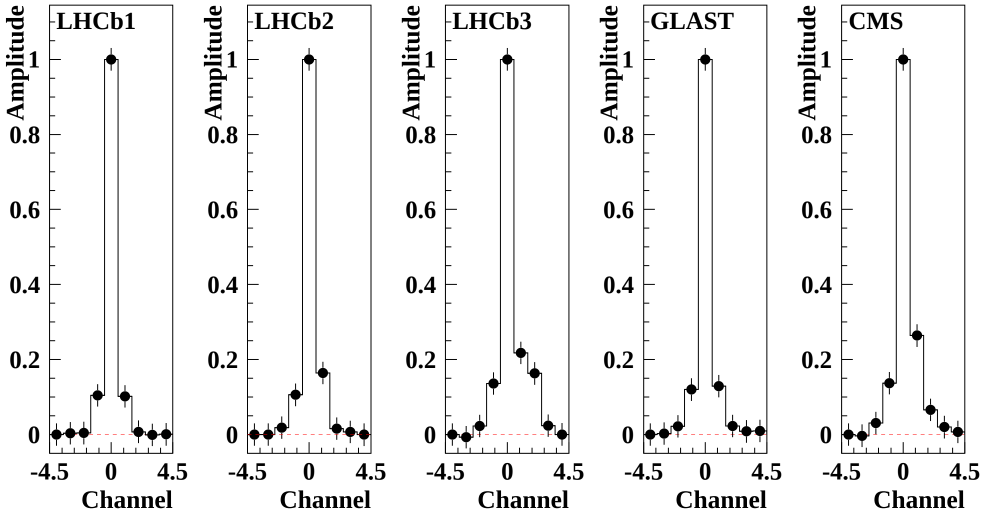

Figure 8.7: Charge depositions shapes for the near strip data, $V_{fs} = 400$ mV, $V2$. The amplitudes have been normalized such that the signal on the illuminated strip is one.

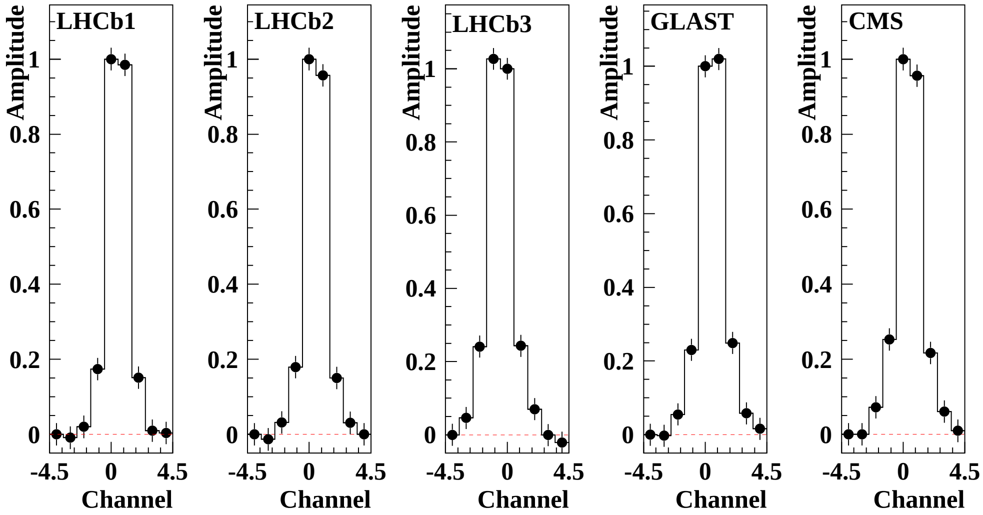

Figure 8.8: Charge depositions shapes for the mid-strip data, $V_{fs} = 400$ mV, $V2$. The amplitudes have been normalized such that the signal on the illuminated strip is one.

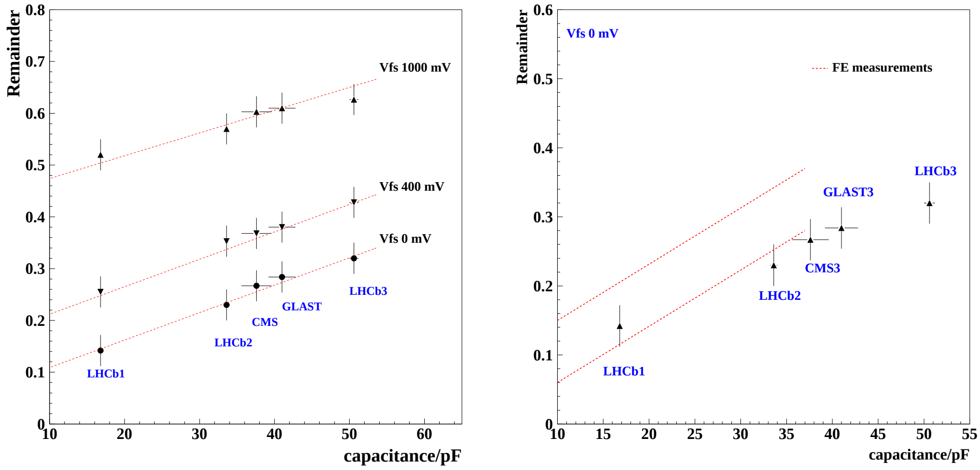

Figure 8.9: On the right, remainder as a function of capacitance for various settings of $V_{fs}$. The dotted lines are to guide the eye. On the left, comparison of the measured remainder with front-end measurements. The front-end measurements lie inside the dotted lines.

on the bias voltage was studied for all the modules. It was found not to depend significantly neither on the bias voltage nor the position of the laser relative to the strip. However, as expected it increases significantly with the Beetle shaping parameter $V_{fs}$ and the load capacitance. This can be seen in Figure 8.9. It can also be seen that a remainder of less than 0.5 can easily be met for values of $V_{fs}$ up to $\sim$ 400 mV.

In the same figure, the results with $V_{fs} = 0$ mV are compared to the Beetle 1.2 front-end measurements described in [19]. These measurements were made with discrete capacitances instead of the sensors, and a $\delta$-function input signal. It can be seen that for the long modules the measured remainder is systematically smaller than expected from those measurements.

Another important characteristic of the pulse-shape is the rise-time which is here defined as the time from 10% to 90% of the signal maximum. Figure 8.10 shows the measured rise-times for the five modules at three Beetle chip shaping parameters $V_{fs}$. As expected, it was found to depend on $V_{fs}$ and the load capacitance Again, the results for $V_{fs} = 0$ mV can be compared to the front-end measurements (right plot in Figure 8.10). It can be seen that the measured rise-times are slightly slower than expected from the front-end measurements.

The dependence of the rise-time on the bias voltage was also investigated.

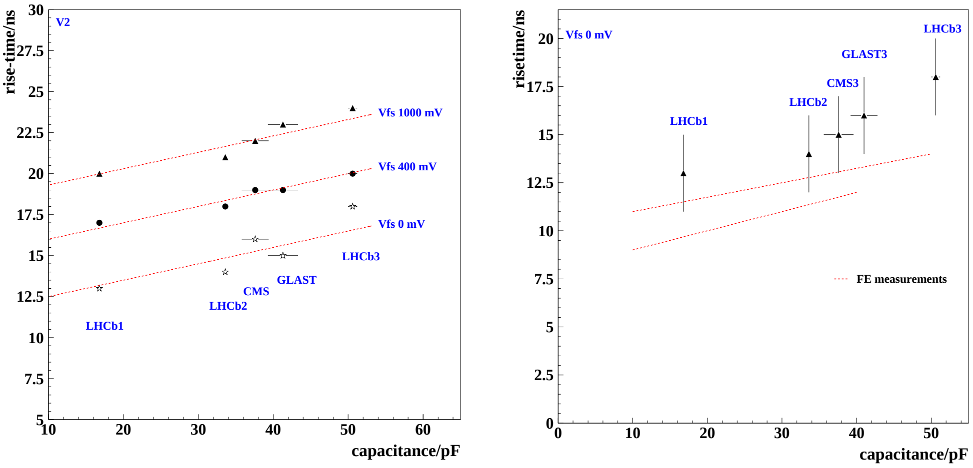

Figure 8.10: On the right, rise-time for the five modules, for three $V_{fs}$ settings: 0, 400 and 1000 mV. The bias voltage was $V2$, and the laser was placed near strip. The error on each point is 2 ns. On the left, comparison of rise-time for $V_{fs} = 0$ mV, near strip $V2$ data with front-end measurements. The front-end measurements lie inside the dotted lines.

As it can be seen in Figure 8.11, the rise-time is faster for the higher bias voltage. This is due to the higher electric field in the sensor which results in faster charge collection.

To understand the data simulation studies modeling both the response of the silicon and the Beetle chips were performed. The first results from such studies are described in [69].

### 8.4.5 Charge loss in between readout strips

In tests performed with the previous generation of ST prototype modules a charge loss of order $10-20\%$ was observed to occur in the region between two readout strips [19, 84]. This effect was also investigated in the laser setup.

For each module, two position scans were made with the bias voltage set to $V1$ and $V2$, respectively. The laser spot was moved across the strip in steps of 5 $\mu$m. As an example, the results of these scans with the bias voltage $V1$ are shown in Figures 8.12 for the five modules. In each plot the signal on the left and right strips is shown together with the sum of the charge on the four strips closest to the laser position. In all plots the charge loss in

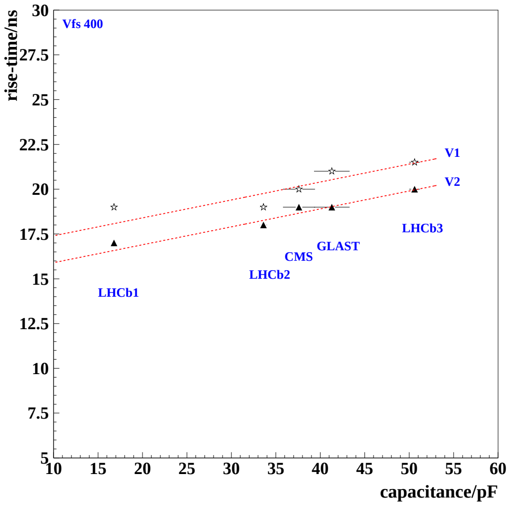

Figure 8.11: Rise-time as a function of the capacitance for the two bias high voltages. The laser position was near strip and $V_{fs} = 400$ mV. The error on each point is 2 ns.

the inter-strip region is clearly visible. In addition it was seen that the total collected charge for the $V2$ data was always higher than for the $V1$. This is consistent with the results of Section 8.4.3 — full charge collection efficiency is not expected for the $V1$ bias voltage. It can also be seen that the left-hand side of each plot is generally higher than the right. This is due to the laser instabilities mentioned in Section 8.2. This effect is most pronounced for the data taken with the GLAST module (Figure 8.12).

To estimate the size of the charge loss, the following procedure was used. The average of the data taken near to the left and right strips was taken as a measure of the near strip charge. The uncertainty on this number was taken to be the difference between the left and right strip values divided by two. The charge mid-strip was taken as the value observed at that position. The relative charge loss, $\Delta_q$, is then estimated as:

$$\Delta_q = \frac{N_{ADC}(\text{near}) - N_{ADC}(\text{mid})}{N_{ADC}(\text{near})}$$

Table 8.5 summarizes the results of the charge loss for the two applied bias voltages. The stability of the laser is not sufficient to make quantitative statements concerning for example the dependence of the dip on the bias

| Module | $\Delta_q$ for $V1$ [%] | $\Delta_q$ for $V2$ [%] |
|---|---|---|
| LHCb1 | $17.5 \pm 0.9$ | $20.2 \pm 1.3$ |
| LHCb2 | $17.4 \pm 1.4$ | $20.5 \pm 1.1$ |
| LHCb3 | $11.6 \pm 1.6$ | $18.0 \pm 1.2$ |
| GLAST | $23.5 \pm 6$ | $24.2 \pm 3$ |
| CMS | $11.3 \pm 1.6$ | $10.5 \pm 1.3$ |

Table 8.5: Values of the relative charge loss, $\Delta_q$ for all the modules. $V_{fs}$ was set to 400 mV.

voltage.

## 8.5 Conclusions

Prototype modules for the ST were studied with in a laser test-stand which has allowed a fast characterization of their performance. For future measurements with the laser setup, the time stability of the pulse height needs to be improved. Alternatively one of the other outputs from the beam-splitter could be monitored with time and used to correct the measured signal for time dependent drifts.

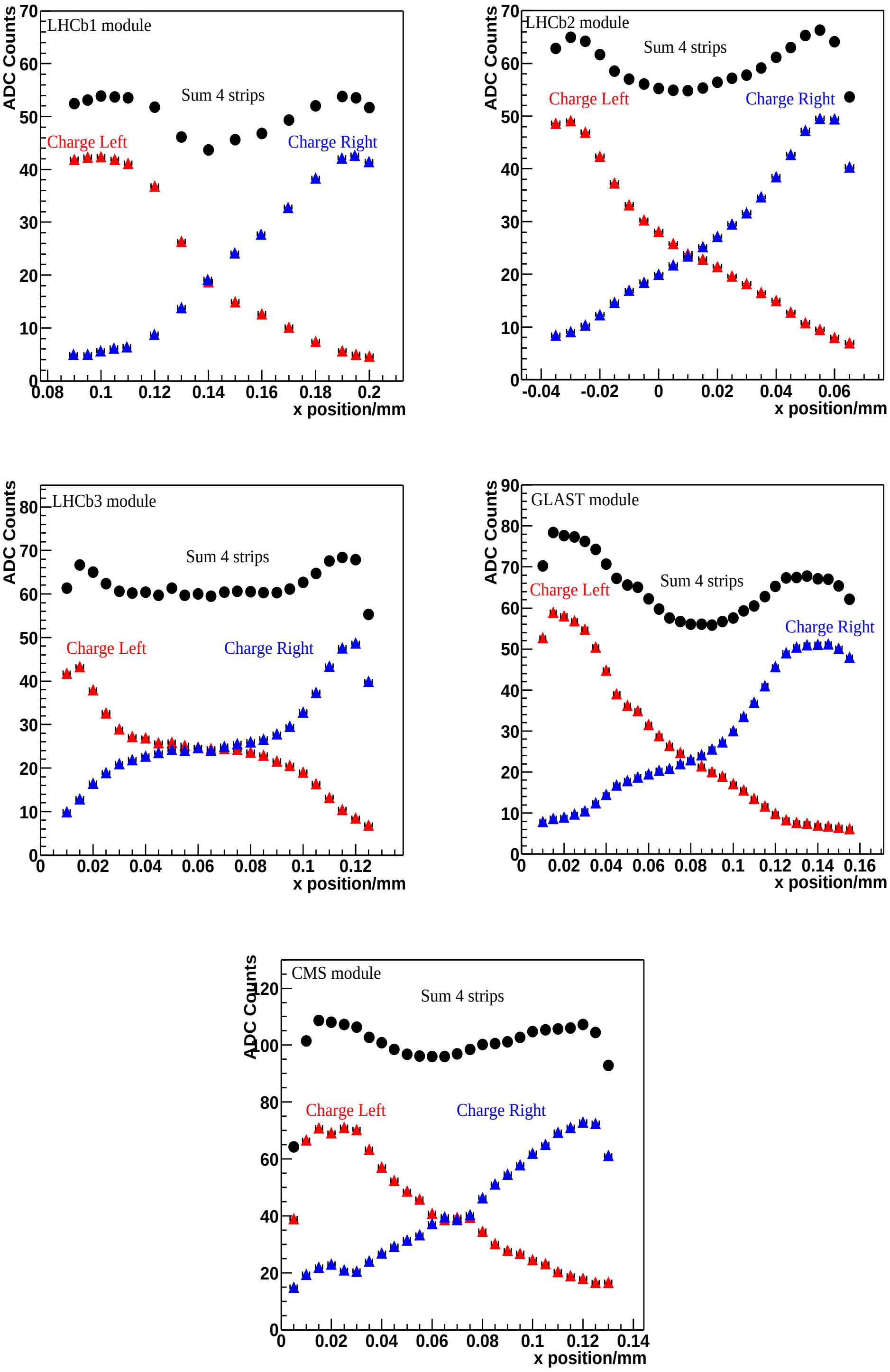

Figure 8.12: Charge sharing and loss for the five modules, with bias voltage set to $V1$ and $V_{fs} = 400$ mV.

# Chapter 9

# Test-beam measurements on prototype modules

In this chapter we describe the results of a comprehensive measurement program carried out at the CERN X7 test facility in May 2003 on prototype modules for the Silicon Tracker.

## 9.1 Introduction

After the decision to construct the Trigger Tracker (TT) station entirely from silicon microstrip technology, it was necessary to verify the design concept for this station. At the location of the TT station, an area of $131.8 \times 159.1$ cm$^2$ has to be covered [1] [19, 86]. In order to minimise the amount of dead material in the acceptance, all the front-end chips will be located at the edge of the detector. Kapton cables ranging in length from 33 to 55 cm will be used to connect the inner sensors to their corresponding hybrids [86]. This gives capacitive loads of $\sim 50\,\mathrm{pF}$ for all the readout sectors.

The detector noise increases with the load capacitance of the readout sectors. Since the capacitance depends on the strip length, the performance of the long modules foreseen for the TT station has to be investigated. Results of earlier tests on modules constructed from 320 $\mu$m thick sensors are reported in [19, 84]. The longest module tested in that work was 22 cm in length and had a capacitance of around 35 pF. The measured signal to noise ($S/N$) performance was found to be just acceptable for the Inner Tracker (IT)

---

[1] The dimensions correspond to the design at the time when the tests were performed, and differ slightly from the final ones (see Chapter 4 or [70]).

application. The extrapolated performance for a 50 pF load capacitance does not meet the requirements of the TT station. However, the available version of the front-end chip — the Beetle 1.2 [77] was expected to provide better $S/N$ performance than the Beetle 1.1 that was used in the previous tests described in [84].

Five prototype modules were constructed, with sensors of 320 $\mu$m, 410 $\mu$m and 500 $\mu$m nominal thickness in order to study the performance with the Beetle 1.2 and to determine the optimal wafer thickness of the sensors for the TT station. First tests of these modules were carried out in a laser test-stand and are described in Chapter 8 and [58]. Here we present the results of a comprehensive measurement program undertaken with a 120 GeV $\pi^-$ beam at the CERN X7 test-beam facility.

The outline of this chapter is the following. In Section 9.2, the properties of the prototype modules are presented. In Section 9.3, the test-beam setup at the CERN X7 test-beam facility and the measurement program are described. In Section 9.4, results of bias voltage scans, pulse-shape studies, signal-to-noise performance, charge loss studies are presented. In Section 9.5, a summary of the test-beam results is given.

## 9.2 Prototype module properties

Three types of sensor were available for module construction: the LHCb multi-geometry prototype sensors used in earlier tests for the Inner Tracker [19], GLAST2000 sensors [81], and CMS-OB2 sensors [47]. From these sensor types the following modules were built: one module with one sensor of LHCb type (called from now on LHCb1), one module with two sensors of LHCb type (LHCb2), one with three sensors of LHCb type (LHCb3), one module with three sensors of GLAST type (GLAST), and one with three sensors of CMS type (CMS). Each module was equipped with three Beetle 1.2 chips.

For the studies in this chapter, the most important properties of the sensors are the thickness, capacitance and implant width. LHCb type sensors have a nominal thickness of 320 $\mu$m, GLAST2000 sensors of 410 $\mu$m, and CMS sensors of 500 $\mu$m.

The total capacitance of each module has two components — the capacitance of the silicon strips themselves and the capacitance of the pitch adapter, $C_p$. The strip capacitance depends on the ratio of the implant width to the strip pitch, $w/p$, therefore the different regions on the modules constructed from LHCb sensors have different capacitances. In addition, each region of

| Type | Pitch ($\mu$m) | Implant width ($\mu$m) | $\rho$ (pFcm$^{-1}$) | $C_p$ (pF) |
|---|---|---|---|---|
| LHCb A | 198 | 50 | 1.41 | 2.5 |
| LHCb B | 198 | 60 | 1.52 | 1.5 |
| LHCb C | 198 | 70 | 1.62 | 2 |
| LHCb D | 240 | 70 | 1.56 | 2 |
| GLAST | 228 | 56 | 1.57 | 2 |
| CMS | 183 | 46 | 1.37 | 2 |

Table 9.1: Prototype sensor properties. The values of $\rho$ are estimated using the numbers given in Chapter 6.

a LHCb sensor maps to a specific area on the pitch adaptor. This leads to different values of $C_p$ for each region. Values for $C_p$ and the strip capacitance per unit length, $\rho$, are given for the all the sensor geometries tested in Table 9.2.[2] The total capacitance for each region can be calculated using:

$$C_{strip} = C_p + \rho \times l.$$

The resulting numbers are summarized in Table 9.2.

## 9.3 Test-beam setup and measurement program

The five prototype modules were tested in a 120 GeV/$c$ $\pi^-$ beam at the CERN X7 test facility in May 2003. Four double-sided silicon strip detectors provided by the HERA-B vertex detector group [87] served as a beam telescope. This allowed the impact point of the $\pi^-$ tracks on the sensors under test to be determined with a resolution of approximately 14 $\mu$m. The readout was triggered by a coincidence of four scintillation counters placed upstream and downstream of the beam telescope. A photograph of the setup is shown in Figure 9.1. All the components were installed in a light-tight aluminium box. This box could accommodate four prototype modules at a time, therefore measurements were initially performed with the LHCb1, LHCb2, GLAST and CMS modules installed. Once the measurement program for the LHCb1 module was completed, it was removed and replaced by the LHCb3 module.

---

[2] Numbers are not given for region E on the LHCb modules as it was not tested.

| Module | Strip length (cm) | $C_{Strip}$ (pF) |
|---|---|---|
| LHCb1A | 10.8 | 17.8 |
| LHCb1B | 10.8 | 17.9 |
| LHCb1C | 10.8 | 19.5 |
| LHCb1D | 10.8 | 18.8 |
| LHCb2A | 21.6 | 33.1 |
| LHCb2B | 21.6 | 34.3 |
| LHCb2C | 21.6 | 37.0 |
| LHCb2D | 21.6 | 35.7 |
| LHCb3A | 32.4 | 48.3 |
| LHCb3B | 32.4 | 50.7 |
| LHCb3C | 32.4 | 54.5 |
| LHCb3D | 32.4 | 52.5 |
| GLAST | 26.3 | 43.3 |
| CMS | 28.9 | 41.6 |

Table 9.2: Calculated capacitances for the different modules and detector regions.

As the acceptance of the beam telescope was smaller than the width of the sensors under test, not all the readout strips on the sensors could be illuminated simultaneously. The modules constructed from LHCb multi-geometry sensors were installed in such a way that regions A-D were illuminated. No data were accumulated for region E, which had been rejected as an option for the ST based on results from earlier measurements [19].

Each test module was mounted on a separate support rail, which allowed the horizontal position to be adjusted such that the beam spot illuminated different regions along the module. To remove the heat generated by the Beetle readout chips, the end of the module carrying the readout hybrid was attached to a copper cooling block. Water at a temperature of 10°C was used as a coolant.

An extensive measurement program was carried out in order to study the performance of the prototype modules. In total, more than 36 million events were saved to disk during the two week test-beam period. Initial bias voltage scans were carried out to determine the working point for all subsequent measurements. The data from these scans were also used to study signal shape parameters as a function of the bias voltage. High-statistics data samples of 250 000 events each were then accumulated for:

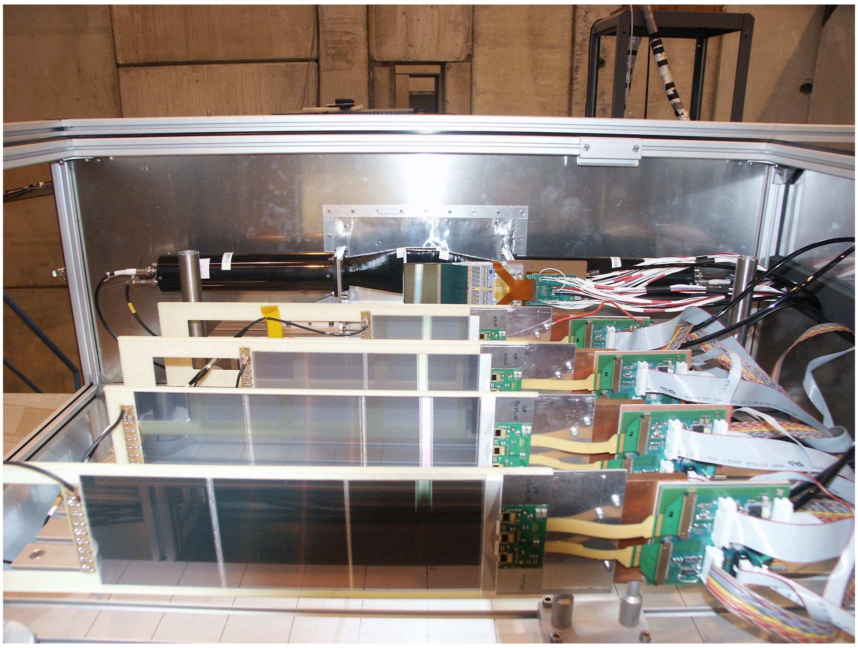

Figure 9.1: Overview of the test-beam setup in X7.

- Two bias voltage settings, $V1 \approx 1.5 \times V_{\mathrm{dep}}$ and $V2 \approx 2 \times V_{\mathrm{dep}}$, where $V_{\mathrm{dep}}$ is the full depletion voltage of the respective sensors.
- Three different signal shaping times of the Beetle preamplifier. The signal shaping time is controlled by programming the internal register $V_{fs}$ of the Beetle chip, and data were accumulated for $V_{fs} = 100$ mV (fast shaping), $V_{fs} = 400$ mV, and $V_{fs} = 1000$ mV (slow shaping).
- Up to five different beam positions along the modules. The beam spot was centered on each of the sensors on a module as well as on the inter-sensor gaps.

Prior to each of these main data runs, a low statistic latency scan was performed in order to determine the optimal signal sampling-time for the Beetle chips. To achieve this, the delay between trigger and signal sampling time was varied in three to four steps of 4 ns around the presumed maximum of the signal, and the most probable value of the signal amplitude was determined for each module and settings. The delay time for the subsequent data taking was then chosen as the one that maximized the most probable signal amplitude averaged over the four modules.[3] The data from the high-

---

[3] The optimum delay is slightly different for each module, since the modules present

statistics runs were used to analyse the signal-to-noise performance and the particle detection efficiency of the modules as a function of bias voltage, signal shaping time and beam position, as well as a function of the $\pi^-$ track position with respect to the readout strip centre. In addition, a study of cluster shapes was performed.

Finally, high-statistics delay scans covering the full duration of the pulse were performed for the two bias voltage settings ($V1$ and $V2$) and for two different shaping times ($V_{fs} = 100$ mV and $V_{fs} = 400$ mV). For these scans, the beam spot was centered on the sensors closest to the readout chips. The data from these runs were used to study signal shapes on the strips closest to the $\pi^-$ track and on the neighbouring strips, as a function of bias voltage, shaping time and track position.

## 9.4 Results

### 9.4.1 Functionality tests

Each module was checked for broken Beetle chips and a search was performed for disconnected and noisy channels. As an example Figure 9.2 shows the noise, i.e. the RMS of the ADC counts registered in absence of particles versus channel number for the GLAST module. It can be seen that the variation in the level of strip noise from channel-to-channel is small. The "spikes" that can be seen are due to channels that were bonded to an external PCB to allow for a charge calibration [58].

Corresponding plots for the other modules, together with pedestals and the distribution of reconstructed clusters as a function of strip number (the "beam profile"), can be found in [59]. From these plots a list of noisy and bad channels was extracted and are summarized in Table 9.3. The entries in this table can be compared to those listed in Chapter 8, on the measurement program with the laser setup that preceded the test-beam. There are additional faults in the test-beam compared to the laser setup, probably attributable to handling errors. In the test-beam, two strips on Beetle E were flagged as noisy, Beetle 16 was non-operational, four strips on the GLAST module were flagged as noisy, and there was one un-bonded strip on the LHCb3 module.

---

different load capacitances to the Beetle chips, resulting in a different peaking time of the front-end amplifier. However, the test-beam setup did not permit to set individual delay times for each module. Based on the results presented in [58], it is estimated that the chosen delay always lay within a window of ± 2.5 ns around the optimum delay time and that the effect on the measured signal amplitude is smaller than ± 1%.

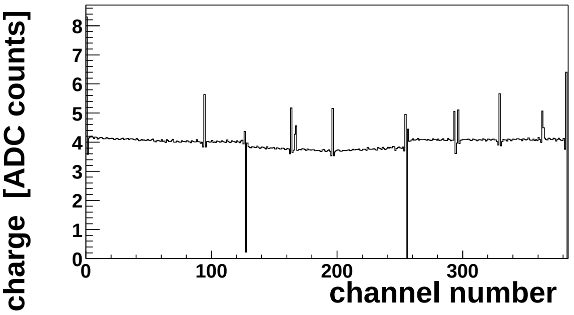

Figure 9.2: Strip noise for the example of the GLAST module with $V_{fs} = 400\,\text{mV}$.

On the other hand, Beetle 10, which was not functional at the time of the laser measurement program, was fixed.

The beam position illuminates the part of the sensor corresponding to the first two chips on each module. This was chosen in order to study effects at the sensor edge. For the LHCb modules this means the behaviour of the three 198 $\mu$m pitch regions can be investigated together with the 238 $\mu$m pitch region D.

### 9.4.2 Bias voltage scans

In order to obtain the working points for each module, bias voltage scans were performed. For each module, the bias voltage was varied over a wide range above the expected depletion voltage. From previous studies [58], it is known that the optimal sampling time depends on the bias voltage. The charge collection time decreases with increasing voltage, which can be explained by an increase of the velocity of the charge carriers in the silicon bulk. Then, for each voltage setting four runs were taken with different sampling times chosen to encompass the actual maximum of the signal for all the modules. For each of these runs the most-probable-value (MPV) of the $S/N$ distribution was determined by fitting a Landau convolved with a Gaussian. From the maximum of this fit, the $S/N$ value and the appropriate delay time can be determined for each bias voltage setting. Figure 9.3 shows the bias voltage scans for the different modules tested. The two sets of points for each module represent the $S/N$ ratio for tracks passing close to a readout

| module | Beetle ID | Working | Calibration channels | Bad bonds channels | Noisy channels |
|---|---|---|---|---|---|
| LHCb1 | B | OK | 55, 94 | | |
| LHCb1 | C | OK | 5, 44, 79, 112 | | |
| LHCb1 | D | Destroyed | | | |
| LHCb2 | E | OK | 94 | | 13, 21 |
| LHCb2 | F | OK | 5, 44, 79, 112 | | |
| LHCb2 | 10 | OK | 19, 48 | | |
| CMS | 14 | OK | | | 123, 124 |
| CMS | 15 | OK | 78 | | |
| CMS | 16 | Dead | | | |
| GLAST | 17 | OK | 94 | | |
| GLAST | 18 | OK | 35, 68 | | 39 |
| GLAST | 19 | OK | 40, 73 | | 37 ,107, 108 |
| LHCb3 | 1A | OK | 55, 94 | | |
| LHCb3 | 1B | OK | 5, 44, 79,1 12 | 51 | |
| LHCb3 | 1C | OK | | | |

Table 9.3: Noisy and dead channels at the end of the test-beam period. Channels are numbered per Beetle chip starting from zero.

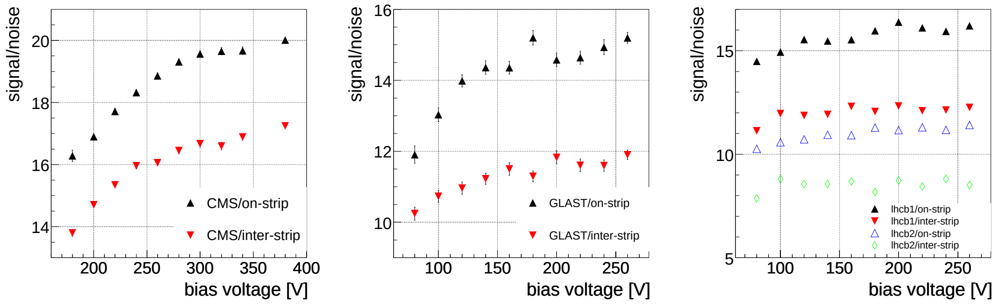

Figure 9.3: The $S/N$ ratio obtained for the CMS, GLAST and LHCb-modules as a function of the bias voltage.

strip and for tracks passing through the inter-strip region.[4]

The bias voltages at which the $S/N$ reaches a *plateau* are compared in

---

[4] The "on-strip" and "inter-strip" regions are defined here as ±0.166 × strip-pitch from the strip centre and the middle between two strips, respectively. These are larger areas than used later in the efficiency determination due to the limited statistics available in the bias voltage scans.

Table 9.4 with the measurements of the depletion voltage via the development of the backplane capacitance [68]. All the modules reach a *plateau* at 2-2.5 times the depletion voltage. The test-beam measurements of the start of the *plateau* are in agreement with those performed with the laser (see Chapter 8) except for the CMS module, that reaches it earlier in the test-beam measurements. This may be due to the difference in charge deposition profiles between the laser and particles, which is most pronounced for the CMS module [58].

| Module | depletion voltage | signal *plateau* |
|---|---|---|
| LHCb1 | 64 V | 120 V |
| LHCb2 | 64 V | 120 V |
| GLAST | 70 V | 150 V |
| CMS | 190 V | 300 V |

Table 9.4: Comparison between the full depletion voltage obtained from $C - V$ curves and the observed *plateau* from the $S/N$ in the test-beam.

A comparison of the $S/N$ measured for large over-depletion between the "on-strip" and "inter-strip" regions, indicates that the charge loss in the inter-strip region cannot be explained by insufficient time to collect all the charge — that is to say a "ballistic deficit", since in that case the difference between the two should become smaller for higher bias voltages.

### 9.4.3 Pulse-shape studies

A series of high statistics scans were taken in order to study the pulse-shape as a function of both the applied bias voltage and the Beetle shaping parameter, $V_{fs}$. In these scans the delay between the trigger signal and the Beetle sampling time was varied in order to observe the full pulse shape. For these studies only tracks that passed within $\pm 0.2 \times$ pitch of the centre of a readout strip were used. As an example in Figure 9.4 the results of these scans are shown for the bias voltage setting $V2$ and for $V_{fs} = 400$ mV. For the modules built from the LHCb multi-geometry sensors results are shown for region A only. In each plot the signal on the strip closest to the particle trajectory is shown together with the two strips to its left and to its right. It can be seen that for all the modules there is a sizeable signal on the neighbouring strips. These signals cannot be due to charge sharing by diffusion between the strips because of the wide pitch of the sensors. In addition the amplitude is too big to be explained by cross-talk within the Beetle chip which has been

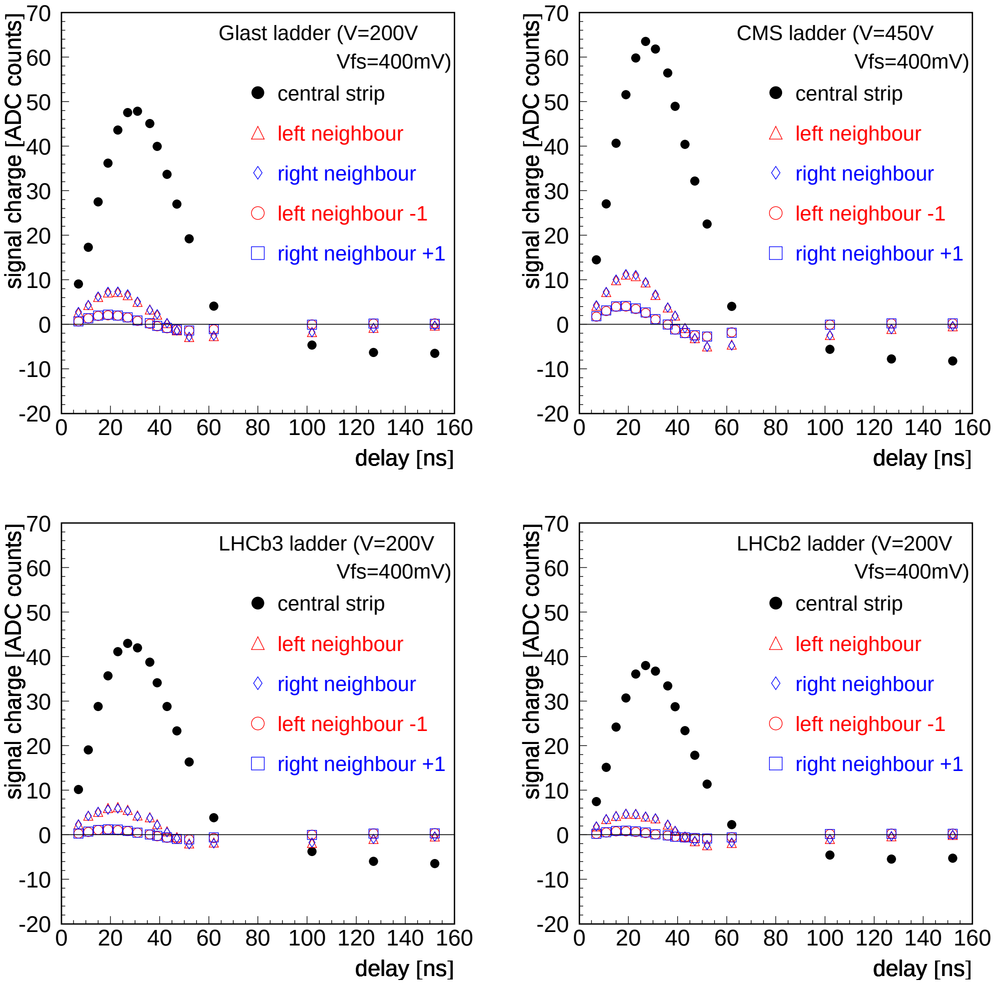

Figure 9.4: Pulse-shape scans.

measured to be $\sim 3\%$ [88]. It can also be seen from these plots that the signals induced on the neighbouring strips have a different time dependence to those on the central strip. Firstly, the time of the maximum amplitude for these signals is earlier in time than that of the central strip. Secondly, these signals undershoot earlier in time. Simulation studies of charge collection in silicon and signal generation in the Beetle chips have shown that these signals can be accurately reproduced if capacitive coupling between the readout strips is taken into account [69, 89].

An important parameter for the operation in the LHCb experiment is the signal remainder 25 ns after the signal maximum — the fraction of the signal

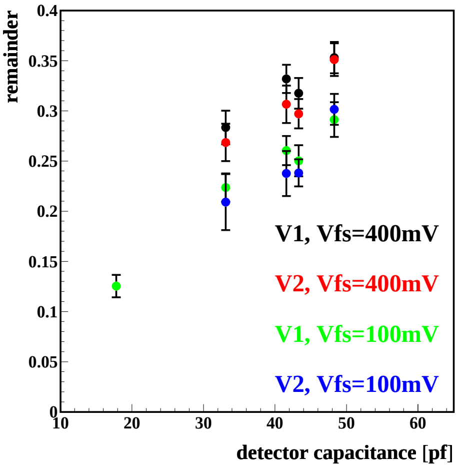

Figure 9.5: Signal remainder 25 ns after the maximum. For the LHCb modules results for region A are shown.

which will be seen in the following LHC bunch crossing. In Figure 9.5 the measured signal remainder is plotted as a function of detector capacitance for each of the two shaping times. As expected, the size of the remainder decreases with decreasing $V_{fs}$. As in [58] a roughly linear dependence on the detector capacitance is observed.The values of the remainders obtained here are in good agreement with the ones obtained with the laser setup.

In Monte Carlo studies of the LHCb performance signal remainders of less than 50% for the 33 cm long 'TT' modules and less than for 30% for the 22 cm long IT modules are assumed [90]. Both these requirements can be met if $V_{fs}$ is set to 400 mV or less.

### 9.4.4 Signal-to-Noise performance

One of the main goals of the test-beam was to investigate the $S/N$ performance of the modules. Two alternative definitions of 'signal' were used. The first is to simply sum the ADC counts of the four strips closest to the predicted impact point of the telescope track. The second is to use the results of the clustering procedure described [59]. A signal significance for each strip is defined as $d^2/n^2$, where $d$ is the pedestal and common mode subtracted ADC value and $n$ is the strip noise. Contiguous regions of strips with positive charge and a signal significance exceeding a given cut parameter were accepted as clusters if the sum of the single strip significances was larger

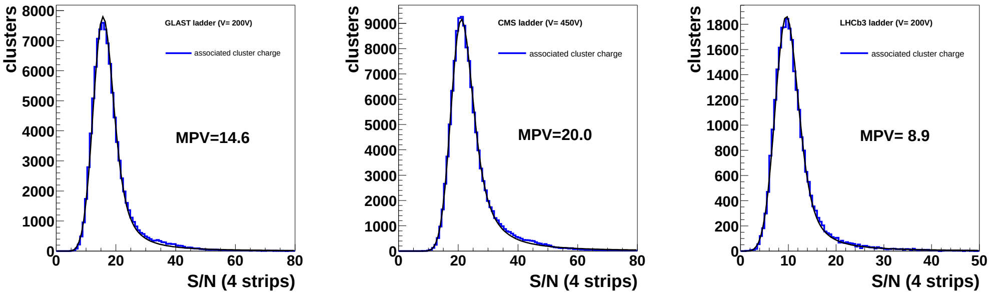

Figure 9.6: $S/N$ derived from the sum of the four strips closest to the extrapolated track impact point. Region C was used for LHCb3 module. $V_{fs}$ was set to 400 mV.

than a second cut parameter. The signal-to-noise ratio ($S/N$) of all clusters was normalized to that of one-strip clusters. Noise clusters were taken to be those clusters not associated to tracks reconstructed by the telescope. Cuts were selected according to the acceptable noise rates and efficiencies for the experiment. Further details can be found in [59].

Figure 9.6 shows the resulting $S/N$ distribution for $V_{fs} = 400$ mV, using the four strip analysis for the GLAST, CMS and LHCb3 modules, while Figure 9.7 shows the $S/N$ distributions obtained with the standard cluster finding algorithm. In both cases, the “noise” was normalized to the level of the single strip noise. The $S/N$ values obtained with the four strip analysis are larger than those obtained with the clustering algorithm analysis. This demonstrates that in the cluster finding algorithm the neighbouring strips are not always included. The difference in $S/N$ between the two clustering schemes is most pronounced for the LHCb3 module (18%) where the average cluster width is 2.2 strips, and least pronounced for the CMS module (5%) where the average cluster width is 3.4 strips [59].

Also shown in these plots are the results of a fit to the distribution of a Landau convolved with a Gaussian and its most probable value (MPV). The plots in Figure 9.7 produced using the cluster finding algorithm also show the noise cluster distribution. It can be seen that for the GLAST and CMS modules there is a clear separation between the tail of the noise distribution and the signal distribution. This is not the case for the LHCb3.

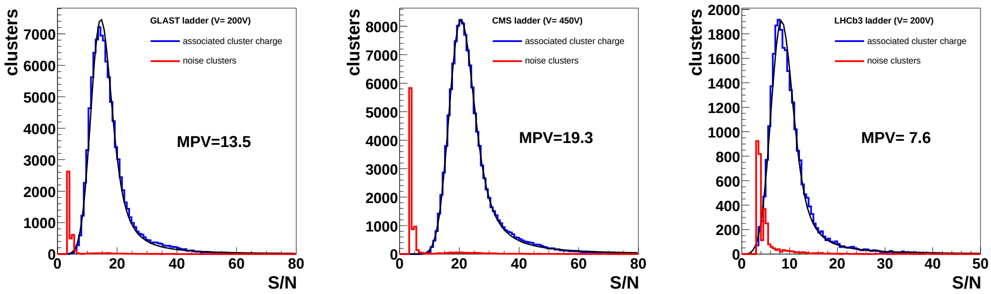

Figure 9.7: $S/N$ obtained with the cluster finding, averaged over the entire inter-strip region. Region C, was used for the LHCb3 module. $V_{fs}$ was set to 400 mV.

### 9.4.5 Charge loss in between readout strips

It had been observed [58, 84] that there is a significant charge loss in the region between two readout strips. This can also clearly be seen in Figure 9.8 where the $S/N$ from the four strip analysis is plotted as a function of the inter-strip position of the extrapolated tracks for all modules. The four strip analysis is used for this plot in order to ensure that the dip in $S/N$ is not caused by some artefact of the clustering algorithm. It can also be seen from these plots that the $S/N$ ratio increases for longer shaping times (larger $V_{fs}$) but the loss in $S/N$ appears independently of the shaping time. The same behaviour was seen in the results obtained using the clustering algorithm [59]. This is consistent with the results of the previous test-beam that indicated that the charge loss in the inter-strip region is not caused by a ‘ballistic deficit’ since this would be reduced for longer shaping times. The effect can be reproduced by simulation if it is assumed that it is caused by charges trapped in the inter-strip region where the electric field lines leave the sensor region before reaching the readout strips [69, 89].

Figure 9.9 shows the cluster finding efficiency is as a function of the track impact point for all the modules. For the CMS and the GLAST modules full efficiency is found for all shaping times, due to the high $S/N$. For the LHCb2 and LHCb3 modules, it can be seen that the charge loss between the two strips translates into a loss in cluster finding efficiency. An increase in the efficiency in the inter-strip strip region is observed as $V_{fs}$ is increased. As expected from the poor $S/N$ performance, this efficiency loss is particularly pronounced for the LHCb3 module where, for tracks passing close to the middle of two readout strips, even for $V_{fs} = 1000$ mV full efficiency cannot be achieved and, for $V_{fs} = 400$ mV the efficiency is below 90%. This is not

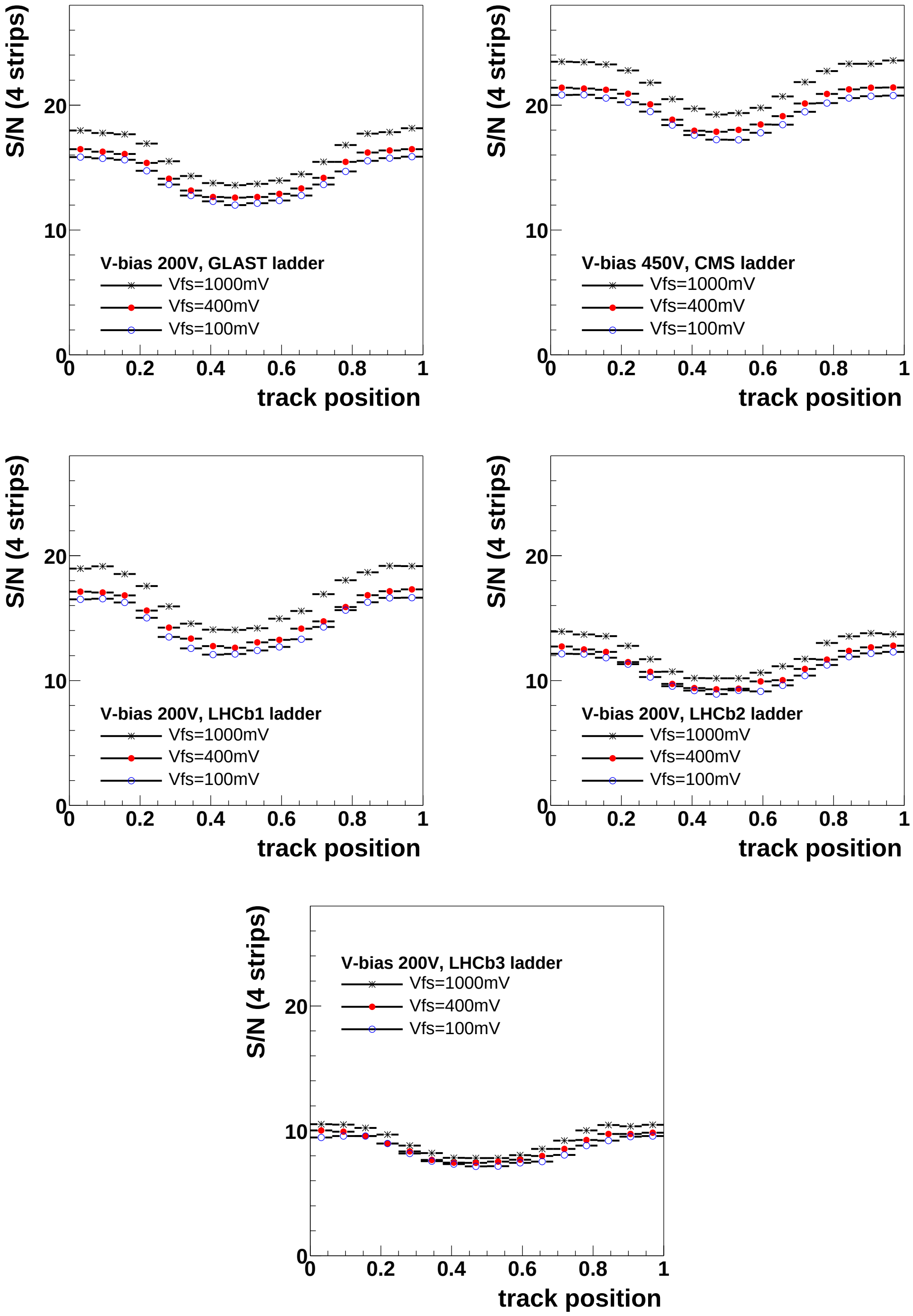

Figure 9.8: $S/N$ as a function of the inter-strip position for the different modules and shaping times ($V_{fs}$). For the LHCb modules, region A is plotted (same $w/p$ as GLAST and CMS module). The $S/N$ was determined from the summed charge on four strips. $V_{fs}$ was set to 400 mV.

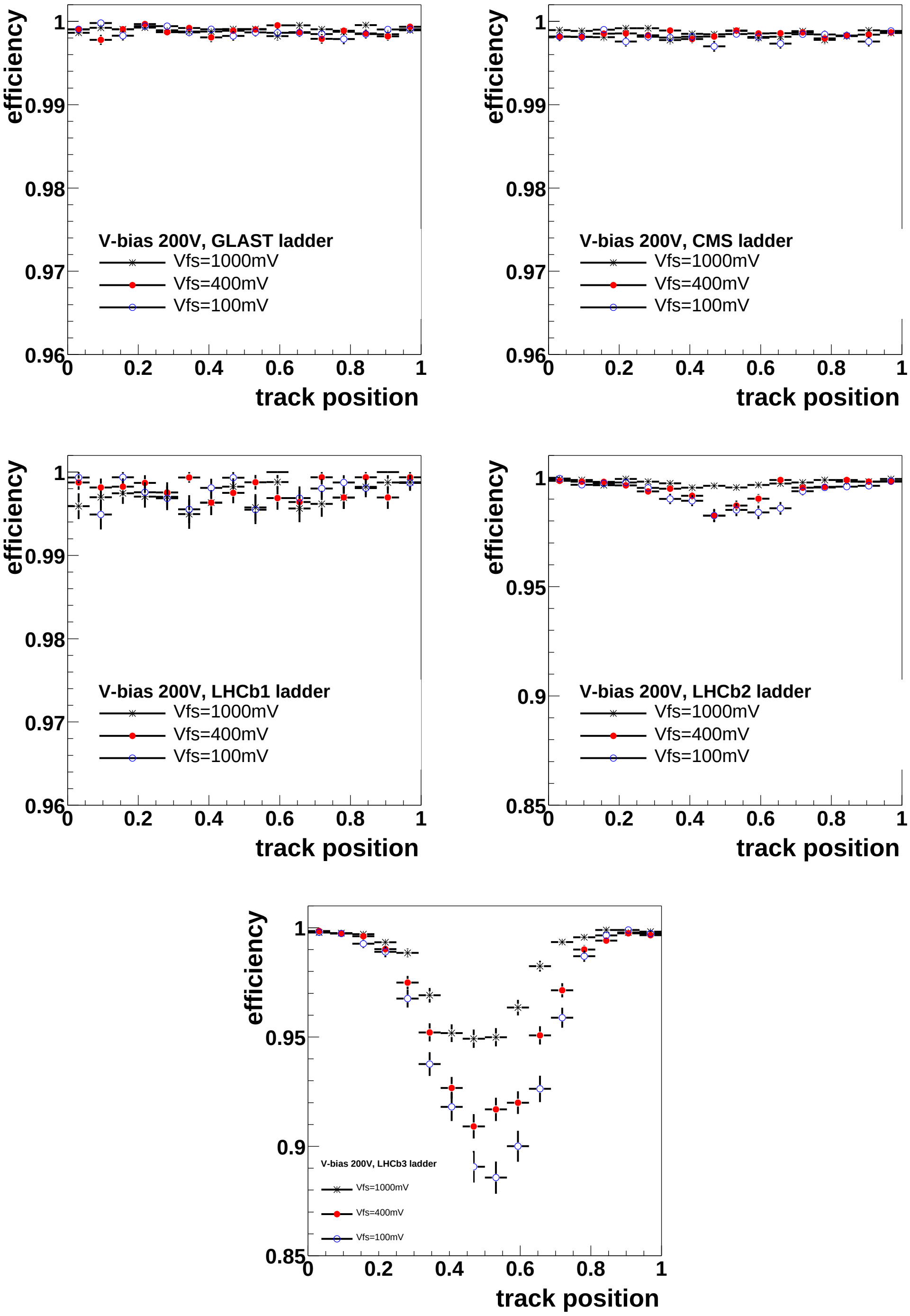

Figure 9.9: Efficiency as a function of the inter-strip position for different shaping times ($V_{fs}$) for all modules under test. For the LHCb modules, Region A is plotted (same $w/p$ as GLAST and CMS module).

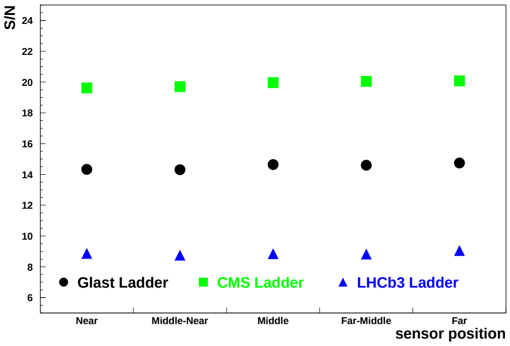

Figure 9.10: $S/N$ versus beam position on along the module. The position marked 'Near' is closest to the readout hybrid.

acceptable for use in LHCb. It is also clear from these plots that the $S/N$ performance obtained with the LHCb2 module is marginal.

The $S/N$ performance has also been investigated as a function of the beam position along the module. The results of this study are shown in Figure 9.10. It can be seen that for all modules there is no significant dependence in the performance with respect to the position along the module.

Since different sensor types have been tested it is possible to investigate the dependence of the charge loss between the strips on the strip geometry. This has been done as follows. First, tracks that pass within $\pm 0.1$ in pitch units around a strip centre are selected. The ADC counts on the three strips closest to the track are then summed and the resulting distribution fitted with a Landau convolved with a Gaussian. The MPV of the Landau from the fit is then taken as the size of the on-strip charge, $C_{on}$. Next, tracks that pass within $\pm 0.1$ of the middle of two readout strips are selected and the four strips closest to the track summed. Again the resulting distribution is fitted with a Landau convolved with a Gaussian. The MPV of the fitted Landau of this distribution is the size of the mid-strip charge, $C_{mid}$. The relative dip, $r_d$ is then defined as:

$$r_d = C_{mid}/C_{on}.$$

In Figure 9.11 $r_d$ is plotted against $x_d = (p - w)/t$ where $p$ is the pitch, $w$ the implant width and $t$ the detector thickness for the sensor geometries that were tested. It can be seen that $r_d$ is approximately linear with $x_d$ in the range investigated. This relationship means that the relative size of the dip can be reduced either by increasing $w/p$ or by increasing the sensor thickness. These numbers are consistent with there being no dip when the size of the

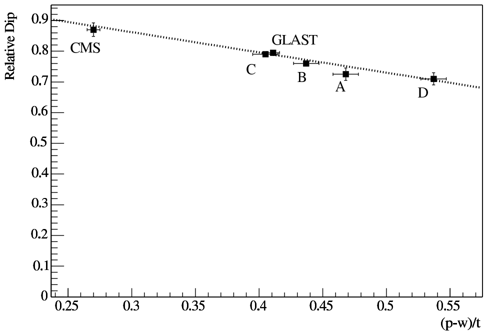

Figure 9.11: Relative dip as function of $x_d$.

inter-strip region becomes zero.

## 9.5 Conclusions

The results of test-beam measurements of silicon detectors with strip length of up to 33 cm and with corresponding capacitances of up to 55 pF have been described in detail. These tests have made use of the Beetle 1.2 front-end chip. The observed $S/N$ performance of the modules was found to be consistent with the expectation based on measurements of the Beetle front-end chip. Signal shapes meeting the specifications of less than 50% remainder for the TT-station and less than 30% remainder for the IT stations can be obtained if the shaping time parameter $V_{fs}$ is set to 400 mV.

The fact that modules with different thickness and with regions of different $w/p$ have been tested simultaneously has allowed the effect on sensor properties such as a capacitive coupling and charge collection efficiency to be investigated. This in combination with knowledge of the Beetle noise performance makes it possible to predict the $S/N$ performance both on and mid-strip for possible sensor geometries that have not been tested. Extrapolations made using the numbers given here were presented in [43].

It is clear from the measurements presented here that 320 $\mu$m silicon does not give sufficiently high $S/N$ to give full detection efficiency for modules with strips of length 33 cm. It therefore seems that modules with a thickness of at least 410 $\mu$m should be used in the TT station. The final choice of sensor thickness for the TT station was described in [43], and corresponds to the numbers given in Chapter 4.

# Chapter 10

# Irradiation of prototype sensors and modules for the Inner Tracker of LHCb

In this chapter we present results of an irradiation study on silicon sensor prototypes for the Inner Tracker carried out in order to investigate their radiation hardness. In addition, measurements of the performance of irradiated modules using an infrared laser system are presented. In particular, the effect of the irradiation on the charge collection and the dependence of the leakage currents on the temperature are studied in detail.

## 10.1 Introduction

The expected particle fluence in the innermost region of the Inner Tracker (IT) detector is approximately $1.8 \times 10^{13}$ cm$^{-2}$ 1 MeV neutron equivalent fluence [1] after 10 years of operation at nominal luminosity [19]. In order to investigate the radiation hardness of the sensors, an irradiation study with prototype sensors for the IT was carried out at the Proton-Synchrotron (PS) accelerator at CERN. Three sensors were irradiated with 24 GeV/c protons up to fluences of $1.9 \times 10^{13}$ p/cm$^2$ and $6.3 \times 10^{13}$ p/cm$^2$. Assuming a hardness factor $k = 0.6$ for 24 GeV/c protons [94], this corresponds to 1 MeV neutron equivalent fluences of $1.14 \times 10^{13}$ cm$^{-2}$ and $3.78 \times 10^{13}$ cm$^{-2}$, respectively.

Two of the irradiated sensors were then used to construct modules. Both

---

[1] A safety factor of two is included in this calculation.

modules were equipped with a readout hybrid carrying three Beetle 1.3 chips [45]. The modules were tested in a 120 GeV/c $\pi^-$ beam at the CERN SPS in July 2004. The analysis of the data taken during the test-beam is on-going and will be reported in detail in [92]. During the test-beam the detectors could only be operated at room temperature and, consequently, drew a large radiation induced leakage current which led to sizeable shot noise. Therefore, it was decided to make further tests of this modules in the laser setup at the University of Zurich described in [58], where the temperature of the modules can be controlled. This allows studies of the size of the leakage current as a function of temperature.

The outline of this chapter is the following. In Section 10.2, the irradiation setup at the CERN irradiation facility is described. In Section 10.3, the measurements on irradiated silicon sensors are explained. Results from the electrical characterization are presented. The leakage current and the full depletion voltage for the irradiated sensors were measured and compared to predictions. In addition, measurements of total strip capacitance, inter-strip capacitance, coupling capacitance, and strip currents were performed on selected strips on the sensors, to check whether there was any change after irradiation. In Section 10.4, laboratory measurements on irradiated prototype modules using an infrared laser system are presented. The laser setup is described, and results of the performance of the modules are given. Bias voltage scans to investigate charge collection efficiency were carried out, and measurements of the sensor current as a function of temperature are presented. In Section 10.5, a summary of the obtained results is given.

## 10.2 Irradiation test

Three LHCb Multi-Geometry prototype sensors (called LHCb 1, LHCb 5, and LHCb 8 in the following) and one CMS OB2 test-structure were irradiated. The LHCb sensors, manufactured by Hamamatsu, are single-sided $p^+n$ silicon sensors with a thickness of 320 $\mu$m and physical dimensions of $11 \times 7.8$ cm$^2$. They consist of five regions with different strip geometries (different strip pitch and different values of the ratio width over pitch). The CMS test-structure, manufactured by ST Microelectronics, contains a monitor diode, a baby-detector, and isolated elements of strips, polysilicon, coupling capacitances, etc. It is produced on $p^+n$ silicon with a thickness of 500 $\mu$m. Further details on the sensors and the test-structure can be found in [60] and [47], respectively. The electrical characterization of the LHCb sensors before irradiation has been described in Chapter 6.

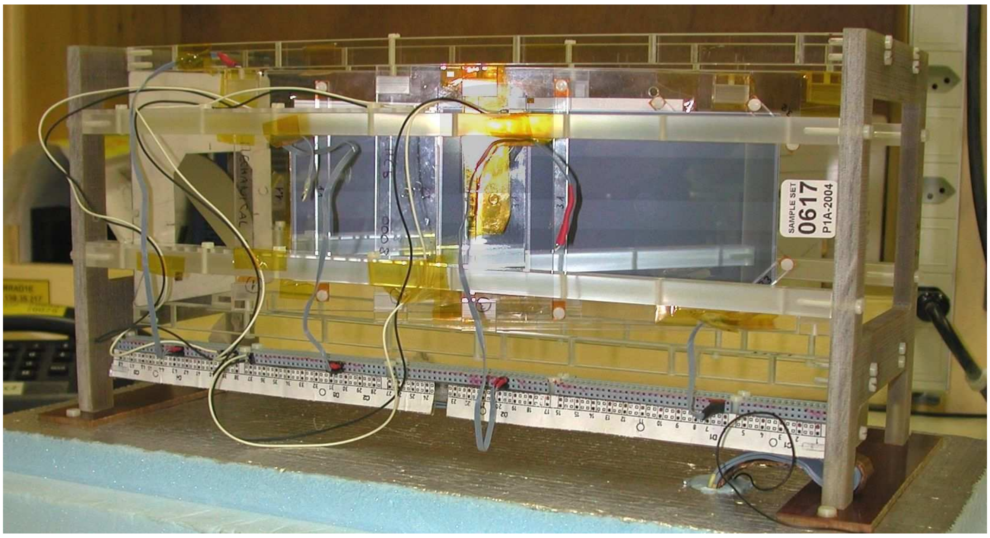

Figure 10.1: Photograph of the sensors mounted in the detector box. The thermal enclosure was not yet installed.

The irradiation was carried out using 24 GeV/c protons at the T7 irradiation facility [95], located at the East Hall area of the PS at CERN. During the irradiation, the detectors were moved with respect to the beam in order to irradiate the largest possible surface as uniformly as possible. A photograph of the setup is shown in Figure 10.1. The detectors were mounted in a thermal enclosure and attached to a x-y moving table, which was provided at the irradiation facility and permitted to scan the sensors through the proton beam. The box could be moved by $7 \times 7$ cm$^2$, which was not enough to cover the full area of the sensors. Hence, there is a region on the sensors which could not be irradiated. The sensors were mounted on Plexiglas holders, and the test-structure was mounted in a ceramic holder.

The detector box was cooled by a chiller and flushed with dry nitrogen. The temperature inside the box was kept constant at $-4$°C.

The sensors were biased at 30 V during the irradiation in order to avoid effects related to charge accumulation underneath the implants, and the detector currents were monitored remotely. Furthermore, the temperature at several points inside the thermal enclosure was monitored throughout the irradiation using PT100 thermistors.

The proton fluence was determined using activation measurements of aluminium foils located behind the sensors. The foils were analysed using gamma ray spectroscopy to detect the decay of $^{22}$Na, which is produced

| Sensor | Fluence (p/cm$^{-2}$) |
|---|---|
| LHCb 5 | $1.9 \times 10^{13}$ |
| LHCb 8 | $6.3 \times 10^{13}$ |
| LHCb 1 | $6.3 \times 10^{13}$ |
| Diode | $6.3 \times 10^{13}$ |

Table 10.1: Average fluence of 24 GeV protons per cm$^2$ received by the sensors in the uniformly irradiated region.

through the activation of the aluminium by protons. In addition, there was a secondary emission counter that was positioned in the beam upstream of the irradiation area. At the start of the irradiation, this counter was calibrated using additional aluminium foils that were placed on each side of the box.

One of the sensors was irradiated to a fluence of $1.9 \times 10^{13}$ p/cm$^2$ while the remaining sensors and the CMS test-structure were irradiated to a fluence of $6.3 \times 10^{13}$ p/cm$^2$. The irradiation was performed in two steps. First, all sensors were irradiated up to the lower fluence. The box was then moved out of the beam, but stayed in the irradiation facility until the next access. Meanwhile, the sensors were kept at a temperature of $-4$°C to avoid annealing effects. Then, sensor LHCb 5 was removed from the box and the remaining sensors were irradiated up to the higher fluence.

The average fluences received by each sensor, obtained from the aluminium foils activation measurements, are summarized in Table 10.1. The profile of the irradiation in the direction perpendicular to the readout strips on the sensors is shown in Figure 10.2. It was obtained by cutting the aluminium foils into about 5 mm wide strips that were analysed separately. It can be seen that a large fraction of the surface of the sensors was uniformly irradiated, but there was a part of the sensors, approximately 2 cm wide, that received a lower dose. This region corresponds to region E of the sensors (80 strips with a pitch of 237.5 $\mu$m [60]). The irradiation along the readout strips on the sensors was uniform. The active elements in the test-structure were uniformly irradiated.

After the irradiation, the sensors were kept in the box and at a temperature of $-4$°C until access to the irradiation area was possible. Then, the sensors were annealed for 80 minutes at 60°C in order to accelerate the effects of short-term annealing,[2] and to be consistent with standard RD48/ROSE

---

[2] According to reference [56], this heat treatment has the same annealing effect on the

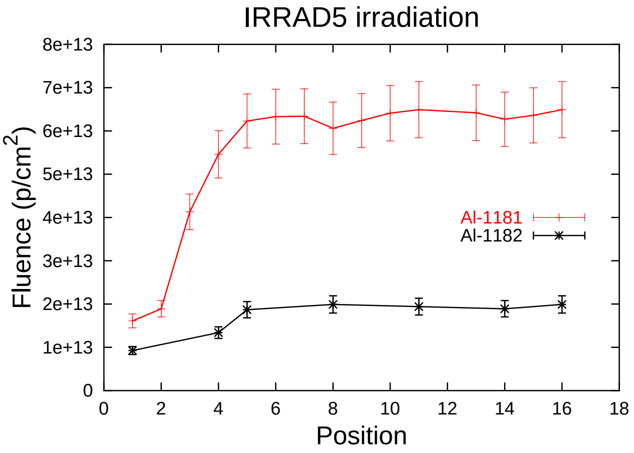

Figure 10.2: Fluence as a function of the position. The values are obtained from the aluminium foils activation measurements. Each position unit corresponds to roughly 0.5 cm. The aluminium foil number 1182 was placed on the back of sensor LHCb 5, and foil number 1181 was on the back of sensor LHCb 8.

prescriptions for annealing [96]. After this heat treatment, the electrical characterization was performed.

## 10.3 Measurements on irradiated silicon sensor prototypes

Bulk damage in irradiated sensors [56, 97] is caused by the displacement of silicon atoms in the lattice due to the non-ionizing energy loss of penetrating particles. The essential changes in macroscopic detector properties due to bulk damage are an increase in leakage current, a degradation in charge collection efficiency, and a change in the effective doping concentration. The last effect leads to a change in the full depletion voltage and usually limits the detector lifetime, since the leakage current can be suppressed by operating the detectors at low temperatures.

In this section, we present measurements of depletion voltages and leakage currents, as well as AC- and DC- strip tests for the irradiated sensors. Between the tests, the sensors were stored in a freezer at −20°C, in order to

---

leakage current as a storage for about 20 days at room temperature.

suppress reverse annealing effects.

### 10.3.1 Depletion Voltage

Radiation damage in the silicon bulk produces a change in the effective doping concentration and thus a change in the full depletion voltage, as

$$V_{depl} = ed^2 \frac{N_{eff}}{2\epsilon\epsilon_0}. \tag{10.1}$$

The full depletion voltage after irradiation depends on the initial doping concentration, the received fluence and the temperature.

To determine the full depletion voltage, we measured the bulk capacitance of the detectors as a function of the bias voltage. The bulk capacitance is proportional to the inverse of the square root of the bias voltage applied to the sensor until full depletion is reached, and then assumes a constant value. The full depletion voltage can thus be determined as the bias voltage at which the detector capacitance reaches a constant value. We plot $1/C^2$ as a function of the applied bias voltage and estimate the full depletion voltage from the intersection of two straight lines fitted to the rising part and the flat part of the curve, respectively.

The capacitance measurements were performed using a Keithley 237 unit working as a voltage source and an HP 4284 LCR-meter between the bias line and the backplane of the sensors. The $C$-$V$ curves were made using the parallel mode of the LCR-meter, with a measuring frequency of 1 MHz and a signal amplitude of 0.1 V. The measurements were performed at room temperature.

Figure 10.3 shows $1/C^2$ as a function of the bias voltage for the three LHCb sensors and the diode on the test-structure. The curves measured before irradiation are included for comparison. As can be seen, the structure of the curves for the highly irradiated sensors is quite complex, and $V_{depl}$ cannot be accurately defined.[3] The two-step structure seen in this curves could be due to the non-uniform irradiation of the sensors, since different regions on the sensor reach full depletion at different bias voltages. We could only measure the bulk capacitance of the sensor as a whole.

In order to obtain an estimation of the full depletion voltages in the uniformly irradiated area of the sensors, two different methods were followed.

---

[3] These measurements could have been improved by using a thermal chuck, which unfortunately was not available. This would have allowed to perform the tests at lower temperature, reducing the leakage currents and their influence on the measurement.

| Sensor | $V_{depl.}$ (V) (method 1) | $V_{depl.}$ (V) (method 2) |
|---|---|---|
| LHCb 5 | 40 | 37 |
| Diode | 115 | 102 |
| LHCb 8 | 130 | 106 |
| LHCb 1 | 130 | 101 |

Table 10.2: Full depletion voltages of the LHCb sensors and the diode on the test-structure. The first column, method 1, are the depletion voltages estimated as the intersection of two straight lines, whilst the depletion voltages in the second column, method 2, were obtained as the voltage at which $1/C^2$ decreased by 5% compared to the value in the *plateau*.

In the first method, we still interpret the full depletion voltage as the intersection of two straight lines, one fitted at high voltages (i.e. in the *plateau*) and the other fitted to the next lower slope segment. In the second method, the full depletion voltage is considered to be the voltage at which $1/\mathrm{C}^2$ decreased by 5% with respect to its value in the *plateau*. The estimated full depletion voltages are shown in Table 10.2. The results obtained using the two methods do not differ by more than 30 V.

Several studies [98] have shown that, beyond a certain fluence, silicon detectors built from $n$-type material behave as $p$-type devices, i.e. they experience a type inversion. Calculations of the expected full depletion voltage as a function of time were performed using the so-called Hamburg model [56], which takes into account the stable damage as well as short-term annealing and long-term reverse annealing of the effective doping concentration [99]. The calculation was performed for the irradiation at $-4$°C, followed by the annealing for 80 minutes at 60°C. Figure 10.4 shows this model for the LHCb sensors, together with the measured full depletion voltages extracted from Table 10.2. The mean of the results obtained from the two methods was considered as the full depletion voltage, and half of the difference among them was assigned as its error.

The model was calculated for two different sets of parameters which are believed to give reasonable descriptions of irradiation data [100]. The mean value of the results was assigned as the expected full depletion voltage, and half of the difference among them was assigned as its error. In addition, a model calculation without the annealing for 80 minutes at 60°C (solid line), which illustrates the stable damage due to irradiation, is included in the plot.

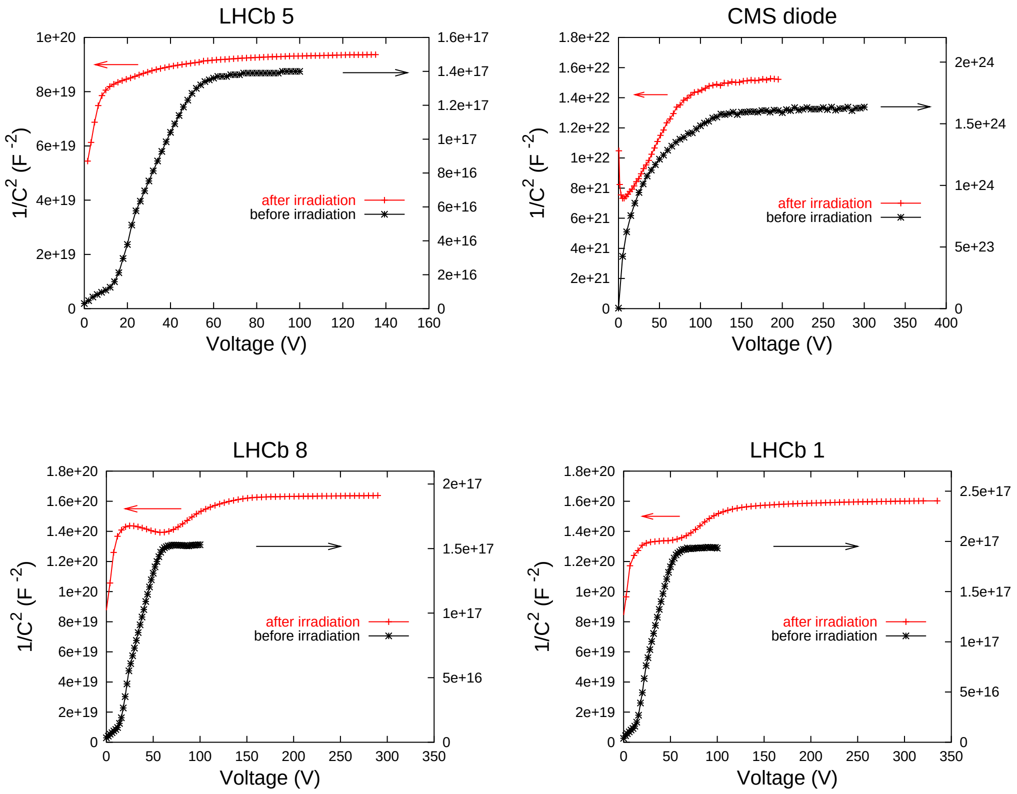

Figure 10.3: Depletion voltages measured on the sensors and the diode, before and after irradiation. The different magnitudes obtained before and after irradiation for each sensor are due to differences in the setup, since different blocking capacitors were placed at the entrance of the LCR-meter. This is not important for the determination of the depletion voltage, since it is only extracted from the shape of the curves.

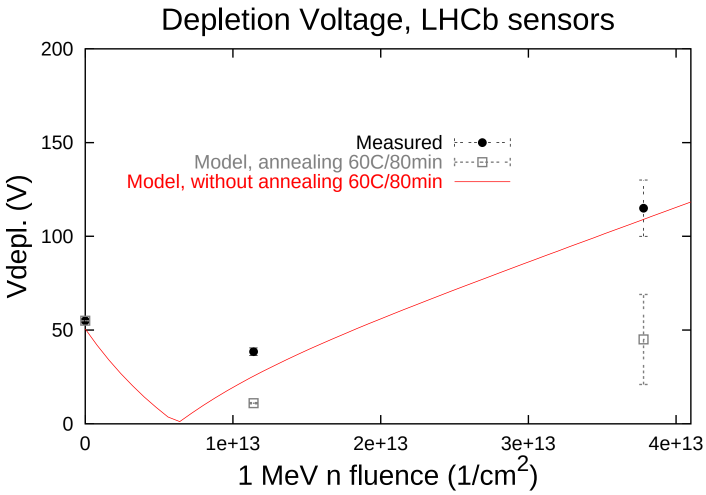

Figure 10.4: Measured full depletion voltages for three LHCb sensors and expected values according to the so-called Hamburg model as a function of the 1 MeV equivalent neutron fluence. A model calculation *without* the annealing for 80 minutes at 60°C (solid line), which illustrates the stable damage due to irradiation, is also included.

The experimental data and the model are not in good agreement, the measured full depletion voltages being significantly higher than predicted by the model. In particular, the model predicts large depletion voltage drops during the annealing step that was performed immediately after the irradiation. Surprisingly, considering only the stable damage, the model calculation ends up with a value very close to the measurements.

Our measurements showed that the sensors could be depleted at about 50 V after the lower fluence. This depletion voltage is lower than the initial depletion voltage and gives enough safety margin to sufficiently overbias the sensors, since we could bias them up to 500 V.

### 10.3.2 Leakage currents

The bulk damage in irradiated detectors produces an increase in the leakage current due to the generation of additional energy levels in the band gap, which allow for easy excitation of electron-hole pairs.

The leakage currents measured before irradiation for the LHCb sensors have been reported in [60] and [68], and are shown in Chapter 6 for two of

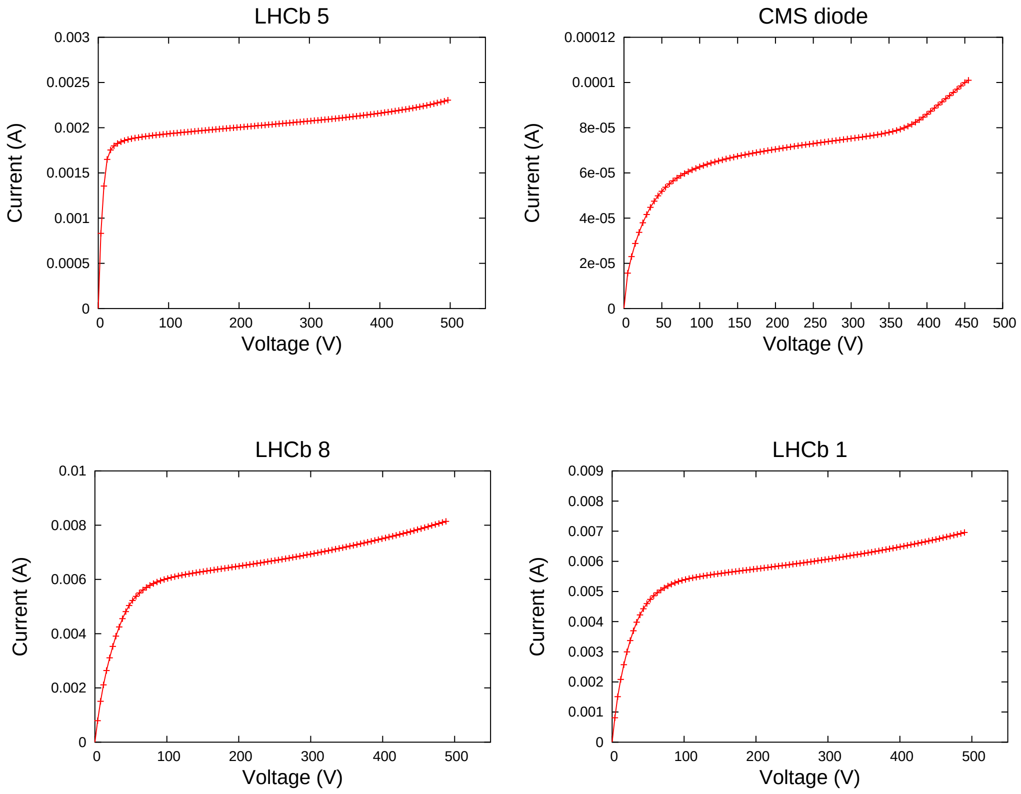

Figure 10.5: Leakage currents after irradiation, measured at temperatures between 24.5°C and 27°C. The diode shows a breakdown at $\sim$ 400 V.

them. The diode current before irradiation was about 5 nA at 300 V.

The measured leakage currents for the three irradiated LHCb sensors and the diode on the test-structure are shown in Figure 10.5. The measurements were carried out at room temperature, between 24.5°C and 27°C, using a Keithley 237 unit (voltage source + amperemeter) and a manual probe-station. The sensor LHCb 1 showed before irradiation an early junction breakdown at about 60 V. This breakdown is not observed after irradiation. The diode shows a breakdown at about 400 V after irradiation.

The leakage current depends exponentially on the temperature $T_m$ of the sensor.[4] For the present analysis, it was normalized to $T = 20$°C according to the relation:

---

[4] This relation could not be checked here since we did not have a thermal chuck. It was verified later in a temperature controlled setup, as will be shown in Section 10.4.4.

| Sensor | $I$ at $V_{depl.}$ (mA) | $I$ at 500 V (mA) |
|---|---|---|
| LHCb 5 | 1.24 | 1.50 |
| Diode | 0.043 | 0.065 |
| LHCb 8 | 3.61 | 4.72 |
| LHCb 1 | 4.14 | 4.82 |

Table 10.3: Leakage currents at $V_{depl.}$ and at 500 V, normalized to $T = 20°$C. LHCb 5 is the sensor irradiated with lower dose, and LHCb 1 and LHCb 8 are irradiated with higher dose.

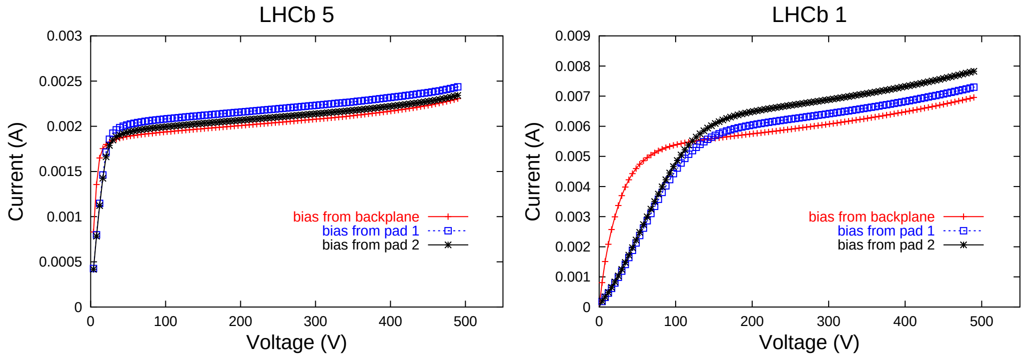

Figure 10.6: Leakage currents after irradiation, measured at room temperature, for sensors LHCb 5 and LHCb 1. The different curves correspond to measurements biasing the sensor from the backplane or from the pads located at the front side of the sensor. Pad 1 and pad 2 refer to the pads located near regions A and E, respectively.

$$I(T) = I(T_m)\left(\frac{T}{T_m}\right)^2 exp\left(-\frac{E_g}{2k_B}\left\{\frac{1}{T}-\frac{1}{T_m}\right\}\right) \tag{10.2}$$

where $E_g = 1.12$ eV is the band gap energy in silicon at room temperature and $k_B$ is the Boltzmann constant. $T$ and $T_m$ are in K. This relation holds true if the current is caused by generation current in the bulk material, which is the case after irradiation. The obtained leakage currents at the full depletion voltage and at 500 V, normalized to $T = 20°$C, are given in Table 10.3.

The functionality after irradiation of the "Nsub" pads (pads on the front side of the sensors that serve as a contact to the backplane, and are foreseen to be used to bias the sensors in LHCb) was also checked. Figure 10.6 shows three different measurements of the leakage current for sensors LHCb 5 and LHCb 1, one of them biasing the backplane directly (by biasing the chuck of the probe-station), and the other two using the aforementioned Nsub pads. It can be seen that the pads are functional after irradiation, and only at low voltages provide less voltage to the sensor than the direct contact to the backplane, due to an increase of the resistance of the implanted vias. The slightly different currents at higher voltages are due to the heating of the sensor while doing the tests.

### 10.3.3 Current related damage constant $\alpha$

The leakage current per unit of volume after irradiation scales linearly with the received fluence. The proportionality factor between the two terms for a given particle type is the current related damage constant $\alpha$,

$$\Delta I = \alpha v \phi \tag{10.3}$$

where $\Delta I$ is the change in the detector leakage current, $v$ is the active volume of the detector, and $\phi$ is the received fluence.

We calculated $\alpha$ using the leakage current of the detectors at $V_{bias}$=$V_{depl.}$, normalized to $T = 20°\mathrm{C}$ (see previous section), and the fluences from the activation measurements of the aluminium foils. Since the fluence was not uniform, we used

$$\Delta I = \alpha \sum (v_i \phi_i) \tag{10.4}$$

where $v_i$ is the silicon volume underneath the aluminium foil strip $i$, and $\phi_i$ the fluence measured for this strip (see Figure 10.2). Results are shown in Table 10.4. The mean value of the current related damage constant, obtained for the 24 GeV proton irradiation, is $\alpha = 2.78 \times 10^{-17}$ A/cm. This result is in good agreement with the value of $2.54 \times 10^{-17}$ A/cm given in [98], which was obtained after annealing for 4 min at 80°C, equivalent to our annealing for 80 min at 60°C.

It is common to normalize any particle fluence $\phi$ to the equivalent 1 MeV neutron fluence

$$\phi(1\ \mathrm{MeV\ eq\ n}) = k_\alpha \phi \tag{10.5}$$

with $k_\alpha$ being the so-called hardness factor. Comparing the $\alpha$ parameter from this irradiation to the value for 1 MeV neutrons, $\alpha = 4.56 \times 10^{-17}$ A/cm quoted in [98, 101], we obtain a hardness factor of $k_\alpha$= 0.61 for 24 GeV

| Sensor | $I$ at V$_{depl.}$ (mA) | $\sum(A_i\phi_i)$ (p) | Thickness ($\mu$m) | $\alpha$ 24 GeV p (A/cm) |
|---|---|---|---|---|
| LHCb 5 | 1.24 | $1.35 \times 10^{15}$ | 320 | $2.86 \times 10^{-17}$ |
| Diode | 0.043 | $3.09 \times 10^{13}$ | 500 | $2.78 \times 10^{-17}$ |
| LHCb 8 | 3.61 | $4.38 \times 10^{15}$ | 320 | $2.58 \times 10^{-17}$ |
| LHCb 1 | 4.14 | $4.38 \times 10^{15}$ | 320 | $2.90 \times 10^{-17}$ |

Table 10.4: Current related damage constant obtained for each detector. The mean value is $\alpha = 2.78 \times 10^{-17}$ A/cm.

protons. This value is in excellent agreement with the value of 0.62 given in [102].

### 10.3.4 Strip tests

In this section, we present AC- and DC- tests performed on selected strips of the irradiated sensors. All sensors were electrically characterized before irradiation, and the results can be found in Chapter 6 and in [60, 68]. However, the capacitance measurements are very sensitive to small differences in the setup and, in order to have a reference for direct comparison, we also repeated all measurements on an unirradiated sensor (LHCb 18).

#### Total strip capacitance

The total strip capacitance is here defined as the sum of the capacitance to the backplane and the capacitances to the two adjacent strips. The effect of the remaining strips was neglected in view of the large pitch of the sensors. The two closest neighbours were AC- coupled to the backplane. A sketch of the measuring setup can be seen in Chapter 6.

Measurements were carried out for one or two strips in each region of the LHCb sensors. The capacitance values obtained at bias voltages above the full depletion voltage are summarised in Table 10.5. Compared to the unirradiated sensor LHCb 18, no significant increase of the total strip capacitance is observed for sensor LHCb 5, whereas the total strip capacitances for the sensors irradiated with the higher fluence are about $\sim$ 15% higher. Since region E was not irradiated, there is no increase of the strip capacitance.

Figure 10.7 shows the bias voltage dependence of the total strip capacitance for sensor LHCb 5. The observed drop in the capacitance towards

| Sensor | Reg. | $C$ (pF) |
|---|---|---|
| LHCb 18 | A | 13.0 |
| | B | 14.0 |
| | C | 15.0 |
| | D | 14.6 |
| | E | 16.8 |
| LHCb 5 | A | 13.8 |
| | B | 14.5 |
| | C | 16.0 |
| | D | 15.1 |
| | E | 15.0 |

| Sensor | Reg. | $C$ (pF) |
|---|---|---|
| LHCb 8 | A | 15.5 |
| | B | 16.4 |
| | C | 17.2 |
| | D | 15.9 |
| | E | 16.7 |
| LHCb 1 | A | 15.6 |
| | B | 16.8 |
| | C | 18.4 |
| | D | 16.5 |
| | E | 17.0 |

Table 10.5: Total strip capacitances measured at 1 MHz. LHCb 18 is unirradiated, LHCb 5 is the sensor irradiated with the lower dose, and LHCb 1 and LHCb 8 are the highly irradiated sensors. The measured strip capacitances before irradiation were roughly the same for all these sensors.

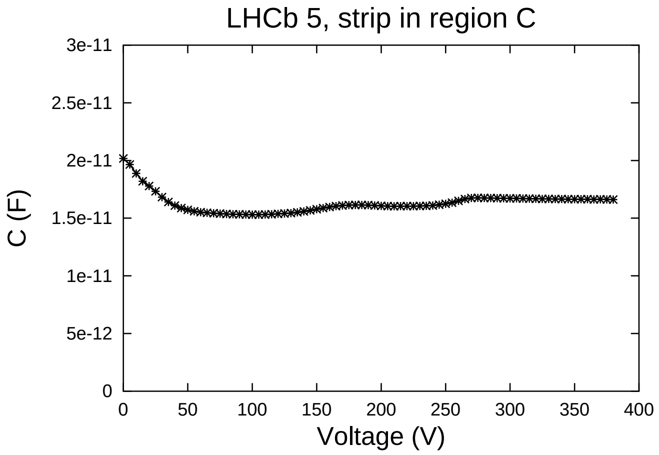

Figure 10.7: Total strip capacitance as a function of the bias voltage for one strip in region C of sensor LHCb 5, after irradiation.

| Sensor | LHCb 18 | LHCb 1 | |
|---|---|---|---|
| Region | $C$ (pF) | $C$ (pF) (strip #1) | $C$ (pF) (strip #2) |
| A | 3.5 | 3.5 | 3.4 |
| B | 3.9 | 3.8 | 3.8 |
| C | 4.3 | 4.4 | 4.4 |
| D | 3.4 | 3.5 | 3.6 |
| E | 3.9 | 3.9 | 3.9 |

Table 10.6: Inter-strip capacitances to one neighbouring strip, measured at 1 MHz, for sensors LHCb 18 (unirradiated) and LHCb 1 (irradiated to the higher fluence). No change after irradiation is observed.

higher voltages is much smaller than for the unirradiated sensors (see Figure 6.6). The same effect was observed for the highly-irradiated sensors, where the variation with the voltage is even smaller.

### Inter-strip capacitance

The inter-strip capacitance as a function of the bias voltage was measured between two pairs of strips in each region of the LHCb 1 sensor, one pair of strips in each region of the unirradiated sensor, and between three pairs of strips on the baby-detector. The LCR-meter was used in Cs-Rs mode, with a signal frequency of 1 MHz and a signal amplitude of 1 V. The inter-strip capacitance was found to be constant above a bias voltage of about 150 V. No change in the inter-strip capacitance after irradiation was observed. The measured inter-strip capacitances for the two sensors are shown in Table 10.6. The capacitance for the baby-detector was 0.77 pF, both before and after irradiation. Similar results, showing no significant increase of the inter-strip capacitance for $\langle 100 \rangle$ silicon (as used for the LHCb sensors and the CMS diode), have been reported in [103]. However, it is puzzling for us that we observed a $\sim 15\%$ increase in the total strip capacitance while the inter-strip capacitance remained unchanged after irradiation.

### Coupling capacitance

The coupling capacitance is the capacitance between the strip implant and the aluminium read-out line. It was measured by connecting the LCR-meter between the AC- and DC- pads on the sensor. In principle, this capacitance

| Sensor | LHCb 18 | | LHCb 1 | |
|---|---|---|---|---|
| Reg. | $C$ (pF) | $C/S$ (pF/mm$^2$) | $C$(pF) | $C/S$ (pF/mm$^2$) |
| A | 810 | 150 | 800 | 148 |
| B | 955 | 147 | 950 | 147 |
| C | 1110 | 147 | 1100 | 146 |
| D | 1100 | 146 | 1100 | 146 |
| E | 1330 | 154 | 1320 | 153 |

Table 10.7: Measured coupling capacitances for sensors LHCb 18 (unirradiated) and LHCb 1 (irradiated to the higher fluence). The values normalized to surface unit are also shown.

should not depend on the applied bias voltage. However, a small variation of the measured capacitance with the first biasing volts was observed. All measurements were performed with the sensors biased at a voltage above the full depletion voltage.

The coupling capacitance was measured as a function of the excitation frequency for one strip in each region of one highly irradiated and one unirradiated LHCb sensor. Due to the finite resistance of the implant and the metal, the circuit behaves as a low-pass filter and the effective capacitance drops off at high frequencies, as shown in Figure 10.8. The true capacitor values were extracted from the measurements at low frequencies and are shown in Table 10.7. They differ from region to region, due to the different implant widths. The values normalized to surface unit are also shown.

The measured coupling capacitances before and after irradiation are in good agreement and we conclude that the irradiation does not change the coupling capacitance.

### Strip currents

Individual strip currents were measured for one of the irradiated sensors to compare the leakage current profile with the irradiation profile obtained from the analysis of the aluminium foils. The measurements were performed by biasing the sensor and contacting a picoamperemeter between the bias line and the DC-contact pad of each strip in turn.

Figure 10.9 shows the currents as a function of the applied bias voltage for selected strips on the sensor LHCb 1. The peaks at low bias voltages are a consequence of the connection of the picoamperemeter in parallel to the

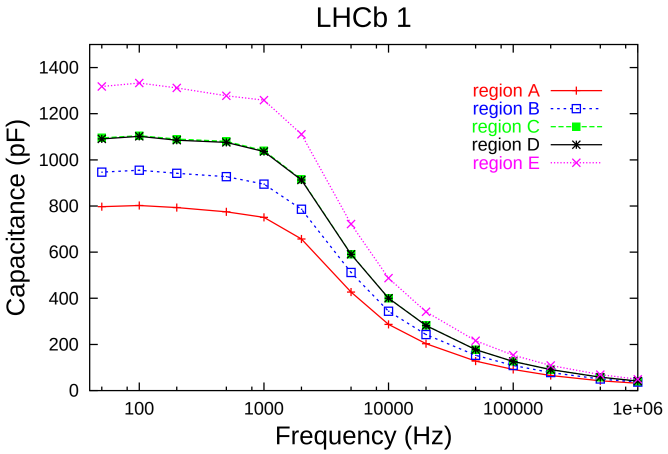

Figure 10.8: Coupling capacitance for the irradiated LHCb 1 sensor.

polysilicon bias resistor. This basically short-circuits this strip to the bias ring, while all other strips are connected to the bias ring via the bias resistor of ∼1.5 MΩ. As a result, the test strip is biased at a higher potential than its neighbours and, unless the sensor is fully depleted, an additional charge flows from the neighbouring strips thus producing the peak at low voltages.

The profile of the currents across the sensor is shown in Figure 10.10, where the value of the currents in the *plateau* is plotted versus the strip number. The currents are uniform for strips located in regions A, B and C; there is an increase in region D due to the change of pitch from 198 $\mu$m to 237.5 $\mu$m, and then the currents decrease towards higher strip numbers due to the lower dose received in this region.

Figure 10.11 shows the currents normalized to the strip volume [5] as a function of the strip number. The normalized currents are uniform from region A to the beginning of region E, and then decrease towards the sensor edge. The current profile agrees well with the irradiation profile obtained from the aluminium foil activation measurements, shown in Figure 10.2, which is included in the plot for comparison.

---

[5] For a single strip, the volume was calculated as the length of the readout strip multiplied by the nominal sensor thickness and the strip pitch.

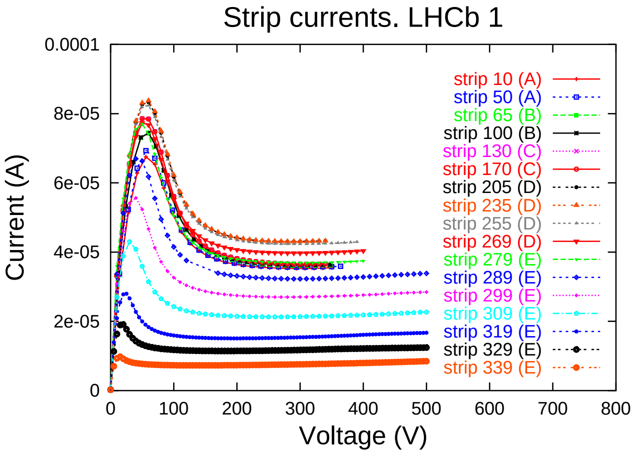

Figure 10.9: Currents for selected strips on sensor LHCb 1. The letters in brackets indicate the region to which the probed strip belongs.

| Module | Sensor ID | 24 GeV/c proton fluence (p/cm$^2$) | Equivalent years of LHCb operation |
|---|---|---|---|
| Irrad1 | LHCb 5 | $1.9 \times 10^{13}$ | 7 |
| Irrad2 | LHCb 8 | $6.3 \times 10^{13}$ | 20 |

Table 10.8: Fluences received by the sensors used in module construction.

## 10.4 Measurements on irradiated prototype modules using an infrared laser system

Two of the irradiated sensors studied above were used to construct modules referred to in the following as Irrad1 and Irrad2. Both modules were equipped with a readout hybrid carrying three Beetle 1.3 chips [45]. Details of the fluence the sensors were exposed to can be found in Table 10.8.

The Irrad1 module was tested in a 120 GeV/c $\pi^-$ beam at the CERN SPS in July 2004. The analysis of the data taken during the test-beam with this module is on-going and will be reported in detail in [92]. During the tes-tbeam the detectors could only be operated at room temperature and, consequently, drew a large radiation induced leakage current. Therefore, further tests were made in the laser setup described in Chapter 8, where the temperature can be controlled. This allows studies of the size of the leakage current as a function of temperature. In addition, the large leakage current

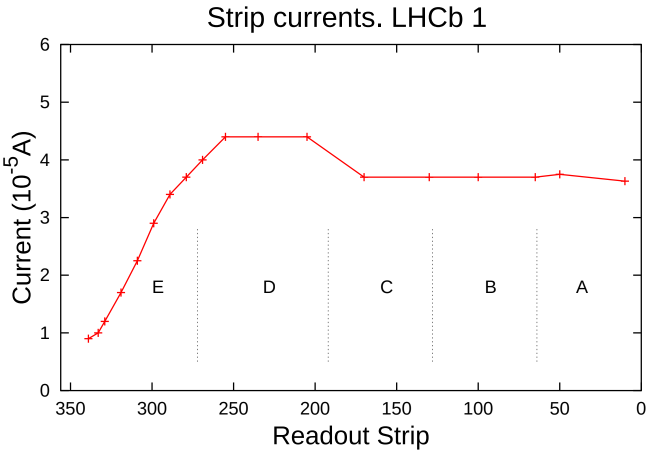

Figure 10.10: Current as a function of the strip number, for sensor LHCb 1. The values are taken from the *plateaus* in Figure 10.9.

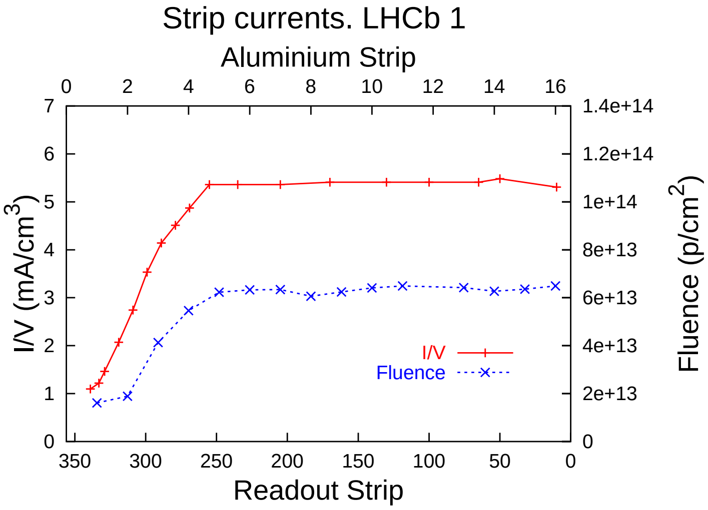

Figure 10.11: Current as a function of the strip number, normalized by the strip volume, and profile of irradiation from the aluminium foil activation measurements, for sensor LHCb 1.

drawn during the test-beam led to a large voltage drop across the resistors of the low pass filter of the bias voltage circuit. In the case of the Irrad2 module this led to one of the resistors burning out making it impossible to complete the measurement program. Before the studies described in this section were carried out, the 10 kΩ resistors on the low pass circuits were replaced with 1 kΩ ones. For the measurements presented here the voltage drop across the low pass filter was negligible.

The measurement program within the laser test-stand consisted of bias voltage scans to investigate charge collection efficiency, pulse shape scans, and measurement of the sensor current as a function of temperature.

In the case of the Irrad1 module this program was carried out for Beetle chip 8 and Beetle chip 9. These chips correspond to Region A and Region C on the LHCb multi-geometry sensors [19]. For the Irrad2 module data was only taken with Beetle chip 9. In addition, many more runs were taken in order to make systematic checks of the behaviour of the system. In total two million triggers were recorded in a data taking period of six weeks.

### 10.4.1 Sensor history

After irradiation annealing of the sensors occurs. This is strongly temperature dependent and can significantly alter the electrical properties of the sensors. Therefore, it is important to keep track of the conditions that the sensors were kept in after irradiation. Immediately after irradiation the sensors were annealed for 80 minutes at 60°C. Following this, the sensors were stored in a freezer at $-20°$C apart from:

- 1-2 days when the electrical characterization was performed,
- 2 weeks during the module assembly,
- 10 days during the test-beam period,
- 4 days during the transport of the modules to Zurich from CERN.

During these periods, which amount to 30 days, the sensors were kept at room temperature.

### 10.4.2 Laser setup

A detailed description of the laser test-stand is given in Chapter 8. The modules were tested in a commercial freezer (Figure 10.12), inside which the temperature can be set in the range −20 to 20°C by the means of an external thermostat. Once the value set has been reached the freezer power cycles such that the measured ambient temperature inside the freezer is stable within ±0.5°C. To avoid condensation during the cooling cycle the freezer was continuously flushed with dry air. This allowed the relative humidity inside the freezer to be kept below 25%.

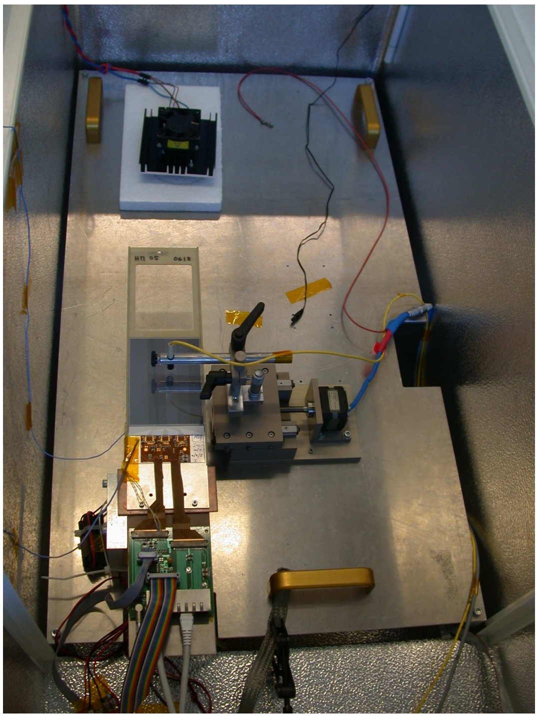

Figure 10.12: Mounting of the Irrad1 module inside the laser box.

The modules were mounted on a water cooled copper block. By varying the temperature of the cooling water, a temperature 15 to 16°C on the readout hybrid was maintained. This temperature was monitored by means of a thermocouple placed on the cooling block adjacent to the hybrid. To measure the temperature on the silicon sensor, another thermocouple was attached to the middle of the backplane of the sensor. This thermocouple was electrically isolated from the backplane by a thin layer of Kapton tape.

To generate charge in the silicon sensor a 1064 nm Nd:YAG laser diode was used. The laser signal is generated outside the box and guided via an optical fibre through a variable optical attenuator and then to a passive beam splitter. One of the outputs of the splitter is fed to an oscilloscope for monitoring whilst the other is guided via optical fibres to an optical focusing unit which is mounted inside the freezer. The shell of this unit is attached vertically to an arm that can be adjusted with a micrometer screw. This allows the laser spot to be focused on the silicon sensor. Typically, a spot size of 12 $\mu$m was achieved using the technique described in Chapter 8. The laser arm is mounted on a sledge whose horizontal position can be adjusted using a computer controlled stepper motor. This allows the position of the laser spot with respect to the strips on the sensor to be adjusted in 5 $\mu$m steps.

Details of the electronic readout chain are given in [58, 104]. The standard operating parameters for the Beetle 1.3 chip were used [6] apart from $V_{fs}$ which was scanned over the range 0 to 1000 mV. It has been observed that the Beetle performance depends on the supply voltage, Vdd. If the value of Vdd is significantly lower than 2.5 V a slower signal will be observed [105]. The value of Vdd in the laser setup was measured to be 2.44 V which is close enough to 2.5 V to ensure good chip performance. The readout mode used was 'Analogue on four ports' [45]. In this mode, which will also be used in LHCb running, the analog data from the 128 input channels per chip are multiplexed into four output ports of thirty-two data channels each, preceded by four header bits.

### 10.4.3 Charge collection studies

The model of charge collection in irradiated sensors proposed in [106] has been used to determine the full depletion voltage from the charge collection curves. In the following, the model and the results obtained are described.

#### The model

After hadron irradiation, defects produced in the lattice act as trapping centres. A fraction of the charge generated in the active volume may be trapped for longer than the integration time of the readout amplifier. Consequently, charge trapping can cause a signal deficit. In the model used here it is assumed that trapping depends on the carrier velocity since slow moving carriers will spend longer in the vicinity of the trapping centers. This means that above full depletion the signal size in irradiated detectors continues to grow until the saturation velocity of the charge carriers is reached. At this point the trapping remains constant and the signal reaches a plateau.

---

[6] $I_{pre} = 596\ \mu A, I_{sha} = 78\ \mu A, I_{currbuf} = 800\ \mu A$ [45].

As a consequence of trapping, only a fraction of the carriers produced at a point $x_0$ will reach another point located at $x_1$. That fraction will be proportional to $exp[-(x_1-x_0)/\lambda]$, with $\lambda$ being the signal attenuation length. A linear relationship between $\lambda$ and $v$ is assumed:

$$\lambda(v) = \lambda_0 + \lambda_1 \frac{v}{v_s} \tag{10.6}$$

and where $v_s$ is the saturation velocity. Then, the signal collected when a bias voltage $V$ is applied is:

$$q(V) = \frac{Q_0}{\omega_0} \int_0^{\omega(V)} exp\Big( - \int_x^{\omega_0} \frac{dx'}{\lambda(x')} \Big) dx \tag{10.7}$$

where $Q_0$ is the total charge deposited inside the detector volume and $\omega_0$ is the thickness of the detector. The outer integral is performed over the position of the charge generation inside the detector's depleted bulk ($x$) whilst the inner integral is performed from that point to the readout plane of the sensor. The different parameters in Equation 10.7 are:

$$\omega(V) = \begin{cases} \omega_0 \sqrt{V/V_{dep}} & \text{if } V < V_{dep} \\ \omega_0 & \text{if } V \geq V_{dep} \end{cases} \tag{10.8}$$

$$\lambda(x) = \lambda_0 + \lambda_1 \frac{v(x)}{v_s} \tag{10.9}$$

$$v(x) = \mu(x)\epsilon(x) \tag{10.10}$$

$$\mu(x) = \frac{\mu_0}{1 + \mu_0 \epsilon(x)/v_s} \tag{10.11}$$

$$\epsilon(x) = \frac{2V_{dep}}{\omega_0^2}\big(\omega(V) - x\big). \tag{10.12}$$

The five free parameters of the model are the total the charge ($Q_0$), the depletion voltage ($V_{dep}$), the saturation velocity ($v_s$) and $\lambda_0$ and $\lambda_1$ which describe the effect of charge trapping. Since $v_s$ is expected to be $\approx 100$ $\mu$m/ns [49] it can be used as a cross-check of the fit procedure. Alternatively, its value can be fixed and the remaining four parameters fitted. Both possibilities will be investigated in the following sections. The value for $\mu_0$ used has been calculated at the temperature of the measurements using the values given in [49]. It should be noted that in the absence of trapping ($\lambda \gg \omega_0$) Equation 10.7 becomes just $q(V) = Q_0\omega(V)/\omega_0$. That is to say the signal amplitude is proportional to the thickness of the depleted region.

### Fit results

Five bias voltage scans for the irradiated sensors were carried out. The conditions for the scans are summarized in Table 2. For all the scans the laser was positioned close to the metalization of a readout strip. It was shown in [58] that the time of the signal maximum depends on the applied bias voltage. Therefore, for each bias voltage, the signal amplitude was determined taking 4-5 runs with different sampling times around the rough position of the signal maximum. A parabola fit to the measured signal as a function of the sampling time was then made and the signal maximum extracted. Then, the signal amplitude as a function of the applied bias voltage is fitted to the model described in the previous section. For each data set two fits were carried out. In the first ('five' parameter fit) the value of $v_s$ was left free whilst in the second ('four' parameter fit) the value of $v_s$ was set to the expected value of 100 $\mu$m/ns. In addition, the same procedure has been applied to the data taken previously with the un-irradiated LHCb 1 module [58].

As an example the result of the five parameter fit for the Irrad2 module with $V_{fs} = 400$ mV is shown in Figure 2. Plots for all scans can be found in [93]. The numerical values obtained for all the fits are given in Table 2 and Table 3.[7]

| Module | Beetle chip | $V_{fs}$ (mV) | $Q_0$ (ADC) | $V_{dep}$ (V) | $v_s$ ($\mu$m/ns) | $\lambda_0$ ($\mu$m) | $\lambda_1$ ($\mu$m) | $V_{dep}(C\text{-}V)$ (V) |
|---|---|---|---|---|---|---|---|---|
| LHCb 1 | B | 400 | 58 | 101 | 1082 | 825 | 39999 | 65 |
| Irrad1 | 8 | 400 | 64 | 45 | 274 | 145 | 14271 | 40 |
| | | 100 | 62 | 47 | 499 | 139 | 15580 | |
| | 9 | 400 | 55 | 47 | 495 | 156 | 17715 | |
| Irrad2 | 8 | 400 | 57 | 137 | 75 | 92 | 3222 | 120 |
| | | 100 | 51 | 146 | 62 | 89 | 2228 | |

Table 10.9: The results of the five parameter fits to the bias voltage scans.

From Table 2 it can be seen that for the five parameter fits the values of $\lambda_1$ decrease with increasing fluence. This result is in agreement with the trend found in [106] and is consistent with trapping increasing with higher radiation dose. However, the values found for the saturation velocity in these fits are systematically too large. For the four parameter fits, where $v_s$ is fixed to 100 $\mu$m/ns, no clear correlation between $\lambda_1$ and the radiation

---

[7] The uncertainties on the obtained fit values are not quoted. This is because they are sensitive to the initial values given to MINUIT [107] and the obtained $\chi^2$ of the fit.

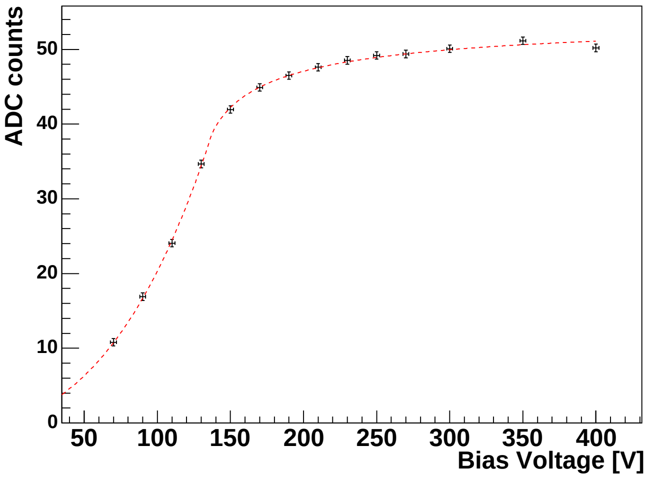

Figure 10.13: Bias voltage scan for the Irrad2 module, Beetle chip 8, $V_{fs} =$ 400 mV. The dashed line is the result of a five parameter fit to the model described in the text.

dose is seen. These results suggest that the model, though providing a good fit to the data is not applicable in our case. One explanation for this is ballistic effects due to the shaping time of the Beetle which is the same order of magnitude as the signal collection in the sensor. This means that in the absence of trapping centers the signal size continues to increase well after the full depletion voltage is reached. This effect is not taken into account in the model, which assumes that the integration time is large enough to collect the non-trapped carriers. From Equation 10.9 there is a strong correlation between $\lambda_1$ and $v_s$. The fit tries to account for the fact that ballistic effect are not modeled by adjusting these values such that the $\chi^2$ is minimized.[8] It is interesting to note that the fit results agree best with those presented in [106] for the Irrad2 where the effects of irradiation are largest. As an additional check for the LHCb 1 module data, a fit with no trapping to the data was made. The depletion voltage obtained agrees well with values obtained in the fits with trapping. This gives some confidence that the problems extracting $\lambda_1$ and $v_s$ do not effect this parameter as well.

For both modules the fitted values of the depletion voltage are 10 to 20 V higher than those found using the $C$-$V$ curve [68, 91]. For the irradiated

---

[8] The radiation dose of the sensors tested in [106] was larger and the readout electronics used were slower.

| Module | Beetle chip | $V_{fs}$ (mV) | $Q_0$ (ADC) | $V_{dep}$ (V) | $\lambda_0$ ($\mu$m) | $\lambda_1$ ($\mu$m) | $V_{dep}(C\text{-}V)$ (V) |
|---|---|---|---|---|---|---|---|
| LHCb 1 | B | 400 | 58 | 101 | 797 | 4274 | 65 |
| Irrad1 | 8 | 400 | 66 | 46 | 145 | 5010 | 40 |
|  |  | 100 | 64 | 42 | 112 | 2884 |  |
|  | 9 | 400 | 57 | 54 | 195 | 3079 |  |
| Irrad2 | 8 | 400 | 57 | 137 | 91 | 4400 | 120 |
|  |  | 100 | 50 | 146 | 90 | 3769 |  |

Table 10.10: The results of the four parameter fits to the bias voltage scans.

modules this could be explained by reverse annealing of the modules during the test-beam period and transport to Zurich when the modules were kept at room temperature. However, since this discrepancy is also seen for the un-irradiated LHCb 1 module it could also point to a systematic shift in the value of the depletion voltage extracted from the fit due to the ballistic effects discussed earlier.

For all further measurements standard bias voltage 'working' points were defined for the two modules. These are 250 V and 300 V for the Irrad1 and Irrad2 modules respectively. Both values are well above the full depletion voltage of the modules. The value for the Irrad1 was chosen to allow comparison with the results given in [92].

### 10.4.4 Leakage current studies

Before irradiation the current drawn by the LHCb multi-geometry sensors is negligible up to the breakdown voltage. As shown in Section 10.3.2, radiation damage in the silicon bulk leads to the generation of a sizeable leakage current. According to Eq. 10.2, the leakage current depends exponentially on the temperature of the sensor. During the electrical characterization, it was not possible to check this dependence since we had not a thermal chuck and measurements had to be performed at room temperature. However, as explained in Section 10.4.2, within the laser test-stand the temperature could be controlled and that dependence could be studied. Figure 10.14 shows the measured leakage current as a function of the sensor temperature for the Irrad1 and Irrad2 modules. Also shown on these plots are fits to the functional form given in Equation 10.2. In these fits the values of $I_{ref}$ and $E_g$ are kept as free parameters. It can be seen that, for both modules tested, the temperature dependence of the current is well described by Equation 10.2. The values of $E_g$ and $I_{ref}$ obtained from these fits are summarized in Table 10.11. For comparison this table also contains the expected leakage currents for the applied bias voltages at a temperature of 20°C extracted from earlier measurements on the irradiated sensors (Section 10.3.2). The values of $E_g$ obtained from the fit are roughly in agreement with the known band-gap of silicon at 293 K of 1.12 [49, 108].[9] The measured leakage currents roughly agree with a linear increase in the received fluence, as expected from Equation 10.2. However, the values for the current obtained from the

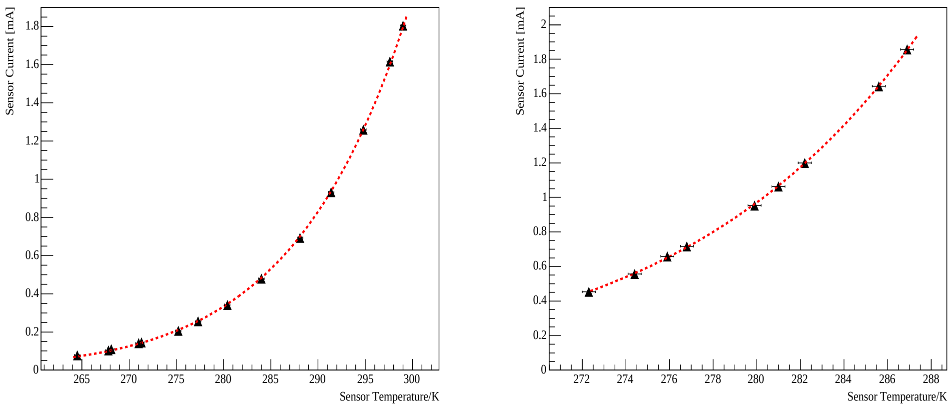

Figure 10.14: Sensor current versus temperature for the Irrad1 (left plot) and for the Irrad2 (right plot) modules. Irrad1 was biased at 250 V, and Irrad2 at 300 V. The dashed lines are fits to the functional dependence given by Equation 10.2.

| Module | $E_g$ (eV) | Sensor Current (mA) | |
|---|---|---|---|
| | | Fit | Expected |
| Irrad1 | $1.18 \pm 0.02$ | $1.1 \pm 0.01$ | 1.35 |
| Irrad2 | $1.20 \pm 0.03$ | $3.25 \pm 0.1$ | 4.0 |

Table 10.11: Fitted values of the band-gap energy, $E_g$ and the sensor current at 293 K. The expected values of the current are estimated using the values in Section 10.3.2.

---

[9] There seems to be some confusion concerning this value within the HEP community. For example the 2004 edition of the PDG gives a value of $E_g = 1.2$ [8]. Other papers, e.g. [109], use the value of 1.12 given in the text.

fit are $\sim$ 25% lower than those expected from the previous measurements. There are two explanations for this difference. First, there may be a systematic difference in the definition of the sensor temperature between the two setups. In Section 10.3.2 the ambient temperature of the probe-station used for the measurements was taken to be that of the silicon. However, due to the heat dissipated by the leakage current, the temperature of the sensor will be higher than the ambient temperature. In the case of the measurements presented here it was found that the temperature on the silicon would rise by $\sim$ 1.0 K when a bias voltage was applied. This effect explains at least half of the discrepancy. In addition, as mentioned before, there was a period of 30 days between the two series of measurements during which the modules were kept at room temperature. During this period further beneficial annealing of the modules will occur. This will lead to a reduction in the damage factor and hence the leakage current. Using the values given in [110] it is estimated that this effect reduces the observed leakage current by 20%.

### 10.4.5 Pulse shape scans

A series of pulse shape scans varying the delay between the laser pulse and the Beetle sampling time were performed. These scans allowed the dependence of the pulse shape on the bias voltage and the Beetle shaping parameter $V_{fs}$ to be investigated. Each scan leads to a plot of signal height versus delay time such as shown in Figure 10.15. Two important quantities can be extracted from these plots. The first quantity is the rise-time which is defined as the time taken for the signal to increase from 10% to 90% of its maximum value. The second is the so called signal remainder — the fraction of signal remaining 25 ns after the signal maximum. To extract this quantity the time ($t_{max}$) and amplitude ($s_{max}$) of the signal maximum are first extracted by making a parabolic fit about the rough position of the signal maximum. The signal amplitude ($s_r$) at $t = t_{max} + 25$ ns is then determined by linear interpolation of the two data points closest to this time. The remainder is then given by:

$$r = s_r/s_{max}. \tag{10.13}$$

The uncertainty on the remainder is estimated to be 1.5%.

Figure 10.16 shows the signal remainder obtained for the Irrad1 and Irrad2 modules as a function of the Beetle shaping parameter $V_{fs}$. As expected, the remainder increases with increasing $V_{fs}$. However, for the chips tested, the remainder is smaller than expected from the the Beetle front-end chip measurements [45] and the earlier laser measurements described in Chapter 8.

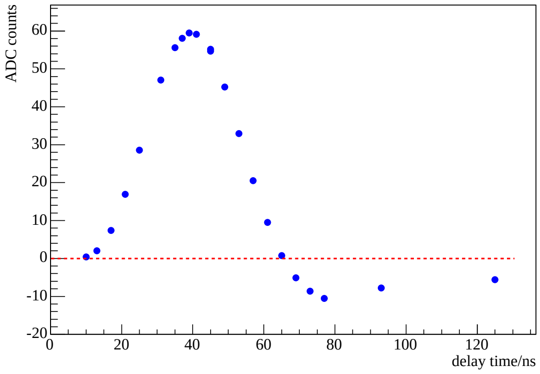

Figure 10.15: Example pulse shape scan for Beetle chip 8 on the Irrad1 module. $V_{fs}$ was set to 400 mV and the bias voltage was 250 V.

This discrepancy decreases with increasing shaping time. In the Irrad1 module, one of the Beetle chips, chip 8, is faster than the other, chip 9.

The dependence of the remainder on the bias voltage has also been investigated, and is shown in Figure 10.17 for the irradiated modules. For the chips tested, it can be seen that the remainder decreases with increasing bias voltage. This effect is most likely due to the higher electric field that will lead to faster charge collection. It should be noted that the remainder continues to decrease even for voltages far above the measured depletion voltage.

Finally, the dependence of the rise-time on $V_{fs}$ has also been measured (Figure 10.18). Again, in the Irrad1 module, Beetle chip 8 has a faster rise-time than Beetle chip 9. The results agree reasonably well with the expectations from the front-end measurements.

### 10.4.6 Systematic checks

Two systematic checks of the accuracy and reproducibility of the remainder measurement have been performed. First, for the case of the Irrad1 module, data has been taken with different temperatures of the water coolant and hence different settings of the readout hybrid temperature. The results of this test show that in the tested range, between 12 and 18°C, and within the uncertainty of the measurement, there is no dependence of the remainder on the readout hybrid temperature.

The second check made was to repeat the remainder measurement but to

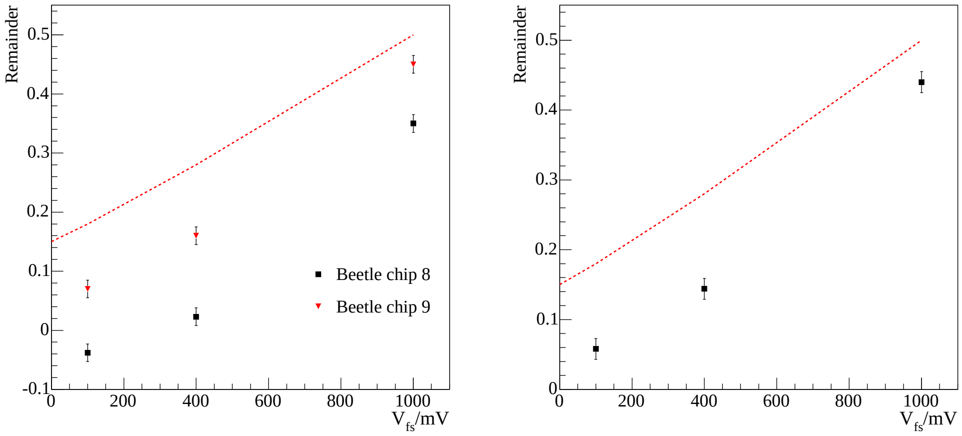

Figure 10.16: Remainder versus $V_{fs}$ for the Irrad1 (left plot) and the Irrad2 (right plot) modules. On each plot, the dashed line is the expectation from the front-end chip measurements [45]. The bias voltage was set to 250 V for the Irrad1 module, and to 300 V for the Irrad2 module.

vary the strip illuminated by the laser. This was done for six strips on Beetle chip 8 on the Irrad2 module. For these measurements $V_{fs}$ was set to 400 mV and the bias voltage was set to 300 V. For each channel the signal remainder was estimated using the procedure described above. The average of the distribution is 14% with a standard deviation of 1%. The latter is consistent with the quoted uncertainty of the remainder measurement of 1.5%. These results indicate that the laser setup is stable and the results are reproducible.

## 10.5 Conclusions

We have performed an irradiation study on three LHCb Inner Tracker prototype sensors and one CMS test-structure, that were exposed to 24 GeV/c protons up to fluences of $1.9 \times 10^{13}$ p/cm$^2$ and $6.3 \times 10^{13}$ p/cm$^2$, equivalent to 7 years or 20 years of operation in the innermost part of the Inner Tracker, respectively. The standard annealing scheme of 80 min at 60°C was followed. The proton fluence was obtained from aluminium foils activation measurements.

It was found that the sensors fully depleted at about 50 V after the irradiation to the lower fluence. This depletion voltage is lower than the initial

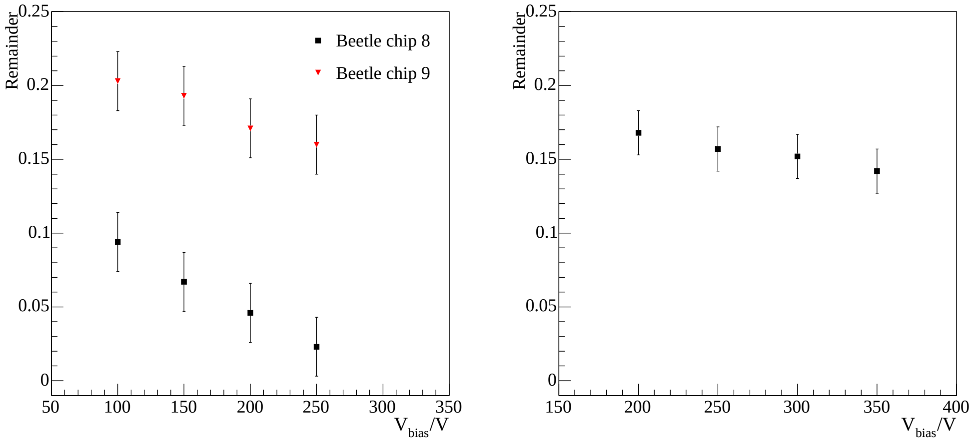

Figure 10.17: Remainder versus bias voltage for the Irrad1 (left plot) and Irrad2 (right plot) modules. $V_{fs}$ was set to 400 mV.

and gives ample safety margin to sufficiently overbias the sensors. The current related damage constant and the hardness factor for 24 GeV protons were extracted from the leakage current measurements and were determined to be $\alpha = 2.78 \times 10^{-17}$ A/cm and $k_\alpha = 0.61$, respectively. Inter-strip capacitances and coupling capacitances remain essentially unchanged after irradiation. The total strip capacitances for the sensors irradiated to the higher fluence showed an increase of about 15% compared to unirradiated sensors. No significant increase was observed after the lower fluence.

A comprehensive measurement program carried out on prototype modules constructed with the irradiated sensors has been reported. A detailed study of the charge collection after irradiation has been performed and it has been found that the model presented in [106] gives a reasonable parameterization of the data. However, due to the modest radiation dose compared to those investigated in [106] the results are sensitive to other effects, such as ballistic deficits due to the fast shaping time of the pre-amplifier. Despite this, the depletion voltages extracted from the fit, after allowing for reverse annealing, are in agreement with the $C$-$V$ measurements.

A study of the dependence of the sensors leakage current as a function of temperature has been made, and was found to follow the expected exponential dependence.

Pulse shape scans were performed for the irradiated modules. The signal remainder for a given setting of $V_{fs}$ was observed to be smaller than in

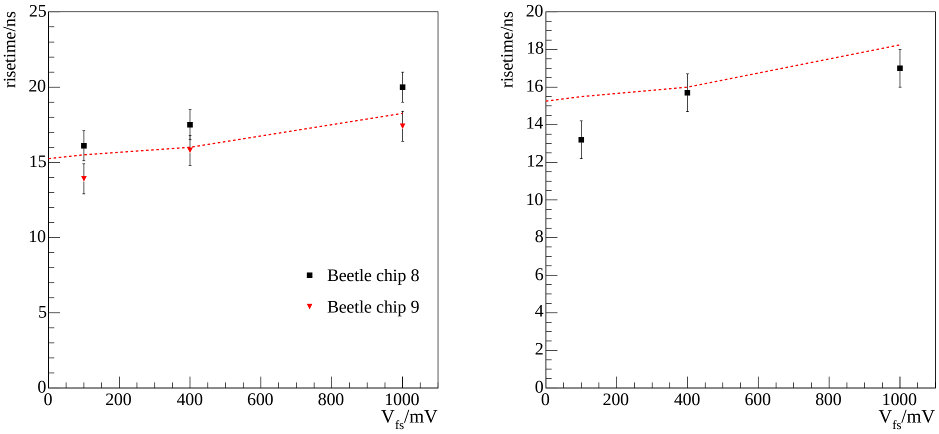

Figure 10.18: Rise-time versus $V_{fs}$ for the Irrad1 (left plot) and Irrad2 (right plot) modules. The bias voltage was set to 250 V for the Irrad1 module, and to 300 V for the Irrad2 module.

previous measurements. Therefore, if chips with properties similar to those tested here were used in the final experiment they could be operated at higher values of $V_{fs}$ in order to obtain the same remainder and noise performance as those tested previously.

These measurements have been useful in gaining experience with the handling of irradiated sensors. In particular, it has been learnt that care must be taken with respect to storage between measurement periods else sizeable annealing can occur.

# Chapter 11

# Final design of the silicon microstrip sensors and quality assurance procedures for the Silicon Tracker

In this chapter we give a description of the three types of sensors that will be used in the Silicon Tracker and present the quality assurance program followed by the Silicon Tracker group together with the results obtained for the first batches of se nsors. About 10% of the total production, including sensors of all three types, are analized in this chapter. All sensors are produced by Hamamatsu Photonics.

## 11.1 Final design of the silicon microstrip detectors for the Silicon Tracker

### 11.1.1 Silicon microstrip detectors for the IT

The "Inner Tracker" (IT) consists of three tracking stations downstream of the spectrometer magnet and covers a cross-shaped area around the beam pipe. Each station consists of four independent detector boxes, above, below and to both sides of the beam pipe, each with four planar detection layers that will be covered by silicon microstrip detectors. One-sensor modules built using 320 $\mu$m thick silicon microstrip detectors are used in the top/bottom boxes, and two-sensor modules built using 410 $\mu$m thick silicon microstrip

| | HPK-320 & HPK-410 |
|---|---|
| Wafer size | 6” |
| Overall width | $(78 \pm 0.005)$ mm |
| Nominal thickness HPK-320 | $(320 \pm 10)$ $\mu$m |
| Nominal thickness HPK-410 | $(410 \pm 10)$ $\mu$m |
| Wafer flatness | $\pm 25$ $\mu$m |
| Cutting line parallelity | $\pm 5$ $\mu$m |
| Overall length | $(110 \pm 0.005)$ mm |
| Minimum active strip length | 108 mm |
| Bulk material | $n$ type |
| Implant | $p^+$ type |
| Crystal orientation | $\langle 100 \rangle$ |
| Pitch | $(198 \pm 1)$ $\mu$m |
| Implant width | $(50 \pm 1)$ $\mu$m |
| # of strips | 384 |
| Biasing | polysilicon |
| Read-out coupling | AC |

Table 11.1: Geometry parameters and characteristics of the Inner Tracker sensors.

detectors will be used in the left/right boxes. A detailed description of the IT can be found in Chapter 4.

A total of 504 sensors will be employed in the IT stations. They have to be tested to ensure their functionality and check whether they pass the specified acceptance criteria.

The two types of IT sensors are identical apart from their different thicknesses. The detectors are single-sided p-on-n type, AC-coupled sensors, produced from 6” wafers. The physical dimensions of the sensors are $78 \times 110$ mm$^2$. The $p^+$ strip pitch is 198 $\mu$m and the implant width is 50 $\mu$m, which results in a $w/p$ ratio of 0.25. The width of the metal strips is 58 $\mu$m (8 $\mu$m wider than the implant strips), which gives rise to a more stable operation with respect to high bias voltages. The nominal thickness of the $n$-type substrate is 320 $\mu$m for the from now on called HPK-320 sensors, and 410 $\mu$m for the so-called HPK-410 sensors. Further details can be found in [114, 115].

The sensors are manufactured by Hamamatsu Photonics (HPK). The total production will comprise 580 sensors: 194 HPK-320 sensors and 386 HPK-410 sensors. A pre-series production of 60 sensors was ordered, out of which

| | HPK-320 & HPK-410 |
|---|---|
| Total leakage current | $< 1$ $\mu$A at V$_{depl}$+100 V |
| Individual strip current | $< 10$ nA at V$_{depl}$+100 V |
| Breakdown voltage | $> 500$ V |
| Full depletion voltage | 50-140 V |
| Coupling capacitance | $> 60$ pF/cm |
| Total strip capacitance | $< 1.6$ pF/cm |
| Bias resistors | (1.5 ± 0.5) M$\Omega$ |
| Bad strips per sensor | $< 1\%$ |

Table 11.2: Specifications and acceptance criteria of the Inner Tracker sensors.

49 sensors were delivered: 14 HPK-320 and 35 HPK-410 sensors. According to the company, they underestimated the production yield and were not able to send the remaining sensors on time, shifting the missing sensors from the pre-series production to main production. As a compensation, 12 mechanical pieces (without implants) and 3 lower-grade sensors (visually bad) were sent to us for free. The sensors were received at CERN and then shipped to Zürich for testing.

### 11.1.2 Silicon microstrip detectors for the TT-Station

The Trigger Tracker (TT) station [20, 43] consists of four planar detection layers that will be entirely covered by silicon microstrip detectors. A detailed description can be found in Chapter 4. It makes use of sensors that were developed for the Outer Barrel of the CMS silicon tracker, type CMS-OB2 [47, 68]. A total of 896 sensors will be employed in the station, and 1100 sensors (including spares) have to be tested to ensure their functionality and check whether they pass the specified acceptance criteria.

The CMS-OB2 detectors, from now on called HPK-500, are single-sided p-on-n type, produced from 6” wafers. The $p^+$ strips are AC-coupled and connected through polysilicon resistors to a common bias ring. Sensors have a thickness of 500 $\mu$m and measure 9.4 cm in length and 9.6 cm in width. The $p^+$ strip pitch is 183 $\mu$m and the width is 46 $\mu$m, which results in a $w/p$ ratio of 0.25. The width of the metal strips is 58 $\mu$m (12 $\mu$m wider than the implant strips), which gives rise to a more stable operation with respect to high bias voltages.

| | HPK-500 |
|---|---|
| Wafer size | 6” |
| Overall width | (96344 ± 20) $\mu$m |
| Overall length | (94326 ± 20) $\mu$m |
| Active area width | 93906 $\mu$m |
| Active area length | 91600 $\mu$m |
| Nominal thickness | (500 ± 15) $\mu$m |
| Bulk material | $n$ type |
| Implant | $p^+$ type |
| Crystal orientation | $\langle 100 \rangle$ |
| Pitch | 183 $\mu$m |
| Implant width | 46 $\mu$m |
| # of strips | 512 |
| Biasing | polysilicon |
| Read-out coupling | AC |

Table 11.3: Geometry parameters and characteristics of CMS-OB2 sensors produced by HPK, the so-called HPK-500.

| | HPK-500 |
|---|---|
| Leakage current at 300 V<br>Leakage current at 450 V | $< 5\mu$A<br>$< 10\mu$A |
| Breakdown voltage | $> 500$ V |
| Full depletion voltage | 100-300 V |
| Coupling capacitance | $\geq 55.2$ pF/cm |
| Bias resistors | (1.5 ± 0.5) M$\Omega$ |
| Bad channel rate | $< 1\%$ |

Table 11.4: Electrical specifications for the CMS-OB2 (HPK-500) sensors [116].

The sensors are manufactured by Hamamatsu Photonics (HPK). Until April 2005 we received 98 sensors from the total production of 1000 sensors.[1] Sensors are received at CERN, and then are shipped to Zürich for testing.

## 11.2 Sensor quality assurance procedures

To ensure the desired performance of the detector modules, a rigorous quality assurance (QA) of the sensors is required. Our QA program consists in two stages: tests performed by HPK prior to shipment and tests performed by our group after reception [111–113]. The first stage is described in Section 11.2.1 and the second in Section 11.2.2.

### 11.2.1 Vendor results: HPK tests

HPK tests the sensors prior to shipment in order to verify that they pass the acceptance criteria, and provides us with the results of these tests. For the IT sensors, these tests include leakage currents up to 500 V, full-depletion voltages, and strip currents on every sensor. For the TT sensors, the tests include leakage currents up to 600 V, full-depletion voltages on monitor diodes, and DC-tests on every sensor. In addition, they perform AC-tests on one out of ten sensors. For all types, they measure the sensor thickness on every sensor and, on a wafer lot basis we receive information on polysilicon resistors, coupling capacitances, breakdown voltage of capacitors, and implant resistances. In addition, HPK provides a list of bad strips.

According to their results, the sensors have excellent quality, with leakage currents below 1 $\mu$A at 500 V and the remaining electrical parameters within specification as well. Out of the 49 IT delivered sensors, there are only two sensors with one bad strip each (one leaky strip and one strip with a pinhole in the coupling capacitor). Out of the 98 TT delivered sensors, there was only one sensor with one bad strip, labeled as leaky by HPK.

As an example,[2] the strip currents at 250 V for two HPK-410 sensors with typical profiles are shown in Figure 11.1. The strip currents are very small for all sensors and out of the 49 IT sensors only one strip was leaky drawing

---

[1] ST Microelectronics produced 100 CMS-OB2 pre-series sensors, that will be kept as spares. Results of sensor qualification on them was reported in [66].

[2] Strip currents are selected as example since we did not measure them.

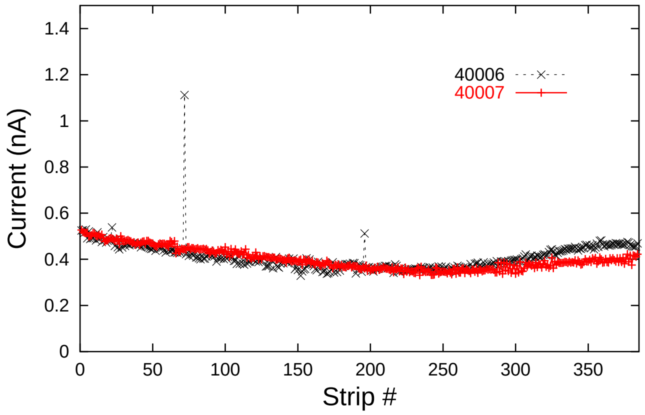

Figure 11.1: Strip currents measured at 250 V by HPK for two HPK-410 sensors.

| Sensor type | Delivered sensors | Total production |
|---|---|---|
| HPK-320 | 14 | 194 |
| HPK-410 | 35 | 386 |
| HPK-500 | 98 | 1000 |

Table 11.5: Sensors delivered until May 2005 and total quantities to be produced.

$\sim$ 230 nA at 250 V. The strip currents for all IT pre-production sensors can be found at [117].

### 11.2.2 Sensor quality control performed by the ST group and results for the first batches of sensors

Until May 2005 we received a total of 147 sensors ($\approx$ 10% of the total), including sensors of all three types that will be used in the ST. Table 11.5 summarizes the types and quantities of the delivered sensors, together with the total quantities that will be produced.

In this section, we describe the quality assurance tests that were performed on the sensors by the ST group, together with the results of our measurements.

| Visual Grade | Number of sensors | | |
|---|---|---|---|
| | HPK-320 | HPK-410 | HPK-500 |
| A | 12 | 24 | 81 |
| B | 2 | 11 | 14 |
| C | - | - | - |

Table 11.6: Number of sensors according to the visual inspection grade.

### Visual Inspection

A visual inspection was performed on all sensors in order to search for macroscopic defects. This is an important test, since large defects are easily detected and can give rise to instabilities in the electrical behaviour of the sensors or an increase of the leakage currents. First, an overall inspection of the strip side and the backplane was performed by eye and using a magnifying glass. Then, the strip side full surface was inspected under a microscope, taking note of scratches and defects, looking for chipped edges, pad bondability or contamination, as well as checking for the overall cleanliness of the sensors. In addition, the serial number on the scratch-pad was checked to be the same as that marked on the envelope.

According to the observed defects, a grading procedure was developed:

- Sensors without deep scratches or chips, and without pad contamination, were classified as A grade.
- Sensors with some superficial scratches (not deep enough to break strips) or acid damage in less than 1% of the strips, or slightly chipped edges, or a combination of these, were classified as B grade.
- Sensors with chipped edges, or deep or long scratches, or acid damage in more than 1% of the strips, or damaged bondings pads, or damaged resistors, or extremely dirty, were classified as C grade.

In Table 11.6, the number of sensors according to the visual grading is shown. In general, sensors were found to be of very good quality in this visual inspection. No deep scratches or big defects were found. About 80% of the sensors were free of defects and classified as A grade sensors. All remaining sensors were classified as B grade. A and B grade sensors can both be used to build silicon modules for use in the experiment.

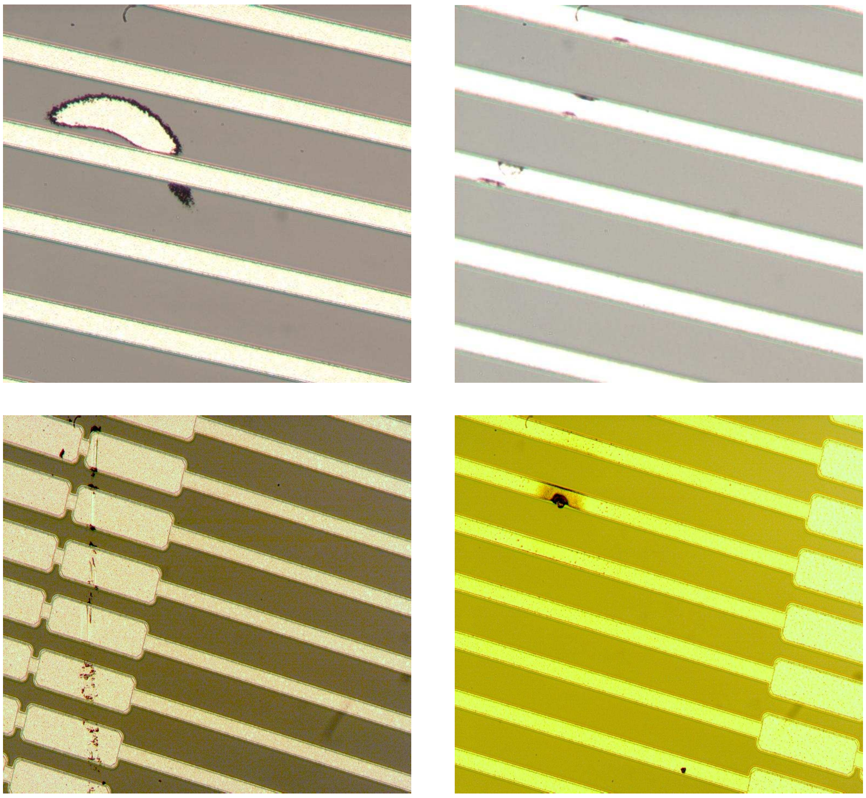

Figure 11.2: Examples of the defects found on sensors that were classified as B grade in the visual inspection. On the top, excess of aluminium between two strips (left) and chipped strips (right) found on IT sensors. At the bottom, scratch over bonding pads (left) and defective strip (right) found on TT sensors.

Some examples of the observed defects, like an excess of aluminium between two strips, scratches over bonding pads, a few slightly chipped strips, or a defective strip are shown in Figure 11.2.

### Leakage currents

The leakage current is the reverse current of the *pn*-junctions. It gives rise to a background noise and is caused by thermally excited minority carriers that are generated in the depleted region and, due to the electric field, drift to the electrodes. For a given bias voltage, the size of the leakage current depends to a certain extent on environmental factors, like temperature, humidity and time of operation of the sensor, but its variation will in general be small (of

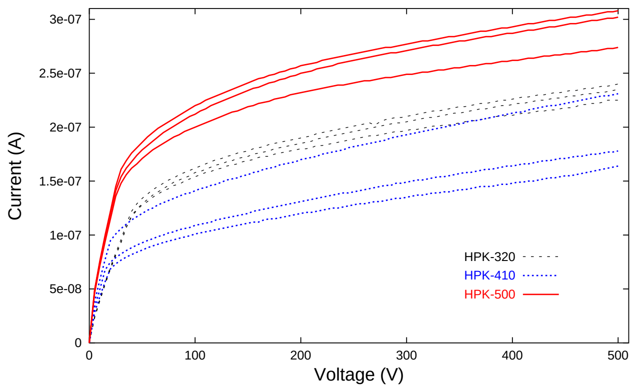

Figure 11.3: Typical IV curves measured on the three types of sensors. No breakdown is observed below 500 V.

the order of a few 100 nA at the full depletion voltage for a good sensor).

In this section, results on leakage currents for the 49 IT pre-series sensors and the 98 TT production sensors are presented, and typical IV curves are shown. The leakage current dependence on the application of vacuum to the chuck of the probe station is investigated, and the stability and repeatability of the currents are studied.

The current between the backplane and the bias ring was measured for all sensors as a function of the reverse bias voltage, using a Keithley 487 unit (picoamperemeter + voltage source). The bias voltage was increased in steps of 5 V up to 500 V, over a period of 5 minutes. The measurements were performed at room temperature, typically about 20°C, and at a relative humidity below 30%.

A great uniformity of the currents from sensor to sensor was found. As an example, typical IV curves are shown in Figure 11.3 for three sensors of each type.

The distribution of the leakage currents measured at 500 V is shown in Figure 11.4. They were found to be very low, typically below 500 nA at 500 V. None of the sensors evidenced breakdown below 500 V,[3] and all sensors are within the acceptance criteria (see Tables 11.4 and 11.2).

It had been observed [66] that the leakage currents for sensors produced

---

[3] Two of the lower-grade HPK-410 sensors supplied as free samples were tested up to higher voltages, and they evidenced breakdown at about 800 V.

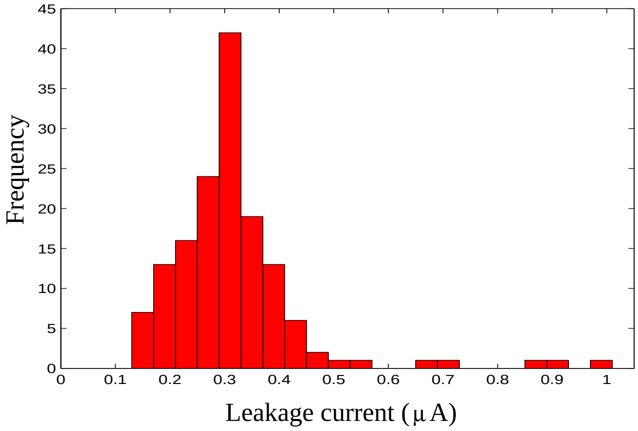

Figure 11.4: Distribution of the leakage currents measured at 500 V on the three types of sensors. All sensors fulfill the specifications.

by other companies depended critically on the application of vacuum to hold the sensors to the chuck of the probe station. To check for a possible effect on the HPK sensors, the leakage currents of 15% of the sensors were re-measured without chuck vacuum. No difference between the currents obtained with and without chuck vacuum was observed for any of the sensors. As an example the measured curves for one of the tested sensors of each type are shown in Figure 11.5.

The repeatability of the IV curves under stable conditions (same strain, temperature and relative humidity) was checked for $\sim$ 10% of the sensors. About 30 IV curves on each sensor were taken automatically over night, waiting for 35 min between two consecutive measurements. Figure 11.6 shows as an example the 30 IV curves obtained for one of the tested sensors. Typically, the IV curves were found to be reproducible within better than 100 nA.

Moreover, the current stability of 10% of the sensors was investigated in a $\sim$ 30 h long biasing test, while temperature and relative humidity were monitored. The leakage currents were stable and reproducible against long term drifts. Only small drifts in current were observed and these were correlated to temperature, as shown in Figure 11.7.

A comparison was made between the currents that we measured and the data provided by HPK. We found currents slightly lower than the values quoted by HPK. Typically, we measured leakage currents of about 150-500 nA at 500 V, whilst HPK measured leakage currents of 250-600 nA at the same voltage. We assume that this difference is due to differences in the setup or

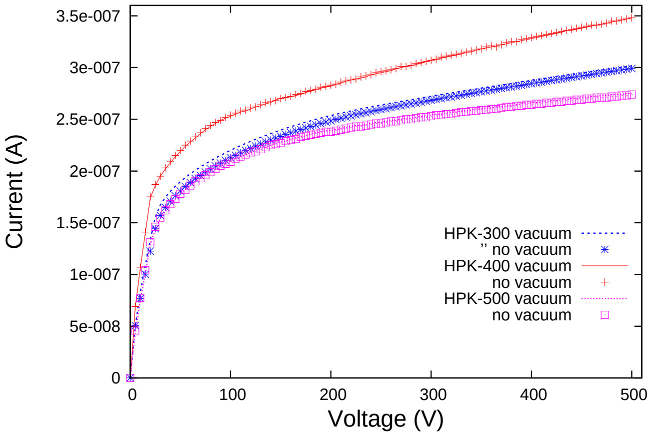

Figure 11.5: Leakage currents measured with and without chuck vacuum for one sensor of each type. The currents do not depend on the application of vacuum to the chuck.

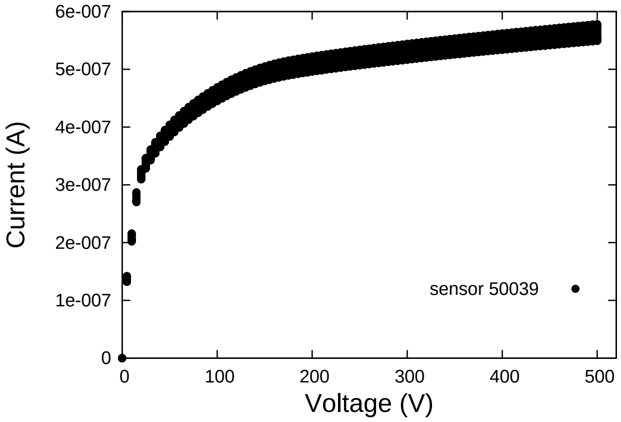

Figure 11.6: Leakage currents taken for sensor HPK-500 50039 as a test of repeatability. The 30 IV curves shown in the plot were taken during night, waiting 35 minutes between them.

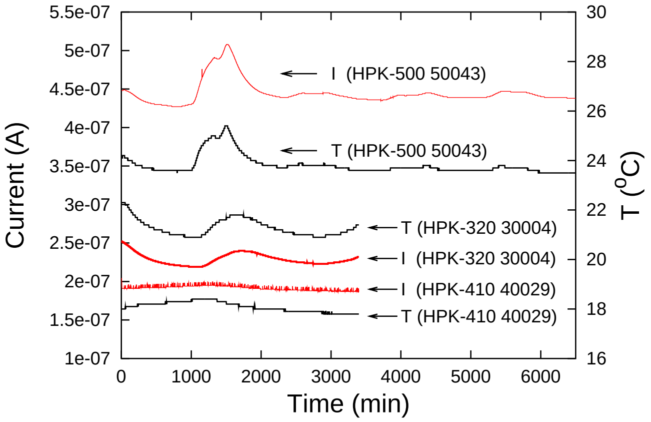

Figure 11.7: Current stability test for one sensor of each type. The sensors were biased at 450 V during between 58 and 110 hours. Drifts in current are fully correlated to ambient temperature (T).

ambient conditions.

### Depletion Voltage

The full depletion voltage determines the operation voltage of the sensors. Therefore, it is a very important information for module assembly, since sensors should be matched in depletion voltage when they are mounted on the same module. We estimated the full depletion voltage from the measurement of the bulk capacitance as a function of the applied bias voltage. The bulk capacitance of the sensor is the capacitance of all readout strips to the backplane. It is proportional to the inverse of the square root of the bias voltage applied to the sensor until full depletion is reached, and then assumes a constant value. We plot $1/C^2$ as a function of the bias voltage and estimate the depletion voltage as the intersection of two straight lines fitted to the rising part and the flat part of the curve, respectively.

The capacitance measurements were performed on all sensors, using a Keithley 487 unit as a voltage source and an HP 4192 LCR-meter to measure the capacitance between the bias line and the backplane. The CV curves were measured using a signal frequency of 1 kHz and a signal amplitude of 1 V. Figure 11.8 shows a typical curve of $1/C^2$ as a function of the bias voltage. The measurements performed by HPK are included to demonstrate the reproducibility of the data.

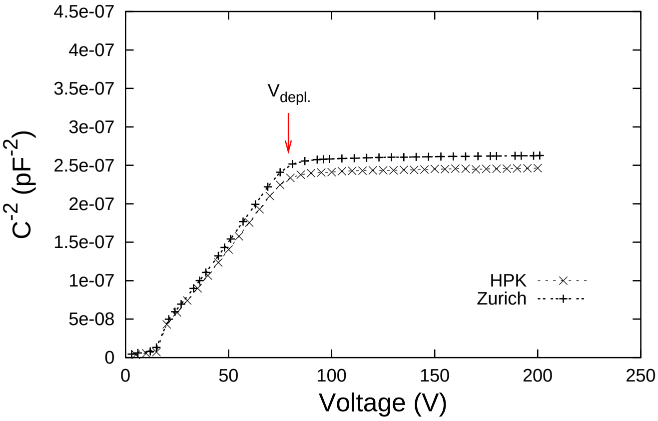

Figure 11.8: Determination of the full depletion voltage from the measurement of $1/C^2$ as a function of the bias voltage. The depletion voltage is determined as the intersection of two straight lines and is indicated by the arrow. Shown is a typical curve, corresponding to sensor HPK-410 40005. The curve measured by the vendor was added to show the reproducibility of the data.

Figure 11.9 shows the distribution of the full depletion voltages for all sensors. All HPK-320 and HPK-410 are between 70 and 140 V, and all HPK-500 deplete between 160 and 250 V, fulfilling the specifications.

In addition, we estimated the full depletion voltages for the HPK-320 and HPK-410 sensors using the method followed by HPK. In this method, the full depletion voltage is considered to be the voltage at which $1/C^2$ decreases by 4% with respect to its value in the *plateau*. In Figure 11.10, the results obtained using this method (method 2) are compared to those obtained from the intersection of two straight lines (method 1). The results using the two methods are in excellent agreement. A comparison between the full depletion voltages that we determined using method 2 and the data provided by HPK is shown in Figure 11.11. Very good agreement between both data sets can be observed.

### Tests with automatic probe station

The coupling capacitance is the capacitance between the strip implant and the read-out aluminium line. Its measurement allows to detect certain classes of bad strips, which are characterized by a metal open, a metal short or a

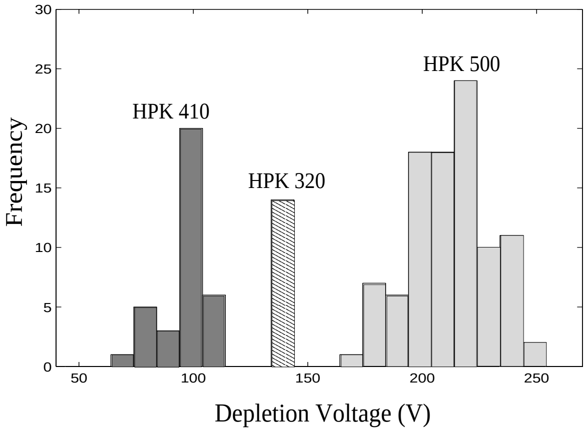

Figure 11.9: Distribution of the measured full depletion voltages. All HPK-320 and HPK-410 sensors deplete between 70 and 140 V, and all HPK-500 deplete between 160 and 250 V, fulfilling the specifications.

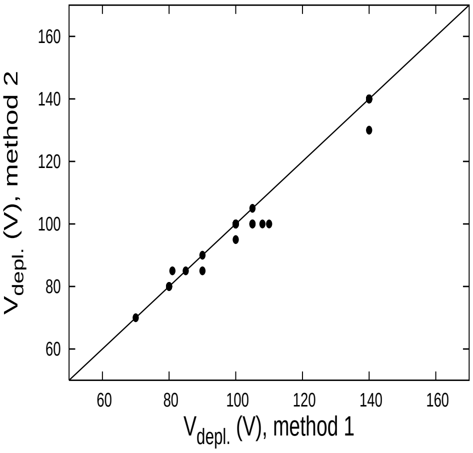

Figure 11.10: Comparison between the full depletion voltages estimated as the intersection of two straight lines (method 1) and as the voltage at which $1/C^2$ decreases by 4% with respect to its value in the *plateau* (method 2) for sensors HPK-320 and HPK-410.

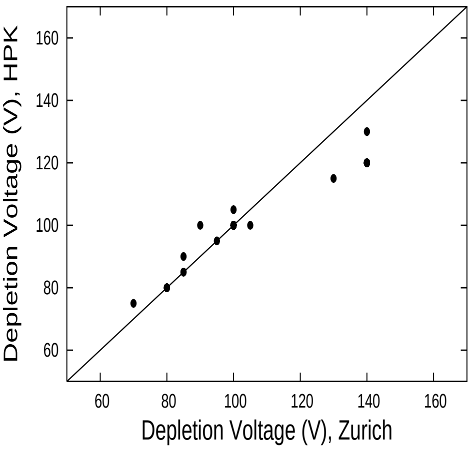

Figure 11.11: Comparison between the full depletion voltages measured by HPK and our measurements (using method 2) for sensors HPK-320 and HPK-410. Excellent agreement between both data sets is observed.

pinhole in the dielectric substrate of the coupling capacitor.

Coupling capacitance measurements were performed using an Electroglas 1034XA6 automatic probe station equipped with a probe card to simultaneously contact AC- and DC- pads on a given strip, and an HP 4192A LCR-meter. The probe station and the LCR-meter were controlled via GPIB bus by Labview programs running on a PC. The measurements were taken at a signal frequency of 1 kHz and a signal amplitude of 1 V [60].

The measurements were carried out on about 20% of the sensors and on the three lower-grade sensors provided by HPK. An example of the obtained coupling capacitance profiles is shown in Figure 11.12. One of the strips has coupling capacitors out of specification due to pinholes in the oxide. The bad channels observed in our coupling capacitor scans are listed in Table 11.7 together with the list of bad strips provided by HPK. Out of the total of 14080 inspected strips, four strips were flagged as bad by HPK as containing pinholes or having capacitance values out of specification. Out of these, we could detect three. We could not verify one strip flagged as pinhole. We did not find any bad strip in addition to those flagged as bad by HPK.

The number of defective strips is specified to be less than $< 1\%$ per sensor. All inspected sensors were below this number.

| Sensor ID | Bad strips (Zürich) | Bad strips (HPK) | |
|---|---|---|---|
| | | Pinholes | Bad Capacitor |
| 30002 | 196 | 196 | - |
| 40027 | - | 269 | - |
| 40037 (low-grade) | 321, 320 | - | 321, 320 |

Table 11.7: List of strips flagged as containing pinholes or capacitor values out of specification by HPK, and strips flagged as bad in our setup.

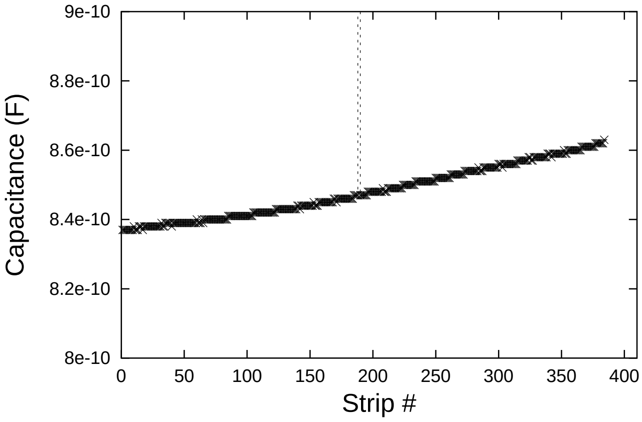

Figure 11.12: Coupling capacitance as a function of the strip number for sensor HPK-320 30002. Strip 196 has a coupling capacitance of 2 mF, which is out of specifications and lays out of the scale of this plot. This is a typical profile of the coupling capacitors across the sensor, which is likely to be related to process inhomogeneities.

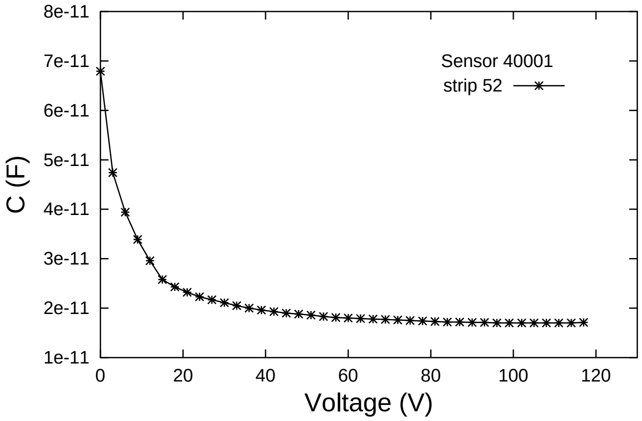

Figure 11.13: Total strip capacitance as a function of the bias voltage for one strip of sensor HPK-410 40001.

### Total strip capacitance

The total strip capacitance is here defined as the sum of the capacitance to the backplane and the capacitance to adjacent strips, measured at a signal frequency of 1 MHz [67]. The effect of the remaining strips was neglected in view of the large pitch of the sensors. The two closest neighbours were AC-coupled to the backplane. A sketch of the measurement setup can be seen in Figure 6.5.

The interest in these measurements lays in the fact that the total strip capacitance limits the achievable signal-to-noise ratio of a sensor connected to fast read-out electronics, since the Johnson noise from the load capacitance at the input of the pre-amplifier is the main contribution to the noise of the front-end amplifier.

Measurements of the total strip capacitance as a function of the bias voltage were carried out for six strips of two lower-grade HPK-410 sensors, and for two strips of the baby-detectors contained in two HPK-320 test-structures. Figure 11.13 shows an example of this dependance for one strip of sensor HPK-410 40001. The obtained capacitance values, at bias voltages above the full depletion voltage, are summarized in Table 11.8. The mean value was calculated for each sensor and the error assigned to it corresponds to the RMS of the individual measurements for this sensor.

| Sensor ID | Strip | $C$ (pF) | $\overline{C}$ (pF) | $\overline{C}$/L (pF/cm) |
|---|---|---|---|---|
| 40001 | # 1 | 16.6 | 16.8 ± 0.7 | 1.56 ± 0.06 |
| | # 2 | 17.6 | | |
| | # 3 | 15.6 | | |
| | # 4 | 16.7 | | |
| | # 5 | 17.3 | | |
| | # 6 | 17.1 | | |
| 40010 | # 1 | 16.3 | 17.2 ± 0.9 | 1.59 ± 0.08 |
| | # 2 | 17.2 | | |
| | # 3 | 17.3 | | |
| | # 4 | 17.2 | | |
| | # 5 | 16.4 | | |
| | # 6 | 18.8 | | |
| Test-structure 30012 | # 1 | 15.4 | 15.3 ± 0.2 | 1.42 ± 0.02 |
| | # 2 | 15.1 | | |
| Test-structure 30013 | # 1 | 16.1 | 15.6 ± 0.5 | 1.44 ± 0.05 |
| | # 2 | 15.1 | | |

Table 11.8: Total strip capacitance for two lower-grade HPK-410 sensors and for two baby-detectors contained in HPK-320 test-structures. The mean value of the capacitance on each sensor and the mean capacitance normalized by the strip length are included. The errors correspond to the RMS of the data.

### Metrology

Metrological measurements were performed on all sensors in order to determine the warp of the sensors and to verify the cutting line precision and parallelity, as well as other geometrical features on the sensors. We measured the diameter of the alignment marks on the sensors, the distance between them, the parallelity between edges, the width of the guard ring, bias ring and selected strips, the distance between the edges and the guard ring, bias ring and selected strips, the overall length and width of the sensor, the distance between consecutive strips, the parallelity between edges and strips, and flatness. The metrology grading procedure was based only on some of them: flatness, overall length and width of the sensor, distance between the edges and the strips, and parallelity between the edges and the strips. All sensors were mechanically classified as A grade. The parallelity and precision of the cut edges are important due to the proposed module assembly procedure [118], which exploits the accuracy of the dicing edge of the sensors for alignment purposes. In an assembly template, the sensors are pushed with their cut edges against positioning pins in order to align them with respect to each other and with respect to alignment pins in the module support.

According to the specifications, the sensor warp should be less than 50 $\mu$m, and the cutting line parallelity should be better than 10 $\mu$m for the HPK-320 and HPK-410 sensors [114, 115], and the sensor warp should be less than 100 $\mu$m, and the dicing accuracy at the level of 20 $\mu$m for the HPK-500 sensors [47].

Figure 11.14 shows the distribution of the measured overall width and length for sensors HPK-320 and HPK-410. On average, the sensors are 9 $\mu$m longer and 6 $\mu$m wider than the nominal dimensions, which is actually outside the given tolerances. The sensor-to-sensor variation in width is however small, with a RMS of 1 $\mu$m and a full range of less than 5 $\mu$m. Variations in length are slightly larger but since this dimension is not critical for the construction of the detectors, one can argue that the specifications were unnecessarily tight and all sensors were accepted.

Figure 11.15 shows the distribution of the measured parallelities between the sensor symmetry axis and a selected strip for sensors HPK-320 and HPK-410. For each sensor, the coordinates of ten points along each edge were measured. By fitting them to straight lines, the edges were reconstructed, and from these the symmetry axis was determined. The same procedure was repeated for the selected strip. The assigned parallelity is $L \tan\theta$, $L$ being length of the sensor edge and $\theta$ the angle between the reconstructed lines. The mean parallelity accuracy was determined to be $\sim 1$ $\mu$m.

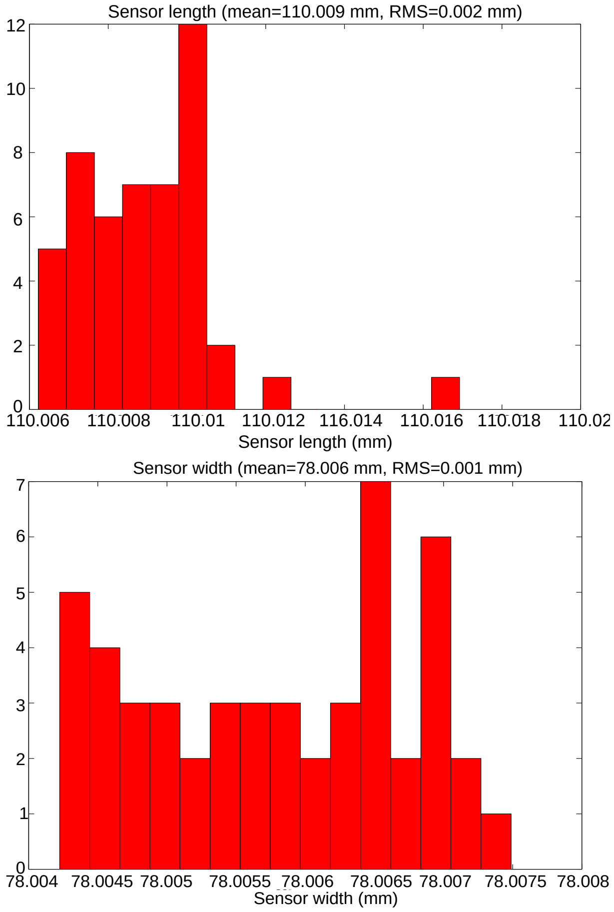

Figure 11.14: Distribution of the measured overall length (top) and width (bottom) for the 49 HPK-320 and HPK-410 sensors. The mean length is 110.009 mm, and the mean width is 78.006 mm. The standard deviation from sensor to sensor is better than 2 $\mu$m.

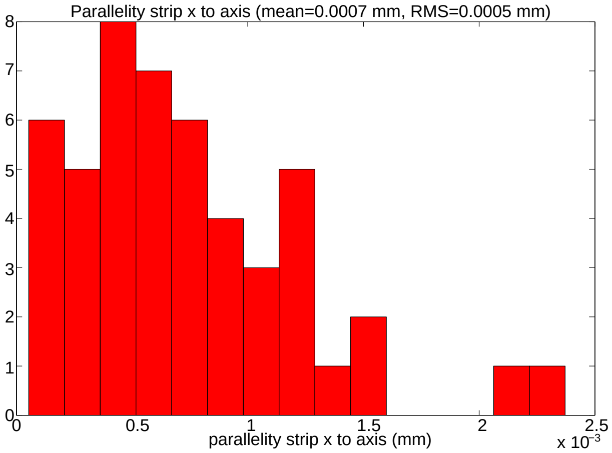

Figure 11.15: Distribution of the measured parallelities between the sensor axis and a selected strip for sensors HPK-320 and HPK-410. The mean parallelity accuracy was determined to be better 1 $\mu$m.

Same measurements were performed for the HPK-500 sensors. Figure 11.16 shows the distribution of the measured overall width and length for HPK-500 sensors. Each distribution shows two prominent peaks, that are caused by the two different measurement techniques that were here applied. Sensors falling in the right peak, i.e. having larger dimensions in width and length, were measured using a thru-light focusing, while the dimensions of the remaining sensors with smaller length and width were obtained by a incident light focusing. The nominal difference of 4 $\mu$m between the two peaks in the width distribution represents a systematic measurement uncertainty on the true dimension by using different focusing techniques and high magnification on an object with 500 $\mu$m thickness. In the thru-light measurement the sensor edges are projected onto the camera causing after focusing a sharp shadow, while in the incident light measurement only averaged space points along the depth profile are taken. Thus, the dimensions in the tru-light measurement are typically 4 $\mu$m larger than in the incident light measurement.

The reason why the two techniques differ in the length distribution by 10 $\mu$m is not intrinsic to the sensors but caused by a non-parallelity of the thru-light in that direction.

Figure 11.17 shows the distribution of the measured parallelities between the sensor symmetry axis and a selected strip for sensors HPK-500. The parallelity accuracy was determined to be better than 1 $\mu$m.

The flatness of the sensors was determined by measuring a profile of the

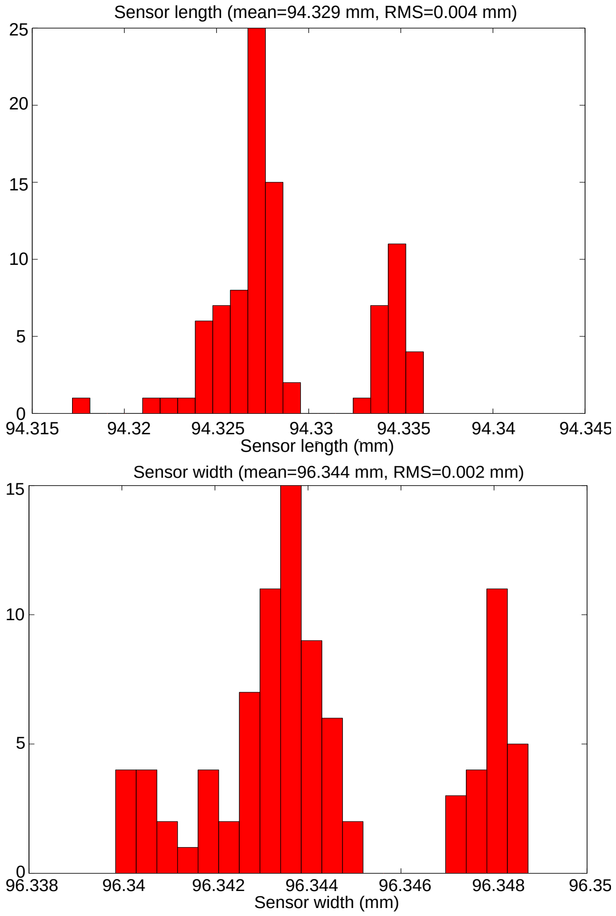

Figure 11.16: Distribution of the measured overall length (top) and width (bottom) for the 98 HPK-500 sensors. The mean length is 94.329 mm, and the mean width is 96.344 mm. The standard deviation from sensor to sensor is better than 4 $\mu$m.

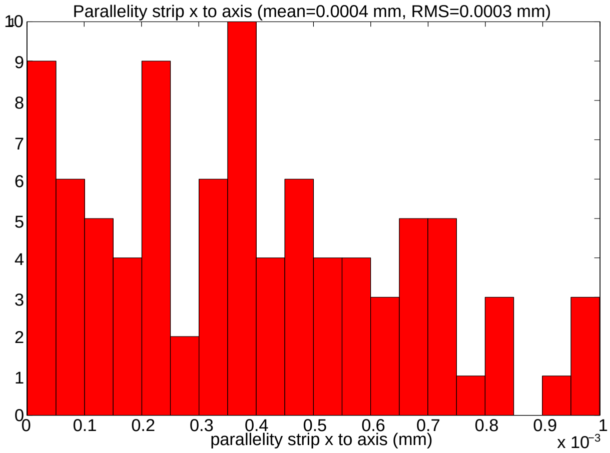

Figure 11.17: Distribution of the measured parallelities between the sensor axis and a selected strip for sensors HPK-500. The parallelity accuracy was determined to be better than 1 $\mu$m.

surface height of the sensor laying freely on a flat surface, with the strip side facing upwards. On each sensor, $z$-coordinates have been recorded on an equidistant grid of $6 \times 6$ points covering the full surface of the sensor. Typical examples of the obtained profiles for each type of sensors are shown in Figure 11.18. It shows a characteristic sensor deflection of 75 $\mu$m for the HPK-320 sensors, a deflection of 55 $\mu$m for the HPK-410 sensors, and of 50 $\mu$m for the HPK-500 sensors over the full surface. The distribution of the measured warp for all inspected sensors is shown in Figure 11.19. The mean warp was determined to be $\sim$ 85 $\mu$m for the HPK-320 sensors, $\sim$ 40 $\mu$m for the HPK-410 sensors, and $\sim$ 56 $\mu$m for the HPK-500. The maximum measured warp was 95 $\mu$m for the HPK-320 sensors, 60 $\mu$m for the HPK-410 sensors, and 67 $\mu$m for the HPK-500 sensors. The warp values for the HPK-320 and HPK-410 sensors are outside the specifications, but this seems to be not a problem. Although more mechanical strain is induced on the sensors when the modules are built, it was demonstrated that this had no effect on the leakage currents.

### Overall sensor grading

Depending on the results of the tests described above, an overall grading was assigned to each sensor. The sensors are classified according to the following criteria:

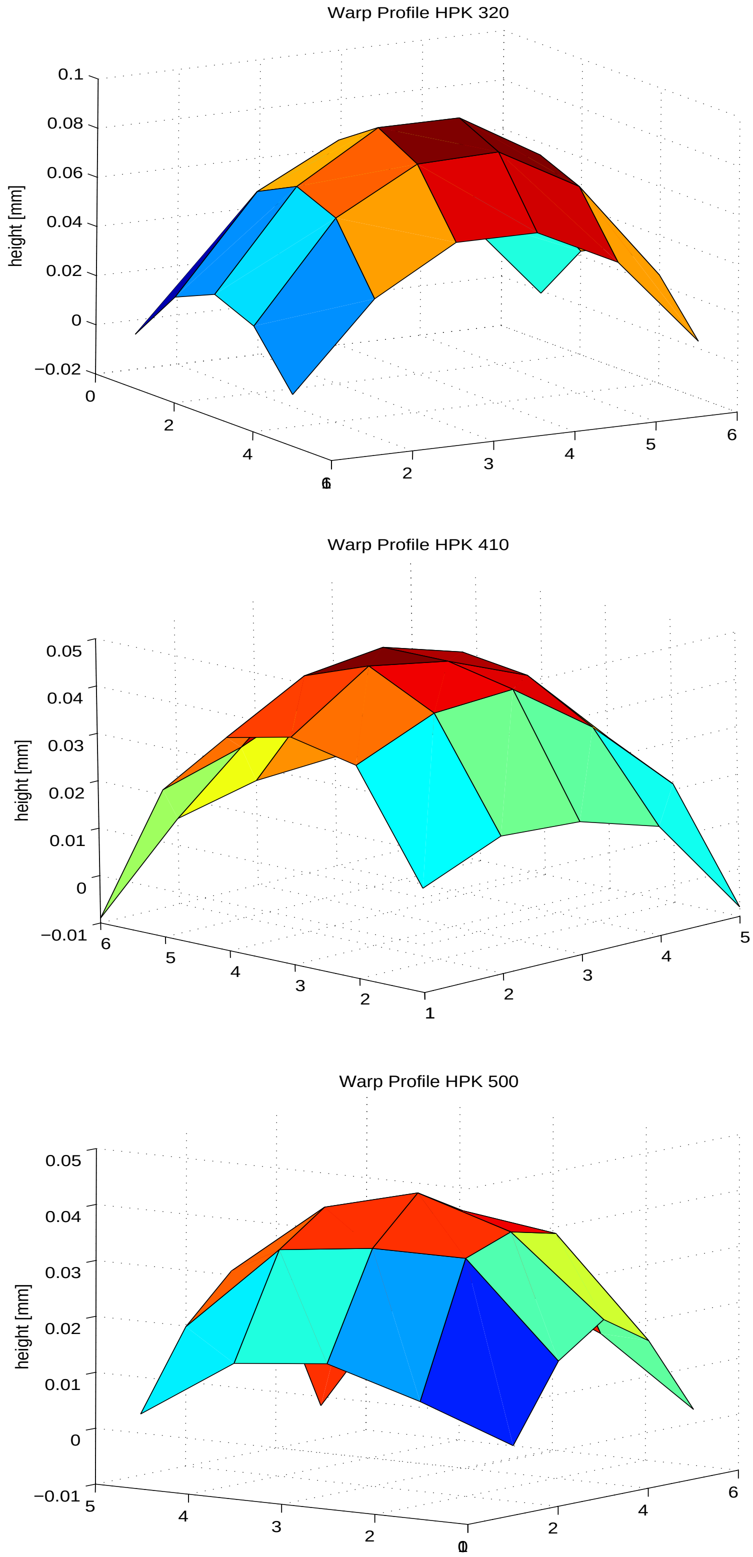

Figure 11.18: The $z$-profile of a sensor of each type is shown. The measured points are connected by surface grid lines. The $z$-coordinates were recorded on an equidistant grid of $6 \times 6$ points covering the full surface of the sensor.

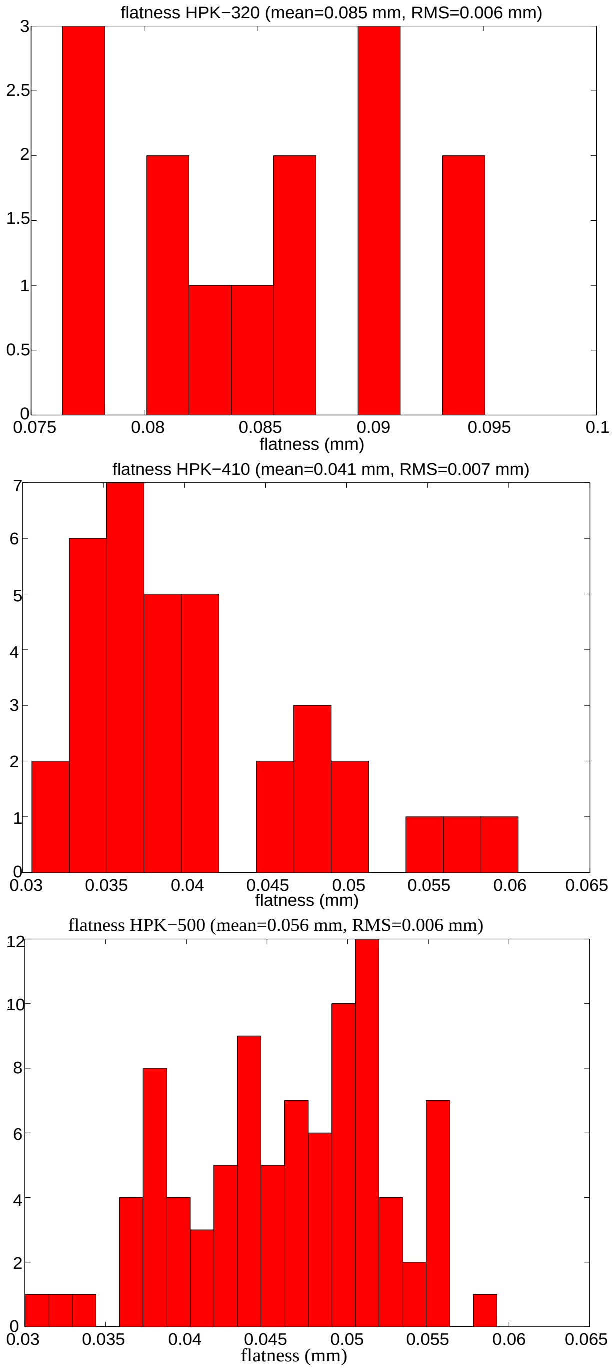

Figure 11.19: Distribution of the measured flatness on the HPK-320 sensors (top), on the HPK-410 sensors (middle), and on the HPK-500 sensors (bottom).

| Overall Grade | Number of sensors | | |
|---|---|---|---|
| | HPK-320 | HPK-410 | HPK-500 |
| A | 13 | 33 | 95 |
| B | 1 | 2 | 2 |
| C | - | - | 0 |
| X | - | - | 1 |

Table 11.9: Number of sensors according to the overall inspection grade.

- Grade-A: good sensors, graded as A or B in the visual inspection, and leakage currents $I < 1$ $\mu$A at $V_{depl} + 100$ V, and less than two bad strips per sensor, and graded as A in the metrology tests.
- Grade-B: medium sensors, graded as B or C in the visual inspection, and leakage currents $I < 1$ $\mu$A at $V_{depl} + 100$ V, or between 2 and 3 bad strips per sensor, and graded as A in the metrology tests.
- Grade-C: poor sensors, graded as C in the visual inspection, or leakage currents $I \geq 1$ $\mu$A at $V_{depl} + 100$ V, or more than 3 bad strips per sensor, or graded as B in the metrology tests.
- Grade-X: destroyed.

Grade-A sensors should be used in the inner parts of the detector where particle densities are highest, whilst grade-B sensors could be used for the outer parts of the detector or as spares. Grade-C sensors should not be used, neither for the detector nor as spare. Concerning metrology measurements, leakage currents and number of bad strips, all tested sensors fulfill the requirements of grade A. After a re-evaluation of the visual grading, five out of the 147 IT tested sensors were given an overall grade B, whereas all other sensors were classified as grade A. No sensor was classified as grade C and one sensor was destroyed. The number of sensors according to the overall grading is shown in Table 11.9.

### 11.2.3 Database and web page

All information from sensor probing of both the IT and TT sensors is stored in a mySQL-based [119] database. A web based query is used, with a PHP-interface [120]. It allows to store, query, and retrieve vendor and testing information on the sensors, and is used to track or select components during

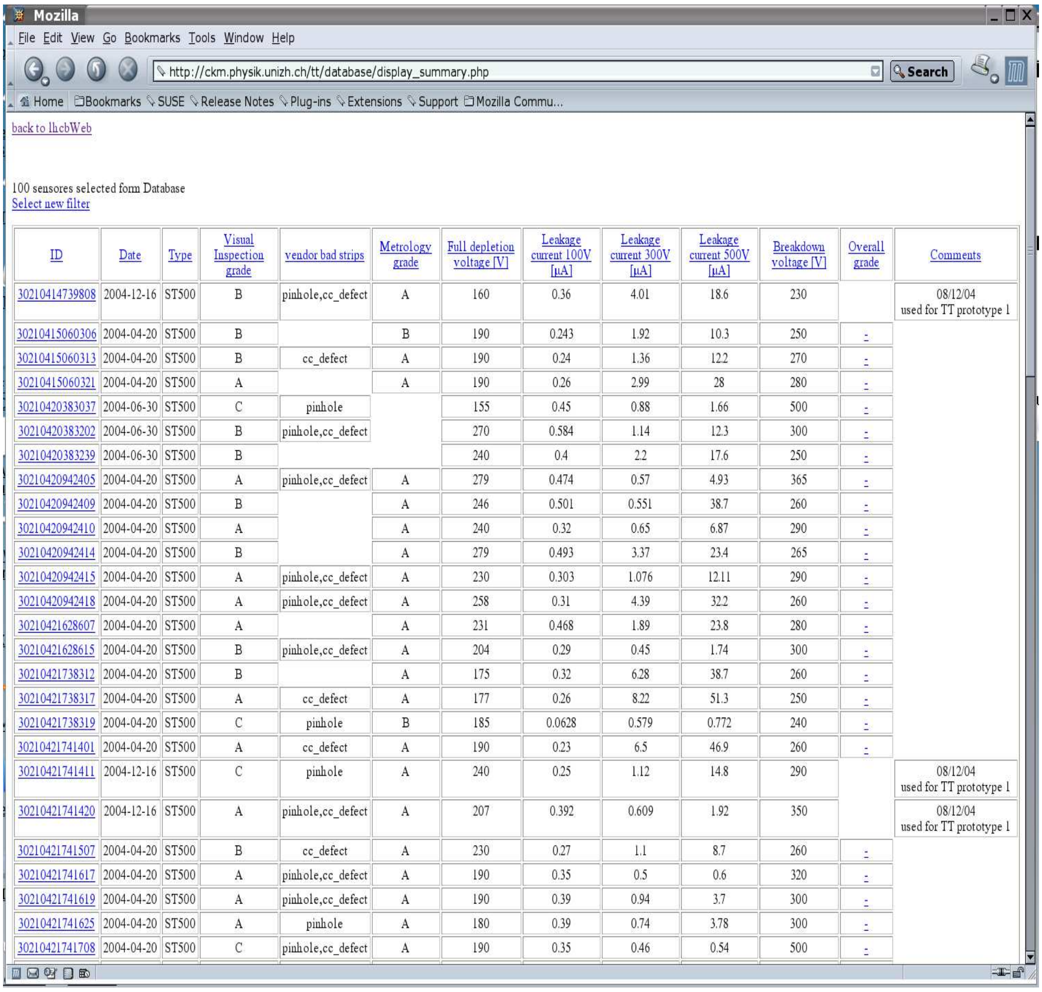

back to lhcbWeb

100 sensores selected form Database
Select new filter

| ID | Date | Type | Visual Inspection grade | vendor bad strips | Metrology grade | Full depletion voltage [V] | Leakage current 100V [µA] | Leakage current 300V [µA] | Leakage current 500V [µA] | Breakdown voltage [V] | Overall grade | Comments |
|---|---|---|---|---|---|---|---|---|---|---|---|---|
| 30210414739808 | 2004-12-16 | ST500 | B | pinhole,cc_defect | A | 160 | 0.36 | 4.01 | 18.6 | 230 | | 08/12/04<br>used for TT prototype 1 |
| 30210415060306 | 2004-04-20 | ST500 | B | | B | 190 | 0.243 | 1.92 | 10.3 | 250 | - | |
| 30210415060313 | 2004-04-20 | ST500 | B | cc_defect | A | 190 | 0.24 | 1.36 | 12.2 | 270 | - | |
| 30210415060321 | 2004-04-20 | ST500 | A | | A | 190 | 0.26 | 2.99 | 28 | 280 | - | |
| 30210420383037 | 2004-06-30 | ST500 | C | pinhole | | 155 | 0.45 | 0.88 | 1.66 | 500 | - | |
| 30210420383202 | 2004-06-30 | ST500 | B | pinhole,cc_defect | | 270 | 0.584 | 1.14 | 12.3 | 300 | - | |
| 30210420383239 | 2004-06-30 | ST500 | B | | | 240 | 0.4 | 2.2 | 17.6 | 250 | - | |
| 30210420942405 | 2004-04-20 | ST500 | A | pinhole,cc_defect | A | 279 | 0.474 | 0.57 | 4.93 | 365 | - | |
| 30210420942409 | 2004-04-20 | ST500 | B | | A | 246 | 0.501 | 0.551 | 38.7 | 260 | - | |
| 30210420942410 | 2004-04-20 | ST500 | A | | A | 240 | 0.32 | 0.65 | 6.87 | 290 | - | |
| 30210420942414 | 2004-04-20 | ST500 | B | | A | 279 | 0.493 | 3.37 | 23.4 | 265 | - | |
| 30210420942415 | 2004-04-20 | ST500 | A | pinhole,cc_defect | A | 230 | 0.303 | 1.076 | 12.11 | 290 | - | |
| 30210420942418 | 2004-04-20 | ST500 | A | pinhole,cc_defect | A | 258 | 0.31 | 4.39 | 32.2 | 260 | - | |
| 30210421628607 | 2004-04-20 | ST500 | A | | A | 231 | 0.468 | 1.89 | 23.8 | 280 | - | |
| 30210421628615 | 2004-04-20 | ST500 | B | pinhole,cc_defect | A | 204 | 0.29 | 0.45 | 1.74 | 300 | - | |
| 30210421738312 | 2004-04-20 | ST500 | B | | A | 175 | 0.32 | 6.28 | 38.7 | 260 | - | |
| 30210421738317 | 2004-04-20 | ST500 | A | cc_defect | A | 177 | 0.26 | 8.22 | 51.3 | 250 | - | |
| 30210421738319 | 2004-04-20 | ST500 | C | pinhole | B | 185 | 0.0628 | 0.579 | 0.772 | 240 | - | |
| 30210421741401 | 2004-04-20 | ST500 | A | cc_defect | A | 190 | 0.23 | 6.5 | 46.9 | 260 | - | |
| 30210421741411 | 2004-12-16 | ST500 | C | pinhole | A | 240 | 0.25 | 1.12 | 14.8 | 290 | | 08/12/04<br>used for TT prototype 1 |
| 30210421741420 | 2004-12-16 | ST500 | A | pinhole,cc_defect | A | 207 | 0.392 | 0.609 | 1.92 | 350 | | 08/12/04<br>used for TT prototype 1 |
| 30210421741507 | 2004-04-20 | ST500 | B | cc_defect | A | 230 | 0.27 | 1.1 | 8.7 | 260 | - | |
| 30210421741617 | 2004-04-20 | ST500 | A | pinhole,cc_defect | A | 190 | 0.35 | 0.5 | 0.6 | 320 | - | |
| 30210421741619 | 2004-04-20 | ST500 | A | pinhole,cc_defect | A | 190 | 0.39 | 0.94 | 3.7 | 300 | - | |
| 30210421741625 | 2004-04-20 | ST500 | A | pinhole | A | 180 | 0.39 | 0.74 | 3.78 | 300 | - | |
| 30210421741708 | 2004-04-20 | ST500 | C | pinhole,cc_defect | A | 190 | 0.35 | 0.46 | 0.54 | 500 | - | |

Figure 11.20: Screen-shot of the graphical user interface.

module construction. A screen-shot of the graphical user interface is shown in Figure 11.20. Shown is a summary of measurements and gradings, together with comments for some of the sensors. Further details can be found in [121].

## 11.3 Conclusions

We have presented the results of sensor qualification for the pre-series production for the IT and the first batch of production sensors for the TT station, all produced by HPK. Our main results are the following:

- Visual inspection over all sensors was performed in order to detect macroscopic defects like scratches, chipped edges, pad contamination, as well as to check the cleanliness of the sensor. About 80% of the sensors were found to be free of defects, and all sensors were judged to be usable for detector production.
- Leakage current measurements were performed on all sensors. Currents were found to be very small, typically below 500 nA at 500 V, and very similar from sensor to sensor. All sensors fulfill the leakage current specifications. None of the sensors evidenced breakdown below 500 V. Furthermore, the currents were found not to depend on the application of vacuum to the chuck of the probe station and were repeatable and stable over time of operation, as was verified on a sample of 15% of the sensor that were chosen randomly.
- Depletion voltages were measured for all sensors. All HPK-320 and HPK-410 show full depletion voltages in the range of 70-140 V, and all HPK-500 deplete between 165 and 250, fulfilling the specifications.
- Coupling capacitance measurements were performed on 20% of the sensors using an automatic probe station. Out of the total of 14080 inspected strips, four strips were flagged as bad by HPK as containing pinholes or having capacitance values out of specification. Out of these, we could detect three. We could not verify one strip flagged as pinhole. We did not find any additional bad strip.
- Metrological measurements were performed on all sensors in order to determine the cutting line precision and parallelity, and the warp of the sensors, as well as other geometrical features. The mean warp was determined to be 85 $\mu$m for the HPK-320 sensors, 41 $\mu$m for the HPK-410 sensors and 56 $\mu$m for the HPK-500 sensors. The mean parallelity was determined to be better than 1 $\mu$m for all three types. For the HPK-320 and HPK-410 sensors, the mean values of the sensor outer dimensions are within 9 $\mu$m of the nominal values, and the standard deviation from sensor to sensor is better than 2 $\mu$m. For the HPK-500 sensors, the mean values of the sensor outer dimensions are within 3 $\mu$m of the nominal values. The standard deviation from sensor to sensor is better than 4 $\mu$m.
- According to the overall grading,five out of the 147 tested sensors were classified an grade B, whereas all other sensors were classified as grade A. No sensor was classified as grade C and one sensor was destroyed.

All sensors have been qualified, and both the IT and TT module production are taking place.

# Conclusions

The work presented in this thesis has been an effort to contribute to the understanding of silicon microstrip detector properties, in order to render its utilization possible by the LHCb experiment. Although silicon detectors have been successfully used for precision vertexing at several accelerator experiments in the last decade,[4] their implementation for a large-surface tracker has required to carry out specific and detailed studies, not only to confirm that their proposed use at the LHC is indeed viable, but also to help the actual implementation by providing knowledge of its main limiting performance parameters.

Several tests on silicon microstrip detectors for the Silicon Tracker [5] have been presented, starting from the characterization of different prototypes up to the final tests on the detectors that are being installed at CERN.

Three groups of prototype sensors, with thicknesses 320, 410, and 500 $\mu$m, respectively, and with strip pitches of approximately 200 $\mu$m were characterized as part of the studies carried out by the Silicon Tracker group for the optimization of the sensor geometry, to guarantee efficient and reliable operation of the detector. In this respect, the first step was a rather exhaustive electrical characterization of all prototype sensors, which has been presented in Chapter 6. The best sensors from each group, mainly according to the results on leakage currents and breakdown voltages, were selected to build modules with strips up to 33 cm in length.

These modules were tested in a laser test-stand and in a test-beam, as it was explained in Chapters 8 and 9, respectively. In order to determine their working points, bias voltage scans were performed for all modules. Results

---

[4] Including LEP, CESR, PEP, KEK, and Tevatron Collider.

[5] The Silicon Tracker group is formed by about 50 researchers from six institutes: Max Plank Institut für Kernphysik, Heidelberg; Kiev Institute for Nuclear Research; Laboratoire de Physique des Hautes Energies, Lausanne; Budker Institute for Nuclear Physics, Novosibirsk; Universidade de Santiago de Compostela; Physik-Institut der Universität Zürich.

showed that they reach a *plateau* at $2 - 2.5$ times the depletion voltage. Signal shape characteristics were studied, and it was seen that signal shapes meeting the specifications of less than 50% remainder (fraction of the signal left in the following bunch crossing) for the TT station and less than 30% remainder for the IT stations can be obtained if the shaping time parameter is appropiately set.

The laser test-stand allowed a fast characterization of the module performance, although it was seen that, for future measurements with the laser setup, the time stability of the pulse-height needed to be improved. The test-beam measurements permitted to investigate in addition the signal-to-noise ($S/N$) ratio, resolution, efficiency and noise rate of the prototype modules. A sizeable loss of the collected charge was observed in the region between two readout strips for all the prototypes. The minimization of this effect had to be taken into account for the final choice of the detector parameters, so that full hit detection efficiencies will be ensured for all IT and TT stations. It is clear from the measurements presented here that 320 $\mu$m silicon does not give sufficiently high $S/N$ to give full detection efficiency for modules with strips 33 cm long. It therefore was decided that modules with a thickness of at least 410 $\mu$m should be used in the TT station. The final choice of sensor thickness for the TT station was based on these results together with simulation studies, and it was finally chosen to be 500 $\mu$m. For the Inner Tracker, two sensor thicknesses were selected: 320 $\mu$m silicon for the 11 cm long modules, and 410 $\mu$m silicon for the 22 cm long modules.

Modules will be built at room temperature but they will be operated below 5°C. Different thermal expansion coefficients of the materials used in the construction of the modules will give rise to mechanical stress. In Chapter 7, we presented results of thermal and thermo-mechanical measurements on a test module. It was seen how the structure formed by the silicon sensors, their mechanical support and the hybrids react to temperature variations, demonstrating that no significant deformations are expected. In addition, the heat profile produced by the readout chips along the half-module was determined. It was shown that the cooling system removes the heat efficiently, and therefore no dramatic effects on the detector performance are expected. It was also shown that the heat is transported by the surrounding air and not by the carbon fiber rails.

Particularly important is the issue of radiation hardness and long-term damage of the sensors in the Silicon Tracker, given the fact that it will cover the low angle region with respect to the LHC colliding beams. As shown in Chapter 10, we have performed an irradiation study on three LHCb IT prototype sensors and one CMS test-structure, which were exposed to 24 GeV/c protons up to fluences of $1.9 \times 10^{13}$ p/cm$^2$ and $6.3 \times 10^{13}$ p/cm$^2$, equivalent to 7 years or 20 years of operation in the innermost part of the Inner Tracker, respectively. The standard annealing scheme of 80 min at 60°C was followed. The proton fluence was obtained from aluminium foils activation measurements. It was found that the sensors fully depleted at about 50 V after the irradiation to the lower fluence. This depletion voltage is lower than the initial and gives ample safety margin to sufficiently overbias the sensors. The current related damage constant and the hardness factor for 24 GeV protons were extracted from the leakage current measurements and were determined to be $\alpha = 2.78 \times 10^{-17}$ A/cm and $k_\alpha = 0.61$, respectively. Inter-strip capacitances and coupling capacitances remain essentially unchanged after irradiation. The total strip capacitances for the sensors irradiated to the higher fluence showed an increase of about 15% compared to unirradiated sensors. No significant increase was observed after the lower fluence.

A comprehensive measurement program carried out on prototype modules constructed with the irradiated sensors has been reported in Chapter 10. A detailed study of the charge collection after irradiation has been performed and it has been found that the model presented in [106] gives a reasonable parameterization of the data. However, due to the modest radiation dose compared to those investigated in [106] the results are sensitive to other effects, such as ballistic deficits due to the fast shaping time of the pre-amplifier. Despite this, the depletion voltages extracted from the fit, after allowing for reverse annealing, are in agreement with the *C-V* measurements. A study of the dependence of the sensors leakage current as a function of temperature has been made, and was found to follow the expected exponential dependence. Pulse shape scans were performed for the irradiated modules. These measurements were useful in gaining experience with the handling of irradiated sensors. In particular, it has been learnt that care must be taken with respect to storage between measurement periods else sizeable annealing can occur. It has been shown that a stable and robust long-term operation in the expected radiation environment can be achieved over the lifetime of the experiment.

In Chapter 11 we have presented the quality assurance program for the ST silicon sensors and the results for the pre-series production for the IT and the first batch of production sensors for the TT station, all produced by Hamamatsu Photonics (HPK). The results for these sensors are very satisfactory. Visual inspection over all sensors was performed in order to detect macroscopic defects. About 80% of the sensors were found to be free of defects, and all sensors were judged to be usable for detector production. Leakage current measurements were performed on all sensors. Currents were found to be very small, typically below 500 nA at 500 V, and very similar from sensor to sensor. All sensors fulfill the leakage current specifications, and none of them evidenced breakdown below 500 V. Furthermore, the currents were found not to depend on the application of vacuum to the chuck of the probe station and were repeatable and stable over time of operation. Full depletion voltages were measured for all sensors. All HPK-320 and HPK-410 deplete between 70 and 140 V, and all HPK-500 deplete between 165 and 250, fulfilling the specifications. Coupling capacitance measurements were performed on 20% of the sensors using an automatic probe station. Out of the 14080 inspected strips, three were found to have pinholes, in accordance with the HPK previous measurements. Metrological measurements were performed on all sensors in order to determine the cutting line precision and parallelity, and the warp of the sensors, as well as other geometrical features, important for the spatial resolution as well as for the assembly procedures. Sensors were finally classified according to an overall grading, which determined their use in the inner parts of the detector, with highest particle densities, or in other parts. All sensors passed the acceptance criteria and can be used for module production.

The results presented in this thesis show that the construction of a low angle large-surface tracker can be accomplished with the required occupancy and efficiency, for measurement of $b$-quark decays from the 14 TeV LHC proton collisions. The understanding of the measurements presented and discussed here have contributed to the final choice of detector parameters and assembly procedures for the LHCb Silicon Tracker. Module production has already started for both the IT and TT stations at CERN (by Lausanne and Santiago groups) and Zürich, respectively. Sensor qualification for module production continues, and full tracker assembly is expected to be completed by the end of 2006.

# List of publications

- G. Baumann *et al. Sensor Qualification for the Trigger Tracker of LHCb.* LHCb note 2005-089 (to be published).
- G. Baumann *et al. Pre-Series Sensor Qualification for the Inner Tracker of LHCb.* LHCb note 2005-037.
- C. Lois. *Silicon sensor probing and radiation studies for the LHCb Silicon Tracker.* Nucl. Inst. and Meth. A, 2006 (accepted for publication), also available as LHCb note 2005-033.
- F. Lehner, C. Lois, M. Pangilinan, and M. Siegler. *Mechanical and Thermal Characterisation of a TT Half-Module Prototype.* LHCb note 2005-007.
- C. Lois, R. Bernhard, M. Needham, A. Vollhardt, and A. Wenger. *Laboratory Measurements on Irradiated Prototype Ladders for the LHCb Inner Tracker.* LHCb note 2004-112.
- M. Agari *et al. Testbeam Measurements on an Irradiated Prototype Ladder for the LHCb Inner Tracker.* LHCb note 2004-111 (to be published).
- G. Baumann *et al. Quality Assurance of 100 CMS-OB2 Sensors.* LHCb note 2004-105.
- F. Lehner, C. Lois, and H. Voss. *Measurements on irradiated silicon sensor prototypes for the Inner Tracker of LHCb.* LHCb note 2004-104.
- M. Agari *et al. Measurements of a prototype ladder for the TT station in a 120 Gev/c* $\pi^-$ *beam.* LHCb note 2004-103.
- M. Agari *et al. Test-beam measurements on prototype ladders for the LHCb TT station and Inner Tracker.* LHCb note 2003-082.
- J. Gassner, St. Heule, F. Lehner, and C. Lois. *Capacitance measurements on silicon micro-strip detectors for the TT station of the LHCb experiment.* LHCb note 2003-081.

- R. P. Bernhard, C. Lois, St. Heule, M. Needham, A. Vollhardt, and D. Volyanskyy. *Measurements of Prototype Ladders for the Silicon Tracker with a Laser.* LHCb note 2003-075.

# Bibliography

[1] P. A. M. Dirac. *The Quantum Theory of the Electron.* Royal Society of London Proceedings Series A **117** (1928) 610.

[2] P. A. M. Dirac. *The Quantum Theory of the Electron. Part II.* Royal Society of London Proceedings Series A **118** (1928) 351.

[3] B. Winstein and L. Wolfenstein. *The search for direct CP violation.* Rev. Mod. Phys. **65** (1993) 1113.

[4] R. G. Sachs. *Time Reversal.* Science **176** (1972).

[5] C. S. Wu, E. Ambler, R. W. Hayward, D. D. Hoppes, and R. P. Hudson. *Experimental Test of Parity Conservation in Beta Decay.* Phys. Rev. **105** (1957) 1413.

[6] T. D. Lee and C. N. Yang. *Question of Parity Conservation in Weak Interactions.* Phys. Rev. **104** (1956) 254.

[7] J. H. Christenson, J. W. Cronin, V. L. Fitch, and R. Turlay. *Evidence for the* $2\pi$ *decay of the* $\mathrm{K}_2^0$ *meson.* Phys. Rev. Lett. **13** (1964) 4 138.

[8] S. Eidelman *et al.* *Review of Particle Physics.* Physics Letters B **592** (2004) 1. `http://pdg.lbl.gov`.

[9] A. D. Sakharov. Sov. Phys. JETP Lett. **5** (1967) 24.

[10] N. Cabibbo. Phys. Rev. Lett. **10** (1963) 531.

[11] M. Kobayashi and T. Maskawa. Prog. Teor. Phys. **49** (1973) 652.

[12] L. de Broglie. *Recherches sur la théorie des quanta.* Ph.D. thesis, Faculté des Sciences de Paris (1924).

[13] A. Einstein. Ann. Phys. (Leipzig) **17** (1905) 891.

[14] `http://lhc.web.cern.ch/lhc/`.

[15] `http://www.cern.ch`.

[16] S. Amato et al. *LHCb Technical Proposal.* CERN-LHCC-98-4 (1998).

[17] `http://lhcb.web.cern.ch`.

[18] LHCb collaboration. *LHCb Outer Tracker Technical Design Report.* CERN/LHCC 2001-024.

[19] LHCb collaboration. *LHCb Inner Tracker Technical Design Report.* CERN/LHCC 2002-029.

[20] LHCb collaboration. *LHCb Technical Design Report, Reoptimized Detector Design and Performance.* CERN/LHCC 2003-030.

[21] U. Straumann. *Research plan for LHCb.* `http://www.physik.unizh.ch/~strauman/nf05.pdf`.

[22] I. I. Bigi and A. I. Sanda. *CP Violation* (Cambridge University Press, 2000).

[23] G. Castelo Branco, L. Lavoura, and J. P. Silva. *CP Violation* (Oxford Science Publications, 1999).

[24] L. Wolfstein. Phys. Rev. Lett. **51** (1983) 1945.

[25] Kazuo Abe. *CP violation in B mesons.* Presented at the LEPTON-PHOTON 2005, Uppsala (Sweden), July 2005.

[26] Belle Collaboration (K. F. Chen *et al.*). *Time-Dependent CP-Violating Asymmetries in* $b \to s\bar{q}q$ *Transitions.* Phys. Rev. D **72** (2005).

[27] G. Sciolla (BaBar Collaboration). *Recent measurements of sin(2beta) at BaBar* (2005). Proc. $10^{th}$ International Conference on B Physics at Hadron Machines (BEAUTY 2005), Assisi, Italy, June 2005, `hep-ex/0509022`.

[28] B. Aubert *et al.* (BaBar Collaboration). *Measurement of CP asymmetries in* $\mathrm{B}^0 \to \phi\mathrm{K}^0$ *and* $\mathrm{B}^0 \to \mathrm{K}^+\mathrm{K}^-\mathrm{K}^0_\mathrm{S}$ *decays.* Phys. Rev. D **71** (2005).

[29] B. Aubert *et al.* (BaBar Collaboration). *Measurement of the Time-Dependent CP Asymmetries in the* $\mathrm{B}^0 \to \phi\mathrm{K}^0$ *decay.* Phys. Rev. Lett. **93** (2004).

[30] B. Aubert *et al.* (BaBar Collaboration). *Branching Fractions and CP Asymmetries in* $\mathrm{B}^0 \to \mathrm{K}^+\mathrm{K}^-\mathrm{K}^0_\mathrm{S}$ *and* $\mathrm{B}^0 \to \mathrm{K}^0_\mathrm{S}\mathrm{K}^0_\mathrm{S}\mathrm{K}^0_\mathrm{S}$. Phys. Rev. Lett. **93** (2004).

[31] B. Aubert *et al.* (BaBar Collaboration). *Measurement of Time-Dependent CP-Violating Asymmetries in* $\mathrm{B}^0$ *Meson Decays to* $\eta'\mathrm{K}^0$ (2004). `hep-ex/0408090`.

[32] B. Adeva, private communication.

[33] R. Forty. *Status of the LHCb experiment.* Proc. Hadron Collider Physics Symposium (HCP05), Les Diablerets, Switzerland, July 4-9, 2005.

[34] J. Bernabeu. Nucl. Phys. Proc. Suppl. **120** (2003) 332. Proc. $8^{th}$ International conference on B-physics at Hadron machines (BEAUTY 2002), Santiago de Compostela, Spain, June 2002.

[35] S. Barsuk. *The LHCb experiment: status and expected physics performance.* LHCb note 2005-068.

[36] G. Raven. *Sensitivity Studies of* $\chi$ *and* $\Delta\Gamma$ *with* $\mathrm{B_s} \to \mathrm{J}/\psi(\mu^+\mu^-)\phi(\mathrm{K}^+\mathrm{K}^-)$. LHCb note 2003-119.

[37] R. Aleksan, I. Dunietz, and B. Kayser. Z. Phys. C **54** (1992) 653.

[38] R. Fleischer. Phys. Lett. B **459** (1999) 306.

[39] M. Gronau and D. Wyler. *On determining a weak phase from CP asymmetries in charged B decays.* Phys. Lett. B **265** (1991) 172.

[40] M. Battaglia *et al. The CKM Matrix and the Unitarity Triangle* (2003). `arXiv:hep-ph/0304132`.

[41] LHCb collaboration. *LHCb Vertex Locator Technical Design Report.* CERN/LHCC 2001-011.

[42] M. Needham. *Status and expected performance of the LHCb tracking system.* LHCb note 2005-059.

[43] J. Gassner, M. Needham, and O. Steinkamp. *Layout and Expected Performance of the LHCb TT Station.* LHCb note 2003-140.

[44] O. Steinkamp. *Silicon strip detectors for the LHCb experiment.* Nucl. Instr. and Meth. A **541** (2005) 83.

[45] N. van Bakel *et al.* *The Beetle Reference manual –chip version 1.3, 1.4, 1.5.* LHCb note 2004.

[46] Achim Vollhardt. *An Optical Readout System for the LHCb Silicon Tracker.* Ph.D. thesis, University of Zurich (2005).

[47] J.-L. Agram *et al.* *The Silicon Sensors for the Compact Muon Solenoid Tracker - Design and Qualification Procedure* (2003). CMS note 2003/015.

[48] Gerhard Lutz. *Semiconductor Radiation Detectors* (Springer, 1999).

[49] S. M. Sze. *Semiconductor Devices, Physics and Technology* (John Willey and Sons, 1985).

[50] A. Peisert. *Silicon Microstrip Detectors* (F. Sauli ed., World Scientific, 1992).

[51] H. Dijkstra. *Overview of silicon detectors.* Nucl. Inst. and Meth. A **478** (2002) 37.

[52] C. J. S. Damerell. *Vertex Detectors: The State of the Art and Future Prospects.* RAL-P-95-008.

[53] Philip Sievers. *A Silicon Inner Tracker for the LHCb Experiment.* Ph.D. thesis, University of Zurich (2002).

[54] Z. Asmamaw. *Breakdown voltage measurements of silicon microstrip detectors.* Fermilab (2001).

[55] H. Pernegger. *The silicon ministrip detector of the delphi very forward tracker.* Ph.D. thesis, Hephy Vienna (February 1996).

[56] M. Moll. *Radiation damage in silicon particle detectors - microscopic defects and macroscopic properties.* Ph.D. thesis, University of Hamburg (December 1999). DESY-THESIS-1999-040.

[57] R. Wunstorf. *Systematische untersuchungen zur strahlenresistenz von silizium detektoren für die verwendung in hochenergiephysik-experimenten.* Ph.D. thesis, University of Hamburg (October 1992). DESY-FHIK-92-01.

[58] R. P. Bernhard, C. Lois, St. Heule, M. Needham, A. Vollhardt, and D. Volyanskyy. *Measurements of Prototype Ladders for the Silicon Tracker with a Laser.* LHCb note 2003-075.

[59] M. Agari *et al.* *Test-beam measurements on prototype ladders for the LHCb TT station and Inner Tracker.* LHCb note 2003-082.

[60] F. Lehner, P. Sievers, O. Steinkamp, U. Straumann, A. Vollhardt, and M. Ziegler. *Description and Evaluation of Multi-Geometry Silicon Prototype Sensors for the LHCb Inner Tracker.* LHCb note 2002-038.

[61] N. Virmani, H. Sadrozinski, and T. Ohsugi. *GLAST LAT Silicon Strip Detector (SSD) Quality and Reliability Assurance.* GLAST LAT-CR-00082-03.

[62] M. Krammer. Experience on silicon sensor performance and quality for a large area detector. Talk at Vertex2002, Hawaii, November 4-8, 2002.

[63] CMS Tracker Sensor Working Group. *Specifications for the Quality Control & Assurance of the CMS Silicon Sensors* (2000).

[64] *Supply of Silicon Micro-strip Sensors for the CMS Silicon Strip Tracker (SST)* (2000). Invitation to Tender: IT-2777/EP/CMS. Technical Specification.

[65] U. Heintz. *Evaluation of F-Disk Silicon Microstrip Detectors.* DØ note 3443.

[66] G. Baumann *et al.* *Quality assurance of 100 CMS-OB2 sensors.* LHCb note 2004-105.

[67] F. Lehner, P. Sievers, O. Steinkamp, U. Straumann, and M. Ziegler. *Description and Characterization of Inner Tracker Silicon Prototype Sensors.* LHCb note 2001-036.

[68] J. Gassner, St. Heule, F. Lehner, and C. Lois. *Capacitance measurements on silicon micro-strip detectors for the TT station of the LHCb experiment.* LHCb note 2003-081.

[69] St. Heule. *Simulation und Messung von Silizium-Streifen-Detektoren (Simulation and Measurements of Silicon-Microstrip-Detectors).* Master thesis, University of Zurich (July 2003).

[70] J. Gassner, F. Lehner, and S. Steiner. *The Mechanical Design of the LHCb Silicon Trigger Tracker.* LHCb note 2004-110.

[71] `http://d0server1.fnal.gov/projects/run2b/Silicon/www/smt2b/readout/analogue.htm`.

[72] `http://www.tokyosokki.co.jp/e/product/strain_gauge/list/flead_list.html`.

[73] `http://www.maxim-ic.com/quick_view2.cfm/qv_pk/2815/ln/en`.

[74] `http://www.tokyosokki.co.jp/e/product/strain_gauge/what_strain`.

[75] F. Giordano, M. N. Mazziotta, and S. Rainò. *GLAST LAT Engineering Model Tray - Thermal Test Plan.* GLAST LAT-TD-1037.

[76] R. Baer, S. Ney, M. Steinzig, and E. Swensen. *GLAST Tracker Tray Assembly - Thermal Test Plan.* GLAST HTN-102050-0008-A.

[77] N. van Bakel *et al.* *Performance of the Beetle Readout Chip for LHCb.* Proc. 8th workshop on Electronics for LHC Experiments, Colmar (France), September 9-13, 2002.

[78] S. Shaheen *et al.* *Characterization and quality control of silicon microstrip detectors with an infra-red diode laser system.* Nucl. Instr. and Meth. A **352** (1995) 573.

[79] I. Abt *et al.* *Characterization of silicon microstrip detectors using an infra-red laser system.* MPI-PhE/98-13.

[80] C. Bauer *et al.* *Characterization of Inner Tracker silicon prototype sensors using a 106 Ru-source and a 1083 nm laser system.* LHCb note 2001-121.

[81] `http://scipp.ucsc.edu/groups/glast/detector/`.

[82] N. van Bakel et al. *The Beetle Reference Manual -chip version 1.2.* LHCb note 2002-055.

[83] Y. Ermoline. *Vertex Detector Electronics: ODE Pre-Prototype.* LHCb note 2001-057.

[84] M. Agari *et al.* *Test Beam Results of Multi-Geometry Prototype Sensors for the LHCb Inner Tracker.* LHCb note 2002-58.

[85] M. Needham. *Silicon Tracker Simulation Performance.* LHCb note 2003-015.

[86] O. Steinkamp. *Layout and R&D for an All-Silicon TT Station.* LHCb note 2002-056.

[87] C. Bauer *et al. First Experience and Results from the Hera-B Vertex Detector System.* Nucl. Instr. and Meth. A **418** (1998) 65.

[88] S. Loechner. *Beetle 1.3 Lab Measurements.* Talk in the Beetle Users Meeting 26/11/2003.

[89] S. Heule *et al. Simulation of signal generation on silicon micro-strip detectors for the Silicon Tracker of the LHCb experiment.* LHCb note 2003-159.

[90] M. Needham. *Tracking Performance and Robustness tests.* LHCb note 2003-020.

[91] F. Lehner, C. Lois, and H. Voss. *Measurements on irradiated silicon sensor prototypes for the Inner Tracker of LHCb.* LHCb note 2004-104.

[92] M. Agari *et al. Testbeam Measurements on an Irradiated Prototype Ladder for the LHCb Inner Tracker.* LHCb note 2004-111.

[93] C. Lois, R. Bernhard, M. Needham, A. Vollhardt, and A. Wenger. *Laboratory Measurements on Irradiated Prototype Ladders for the LHCb Inner Tracker.* LHCb note 2004-112.

[94] A. Vasilescu (INPE Bucharest) and G. Lindstroem (University of Hamburg). *Displacement damage in silicon.* on-line compilation.

[95] M. Glaser *et al. New irradiation zones at the CERN-PS.* Nucl. Instr. and Meth. A **426** (1999) 72.

[96] M. Moll, E. Fretwurst, and G. Lindström. *Leakage current of hadron irradiated silicon detectors - material dependence.* Nucl. Instr. and Meth. A **426** (1999) 87.

[97] Su Yong Choi and Frank Lehner. *What do we know about radiation damage in silicon detectors?* DØ note 3803.

[98] D. Bechevet *et al. Results of irradiation tests on standard planar silicon detectors with 7-10 MeV protons.* Nucl. Instr. and Meth. A **479** (2002) 487.

[99] M. Siegler, F. Lehner, M. Needham, and O. Steinkamp. *Expected Particle Fluences and Performance of the LHCb Trigger Tracker.* LHCb note 2004-070.

[100] M. Moll, private communication.

[101] E. Fretwurst *et al.* Proceedings of the Defect Engineering of Advanced Semiconductor Devices Workshop, pp. 39-49, Santorini, Greece, 21-22 April, 1999.

[102] G. Lindström *et al.* (The RD48 (ROSE) Collaboration). *Radiation hard silicon detectors.* Nucl. Instr. and Meth. A **466** (2001) 308.

[103] S. Braibant *et al. Investigation of design parameters for radiation hard silicon microstrip detectors.* Nucl. Instr. and Meth. A **485** (2002) 343.

[104] J. Gassner *et al. Measurements of prototype ladders for the TT station with a Laser.* LHCb note 2004-102.

[105] Minutes of the Beetle Users Meeting 30/11/2004.

[106] S. Marti i Garcia *et al. A model of charge collection for irradiated p+n detectors.* Nucl. Instr. and Meth. A **473** (2001) 128.

[107] F. James. *Minuit.* CERN Program Library Long Writeup D506, 1993.

[108] N. W. Ashcroft and N. D.Mermin. *Solid State Physics* (W. B. Saunders Company, 1976).

[109] G. Lindström, M. Moll, and E. Fretwurst. *Radiation hardness of silicon detectors - a challenge from high-energy physics.* Nucl. Instr. and Meth. A **426** (1999) 1.

[110] M. Moll, E. Fretwurst, M. Kuhnke, and G. Lindström. *Relation between microscopic defects and macroscopic changes in silicon detector properties after hadron irradiation.* Nucl. Instr. and Meth. B **186** (2002) 100.

[111] B. Adeva *et al. Silicon sensor probing and radiation studies for the LHCb Silicon Tracker.* LHCb note 2005-033.

[112] G. Baumann *et al. Pre-Series Sensor Qualification for the Inner Tracker of LHCb.* LHCb note 2005-037.

[113] G. Baumann *et al. Sensor Qualification for the Trigger Tracker of LHCb.* LHCb note 2005-089.

[114] F. Lehner and O. Steinkamp. *Specifications for the Inner Tracker Silicon Sensors* 320 *$\mu m$ thick.* `http://ckm.physik.unizh.ch/tt/sensorprob/`.

[115] F. Lehner and O. Steinkamp. *Specifications for the Inner Tracker Silicon Sensors* 410 $\mu m$ *thick.* `http://ckm.physik.unizh.ch/tt/sensorprob/`.

[116] *Sensor Specifications for the CMS-OB2 HPK Sensors.* `http://lhcb.physik.unizh.ch/tt/sensorprob/S9153-04B.pdf`.

[117] `http://ckm.physik.unizh.ch/tt/sensorprob/`.

[118] J. Gassner, F. Lehner, and S. Steiner. *The Production, Testing and Assembly of the LHCb Silicon Trigger Tracker.* LHCb note 2004-109.

[119] `http://www.mysql.com`.

[120] `http://www.php.net`.

[121] `http://ckm.physik.unizh.ch/tt/`.

# Resumo

Un dos obxectivos principais da física de partículas é a determinación da estrutura fundamental da materia. O modelo actualmente aceptado para a física de partículas elementais, o Modelo Estándar, precisa 12 partículas de materia elementais e catro partículas portadoras de forza para resumir todo o que ata o momento sabemos acerca dos constituíntes máis elementais da materia e as súas interaccións. O Modelo Estándar explica e predí unha ampla variedade de fenómenos, e efectos finos preditos polo modelo foron repetidamente verificados en experimentos de altas enerxías. Sen embargo, hai aspectos que permanecen inexplicados, como a orixe das masas das partículas ou os valores dalgúns parámetros fundamentais.

Calquera teoría de física de partículas require que cada partícula (por exemplo un protón) teña unha antipartícula (neste caso chamado antiprotón), como foi primeiramente sinalado por Dirac [1, 2]. Unha antipartícula ten a mesma masa que a correspondente partícula, pero con algúns números cuánticos, coma a carga eléctrica, opostos. Cando unha partícula atopa a súa antipartícula, ambas se aniquilan e as súas masas transfórmanse en radiación. A existencia de antimateria foi extensamente probada no último século e hoxe en día ten aplicacións na vida cotiá, como é o caso do uso de antielectróns (chamados positróns) en aparellos médicos de imaxe tales coma os tomógrafos PET.[6]

As teorías cosmolóxicas aceptadas actualmente requiren que cantidades iguais de materia e antimateria foran creadas despois do Big Bang. Sen embargo, obsérvase unha asimetría na cantidade de materia e de antimateria presente na Natureza, o cal constitúe unha das características do noso

---

[6] PET (Positron Emission Tomography) é un aparello médico que produce imaxes para a diagnose de enfermidades. Inxéctanse no paciente núcleos radiactivos que se acumulan nos tecidos ou áreas que se queren estudar. Positróns procedentes deses núcleos radiactivos aniquílanse con electróns dos núcleos cercanos, producindo enerxía que emerxe en forma de fotóns. A colecta destes fotóns permite a reconstrucción da área a estudo.

mundo.[7] O desequilibrio observado pode ter a súa orixe na violación CP, un efecto que soamente ocorre con certo tipo de partículas elementais.

O teorema CPT é un dos preceptos máis básicos en física de partículas e trata coas tres transformacións independentes C (conxugación de carga), P (paridade ou inversión espacial), e T (inversión temporal). O teorema CPT afirma que a operación combinada de inversión temporal, conxugación de carga e inversión espacial, en calquera orde, é unha simetría exacta de calquera interacción, é dicir, que baixo as tres transformacións calquera lei física debe ser invariante.[8] Dito doutro xeito, se cada partícula é reemprazada pola súa antipartícula, e as coordenadas espaciais e temporais son invertidas, as leis físicas permanecen inalteradas [4]. No mundo macroscópico estas tres simetrías cúmprense por separado. Por exemplo, un obxecto que vaia de A a B seguirá exactamente a mesma traxectoria pero á inversa, se o tempo é invertido, para volver de B a A.

Sen embargo, o teorema CPT non di nada sobre a operación por separado de unha ou dúas destas transformacións no mundo das partículas elementais. Por exemplo, foi comprobado [5], despois da suxerencia feita por Lee e Yang [6], que cando un aplica a transformación P a unha partícula chamada neutrino, a partícula resultante non existe. Un atopa na Natureza neutrinos a esquerdas e antineutrinos a dereitas, pero non neutrinos a dereitas nin antineutrinos a esquerdas. Este feito é chamado violación de P en interacción feble, que é a interacción que goberna a dinámica destas partículas. A simetría desta interacción é restablecida cando se aplica a transformación CP combinada, o que significa que os neutrinos a esquerdas seguen as mesma leis que os antineutrinos a dereitas.

En 1964 observouse que a simetría CP violábase en sistemas de mesóns-K neutros [7, 8]. Ó contrario que os neutrinos, que son leptóns, os mesóns-K son hadróns, o que significa que, ó igual que os protóns ou neutróns, están formados por quarks. A violación CP pode explicar por que o noso mundo está formado por moita máis materia que antimateria, debido ás pequenas diferencias en que os quarks e antiquarks interaccionan a través da interacción feble. De feito, a violación CP foi proposta tempo atrás por Sakharov [9] coma unha das tres condicións que teñen que ser satisfeitas para ter un Universo con cantidades diferentes de materia e antimateria.

No Modelo Estándar, a violación CP está necesariamente vencellada á

---

[7] Se existiran cantidades iguais de materia e antimateria, acabarían aniquilándose entre elas, deixando un Universo formado só por luz.

[8] De xeito máis preciso, o que son invariantes son os Hamiltonianos que gobernan a dinámica desas partículas.

existencia de polo menos seis sabores de quarks, e está completamente descrita por un único parámetro. Este é unha fase complexa na matriz de Cabibbo-Kobayashi-Maskawa (CKM) [10, 11], a cal parametriza transicións entre diferentes xeracións de quarks a través dun conxunto de catro parámetros independentes.

En calquera caso, a violación CP en mesóns-K neutros é pequena, ó nivel do 0.2%, dificultando a determinación da orixe destas diferencias nas teorías de partículas elementais, como é o caso desta fase complexa na matriz CKM.

Para investigar e medir os parámetros que describen a materia, os físicos fan uso de aceleradores de partículas co fin de romper estas nos seus constituíntes fundamentais. Os principios desta técnica son os seguintes. Un feixe de partículas coñecidas, coma electróns ou protóns, é acelerado a moi altas enerxías empregando campos eléctricos. As partículas son así aceleradas ata velocidades próximas á velocidade da luz, co que adquiren enormes enerxías cinéticas. Usando sofisticados sistemas de imáns, o feixe de partículas é curvado e focalizado. En determinado momento, o feixe é dirixido contra un branco (experimentos de branco fixo) ou contra un segundo feixe de partículas que viaxan en sentido contrario (experimentos colisionadores). Xeralmente, o segundo feixe ten a mesma magnitude pero oposta velocidade, e entón, este tipo de colisión, recibe nome de colisión no centro de masas.

Cando ten lugar a colisión, e debido á alta enerxía das partículas, podemos non só estudar a súa estrutura interna senón tamén crear novas partículas exóticas que non existen no mundo de macroscópico. Nestas colisións altamente enerxéticas, o que interacciona non son as propias partículas que colisionan senón os seus constituíntes fundamentais. Esto é debido á coñecida fórmula de de Broglie [12], a cal, dacordo co principio de dualidade onda-partícula, relaciona a enerxía da partícula coa súa lonxitude de onda asociada segundo $\lambda \propto 1/E$. É preciso usar ondas con lonxitude de onda do mesmo tamaño que os detalles que queren observar. Así, colisións de partículas con altas enerxías permiten o estudo da súa estrutura interna.

Nas colisións entre partículas altamente aceleradas, a súa enorme enerxía está dispoñible non só coma enerxía cinética das partículas resultantes senón tamén coma masa para crear novas partículas. Esto exprésase a través da equivalencia entre masa e enerxía formulada por Einstein no seu famoso artigo de 1905 [13] coma $E = mc^2$. A enerxía ($E$) pode converterse en masa ($m$) e viceversa, co cadrado da velocidade da luz coma factor de conversión. Se as partículas incidentes teñen suficiente enerxía, poden crear novas partículas máis pesadas que elas mesmas. O conxunto de partículas producidas depende esencialmente de varias leis de conservación e da enerxía en centro de masa dispoñible na colisión. Así, os experimentos de altas enerxías, a través de colisións moi enerxéticas de outras partículas, permiten observar partículas máis masivas e máis exóticas que as iniciais, que non se producen baixo circunstancias normais na Natureza.

Moitas das partículas creadas na colisión son altamente inestables, e desintégranse en estados máis estables dando lugar a máis partículas. Esencialmente, a vida media das partículas antes da súa desintegración vén dada pola forza da interacción que está implicada, e varía entre uns $10^{-23}$ s para a interacción forte e uns $10^{-10}$ s para interacción feble. Ó final, remátase de novo con un conxunto de partículas "estables" e ben coñecidas, coma protóns, neutróns, electróns, neutrinos e muóns. Xeralmente prodúcese un número moi elevado delas: tras a colisión entre dous protóns a moi altas enerxías, remátase tipicamente con centos de partículas.

A produción e desintegración dunha determinada partícula depende das forzas que gobernan o comportamento dos seus constituíntes e, polo tanto, contén información acerca de como interaccionan os constituíntes básicos da materia. Pódese extraer esta información a partir do estudo das características de novas partículas, como as masas e vidas medias, ou a través do estudo das probabilidades das diferentes canles de desintegración de estados inestables en distintos estados. Sen embargo, para comprender a dinámica subxacente, temos que analizar a cinemática. Por tanto, tras a colisión, precisamos contar, localizar e identificar todas as partículas producidas para poder reconstruír o proceso. Esto faise cun conxunto de detectores de partículas moi sensibles e especializados, que son capaces de medir un determinado grupo de propiedades das partículas tales coma carga, masa ou enerxía.

O obxectivo desta tese é a descrición do funcionamento e características dos detectores de micropistas de silicio que van ser empregados no Silicon Tracker do experimento LHCb. O LHCb vai ser instalado no Large Hadron Collider (LHC) [14], un acelerador de partículas que está sendo construído no CERN [15], nun anel subterráneo de 27 km de circunferencia situado na fronteira entre Francia e Suíza. En LHC, dous feixes de protóns a unha enerxía en centro de masas de 14 TeV, colisionarán en catro puntos diferentes ó longo do túnel. Ao redor dun destes puntos de colisión estará instalado o espectrómetro LHCb (ver Figura 11.21). Unha vez rematado o LHC, ademais de ser o acelerador con máis alta enerxía, vai ter os feixes máis intensos nunca acadados.

Dada a enorme enerxía de LHC, novas partículas, non observadas nunca, poden aparecer tras as colisións. Estas desintegraranse moi rápido, pero ofre-

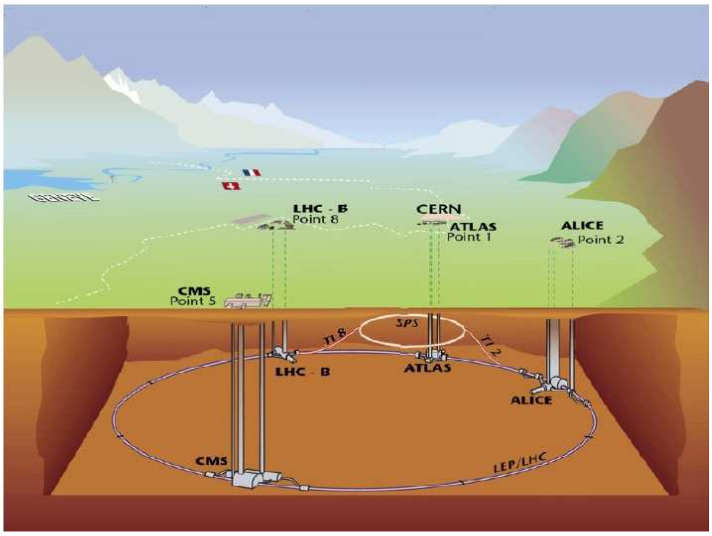

Figure 11.21: O acelerador LHC no CERN, cos catro puntos de colisión sinalados cos nomes dos experimentos que se van instalar en cada un deles.

cerán a posiblidade de explorar a dinámica e interaccións entre constituíntes básicos da materia. Estudando as taxas de desintegración nas diferentes canles e outros fenómenos pouco frecuentes, os físicos de partículas esperan medir parámetros que describen as interaccións entre os constituíntes fundamentais da materia e, en particular, esperan comprobar se o Modelo Estándar é un modelo axeitado para a descrición das forzas e partículas fundamentais.

O experimento LHCb [17, 19] foi deseñado para realizar medidas de alta precisión de fenómenos de violación CP e desintegracións raras nos sistemas de mesóns-B. Os mesóns-B son estados ligados dun antiquark $b$ e un quark máis lixeiro [8]. O estudo de mesóns-B é un proceso clave na determinación precisa de fenómenos de violación CP dado que, segundo o Modelo Estándar, predinse neles efectos importantes de violación CP. Ademais, acádanse altas estatísticas xa que, en interaccións entre protón-protón ás enerxías empregadas en LHC, estímase que se producirán uns $10^{12}$ pares $b\bar{b}$ anuais.[9] A violación CP espérase que se poña de manifesto en asimetrías dependentes do tempo nas taxas de desintegración de B e $\overline{\mathrm{B}}$ no mesmo estado final, e en asimetrías nas taxas de desintegración de B e $\overline{\mathrm{B}}$ en estados finais CP conxugados específicos. Ademais, será posible realizar as medidas en moitas canles de

---

[9] Ás enerxías empregadas en LHC, a sección eficaz de produción de mesóns-B estímase que andará en torno ós 0.5 mb, o que dará lugar a uns $10^{12}$ pares $b\bar{b}$ anuais á luminosidade nominal de $\mathcal{L}= 2 \times 10^{32}$ cm$^{-2}$ s$^{-1}$.

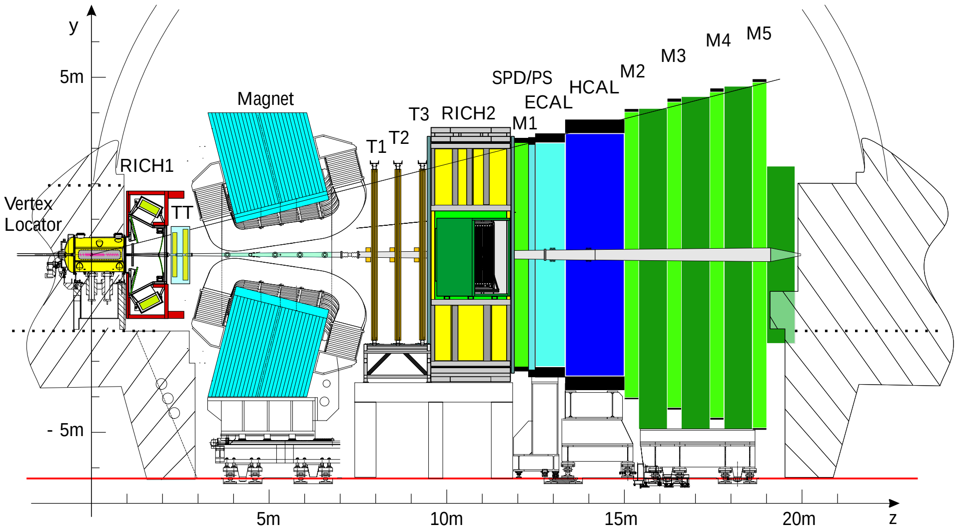

Figure 11.22: Sección vertical do espectrómetro LHCb.

desintegración diferentes, permitindo sobre-restrinxir os parámetros e, posiblemente, atopar inconsistencias que suxiran a existencia de nova física máis alá do Modelo Estándar.

Como foi sinalado anteriormente, para medir as taxas das diferentes desintegracións, todos os produtos da desintegración teñen que ser identificados. Para facer esto, detectores de partículas especializados miden un conxunto específico de propiedades das partículas, tales coma momento, carga, masa ou enerxía. Un elemento central de calquera experimento de altas enerxías é o sistema de trazado, o cal rexistra as traxectorias das partículas cargadas creadas na colisión. Xunto cun campo magnético, permite ademais a determinación do momento de ditas partículas.

Unha sección vertical do espectrómetro LHCb amósase na Figura 11.22. En LHCb, precísase unha excelente resolución en momento tanto para a medida precisa da masa invariante dos candidatos a desintegracións de mesóns-B, coma para separar o sinal dos mesóns-B do fondo. Para iso, é necesaria unha determinación precisa das traxectorias. Decidiuse construír o sistema de trazado combinando dúas tecnoloxías de detección diferentes: a rexión externa, lonxe da tubería do feixe, está cuberta por tubos de deriva e recibe o nome de Outer Tracker. A rexión interna, en torno á tubería do feixe, onde a densidade de partículas é maior, está cuberta por detectores de micropistas de silicio e recibe o nome de Silicon Tracker. Estudos baseados en simulacións indican que unha resolución dunhas 60 $\mu$m é adecuada para o Silicon

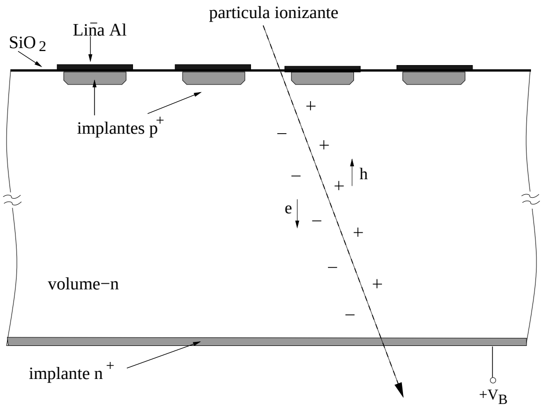

Figure 11.23: Esquema da operación básica dun detector de silicio con volume de detección tipo $n$, onde se amosan os implantes $p^+$ illados dos electrodos de Al por unha capa de $SiO_2$. Basicamente, é un díodo polarizado en inversa, operado a unha voltaxe suficiente para baleirar de portadores libres de carga todo o volume $n$.

Tracker. Os detectores de micropistas de silicio son obleas de silicio dopado $n$ moi finas, con espesores entre 320 e 500 $\mu$m, onde se empregan técnicas fotolitográficas e de gravado para introducir pistas moi finas de silicio dopado $p^+$. A sección vertical dun destes aparellos amósase na Figura 11.23. Os tamaños dos sensores típicos son uns $10 \times 10$ cm$^2$ con ao redor de 500 pistas paralelas dunhas 50 $\mu$m de anchura, con centros separados 200 $\mu$m aproximadamente. Cada unha das micropistas forma co volume de silicio $n$ unha unión $pn$. Cando unha partícula cargada atravesa o detector de micropistas xera pares electrón-oco. Aplicando unha polarización inversa ás unións $pn$, a carga é recollida nas pistas $p^+$. Unha lectura indivual das pistas $p^+$ permite a determinación da posición pola que a partícula atravesou o detector mediante a análise dos sinais xerados en cada pista. Unha profunda comprensión das propiedades dos detectores de micropistas de silicio e a optimización dalgúns dos parámetros do seu deseño, coma por exemplo o espesor ou a separación entre os centros das pistas para alcanzar o rendemento desexado, son os principais obxectivos desta tese.

O traballo presentado nesta tese supón unha importante contribución á comprensión das propiedades de detectores de micropistas de silicio para facer posible a súa utilización no Silicon Tracker [10] do experimento LHCb. Anque

---

[10] O grupo Silicon Tracker está composto por uns 50 investigadores de seis institutos: Max Plank Institut für Kernphysik, Heidelberg; Kiev Institute for Nuclear Research; Laboratoire de Physique des Hautes Energies, Lausanne; Budker Institute for Nuclear Physics,

este tipo de detectores foron utilizados con éxito na última década para a localización precisa de vértices en varios experimentos de colisionadores,[11] o seu emprego nun tracker de grande superficie requeriu da realización de estudos específicos e detallados, non só para demostrar que o seu uso en LHCb é viable, senón tamén para axudar na súa implementación proporcionando coñecementos sobre os seus parámetros de funcionamento.

Presentáronse varias probas realizadas en sensores de micropistas de silicio para o Silicon Tracker, empezando pola caracterización de diferentes prototipos ata as probas finais nos detectores que están sendo instalados no CERN.

Tres grupos de sensores, con espesores de 320, 410 e 500 $\mu$m, respectivamente, e con distancias entre centros das pistas de aproximadamente 200 $\mu$m, foron caracterizados coma parte dos estudos levados a cabo polo grupo Silicon Tracker para a optimización da xeometría dos sensores, co fin de garantir un funcionamento eficiente e fiable do detector. A este respecto, o primeiro paso foi unha caracterización eléctrica exhaustiva de todos os sensores prototipo, que foi presentada no Capítulo 6. Os mellores sensores de cada grupo, baseándose fundamentalmente nos resultados das correntes de fuga e voltaxes de ruptura, foron seleccionados para construír módulos con pistas de ata 33 cm de lonxitude.

Estes módulos foron probados con láser e en probas con feixe, como foi explicado nos Capítulos 8 e 9, respectivamente. Para determinar os seus puntos de traballo, leváronse a cabo varridos de voltaxe de polarización para todos os módulos. Os resultados amosan que a carga recollida nos módulos alcanza un *plateau* a $2-2.5$ veces a voltaxe de baleiramento dos sensores. Estudáronse características da forma do pulso, e viuse que formas de pulso que satisfán as especificacións para o Silicon Tracker poden alcanzarse se se usan parámetros de forma do pulso nos chips de lectura, $V_{fs}$, de 400 mV ou menos. Ademais, viuse unha clara perda da carga recollida na rexión situada entre dúas pistas de lectura en todos os prototipos que tivo que ser considerada no espesor final dos sensores.

A bancada de probas co láser permitiu unha caracterización rápida do funcionamento dos módulos, anque se viu que, para medidas futuras con esta montaxe, era necesario mellorar a estabilidade da altura do pulso. As medidas nas probas con feixe permitiron investigar, ademais, o cociente sinal-ruído, resolución, eficiencia e taxa de ruído dos módulos prototipo. Como se

---

Novosibirsk; Universidade de Santiago de Compostela; Physik-Institut der Universität Zürich.

[11] Incluíndo LEP, CESR, PEP, KEK, e Tevatron.

pode ver claramente nas medidas aquí presentadas, os sensores de 320 $\mu$m de espesor non dan suficiente $S/N$ para proporcionar plena eficiencia de detección en módulos con pistas de 33 cm de lonxitude. Polo tanto, decidiuse que sensores cun mínimo de 410 $\mu$m de espesor deberían usarse na estación TT. A decisión final do espesor dos sensores que se empregarían baseouse nestes resultados xunto con estudos de simulación de dispersión múltiple no detector, e finalmente escolleuse que fora 500 $\mu$m. Para o Inner Tracker, escolléronse sensores de dous espesores: silicio de 320 $\mu$m para os módulos de 11 cm de lonxitude, e silicio de 410 $\mu$m para os módulos de 22 cm de lonxitude.

Os módulos vanse construír a temperatura ambiente, pero van ser operados por debaixo de 5°C. Os diferentes coeficientes de expansión térmica dos materiais usados na construción dos módulos van producir estrés mecánico. No Capítulo 7, presentamos resultados de medidas térmicas e termomecánicas realizadas nun módulo de proba. Estudouse como a estrutura formada polos sensores de silicio, os seus soportes mecánicos e os híbridos reacciona ante cambios de temperatura, demostrando que non se producen deformacións significativas. Ademais, foi determinado o perfil de calor producido polos chips de lectura ó longo do módulo. Amosouse que o sistema de enfriamento elimina a calor eficientemente e, polo tanto, non se prevén efectos importantes no funcionamento dos detectores. Foi tamén demostrado que a calor é transportada polo aire circundante e non polos raís de fibra de carbón.

Particularmente importante é, ademais, a cuestión da resistencia á radiación e o dano a longo prazo dos sensores no Silicon Tracker, dado o feito de que este vai cubrir a rexión de baixo ángulo con respecto á tubería do feixe en LHC. Como se amosou no Capítulo 10, levamos a cabo un estudo de irradiación con tres sensores LHCb IT prototipo e unha estrutura de probas CMS, que foron expostos a protóns de 24 GeV/c ata fluencias de $1.9 \times 10^{13}$ p/cm$^2$ e $6.3 \times 10^{13}$ p/cm$^2$, equivalentes a 7 e 20 anos de operación na parte máis interna do Inner Tracker, respectivamente. Seguiuse o esquema estándar de temperado durante 80 minutos a 60°C. As fluencias de protóns obtivéronse a partir de medidas de activación de follas de aluminio. Viuse que os sensores alcanzaban o total baleiramento en torno ós 50 V despois da irradiación coa dose máis baixa. Esta voltaxe de baleiramento é máis baixa incluso cá inicial, e dá suficiente marxe para sobre-polarizar os sensores. A constante de dano por radiación e o factor de dureza foron extraídos para protóns de 24 GeV a partir das medidas de corrente de fuga, e obtivéronse os valores $\alpha = 2.78 \times 10^{-17}$ A/cm e $k_\alpha$= 0.61, respectivamente. As capacidades inter-pista e as capacidades de acoplo permanecen basicamente inalteradas tras a irradiación. A capacidade total das pistas dos sensores irradiados á fluencia máis alta amosaron un incremento do 15% en comparación cos valores dos non irradiados. Non se observou un incremento significativo tras a irradiación á fluencia máis baixa.

Un exhaustivo programa de medidas foi levado a cabo cos módulos prototipo construídos cos sensores irradiados. Fíxose un estudo detallado da recolección de carga despois da irradiación e atopouse que o modelo presentado en [106] dá unha boa parametrización dos datos. Sen embargo, dada a modesta dose de radiación comparada coa investigada en [106], os resultados son sensibles a outros efectos, como déficits balísticos debido ó corto tempo de recollida de carga do preamplificador. A pesar disto, as voltaxes de baleiramento extraídas dos axustes, despois de considerar o efecto inverso do temperado, están en bo acordo coas medidas $C-V$. Levouse a cabo un estudo da dependencia das correntes de fuga coa temperatura, e atopouse a esperada dependencia expoñencial. Realizáronse varridos de pulso para os módulos irradiados. Estas medidas foron de gran utilidade para gañar experiencia coa manipulación de sensores irradiados. En particular, aprendiuse que se debe ter coidado co almacenamento dos sensores entre medidas xa que pode aparecer un efecto significativo polo temperado.

No Capítulo 11 presentamos os resultados do control de calidade realizado nos sensores de pre-produción do Inner Tracker e nos primeiros lotes de sensores recibidos para a estación TT, todos eles fabricados por HPK. Leváronse a cabo inspeccións visuais de todos os sensores para detectar posibles defectos macroscópicos. Atopáronse libres de defectos en torno ó 80% dos sensores, pero foron considerados como válidos para a produción do detector o total dos recibidos. Realizáronse medidas de corrente de fuga en todos os sensores. Viuse que estas eran moi pequenas para todos eles, tipicamente por debaixo de 500 nA a 500 V, e moi parecidas entre sensores. Todos os sensores verifican as especificacións no tocante ás correntes de fuga. Ningún sensor amosou ruptura por debaixo de 500 V. Ademais, comprobouse que as correntes non variaban coa aplicación de baleiro para a suxeición dos sensores á estación de probas e que, asimesmo, eran repetibles e permanecían estables ó longo do tempo de funcionamento, tal e como foi verificado nunha mostra do 15% dos sensores escollidos ó chou. Medíronse as voltaxes de baleiramento de todos os sensores. Os sensores HPK-320 e HPK-410 teñen voltaxes de baleiramento entre 70-140 V, e os sensores HPK-500 alcanzan o total baleiramento entre 165-250 V, cumprindo as especificacións. Medíronse as capacidades de acoplo nun 20% dos sensores usando unha estación de probas automática. Das 14080 pistas inspeccionadas, catro foran sinaladas por HPK coma defectuosas por ter buratos no óxido ou por ter valores da capacidade fóra das especificacións. Destas, nós puidemos atopar tres. Non atopamos, sen embargo, unha sinalada como contendo buratos no óxido. Non atopamos ningunha pista mala adicional. Realizáronse medidas metrolóxicas en todos os sensores para determinar o paralelismo e a precisión no corte dos sensores, o alombamento dos sensores, así coma outras características xeométricas, importantes para a resolución espacial e os procesos de ensamblaxe. Segundo a clasificación global, cinco dos 147 sensores analizados clasificáronse coma grao B, mentres que todos os demais acadaron o grao A. Os sensores de grao-A débense usar nas partes internas do detector, onde a densidade de partículas é maior, mentres que os de grao-B poderían usarse para as partes externas ou gardarse para recambios. Todos os sensores pasaron os criterios de aceptación e pódense usar para a produción de módulos.

Os resultados presentados nesta tese amosan que a construción dun detector de trazas de grande superficie pode ser conxugado cos requerimentos de ocupación e eficiencia do LHCb. A comprensión das medidas presentadas e discutidas aquí contribuíron á decisión final dos parámetros do detector e dos procedementos de montaxe para o Silicon Tracker. A produción dos módulos para a estación TT e o Inner Tracker xa comenzou en Zurich e no CERN, respectivamente. O control de calidade dos sensores e módulos continúa, e espérase que o detector de trazas ó completo sexa rematado a finais de 2006.